# Aerosol Cloud Interaction for Cooling (ACtIon4Cooling)

## Final Report (D9)

| | |
|---|---|
| Doc. ID | ACtIon4Cooling_FR_D9 |
| Issue | 2.9 |
| Date | 2026-02-20 |
| Prepared by | A. Argyrouli, P. Hedelt |
| Status | Under review |

German Aerospace Center - Remote Sensing Technology Institute (DLR-IMF)
German Aerospace Center – Physics of the Atmosphere Institute (DLR-IPA)
National Observatory Athens (NOA ReACT)
University Leipzig

ACtIon4Cooling - ESA contract number 4000147715

| | NAME | DATE | Signature |
|---|---|---|---|
| LEAD AUTHOR(S) | Pascal HEDELT<br>Athina ARGYROULI | 20/02/2026 | |
| Contributing authors | D. Efremenko, S. Gross, Q. Li,, V. Amiridis, A. Tsekeri, A. Gialitaki, J. Quaas, A. Karipis, H. Luo | | |
| REVIEWED BY | Michael EISINGER | XX/XX/2026 | |
| | Christian RETSCHER | XX/XX/2026 | |
| DISTRIBUTED TO | ESA<br>ACtIon4Cooling Consortium | | |

## CHANGE RECORD

| Issue | Date | Change |
|---|---|---|
| 1.9 | 2025-12-03 | First version including RB 1.9 and TN1.9 |
| 2.0 | 2026-02-09 | Updated version 2.0 including ESA feedback from 30. January 2026 |
| 2.9 | 2026-02-20 | Version submitted for FR. Changes/Updates:<br>Updated Chapter 2<br>Updated Chapter 3<br>New Chapter 4: Scientific Analysis<br>New Chapter 5: Datapool<br>Updated References |
| | | |

# TABLE OF CONTENTS

# List of Figures

# List of Tables

# Applicable Documents

The following project documents contain provisions which, through reference in this text, become applicable to the extent specified in this document.

**Table 1** List of Applicable Documents

| Document Title | | Document ID | Issue |
|---|---|---|---|
| [AD01] | AEROSOL AND CLOUD INTERACTIONS IMPACT IN THE CONTEXT OF SOLAR RADIATION MANAGEMENT - EXPRO+ Statement of Work | ESA-EOP-S-SOW-0195 | 1.0 |

# Reference Documents

The following documents are referenced in this document. They have been used (in the sense of tailoring) to prepare the document on hand.

**Table 2** List of reference documents

| Title | |
|---|---|
| [RD01] | European Commission, Joint Research Centre, Bailey, G., Farinha, J., Mochan, A. and Polvora, A., Eyes on the Future - Signals from recent reports on emerging technologies and breakthrough innovations to support European Innovation Council strategic intelligence - Volume 1, Publications Office of the European Union, Luxembourg, 2024, https://data.europa.eu/doi/10.2760/144136, JRC137811. |
| [RD02] | United Nations Environment Programme (2023). One Atmosphere: An independent expert review on Solar Radiation Modification research and deployment. Kenya, Nairobi. |
| [RD03] | World Meteorological Organization (WMO). (2024). *State of the Global Climate 2023*. WMO-No. 1347.Available online: https://library.wmo.int/idurl/4/68835 (accessed: 02/05/2024) |
| [RD04] | UNEP (2024). Executive summary. In Emissions Gap Report 2024: No more hot air … please! With a massive gap between rhetoric and reality, countries draft new climate commitments. United Nations Environment Programme (UNEP). Nairobi. https://doi.org/10.59117/20.500.11822/46404 |
| [RD05] | NASEM. Reflecting Sunlight: Recommendations for Solar Geoengineering Research and Research Governance. National Academies Press; 2021. https://doi.org/10.17226/25762 |
| [RD06] | European Commission: Directorate-General for Research and Innovation & Group of Chief Scientific Advisors. (2024). Solar radiation modification. Publications Office of the European Union. DOI 10.5281/zenodo.14283096 |
| [RD07] | European Commission: Directorate-General for Research and Innovation, Opinion on solar radiation modification – Ethical perspectives, Publications Office of the European Union, 2024, https://data.europa.eu/doi/10.2777/951016 |
| [RD08] | European Commission: Group of Chief Scientific Advisors and Directorate-General for Research and Innovation, Solar radiation modification, Publications Office of the European Union, 2024, https://data.europa.eu/doi/10.2777/391614 |
| [RD09] | Copernicus Climate Change Service (C3S) and World Meteorological Organization (WMO), 2025: European State of the Climate 2024, climate.copernicus.eu/ESOTC/2024, doi.org/10.24381/14j9-s541 |
| [RD10] | Redmond Roche, B.H. and Irvine, P.J. (2024) Deliverable 2.1: Scoping notes on the state of solar radiation modification (SRM) research, field tests, and related activities. Co-CREATE Project. Available on the Co-CREATE Website (pending EC approval) |
| [RD11] | Redmond Roche, B. H. and Irvine, P. J. (2025). Deliverable 2.3: Case studies of solar radiation modification (SRM) field tests and related activities. Co-CREATE Project. Available on the Co-CREATE Website (pending EC approval) |
| [RD12] | National Academies of Sciences, Engineering, and Medicine. (1992). *Responsible science: Ensuring the integrity of the research process: Volume I*. Washington, DC: The National Academies Press. https://doi.org/10.17226/1864 |
| [RD13] | Burns, W. and Talati, S. (2025). *The Solar Geoengineering Ecosystem: Key Actors Across the Landscape of the Field*. Jan. 2025, https://www.sgdeliberation.org/dsg-publications/the-solar-geoengineering-ecosystem-key-actors-across-the-landscape-of-the-field |
| [RD14] | World Meteorological Organization (WMO). (2023). State of the Global Climate 2022. WMO-No. 1316. Available online: https://public.wmo.int/publication-series/state-of-global-climate-2022 (accessed 02 May 2024). |

# Relevant Websites

**Table 3** List of relevant websites

| Reference ID | | URL | Last accessed |
|---|---|---|---|
| [URL01] | ESA ACtIon4Cooling project website | https://climate.esa.int/en/solar-radiation-modification/action4cooling/ | 14 Feb 2026 |
| [URL02] | ESA ACtIon4Cooling LinkedIn Group | https://www.linkedin.com/groups/10061777 | 14 Feb 2026 |
| [URL03] | Co-CREATE | https://co-create-project.eu | 14 Feb 2026 |
| [URL04] | European Group on Ethics | https://research-and-innovation.ec.europa.eu/strategy/support-policy-making/scientific-support-eu-policies/european-group-ethics_en | 14 Feb 2026 |
| [URL05] | CleanCloud | https://projects.au.dk/cleancloud/cleancloud-project | 14 Feb 2026 |
| [URL06] | CleanCloud Arctic campaigns | https://projects.au.dk/cleancloud/cleancloud-project/objectives/activities/campaigns/arctic-spring-campaign | 14 Feb 2026 |
| [URL07] | SilverLining (co-founder to University of Washington MCB program) | https://www.silverlining.ngo/university-of-washington-marine-cloud-brightening-program | 14 Feb 2026 |
| [URL08] | SilverLining Roadmap for Climate Intervention Research | https://www.silverlining.ngo/reports/roadmap-for-climate-intervention-research | 14 Feb 2026 |
| [URL09] | University of Washington MCB program | https://atmos.uw.edu/faculty-and-research/marine-cloud-brightening-program/ | 14 Feb 2026 |
| [URL10] | ACTRIS | https://www.actris.eu/ | 14 Feb 2026 |
| [URL11] | Climate Intervention | https://climateinterventions.org/explore-interventions/ | 14 Feb 2026 |
| [URL12] | Stratospheric Controlled Perturbation Experiment (SCoPEx) Advisory Committee | https://salatainstitute.harvard.edu/wp-content/uploads/2025/04/Final-SCoPEx-AC-Report-With-Appendices.pdf | 14 Feb 2026 |
| [URL13] | SPICE Project Cancelled – The Guardian | https://www.theguardian.com/environment/2012/may/16/geoengineering-experiment-cancelled | 14 Feb 2026 |
| [URL14] | EMODnet Human Activities | https://emodnet.ec.europa.eu/en/human-activities | 14 Feb 2026 |
| [URL15] | ARIA – Exploring Climate Cooling | https://www.aria.org.uk/opportunity-spaces/future-proofing-our-climate-and-weather/exploring-climate-cooling | 14 Feb 2026 |
| [URL16] | ARIA (Advanced Research and Invention Agency) | https://www.aria.org.uk/ | 14 Feb 2026 |
| [URL17] | AERIS Calipso (Cloud-Aerosol Lidar and Infrared Pathfinder Satellite Observation ) | https://www.aeris-data.fr/en/projects/calipso-4/ | 14 Feb 2026 |
| [URL18] | EarthCare | https://earth.esa.int/eogateway/missions/earthcare | 14 Feb 2026 |
| [URL19] | Earthdata portal | https://www.earthdata.nasa.gov/ | 14 Feb 2026 |
| [URL20] | GRASP project | https://www.grasp-open.com | 14 Feb 2026 |
| [URL21] | Polder product | https://www.grasp-open.com/products/polder-data-release/ | 14 Feb 2026 |
| [URL22] | ESA-ECAMS project | https://www.grasp-earth.com/portfolio/ecams/ | 14 Feb 2026 |

| | | | |
|---|---|---|---|
| [URL23] | NOASS B2SAP project | https://csl.noaa.gov/projects/b2sap/ | 14 Feb 2026 |
| [URL24] | EO datasets for radiation and aerosol monitoring | https://csl.noaa.gov/research/erb/projects/observations.html | 14 Feb 2026 |
| [URL25] | EARLINet Database | https://www.earlinet.org | 14 Feb 2026 |
| [URL26] | CALIPSO database | https://subset.larc.nasa.gov/calipso/login.php | 14 Feb 2026 |
| [URL27] | CALIPSO VFM user guide | https://www-calipso.larc.nasa.gov/resources/calipso_users_guide/data_summaries/vfm/index_v420.php | 14 Feb 2026 |
| [URL28] | MAAP portal | https://portal.maap.eo.esa.int/ | 14 Feb 2026 |
| [URL29] | AERONET | https://aeronet.gsfc.nasa.gov/index.html | 14 Feb 2026 |
| [URL30] | OPAC database | https://aeris-geisa.ipsl.fr/geisa_files/2011/Aerosols/OPAC/ | 14 Feb 2026 |
| [URL31] | Global Volcanism Program, Mount Ruang eruption report | https://volcano.si.edu/volcano.cfm?vn=267010#April2024 | 14 Feb 2026 |

# Terms and Abbreviations

Abbreviations and terms specific to this document are summarized below.

**Table 4** List of abbreviations

| Abbreviation | Meaning |
|---|---|
| **ACI** | Aerosol-Cloud Interactions |
| **AAI** | Absorbing Aerosol Index |
| **ACTRIS** | Aerosol, Clouds, and Trace gases Research Infrastructure |
| **AE** | Ångstrom exponent |
| **AERONET** | AErosol RObotic NETwork |
| **AIMS** | Australian Institute of Marine Science |
| **AIS** | Automated Identification Signal |
| **AOD** | Aerosol Optical Depth |
| **AOT** | Aerosol Optical Thickness |
| **ASKOS** | Atmospheric Sounding of the Kerguelen Archipelago |
| **ATLID** | ATmospheric LIDar |
| **C3S** | Copernicus Climate Change Service |
| **CA** | Cloud Albedo |
| **CAARE** | Coastal Atmospheric Aerosol Research and Engagement |
| **CAS** | Cloud Aerosol Spectrometer |
| **CALIPSO** | Cloud-Aerosol Lidar and Infrared Pathfinder Satellite Observation |
| **CALIOP** | Cloud-Aerosol Lidar with Orthogonal Polarization |
| **CBH** | Cloud Bottom Height |
| **CCN** | Cloud Condensation Nuclei |
| **CCP** | Cloud Combination Probe |
| **CCS** | Carbon Capture and Storage |
| **CCT** | Cirrus Cloud Thinning |
| **CDR** | Carbon Dioxide Removal |
| **CER** | Cloud Effective Radius |
| **CF** | Cloud Fraction |
| **CGT** | Cloud Geometrical Thickness |
| **CIRRUS-HL** | Cirrus in High Latitudes |
| **CIP** | Cloud Imaging Probe |
| **CMIP6** | Coupled Model Intercomparison Project Phase 6 |
| **COT** | Cloud Optical Thickness |
| **CTH** | Cloud Top Height |
| **DEGREES** | DEveloping country Governance REsearch and Evaluation for SRM |
| **DIAL** | DIfferential Absorption Lidar |

| | |
|---|---|
| **DSCOVR** | Deep Space Climate Observatory |
| **E-PEACE** | Eastern Pacific Emitted Aerosol Cloud Experiment |
| **EARLINET** | European Aerosol Research LIdar NETwork |
| **EarthCARE** | Earth Clouds, Aerosols and Radiation Explorer |
| **EDF** | Environmental Defense Fund |
| **EGD** | European Green Deal |
| **EGE** | European Group on Ethics |
| **EMODnet** | European Marine Observation and Data Network |
| **ENVISAT** | ENVIromental SATellite |
| **EO** | Earth Observation |
| **EPIC** | Earth Polychromatic Imaging Camera |
| **EPSRC** | Engineering and Physical Sciences Research Council |
| **ERFaci** | Effective radiative forcing due to aerosol-cloud interactions |
| **ESOTC** | European State of the Climate |
| **ERS-2** | European Remote Sensing Satellite |
| **EU** | European Union |
| **FCI** | Flexible Combined Imager |
| **GCSA** | Group of Chief Scientific Advisors |
| **GEMS** | Geostationary Environmental Monitoring Spectrometer |
| **GEOS-5** | Goddard Earth Observing System, Version 5 |
| **GCM** | Global Climate Model |
| **GHG** | Greenhouse Gas |
| **GOME** | Global Ozone Monitoring Experiment |
| **HALO** | High Altitude and LOng range research aircraft |
| **HITRAN** | High-Resolution Transmission Molecular Absorption Database |
| **HSRL** | High Spectral Resolution Lidar |
| **ICON** | ICOsahedral Non-hydrostatic |
| **IMO** | International Maritime Organization |
| **INP** | Ice Nucleating Particle |
| **IRS** | InfraRed Sounder |
| **KNN** | K-Nearest Neighbors |
| **LR** | Longwave Radiation |
| **LWP** | Liquid Water Path |
| **MCB** | Marine Cloud Brightening |
| **ML-CIRRUS** | Formation, Lifetime, Properties and Radiative Impact of Mid-Latitude Cirrus Clouds |
| **MMSI** | Maritime Mobile Service Identity |

| | |
|---|---|
| **MODIS** | MODerate resolution Imaging Spectroradiometer |
| **MODTRAN** | MODerate resolution atmospheric TRANsmission |
| **MSG** | Meteosat Second Generation |
| **MSI** | MultiSpectral Instrument |
| **MTG** | Meteosat Third Generation |
| **NGO** | Non-Governmental Organization |
| **OCRA** | Optical Cloud Recognition Algorithm |
| **OLCI** | Ocean and Land Colour Instrument |
| **OLR** | Outgoing Longwave Radiation |
| **OPAC** | Optical Properties of Aerosols and Clouds |
| **PACE** | Plankton Aerosol Cloud ocean Ecosystem |
| **PANGEA** | Paleoclimate, Archaeology, and Geophysics of Antikythera Island and the Aegean |
| **PCA** | Principal Component Analysis |
| **PIP** | Precipitation Imaging Probe |
| **PLDR** | Particle Liner Depolarization Ratio |
| **PBL** | Planetary Boundary Level |
| **pyDOME** | python-based Discrete Ordinate Method with Matrix Exponential |
| **RF** | Radiative Forcing |
| **RFaci** | Radiative forcing due to aerosol-cloud interactions |
| **RHi** | Relative Humidity with respect to Ice |
| **ROCINN** | Retrieval of Cloud Information using Neural Networks |
| **RTM** | Radiative Transfer Model |
| **SAGE** | Stratospheric Aerosol and Gas Experiment |
| **SAI** | Stratospheric Aerosol Injection |
| **SAPEA** | Science Advice for Policy by European Academies |
| **SATAN** | Stratospheric Aerosol Transport And Nucleation |
| **SCIAMACHY** | SCanning Imaging Absorption spectroMeter for Atmospheric CartograpHY |
| **SCoPEx** | Stratospheric Controlled Perturbation Experiment |
| **SLSTR** | Sea and Land Surface Temperature Radiometer |
| **SPICE** | Stratospheric Particle Injection for Climate Engineering |
| **SO** | Scientific Opinion |
| **SR** | Shortwave Radiation |
| **SSA** | Single-Scattering Albedo |
| **SST** | Sea Surface Temperature |
| **SRM** | Solar Radiation Modification |
| **Suomi NPP** | Suomi National Polar-orbiting Partnership |
| **TEMPO** | Tropospheric Emissions: Monitoring of Pollution |
| **TOA** | Top Of Atmosphere |

| | |
|---|---|
| **TROPOMI** | Tropospheric Monitoring Instrument (aboard Sentinel-5 Precursor) |
| **UAV** | Uncrewed Aerial Vehicle |
| **UN** | United Nations |
| **UNCBD** | United Nations Convention on Biological Diversity |
| **UNEP** | United Nations Environment Programme |
| **UNFCCC** | United Nations Framework Convention on Climate Change |
| **UV-Vis** | Ultraviolet and visible spectral range |
| **VFM** | Vertical Feature Mask |
| **VIIRS** | Visible Infrared Imaging Radiometer Suite |
| **WALES** | WAter vapor Lidar Experiment in Space |

# 1. Introduction

Solar geo-engineering has attracted significant attention in the recent decades. The European Innovation Council's report "Eyes on the future" demonstrates the thematic on "Exploring solar geoengineering as a piece in multifaceted climate change mitigation strategy" [RD01] as a trend of emerging technology and breakthrough innovation. The *ACtIon4Cooling* project is designed to contribute to the global understanding of Solar Radiation Modification (SRM) and its potential role in mitigating climate change. The independent expert review on SRM research by the United Nations Environment Programme (UNEP) [RD02] suggests that our understanding of Aerosol-Cloud Interactions (ACI) could allow for the deployment of SRM approaches with the goal of cooling the Earth within a few years. Such a deployment could potentially help to slow the surface temperature increase and potentially meet the Paris Agreement target of limiting global warming to well below 2°C. According to the State of Global Climate 2023 [RD03], the average global temperature had reached a warming of 1.45°C above the pre-industrial levels in 2023 and future projections show that the warming could reach up to 2.7°C by 2100 [RD04].

While global efforts to reduce Greenhouse Gas (GHG) emissions have been ongoing, including policies to transition to a net-zero energy system (Patt et al., 2022), the severe impacts of climate change persist. Mitigation approaches aimed at reducing carbon dioxide ($CO_2$) emissions and removing excessive GHG concentrations from the atmosphere will likely take decades to produce measurable results, without the deployment of SRM techniques (Parker and Geden, 2016; Matthews and Caldeira, 2007).

This situation highlights the need for further research into SRM techniques that could serve as a temporary or complementary approach to address global temperature rise in the face of urgent climate impacts. Solar Radiation Modification (SRM) refers to deliberate interventions in the Earth's climate system, aiming to modify the Earth Radiation Budget to offset some of the adverse effects of global warming. SRM is not a substitute for emissions reductions, but rather a potential complementary measure that could reduce peak warming and associated risks, particularly if mitigation and adaptation actions are insufficient. Combining climate change mitigation with SRM in a peak-shaving scenario has been proposed to restrict harm into organisms and ecosystem processes (Zarnetske et al., 2021). This peak-shaving strategy considers SRM techniques only as a temporary solution to reduce the peak of mean global temperature rise while reductions on GHG emissions and decarbonization approaches are applied. Assessment of the timeframes for potential SRM deployment is critical [RD05]. Research should not focus solely on the technical feasibility of SRM, but also on the strategic question of when deployment might be appropriate—particularly in relation to the risk of crossing climatic tipping points. One possible scenario involves a climate emergency in which global warming triggers catastrophic consequences, such as extremely high mortality rates or large-scale destruction of infrastructure. In such a case, a planned operational SRM deployment might be activated for a defined duration (Caldeira and Keith, 2010; Buck et al., 2020). In less urgent situations, other SRM deployment frameworks have been proposed. These include phased deployments that become a standard component of climate policy either as a partial or complete substitute for GHG mitigation (MacMartin et al., 2018) or approaches aimed at slowing the rate of warming to maintain a stable rate of temperature change alongside mitigation efforts. SRM could also be used to prevent overshoot of temperature targets in scenarios where mitigation is delayed, thereby flattening the peak of global warming (de Coninck et al., 2018). The SAPEA (Science Advice for Policy by European Academies) Evidence Review Report [RD06] presented the scientific, technical, and societal aspects of Solar Radiation Modification (SRM) as a potential response to climate change.

Importantly, SRM must be viewed as a complementary measure to GHG reduction strategies, not a replacement. This distinction becomes clear when considering impacts that SRM cannot address—such as ocean acidification—which results from elevated atmospheric $CO_2$ concentrations and would persist regardless of SRM deployment (Jin et al., 2022).

## 1.1 Purpose

The *ACtIon4Cooling* project aims to contribute to this research by investigating existing Earth Observation (EO) data to enhance our understanding of SRM-related processes and improve monitoring capabilities. The project's work focuses on SRM detection and attribution, with an emphasis on leveraging natural analogues to study potential radiative effects.

Starting from the scientific understanding of aerosol and cloud effects related to SRM, a solid scientific basis for monitoring, detection capabilities of SRM activities is developed. By making use of observations

from space-borne, ground-based, air-borne and in-situ platforms, *ACtIon4Cooling* will actively contribute to define the requirements for a future satellite mission dedicated to monitoring SRM activities.

This document is the Final Report (Deliverable D9) of the *ACtIon4Cooling* project, which is structured as follows: Chapter 2 provides consolidated preliminary scientific requirements for the *ACtIon4Cooling* project, including a detailed review, assessment and cross-comparison of existing relevant products, datasets, methods, models and algorithms, as well as related range of validity limitations, drawbacks and challenges in. Furthermore, this chapter includes a survey of all accessible associated datasets and models to be used for development and validation and a provision of requirements on improving model estimations, space-borne, air-borne and ground-based data in the context of SRM. Chapter 3 describes the development methods and validation mechanisms. Chapter 4 describes the scientific and technical analysis, impact assessment, risk assessment and scientific and technical roadmap. Chapter 5 provides a description of the pool of all input and output data used in the *ACtIon4Cooling* project. All public outreach activities are described in Chapter 6.

## 1.2 Scope and Limitation

The *ACtIon4Cooling* project focuses on observational analysis and detection challenges relevant to the following three SRM key mechanisms:

- Stratospheric Aerosol Injection (SAI) – releasing reflective particles (e.g., sulfates) into the stratosphere to scatter incoming solar radiation.
- Marine Cloud Brightening (MCB) – enhancing the albedo of marine clouds to reflect more sunlight.
- Cirrus Cloud Thinning (CCT) – modifying high-altitude cirrus clouds to increase outgoing longwave radiation.

It must be emphasized, that *ACtIon4Cooling* does not advocate for SRM deployment but investigates how Earth Observation data can support the monitoring and attribution of SRM-like effects in the atmosphere. None of these technologies can fully counter the effects of elevated GHG concentrations, and each carries substantial uncertainties and risks, requiring rigorous scientific evaluation.

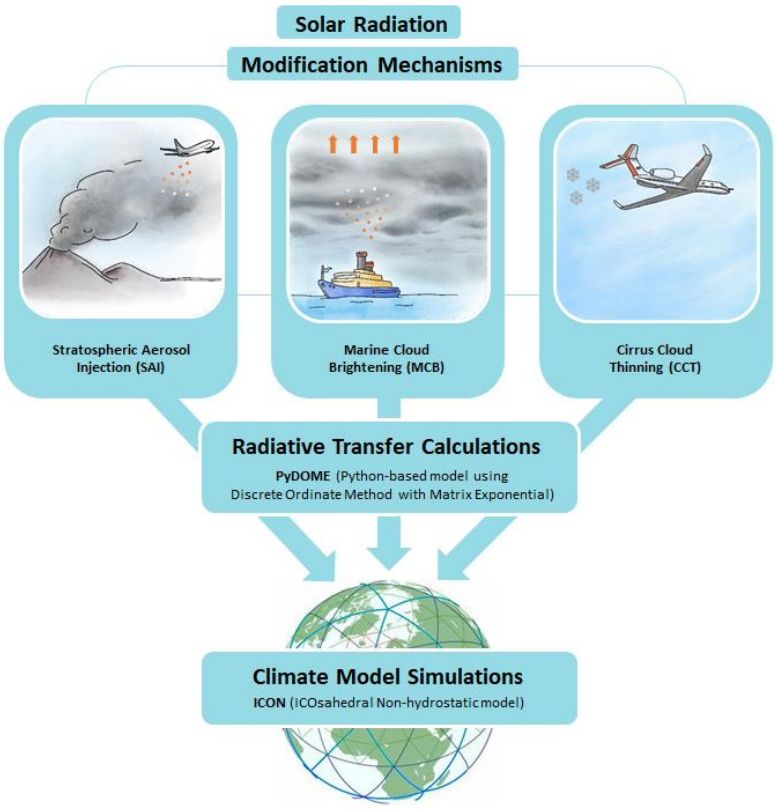


**Figure 1** *ACtIon4Cooling* scheme

The proposed scheme of the *ACtIon4Cooling* research objectives is illustrated in Figure 1. The key SRM mechanisms SAI, MCB and CCT are studied via their natural analogues as proposed in literature. The radiation effects are simulated with the use of pyDOME(python-based Discrete Ordinate Method with Matrix Exponential, Efremenko et al., 2017) radiative transfer model (RTM) and their climatic consequences are studied via ICON (ICOsahedral Non-hydrostatic, Hohenegger et al., 2023) climate model simulations.

The project has the limitation to use only existing datasets, algorithms, models and to report knowledge gaps. Furthermore no new theories or algorithms will be developed in the limited time (one year) of this project. Furthermore, research activities are limited to the fields of own expertise. This implies that impact analysis and risk assessment of SRM on potentially affected areas is mostly restricted to the weather and climate impacts, even though the areas relevant for SRM side-effects assessment are numerous. The major SRM-affected areas are summarized in Table 5.

**Table 5** Areas Affected by a potential SRM deployment

| SRM-Affected Area | Key Impacts | Observational/Modeling Requirements |
|---|---|---|
| Weather & Climate | Changes in global and regional temperature, precipitation, extreme weather (Irvine et al., 2019) | High-resolution climate models, reanalysis data, regional downscaling (Kravitz et al., 2013) |
| Terrestrial Ecosystems | Altered vegetation growth, phenology shifts, terrestrial carbon sink variation (Arora et al., 2014) | Vegetation dynamics models, land surface models (Lombardozzi et al., 2020) |
| Marine Ecosystems | Ocean warming, acidification, shifts in productivity and fish migration (Patti et al., 2022) | Coupled ocean-atmosphere models, biogeochemical models (Dutkiewicz et al., 2015) |
| Biodiversity | Habitat loss, migration barriers, extinction risks (Trisos et al., 2018) | Species distribution modeling, biodiversity-climate interaction models (Urban et al., 2016) |
| Agriculture & Soil | Crop yield changes, soil respiration, degradation (Cheng et al., 2019) | Crop and soil models, land management simulations (Proctor et al., 2018) |
| Food Security | Regional crop failure, global market effects (Pongratz et al., 2012) | Crop forecasting systems, agro-economic models (Fujimori et al., 2019) |
| Water Resources | Altered rainfall, glacial melt, hydrological cycle shifts (Keller et al., 2014) | Watershed models, hydrological cycle simulations (Tilmes et al., 2013) |
| Public Health | UV reduction affecting vitamin D, respiratory impacts from aerosols (Effiong and Neitzel, 2016) | Health risk models, UV-B exposure models (McKenzie et al., 2011) |
| Vitamin D & UV-B | Reduced UV-B limits vitamin D synthesis (Norval et al., 2011) | Radiative transfer modeling with stratospheric aerosols |
| Disease Spread | Vector ecology change (malaria, dengue) (Carlson et al., 2020) | Disease transmission models, mosquito lifecycle models (Ryan et al., 2019) |
| Solar Energy | Reduced photovoltaic output from aerosol scattering (Crook et al., 2017) | Solar irradiance simulation, aerosol-cloud interaction modeling |
| Air Quality | Stratospheric aerosols affect ground-level pollutants (Visioni et al., 2020) | Chemistry-climate interaction models, air quality modeling (Emmons et al., 2020) |
| Local Communities | Cultural, economic, and social disruption (Sugiyama et al., 2020) | Socio-environmental impact assessment, participatory approaches |
| Tourism | Snow and coral-dependent tourism declines (Scott et al., 2020) | Sector-specific modeling, climate impact projections |
| Geopolitics & Governance | International conflict, inequity (Contzen et al., 2024) | Scenario analysis, global risk modeling |
| Ethical & Intergenerational | Intergenerational risk, equity, justice (Macnaghten & Szerszynski, 2013) | Normative foresight analysis, stakeholder deliberation |

More SRM approaches including the surface brightening option by artificially changing the surface albedo properties and the space-based reflectors placed between the Earth and the Sun to block a fraction of solar radiation to enter at the Earth's atmosphere (Baum et al., 2022) have been also conceptually proposed in the literature, but are not addressed in *ACtIon4Cooling*.

## 1.3 Ethical, Governance, and Scientific Advisory Context for SRM Research

The governance of SRM technologies and their ethical implications are central to their development and deployment. There are ongoing debates about the potential risks and benefits of SRM, with some groups strongly opposing it, while others conduct experimental studies in outdoor environments. In the middle ground, there are calls for a balanced approach. Governance frameworks, such as those being examined by the Co-CREATE EU project [URL03] seek to establish principles for responsible SRM research. This includes critical questions on who would finance, control, and regulate SRM technologies, and the potential geopolitical risks that could arise.

The European Group on Ethics in Science and New Technologies (EGE) [URL04] plays a central role in providing independent, multi-disciplinary advice on the ethical and societal implications of SRM and related technologies. In its report, EGE highlights substantial knowledge gaps concerning the effects and risks related to SRM research and potential deployment. It emphasizes that the uncertainties of SRM impacts and risks are of a magnitude that exceed those associated with conventional climate change mitigation and adaptation measures. According to EGE, these potential unintended negative side effects and risks primarily arise from the scientific and technical complexity inherent in SRM systems. On this basis, EGE recommends the establishment of a moratorium on SRM research.

The SAPEA Evidence Review Report [RD06] underscores the complex sociotechnical character of the SRM system. It describes SRM as comprising of biophysical impacts (i.e. changes in temperature and precipitation patterns), energy consumption aspects, infrastructure and technology but also non-technical aspects such as cultural norms and policy frameworks. SAPEA characterized the system as co-evolutionary and dynamic. The report was prepared by an interdisciplinary working group of Europe's leading independent experts and provides a comprehensive overview of the current state of scientific knowledge on SRM. Subsequently, the Group of Chief Scientific Advisors (GCSA) drew on this evidence review to formulate their Scientific Opinion (SO) and corresponding recommendations [RD08].

***SO Recommendation 1*** *- Prioritize reducing GHG emissions as the main solution to avoid dangerous levels of climate change*

The European Green Deal (EGD), the "Fit for 55 package", the goal of 90% emissions reductions by 2040, and achieving net-zero by 2050 are the most important EU climate targets. The suggestion is to continue to treat emissions reductions and adaptation to climate change as the highest priority in reaching net zero by mid-century and minimize "overshoot" and its adverse effects

- Efficiency improvements and substitution of fossil through carbon-free energy sources
- Mitigation of land-use emissions and enhancing sinks (nature-based solutions)
- Carbon Capture and Storage (CCS): A technology aimed at capturing carbon dioxide ($CO_2$) emissions from fossil fuel use in electricity generation and industrial processes, preventing $CO_2$ from entering the atmosphere by storing it underground
- Carbon dioxide removal (CDR) from the atmosphere
- Continue to actively and vigorously invest in research on and deployment of climate mitigation and adaptation.

***SO Recommendation 2*** *- Agree on a EU-wide moratorium of SRM deployment as a measure for offsetting climate warming (and reevaluate periodically, every 5-10 years)*

The many climatic, ecological and social risks and uncertainties of SRM deployment remain high, insufficiently understood and inherently not fully predictable.

- Acknowledge that there is currently insufficient scientific evidence that SRM would avoid dangerous climate change by reducing some of the resulting global warming.
- Model simulations, observations and theoretical considerations indicate that SRM would not completely offset or reverse dangerous climate change but only temperature raise with differing regional changes.

- Recognize that the deep uncertainties associated with possible SRM deployment are inconsistent with the precautionary and “do not harm” principles. The "do no harm" principles refer to a set of ethical and legal guidelines that aim to avoid causing harm to people, the environment, or society, particularly when designing and implementing policies or technologies.

***SO Recommendation 3 -*** *Proactively negotiate a global governance system for research and deployment of SRM by means of a multilateral process with international legitimacy. Given the current state of knowledge, the EU position in these negotiations should be for the non-deployment of SRM in the foreseeable future*

The proposed governance system under the aegis of UN organizations such as UNFCCC, UNEP, WMO, UNCBD

- Base the EU negotiating position on relevant international and EU law.
- Carry out a broad and inclusive public consultation to inform the negotiation of the international agreement.
- Include an exemption in the international treaty, with a clear permitting process that specifies conditions under which to authorize some limited outdoor SRM research, with appropriate consideration of the risks this research poses to the environment and associated social, economic and cultural impacts.
- Ensure that the global governance system addresses the risk of militarization of SRM technologies in an international treaty.
- Invest in operational Earth observation satellite and other technologies to improve the EU’s capability to detect and quantify any undeclared deployment of SRM by public or private actors, anywhere in the world.
- Oppose the use of “cooling credits” derived from SRM technologies in future negotiations on the implementation of multilateral climate agreements.

***SO Recommendation 4 -*** *Ensure that research on SRM is conducted with scientific rigor, responsibly and in accordance with EU ethical principles in research. This should include research into the full range of the direct and indirect effects and unintended impacts of SRM on the climate system, biosphere and humankind, including governance and justice issues.*

The high uncertainties in the potential benefits and risks at the ecosystem, solar energy production, food production, communities of SRM can only be addressed by further research, which should be supported by public funding.

- Create clear ethical requirements for research projects on SRM, whether they are funded publicly or privately.
- Develop guidelines for outdoor research project on SRM.
- Ensure that any public funding for SRM research is additional to and not instead of public funding for research on climate change mitigation and adaptation.
- Impose a moratorium on large-scale outdoor SRM experiments.

***SO Recommendation 5 -*** *Reassess the scientific evidence on risks and opportunities of SRM research and deployment periodically, every 5-10 years*

Including research on both atmospheric physics and chemistry, and on the governance related to SRM could evolve quickly.

- Consider supporting the participation of the scientific community in intergovernmental assessments.
- Set-up citizens’ assemblies to initiate a debate on SRM, promote transparency and develop fair governance.

- Support for the development or adaptation and operationalization of detection-attribution modelling tools, which could cover the range of time horizons and deployment scenarios under consideration.

The aforementioned SO Recommendations from the Group of Chief Scientific Advisors have been taken into consideration by the *ACtIon4Cooling* consortium while conducting the research plan and writing this document.

The goal of *ACtIon4Cooling* is to contribute to SRM research via examination of the so-called “Observational evidence” from existing EO datasets. The modelling capabilities make suggestions on the potential positive and negative climatic effects. *ACtIon4Cooling* cannot examine SRM impacts and risks on soil production, public health, biodiversity, local communities and many other fields where SRM deployment could have an impact. *ACtIon4Cooling* will not deepen into the SRM Governance issues, but it will follow and comply to findings in other relevant EU projects like Co-CREATE and the other relevant funded projects. None of the *ACtIon4Cooling* partners advocate SRM as an alternative to climate change mitigation techniques aiming to the reduction of GHG concentrations emitted to the Earth’s atmosphere.

# 2. Requirements Baseline: User and Scientific Requirements

This chapter provides an overview of the user and scientific requirements related to SRM research, providing the analytical foundation for the *ACtIon4Cooling* project. Section 2.1 provides an overview about aerosol-cloud interactions and the relevance for climate. Section 2.2 describes the general user and scientific needs, giving an overview about knowledge gaps related to SRM as well as apart and current SRM-relevant activities. In addition to this, Section 2.3 presents the scientific objectives and observational needs of each SRM mechanism that will be investigated as part of *ACtIon4Cooling* as well as the objectives and needs related to radiative transfer modelling and global climate modelling. Section 2.4 describes the gaps in existing observational and modelling infrastructure and how *ACtIon4Cooling* will investigate the three SRM mechanisms. To ensure that the *ACtIon4Cooling* requirements baseline reflects the broader expertise in the field of climate intervention and Earth Observation (EO), the results of a targeted survey are described in Section 2.5. A final summary of requirements is provided in Section 2.6.

## 2.1 Aerosol-Cloud Interactions and Climate Relevance

Earth's climate is a complex perturbed system, in which a wealth of chemical, physical and biological processes take place on a wide range of spatial and temporal scales. Global, regional and local regimes are increasingly changing and are driven by changes in the components of the surface-atmosphere system. It is understood that human well-being is subject to climate settings, this specifically holding for populations dependent on favorable climate conditions (Samson et al., 2011) as well as on access to natural resources in specific hot-spot regions. At the same time, specific regions can be considered as natural laboratories for complex processes occurring at the interface between the surface and the atmosphere. Knowledge of the underlying mechanisms driving actual and future climate evolution is identified as one of the grand challenges of Earth Sciences, calling for interdisciplinary approaches.

Among the forcings exerted on these local ecosystems, energy consumption, changes in land and water use, carbon uptake, and injection of aerosols in the atmosphere play a prominent role in cooling the surface and reducing the total precipitation (Levy et al. 2013). Specifically, the latter may change cloud optical properties such as cloud optical thickness (COT) and in consequence cloud albedo (CA) via modulation of the droplet and ice crystal size spectrum and also perturb clouds' lifetime and physical features such as cloud geometrical thickness (CGT), and with it, cloud top height (CTH), as well as horizontal extent (i.e. cloud fraction(CF)). Aerosol-induced alterations of these cloud optical properties are essential to assess and quantify aerosol-cloud interactions (Bellouin et al., 2020; Quaas and Gryspeerdt, 2022). The radiative forcing due to aerosol-cloud interactions (RFaci, also known as Twomey effect or first aerosol indirect effect) is the response of cloud droplet number concentration, Nd, to aerosol and the subsequent cloud albedo change. The adjustments to ACI (a part of which previously was called cloud lifetime effect or second aerosol indirect effect) are the responses of cloud liquid water path (LWP), CGT and CF to these perturbations in Nd. Taken together, the RFaci and the adjustments form the effective radiative forcing due to aerosol-cloud interactions (ERFaci) (Watson-Parris et al., 2022; Forster et al. 2021 IPCC AR6 Chapter 7). Despite extensive research in ACI, there is still at least a 50% spread in total aerosol forcing estimates (Li et al. 2022). This uncertainty is partly linked to the high uncertainty of aerosol absorption monitoring. Eventually, but not exclusively, aerosols can alter the hydrological cycle, mediated by the clouds which act as water reservoirs in the atmosphere and which produce precipitation. It is well-known that aerosol particles can alter the precipitation formation efficiency of clouds, from drying the atmospheric column via direct absorption of sunlight or by serving as cloud condensation nuclei (CCN), thus modulating diffusion and coalescence processes (Wei-Kuo et al., 2012). This brief, yet incomplete, overview of mutual impacts that aerosols and clouds experience in the atmosphere is termed aerosol-cloud-interactions (ACI, Rosenfeld et al., 2013, Fan et al., 2016) and highlights their role as structural proxies for a multitude of chemical and physical atmospheric processes. Therefore, combined monitoring of cloud and aerosol properties together over time and space unveils one of the underlying drivers of a changing climate.

While aerosols are physically categorized according to their size, shape, and chemical composition, satellite-based estimates of aerosol properties rely on their interaction with electromagnetic radiation - mostly at visible or near-visible wavelengths. Passive sensors focus on the aerosols' ability to attenuate impinging sunlight throughout the atmospheric column. The corresponding aerosol optical thickness (AOT) is a measure of aerosol load while its spectral gradient - the Ångstrom exponent (AE) - is an indicator of the effective size of the bulk particles. Long-term AOT patterns are pivotal in setting the spatio-temporal constraints of possible interactions of aerosols with water vapor and clouds. Size is the property that determines

a particle's ability to nucleate a cloud droplet or an ice crystal. The partition of aerosols into absorbing and non-absorbing at ultraviolet (UV) wavelengths through the aerosol index (UVAI) provides further information on particle properties. Active remote sensing instruments, such as lidar and radar, are capable of providing height-resolved observations of aerosols and clouds, respectively, though with much smaller spatio-temporal coverage compared to passive observations. These measurements offer the needed information to verify that observed aerosol layers are indeed occurring at cloud level and, thus, in a position to interfere with them (Costantino and Bréon, 2013). It can therefore be expected that sensors with different spectral, spatial and temporal samplings observe different parts of the aerosol-cloud system.

An increased spatio-temporal resolution of space-borne observations is beneficial to the accuracy of retrieved atmospheric properties, which relies inherently on properly separating between cloudy and cloud-free measurements and on the quantitative inference of the aforementioned aerosol and the concurrent surface and cloud properties. The first procedure is called cloud masking (or clearance) and is not only a prerequisite for an accurate radiation transfer throughout the atmospheric column but also complements the retrieval of aerosol properties for ACI studies, thereby curbing uncertainties in RFaci by constraining the aerosol behavior in clean, pristine, conditions (Gryspeerdt et al., 2023).

The aerosol response to local thermodynamics is a function of temperature, emission rates and particle injection height, which in turn dictate supersaturation levels and updraft velocities inceptive of ACI (Zheng and Rosenfeld, 2015, Chen et al., 2018, Jia et al., 2022). At the same time, the sign and magnitude of height-resolved ACI are still uncertain (Ma et al., 2018). It becomes then clear that the concurrent retrieval and analysis of the vertical layering of aerosols and clouds is one of the cornerstones ACI studies are based upon. This is because any adjustment of in-cloud microphysical properties, such as CER, Nd and LWP to aerosol perturbation will propagate to changes of cloud macro-physical properties such as CTH and CBH (Lelli, 2019).

Quaas et al. (2020) summarized the challenges in quantifying RFaci from satellite retrievals. The problems on the side of aerosol retrievals from passive observations include the lack of (i) vertical information, (ii) proper proxies for the concentration of those particles that are relevant for cloud processes (CCN and INP rather than bulk aerosol; Stier, 2016), and (iii) aerosol data very close to clouds and particularly for cloudy pixels. On the side of the cloud retrievals, the issues include that (i) parameters are not retrieved independently, i.e. Nd is typically computed from COT and CER retrievals (Grosvenor et al., 2018; Dipu et al., 2022), (ii) passive observations generally relate to conditions near cloud top, and (iii) in-cloud conditions and processes such as droplet activation, coagulation and adiabaticity have to be assumed for determining Nd.

## 2.2 General User and Scientific Needs

### 2.2.1 Overview of the knowledge gaps on SRM

#### 2.2.1.1 Knowledge gaps in SAI mechanism

SAI has been reported as the most efficient SRM mechanism to reduce the global mean temperature of the Earth's atmosphere and surface, in an environment with increasing concentrations of GHGs (SAPEA Evidence Review Report [RD06]). Investigation on SAI has been partly motivated by the climate response to large volcanic eruptions of the past (e.g. Hansen et al., 1992; Trenberth et al., 2007; Pitari et al., 2014), which provided strong empirical evidence on the global mean surface temperature reduction after the release of large amounts of reflective particles in the stratosphere. Although volcanic eruptions are imperfect analogues for SAI research - due to the limited time scale and location of particle injections, and the narrow range of the chemical, microphysical and optical properties of the particles injected in the stratosphere - they provide useful insights for SAI research.

The main knowledge gaps related to SAI are:

- **Uncertainties related to climate response:** Although climate models consistently show that SAI can reduce global mean temperature, the magnitude, spatial pattern, and persistence of cooling effects remain uncertain and regional responses can differ substantially.
- **Insufficient understanding of side effects:** SAI may induce changes in atmospheric circulation, stratospheric chemistry, and global precipitation patterns. Potential consequences include ozone depletion, altered precipitation regimes, uneven hemispheric cooling, and impacts on ecosystems.

The risk of regional droughts, shifts in storm tracks, and weakening of monsoon systems is not well quantified.

- **Uncertainties related to injection location and altitude:** Injection latitude and altitude strongly control SAI effectiveness and side effects. Tropical injections are reported to produce longer-lasting and more uniform global cooling than Arctic injections, which are short-lived but regionally focused (Robock et al., 2008; Lane et al., 2007). Injections near the equator at high altitudes (i.e. >20km) are generally more effective than higher-latitude or lower-altitude deployments (Volodin et al., 2011), though the strongest cooling would occur over high-latitude land areas. High-altitude equatorial injections may also weaken the QBO by confining aerosols in the tropics (Aquila et al., 2014; Niemeier et al., 2020). There are indications that multi-latitude (e.g., 15° and 30° N/S) injections may improve performance, since they would produce a more uniform aerosol distribution than equatorial injection alone and may reduce hemispheric AOD imbalance and regional climate risks (MacMartin et al., 2017; Kravitz et al., 2016; Tilmes et al., 2018). A non-uniform global AOD distribution and uneven cooling of the two hemispheres, could lead in reduction in tropical cyclones frequency and droughts in in semi-arid regions close to the tropics (e.g. Haywood et al., 2013; Jones et al., 2017).
- **Uncertainties related to the nature of the injected materials and environmental risks:** Aerosols of sulfuring nature are associated with ozone depletion and adverse regional effects on temperature and water cycles (e.g. Abiodun et al., 2021; Quaraine et al., 2025), which counter the potential SAI benefits. For example, direct injections of condensable $H_2SO_4$ vapor have been suggested as potentially more effective compared to non-condensable $SO_2$ vapor, as it would prevent the particles from becoming too large (and thus less efficient in sun-light scattering; e.g. Weisenstein et al., 2022), but also it may exert heating of the lower stratosphere with effects on atmospheric composition and climate. Direct injections of $H_2S$ also aid in faster formation of $H_2SO_4$ while due to its lower molecular weight, the mass of $H_2S$ needed would be half that of $SO_2$ (Moore et al., 2010; Robock et al., 2009). Ultra-fine particles from alternative materials such as calcium carbonate, alumina, diamond or titania (Pope et al., 2012; Keith et al., 2016) have also been proposed to partly alleviate some of the side-effects of sulfates. Nevertheless, to date research on alternative materials for SAI remains limited both in terms of laboratory studies and modelling efforts. As a result, key aspects such as their efficiency and potential side effects in atmospheric chemistry, radiation and atmospheric dynamics are not well understood yet.
- **Termination shock risk:** SAI may mask warming, but an abrupt termination would result in high temperature re-emergence, which may be more damaging for the natural and social ecosystems, than the gradual increase of temperature due to climate change, since they will have a much shorter time to adapt. Different methodologies have been proposed for SAI temporary intervention, with (a) gradual increase of SAI (Kravitz et al., 2015), (b) temporary intervention, that will last decades or centuries, for preventing dangerous tipping-points (Lawrence et al., 2018; MacMartin et al., 2018; Tilmes et al., 2016; 2020), and (c) gradual phasing in and gradual phase out.
- **Modeling related uncertainties:** To accurately capture the multifaceted nature of SAI, a wide array of climate model capabilities is required including:
  - Fully interactive aerosol microphysics, chemistry, radiation, transport and dynamics in the stratosphere and troposphere: The distribution of the particles in the stratosphere after the injections strongly depend on the aerosol representation in the model (e.g. see Laakso et al., 2021; 2024) as well as any chemical, dynamical and radiative processes the particles may undergo in the stratosphere (Pitari et al. 2014; Mills et al. 2017).
  - Land, ocean and cryosphere coupling
  - High spatial resolution, for properly describing the sub-grid atmospheric processes.
- To date, only few climate models have the necessary capabilities (Pitari et al., 2014; Tilmes et al., 2022; Visioni et al., 2021). Further, multi-model ensemble experiments such as the Geoengineering Model Intercomparison Project (GeoMIP), have revealed substantial inter-model spread in predicted modeling outcomes (Pitari et al., 2014; Kravitz et al., 2015; Tilmes et al., 2021) [RD14]. Thus, an multi-model ensemble framework would be best suited for SRM research as it could aid in constraining simulations, quantifying model uncertainties, and evaluating how various elements

influence the effectiveness of SAI, and why. Long simulation times (century scale) are also required to capture changes in particular processes and weather extremes (e.g. Moore et al., 2010).

- **Limited observational constraints:** Observations of stratospheric aerosols remain sparse. Satellite retrievals have limited capability to accurately resolve particle size and composition, and in situ aircraft measurements are rare and geographically constrained. This limits model validation and understanding of aerosol evolution.
- **Low level of technological readiness:** The level of technological readiness for the deployment of SAI is currently very low, since there is a limited number of platforms which could potentially carry and inject megaton-scale aerosol amounts at stratospheric altitudes. This also makes an initial analysis of the energy budget needed for SAI extremely challenging. While specialized aircraft designs and balloon-based systems have been proposed, none have been demonstrated at scale. Infrastructure costs, engineering challenges, and environmental waste (e.g., balloon debris) remain poorly addressed. Existing aircrafts -including military jets and research planes- could potentially be adapted for SAI purposes, with the choice of aircraft depending largely on the required injection altitudes (e.g. see Duffey et al., 2025). However, current aircraft are not capable of sustained operation at the necessary altitudes over extended periods, and their payload capacities are limited, thus a large number of flights would be required to achieve meaningful injection levels. An alternative method involves the use of tethered balloon systems. This approach has been highlighted by the Committee on Science, Engineering, and Public Policy (COSEPUP) in its 1992 report Responsible Science: Ensuring the Integrity of the Research Process [RD12] and examined by following studies (e.g. Robock et al., 2009). It was estimated that injecting 1 Tg of H2S into the stratosphere via balloons would cost approximately $20 million (at the time of the study). However, this method would also generate significant environmental waste, with millions of kg of plastic from burst balloons falling back to Earth each year. Rockets, jet-hybrid rockets or guns (e.g. light-gas guns) may also be used. It has yet to be demonstrated that for either of the proposed solutions (existing or future ones) the aerosol cloud formed would be optimum in terms of the particle sizes and lifetimes. Other methods, as using solar-lofting of absorbing particles injected into the upper troposphere instead to the stratosphere are also reported in the literature (Gao et al., 2021), but they need further investigation.
- **Cost and energy budget uncertainty:** The Pinatubo eruption released 20 Tg of $SO_2$ into the lower stratosphere which cooled down the surface for about 2 years. It is estimated that injections between 2–10 Tg $yr^{-1}$ of aerosols would be required to mimic the Pinatubo effect and halt greenhouse warming of +2K (Wigley, 2006; Izrael et al., 2007; Robock et al., 2008). However, the energy requirements, operational logistics, and long-term economic impacts remain uncertain.

---

**The knowledge gaps in SAI mechanism that will be investigated in the *ACtIon4Cooling* project:**

- Deriving the microphysical and radiative properties of volcanic aerosols, and their evolution with time, used as a natural analogue of SAI.
- Defining the optical properties of alternative materials, for effective cooling of global climate, avoiding the adverse effects of sulfur particles.
- Effects on precipitation patterns and the weather system (if possible)
- Depletion of stratospheric ozone (if possible)
- Overcooling at the tropics or undercooling in the high latitudes (if possible)
- Potential loss of critical habitats resulting from alterations in temperature and ocean chemistry with unpredictable effects for the humans and the ecosystem (if possible)

---

#### 2.2.1.2 Knowledge gaps in MCB mechanism

Unlike SAI, MCB could be more limited in its effectiveness to influence the global mean temperatures but it can have other positive impacts for the Earth's climate, as leading to regional temperature effects (Kravitz et al., 2013) and may partially offset certain impacts of climate change, such as extreme weather events, prolonged droughts, and heatwaves. However, substantial uncertainties remain regarding its climatic effectiveness and possible adverse regional impacts—including pronounced cooling in high-latitude

regions, overcooling of the tropics, residual warming at mid–high latitudes, and modifications to regional precipitation patterns (Stjern et al., 2018). The latter is directly investigated in *ACtIon4Cooling*, which evaluates precipitation shifts associated with natural and anthropogenic MCB analogues.

For MCB studies, the most effective material proposed to feed the marine clouds is the Sea Salt particles (Hernandez-Jaramillo et al., 2023), even though other materials like smoke particles and sodium chloride (salt) particles have been proposed to the literature too. The most widely known technology to persistently feed clouds with appropriate aerosols at the Planetary Boundary Level (PBL) is via using engineering Spray Nozzles (Hernandez-Jaramillo et al., 2023). Efficiency depends on meteorological conditions, aerosol size distribution, humidity, and thermodynamic instability. Key uncertainties remain regarding optimal particle properties, meteorological targeting, side effects, and detectability—all of which intersect with *ACtIon4Cooling* 's research aims. Major knowledge gaps include:

- **Uncertainties in Spray Parameters and Delivery Strategy:** There is limited understanding of the optimal droplet size, spray flux, nozzle design, and marine location for MCB. The effectiveness of cloud brightening depends on background cloud properties (LWP, CCN), updraft conditions, and aerosol-cloud interactions that are poorly constrained. Variability in outcome across modeling studies is large. The effects of timing and rate of marine cloud brightening aerosol injection on albedo changes are examined during the diurnal cycle of marine stratocumulus clouds (Jenkins et al., 2013).
- **Cloud-Aerosol Interaction Complexity:** Enhancing cloud albedo through increased cloud droplet number concentration (CDNC) is non-linear and sensitive to cloud regime (e.g., stratocumulus vs. trade cumulus). Feedbacks such as cloud thinning, precipitation suppression, or evaporative invigoration create response diversity (Quaas et al., 2009; Diamond et al., 2020). *ACtIon4Cooling* will evaluate these effects using ship-emission analogues and EO-based aerosol/cloud retrievals.
- **Environmental and Climatic Side Effects:** MCB may disrupt precipitation patterns or alter heat fluxes and circulation (Kravitz et al., 2013; Stjern et al., 2018). *ACtIon4Cooling* explicitly studies precipitation modification and regional climate responses using existing model output and Earth Observation (EO).
- **Model Uncertainty and Incomplete Representation:** Most climate models simplify marine low cloud processes, often lacking explicit cloud microphysics or resolving mesoscale organization. Cloud feedbacks and aerosol indirect effects in MCB scenarios remain uncertain, as revealed by GeoMIP and MCB-specific modeling studies. The models does not fully capture cloud dynamics, aerosol dispersion, or feedbacks in the real Earth system, limiting confidence in the spatial precision of predicted impacts (Jones et al., 2009). Regional climate responses—such as shifts in tropical rainfall and monsoonal behavior—underscore the model's limited ability to represent complex coupled interactions between atmosphere, ocean, and land. Latham et al. (2012) provide a comprehensive review of MCB modeling and underscore key uncertainties in representing mesoscale cloud dynamics, and the organization of marine stratocumulus systems. They stress that current global models often lack the spatial resolution and process-level detail necessary to simulate cloud microphysics and feedbacks that influence regional climate responses, such as monsoonal shifts and hydrological changes. The findings from Alterskjær et al. (2012), who used the NorESM model to investigate the effects of MCB on marine stratocumulus clouds, reveal that the effectiveness of MCB is highly sensitive to model representations of cloud microphysics, boundary layer processes, and aerosol–cloud interactions. Moreover, they show that regional radiative responses vary strongly depending on model configuration, pointing to persistent uncertainties in simulating feedback mechanisms and cloud-aerosol dynamics.
- **Technological Feasibility and Operational Control:** No scalable and controllable spray technology exists. Prototypes for sea-salt particle generation or/and marine vessel delivery remain in the experimental phase, with concerns about energy requirements, particle dispersion, and operational safety. An initial analysis of the energy budget needed for MCB would imply that the intervention is translated into energy needs. MCB would require the sustained generation and dispersion of large quantities of submicron sea-salt particles over extensive ocean regions in order to measurably enhance cloud albedo. Although conceptual studies suggest that such interventions could modify cloud reflectivity under favorable meteorological conditions, the total mass flux of particles required,

the number of deployment platforms, and the spatial coverage necessary to achieve climatically significant forcing remain highly uncertain. Consequently, the associated energy demand, operational logistics, technological scalability, and long-term economic implications of continuous aerosol generation and delivery are not yet well quantified.

- **Detectability and Attribution Challenges**: Because MCB effects are expected to be subtle and localized, distinguishing them from natural variability and anthropogenic aerosol signals is difficult. Detecting changes in cloud albedo, microphysical properties, or radiative forcing requires high-resolution, long-term EO datasets and robust attribution frameworks (Bender et al., 2016). Developing such detection and attribution tools is a core goal of *ACtIon4Cooling***.**
- **Ethical and Governance Issues:** Targeting specific marine regions for MCB (e.g., off the coasts of developing nations or vulnerable ecosystems) raises ethical concerns. Unlike SAI, MCB might require more decentralized deployment, complicating international governance and public consent frameworks (Reynolds, 2019).

---

***ACtIon4Cooling* investigates the following MCB-related gaps using analysis of natural/anthropogenic analogues (e.g., ship tracks):**

- Identification of Potential MCB-Susceptible Regions
- Using cloud susceptibility metrics, identify where marine low clouds are most responsive to aerosol perturbations and assess associated precipitation modifications on regional/global scales.
- Monitoring Cloud Microphysics and Radiative Changes
- Analyze how aerosol and trace gas perturbations affect cloud optical depth and other cloud properties, as well as the top-of-atmosphere (TOA) reflectance, building EO-based indicators for MCB-like events.
- Providing Empirical Benchmarks to improve model constraints
- Through ship-track datasets and radiative transfer simulations, deliver observational constraints for aerosol–cloud interaction schemes in models. Distinguishing signals from other ACI
- Develop methods to separate MCB-like signals from natural variability and anthropogenic aerosol effects using EO data and classification tools.

---

#### 2.2.1.3 Knowledge gaps in CCT mechanism

CCT aims at cooling the planet by reducing high-level cirrus clouds that trap outgoing longwave radiation from the Earth's surface (Mitchell and Finnegan, 2009; Lohmann and Gasparini, 2017). The core mechanism behind CCT is to artificially inject efficient INPs into regions where cirrus clouds form to trigger ice crystal formation via heterogeneous nucleation at relatively warmer temperatures and lower supersaturation. This could lead to the formation of fewer and larger ice crystals due to the competition for available water vapor. As these ice crystals grow larger and heavier, their sedimentation rates increase, thinning cirrus clouds and reducing their optical thickness. Therefore, the resulting thinner cirrus clouds become more transparent to outgoing longwave radiation from the Earth's surface and underlying atmosphere, leading to a cooling effect.

- **Fundamental Uncertainty in Climate Efficacy:** Unlike SAI or MCB, CCT aims to *reduce longwave forcing* by seeding cirrus clouds to reduce their optical thickness or frequency. However, the net radiative impact of cirrus clouds is highly variable and dependent on local cloud properties, vertical motion, and moisture content. Whether thinning them leads to cooling or warming remains uncertain in many regimes (Storelvmo et al., 2013; Gasparini & Lohmann, 2016).
- **Limited Knowledge of Optimal Seeding Conditions**: Yet, the effectiveness of seeding depends on the pre-existing aerosol background, temperature, updraft strength, and cirrus origin, which are poorly constrained (Storelvmo et al., 2014). Some of potential climate side effects for CCT are related to seeding procedure of artificial INPs which could eventually prevent natural cloud formation processes due to the competition for available water vapor. The large ice crystals falling out of high altitudes could cause droughts or shifts in precipitation, altering atmospheric circulation patterns. Unexpected overcooling in

specific regions may disturb local ecosystems and weather patterns. There are no long-term effects reported for CCT but this needs to be further verified. Despite the experimental and theoretical progresses in understanding CCT mechanism, the microphysical properties of cirrus cloud including ice crystal size and habit affect their radiative forcing and sedimentation rate, which is, however, not fully quantified. The balance between homogeneous and heterogeneous nucleation and the relative importance under varying conditions are still poorly constrained. The role that aerosol particles play in initiating ice crystal formation are still poorly understood and the effect of aerosols in terms of type and size on CCT is highly uncertain. Observing the cirrus cloud properties comprehensively is still challenging due to the limitations of probing instruments: satellite instruments suffer from resolving thin cirrus and aircrafts provide limited temporal and spatial coverage. The coordinate of observations on different platforms is hence important and imperative.

- **Risk of Overcompensation or Warming:** The risk of "overseeding" and a positive radiative forcing instead (Gasparini & Lohmann, 2016), if the background cirrus clouds are already formed by heterogeneous nucleation, remains uncertain. If CCT is deployed inappropriately—e.g., in regions with cirrus that already have a net cooling effect—it could reduce cloud cover that was beneficial, thereby causing *net warming*. Identifying “safe” regions and seasons for CCT is an unsolved problem (Storelvmo et al., 2014; Gruber et al., 2019).
- **Lack of Real-World Technology and Testing:** CCT assumes a capability to inject INPs (e.g., bismuth tri-iodide or mineral dust) into the upper troposphere (~8–12 km altitude). No current technology is proven to deliver sufficient particle concentrations with the required precision or environmental safety. The ice nucleation properties of candidate materials remain poorly characterized under real atmospheric conditions (Kuebbeler et al., 2012; Cziczo et al., 2015). So far, small-scale field tests have not been conducted yet. The relevant studies of CCT remain primarily in global climate model simulations (e.g. with CESM and ECHAM) (Storelvmo et al., 2013; Gasparini and Lohmann, 2016). Laboratory and chamber studies provide supports to the basic physics behind CCT (Vogel et al., 2022). Mineral dust particles as effective INPs have been proposed as the most efficient material for CCT, while sulfates via homogenous freezing and Bismuthtriiodide (BiI~3~) are also reported in the literature to play a role (Mitchell and Finnegan, 2009).
- **Modeling Limitations:** Few models simulate cirrus microphysics in enough detail to evaluate CCT strategies robustly. Large inter-model differences exist in cirrus representation, ice nucleation schemes, and aerosol interactions. Most GeoMIP models are not yet equipped to evaluate realistic CCT scenarios (Gasparini et al., 2020; Gettelman et al., 2021).
- **Observational Detection is a challenge:** Cirrus clouds are thin, transient, and vary on short timescales, making it difficult to detect CCT-induced changes against natural variability. Detecting reduced ice crystal number concentrations, changes in effective radius, or alterations in longwave cloud radiative effect requires hyperspectral and lidar data with high vertical resolution (Campbell et al., 2016).
- **Potential environment risks:** Injecting artificial INPs into the upper troposphere introduces unknown chemical and environmental risks. Long-range transport, toxicity, and interactions with natural aerosols are poorly studied. Bismuth-based compounds or modified mineral dusts might pose ecological risks or affect stratospheric chemistry (Cziczo & Froyd, 2014).

---

***ACtIon4Cooling* investigates the following CCT-related gaps:**

- Identification of natural analogue for CCT to monitor changes in cirrus cloud properties (microphysical and optical) responding to aviation impacts.
- Characteristics of specific clouds forming and evolving in either high aviation-emission regions or more. pristine regions using a backward trajectory analysis with airborne measurements on a campaign basis (ML-CIRRUS).
- Comparison in cirrus cloud optical depth and depolarization as well as microphysical parameters between midlatitudes with high aviation emissions and aerosol-poor high latitudes; Classifying the CCT-like effects in different regions (e.g. midlatitudes vs high latitudes); The influence of meteorological conditions, however, should be distinguished and compared with the ERA-5 data.

- Determination of long-term evolution of cirrus cloud properties in the midlatitude regions with increasing aviation emissions in the last years with CALIPSO.
- Potential CCT effects on precipitation patterns and regional weather system.
- Calculation of radiative forcing of CCT-like effects in cirrus cloud perturbations using RT model;

Providing sophisticated datasets for ICON simulation for further model constrains.

---

### 2.2.2 Past and Current SRM-relevant activities

#### 2.2.2.1 Overview of field experiments

A survey on the past and current activities relevant to SRM research is helpful to identify what has been studied and which are the facts and limitations of each SRM mechanism. The Co-CREATE [URL03] project in their Scoping note on the state of Solar Radiation Modification (SRM) research, field tests, and related activities [RD10] presented a list of field campaigns and relevant to SAI and MCB activities. A comprehensive overview of the solar geoengineering activities is also presented in the report from The Alliance for Just Deliberation on Solar Geoengineering & Forum for Climate Engineering Assessment (2025, January) [RD13]:

- Field Experiments during 2008-2009 in Saratov Oblast, Russia (Izrael et al., 2009) have been reported as potential geo-engineering activities. They appear controversial in references [RD10], [RD13] as candidate experiments for SAI, but the particles were released in the troposphere by a moving vehicle and helicopter. Later, as a continuation of the earlier investigations in 2008 and 2009, Izrael et al., (2011) describes an outdoor field experiment carried out in 2010 on the creation of artificial aerosol layers and the resulting effects on solar insolation and surface-layer meteorology.

- SPICE (Stratospheric Particle Injection for Climate Engineering) [URL13] was a research project (2010–2014), funded by the UK Engineering and Physical Sciences Research Council (EPSRC) and involved leading English universities that aimed to investigate the feasibility, risks, and effectiveness of SAI. Among its objectives were to: (a) Evaluate the technical feasibility of delivering aerosol particles to the stratosphere (e.g., via tethered balloons, aircraft, or other means). (b) Study atmospheric processes and particle behaviour. (c) Assess the governance, ethical, and environmental issues of SAI. (d) Engage in public dialogue and stakeholder consultation about geoengineering. A small-scale outdoor engineering test to trial a balloon and hose delivery system was proposed but it was cancelled before starting due to governance concerns and public opposition.

- SCoPEx (Stratospheric Controlled Perturbation Experiment) is a small-scale scientific field experiment, led by American researches at Harvard University, to explore the feasibility, risks, and effectiveness of SAI. SCoPEx targeted to improve understanding of: (a) How aerosol particles behave in the stratosphere, (b) Their impact on stratospheric chemistry, particularly ozone (c) How they scatter sunlight and potentially cool the planet, (d) How they interact with atmospheric dynamics. They proposed an experimental set-up with a balloon-borne platform to release a small amount of aerosol, such as calcium carbonate ($CaCO_3$) or sulfate particles, at about 20 km altitude. The platform would carry instruments to measure: aerosol properties, atmospheric chemistry, light scattering and particle dispersion. The scientific objectives of SCoPEx were to test models of aerosol behavior in the stratosphere, validate how well these particles reflect sunlight and investigate potential side effects, like ozone depletion or stratospheric heating. SCoPEx planned its initial test flight in Sweden but it was cancelled before starting, similar to SPICE due to public opposition and ethical concerns. The Advisory Committee (co-chairs and members) composed and published in March 2024 their final report, see Jinnah et al. (2024) and [URL12].

- E-PEACE (Eastern Pacific Emitted Aerosol Cloud Experiment) (Russell et al., 2013) was a major field campaign conducted in 2011 off the coast of California, designed to study ACI, especially those relevant to MCB and the broader science of climate intervention via aerosol emissions. The experiment aimed to improve understanding of: (a) How aerosols from ships and controlled sources influence cloud microphysical and radiative properties (b) The formation of ship tracks (long brightened cloud features caused by ship emissions) (c) The sensitivity of marine stratocumulus clouds to artificial aerosol perturbations. Key components of the experiment were:

  (1) Controlled aerosol releases: An aircraft released monodisperse aerosols into the marine boundary layer, mimicking MCB-relevant interventions.

(2) Ship-based emissions: A ship released targeted aerosol plumes under measured conditions.
(3) Multiple aircraft platforms: Aircraft carried instruments to measure cloud microphysics, aerosol concentration, droplet size distribution and radiation.
(4) Multiple aircraft platforms: Aircraft carried instruments to measure cloud microphysics, aerosol concentration, droplet size distribution and radiation.
(5) Satellite validation: Observations were compared to satellite data (e.g., MODIS, CALIPSO) to validate remote sensing of ACI.

E-PEACE was one of the first controlled experiments relevant to the feasibility of MCB while it provided experimental evidence on: cloud albedo response to aerosol injection and cloud adjustments (i.e., liquid water path and precipitation suppression). Its findings informed model development and observational strategies for future geoengineering and climate monitoring studies.

- The Great Barrier Reef Marine Cloud Brightening (MCB) project, led by Australian scientists from Southern Cross University and the Australian Institute of Marine Science (AIMS) is a pioneering field trial exploring the potential of MCB to help mitigate the impacts of ocean warming on coral reefs, particularly the coral bleaching (Tollefson et al, 2021). The project aims to cool ocean surface temperatures over the Great Barrier Reef by increasing the reflectivity of low-level marine clouds. This is done by spraying tiny sea salt particles into the atmosphere, acting as CCNs and leading to brighter and longer-lasting clouds that reflect more sunlight. The experiment contributes to assess feasibility, safety, and effectiveness of MCB as a local climate intervention to reduce sea surface temperature during marine heatwaves and protect coral ecosystems from bleaching. The outdoors experiments were conducted on and around the Great Barrier Reef, Australia for the period 2020-2021 and the method involved specialized nozzles on boats or platforms atomize seawater into micron-scale salt particles and spray them into the air under suitable meteorological conditions. Hernandez-Jaramillo et al., (2024) established a new airborne research platform, designed primarily for MCB field studies. This platform, comprising a Cessna 337 aircraft was outfitted with a comprehensive suite of meteorological, aerosol, and cloud microphysical instrumentation normally only found on much larger aircrafts. The aircraft has completed its first field deployment over the Great Barrier Reef supporting the Reef Restoration and Adaptation Program.
- The University of Washington's MCB Program [URL09] is a leading research initiative by atmospheric scientists at the University of Washington. Key partners include SRI International and the nonprofit organization SilverLining [URL07], which funds the program through its Safe Climate Research Initiative. Additional support comes from various foundations and individual donors committed to advancing climate research. The MCB Program goals are:
  - Enhance understanding of ACI and their impact on climate.
  - Investigate the feasibility of using sea salt aerosols to increase cloud reflectivity.
  - Assess the potential benefits, risks, and efficacy of marine cloud brightening as a climate intervention strategy.

  Researchers employed a combination of computer modeling, observational studies, and controlled field experiments to study these interactions. For instance, they analyze ship-tracks to understand how aerosols affect cloud properties. Additionally, they conduct small-scale field studies using instruments designed to generate controlled amounts of sea salt aerosols to observe their effects on cloud brightness [URL09].

  To facilitate field research and public engagement, the MCB Program established the Coastal Atmospheric Aerosol Research and Engagement (CAARE) facility aboard the USS Hornet, a decommissioned aircraft carrier in Alameda, California. This platform allows scientists to conduct experiments in a marine environment and engage with the public through educational displays and demonstrations [URL09] . However, in 2024, the city of Alameda requested a pause in the experiments conducted on the USS Hornet.
- The CLOUDLAB project, led by Swiss scientists, used supercooled stratus clouds as a natural laboratory for targeted glaciogenic cloud seeding to advance the understanding of ice processes: Ice nucleating particles are injected from an uncrewed aerial vehicle (UAV) into supercooled stratus clouds to induce ice crystal formation and subsequent growth processes. These experiments focused on

wintertime stratus clouds as a natural laboratory to study ice crystal formation from injected particles, for model validation purposes (Hanneberger et al., 2023).

#### 2.2.2.2 Overview of modelling activities

In contrast to field experiments, most scientific understanding of SRM is derived from numerical modelling studies. Due to the absence of large-scale experiments, climate and Earth system models constitute the primary tools for assessing potential climatic, chemical, and dynamical impacts of SRM approaches.

***Global Climate Modelling and Intercomparison Efforts***

The most important coordinated modelling activity is the Geoengineering Model Intercomparison Project (GeoMIP), conducted within the framework of the Coupled Model Intercomparison Project (CMIP) (Kravitz et al., 2011; Kravitz et al., 2015). GeoMIP provides standardized experimental protocols to investigate SRM scenarios across multiple global climate models.

GeoMIP experiments include:

- Solar constant reduction experiments (idealized solar dimming)
- SAI simulations
- Abrupt termination scenarios
- Feedback and hydrological response analyses

More recent phases (GeoMIP6 within CMIP6; Kravitz et al., 2015; Tilmes et al., 2018) include interactive stratospheric aerosol schemes and chemistry–climate coupling. These coordinated simulations have shown:

- Robust global mean temperature reduction under SAI-like forcing
- Substantial inter-model spread in regional precipitation response
- Shifts in monsoon systems
- Persistent uncertainties in stratospheric heating and ozone impacts

GeoMIP remains the primary international framework for systematically evaluating SRM climate responses and uncertainty ranges.

***Chemistry–Climate Modelling of SAI***

For SAI, chemistry–climate models (CCMs) have been used to simulate:

- Aerosol microphysical evolution (e.g., sulfate growth and sedimentation)
- Stratospheric heating rates
- Heterogeneous chemical reactions affecting ozone

Seminal modelling work (e.g., Tilmes et al., 2008; Pitari et al., 2014) demonstrated potential ozone depletion risks and highlighted the sensitivity of outcomes to particle size distribution and injection strategy. These studies underscore that stratospheric composition changes remain one of the largest uncertainties in SAI impact assessments.

***Marine Cloud Brightening Modelling***

MCB research relies strongly on high-resolution modelling of aerosol–cloud interactions, using large-eddy simulations (LES) and cloud-resolving models. Studies such as Latham et al. (2008), Wang et al. (2011), and Rasch et al. (2009) investigated:

- Cloud droplet number sensitivity to sea salt injection
- Cloud albedo enhancement
- Liquid water path adjustments
- Precipitation suppression effects

Results indicate that cloud responses are highly nonlinear and strongly dependent on background meteorological conditions. Parameterization of these processes in global models remains a key limitation.

#### 2.2.2.3 Non-Governmental Organizations (NGOs)

- SilverLining [URL08] is a U.S.-based nonprofit organization dedicated to advancing scientific research and policy development aimed at addressing near-term climate risks, particularly via SRM techniques. SilverLining had funded the University of Washington's MCB Program [URL07].
- The Degrees (DEveloping country Governance REsearch and Evaluation for SRM) Initiative is a UK-based NGO that seeks to engage the Global South on SRM issues.
- SRM360 launched in November 2024 as a “non-profit knowledge hub that explores the science and evidence behind” SRM.
- Operaatio Arktis is a youth-led Finnish science outreach project promoting equitable climate intervention research with central goal to preserve the Arctic Sea ice.
- Environmental Defense Fund (EDF) announced it would be creating an SRM research program to fund impacts-focused research.

Exploring potential field campaigns are also one of the objectives of Co-CREATE project, where in their latest report [RD11], five hypothetical SRM experiments were presented. One of those hypothetical field studies refers to smaller-scale CCT experiment in Arctic Norway, exploring the use of ice-nucleating particles to enhance the escape of longwave radiation and reduce the effects of Arctic Amplification, while addressing the challenges of conducting research in the Arctic. The EU CleanCloud [URL05] project aims to get a better understanding of ACI mechanisms in the Arctic via their Arctic Spring & summer campaigns [URL06] that took place in 2024.

A major concern on field experiments (even small-scale) is that they could inevitably lead to SRM deployment, and thus the risk of a “Slippery slope” is foreseen, which could happen if incremental steps towards broader SRM implementation occur without sufficient public debate, transparent decision-making, or robust governance frameworks [RD10]. And an SRM deployment has the risk of termination shock. which refers to the rapid and severe climate consequences that could occur if SRM deployment (i.e., SAI) were suddenly stopped after being deployed for some time.

#### 2.2.2.4 ARIA (Advanced Research Intervention Agency)

ARIA (Advanced Research Intervention Agency [URL16]) is a UK public research funding agency that funds breakthrough R&D research and development in underexplored and interdisciplinary areas. It empowers scientists and engineers to pursue ambitious, speculative ideas that are difficult to fund elsewhere, with programmes designed and led by expert Programme Directors. Operating independently but with strong accountability to Parliament and its Board, ARIA aims to responsibly catalyse technological breakthroughs that create long-term benefits.

ARIA is funding the Exploring Options for Actively Cooling the Earth Programme [URL15] which aims to answer fundamental questions of climate cooling approaches that have been proposed as potential options to delay or avert damaging climate tipping points through indoor and (where necessary) small, controlled, outdoor experiments. The programme includes not only experiments but also modelling, simulation, observation and monitoring funded activities required to support the experiments, as well as research into the ethical, governance, law, and geopolitical dimensions of the climate cooling approaches. The information gathered by this programme will allow for more definitive assessments on whether one or more of the approaches examined may one day be used responsibly and ethically to delay or avert the onset of temperature-induced climate tipping points.

##### 2.2.2.4.1 Planned modelling activities

**GRID-CC: Global to Regional Impacts Downscaling for Climate Cooling** [The Degrees Initiative – University of Cape Town | Cornell University]
Understanding the regional impacts of Earth cooling strategies is essential—especially for communities in the Global South that may be disproportionately affected. However, research capacity is often centered elsewhere. This project addresses that gap by empowering researchers in the Global South through computational efforts. It will develop an open-access repository of detailed climate data specific to the Global South, enabling more accurate global and regional impact models. Alongside new research tools, expert workshops will support scientists in these regions to build a robust evidence base for scientifically informed decision-making about Earth cooling approaches.

**Ecological Impact Assessment of Earth Cooling Experiments in the Arctic (Eco-ICE)** [British Antarctic Survey | University of Oxford]
Polar ecosystems are fragile yet crucial to the global climate system, but the ecological effects of climate interventions in these regions remain poorly understood. Combining laboratory experiments with climate and ecosystem modelling, this project offers an independent, comprehensive assessment of potential interventions in the Arctic marine environment. By integrating biogeochemical and biological data, the team aims to deliver best-practice guidelines for ecological risk assessment, ensuring future Arctic interventions are evaluated with scientific rigor and environmental caution.

**Investigating the Impacts of Earth Cooling on West African Monsoon Variability and Wet-Dry Spells** [Institut Polytechnique Rural de Formation et de Recherche Appliquée (IPR/IFRA) | University of Cape Town]
The West African Monsoon sustains millions through agriculture and water resources. This project examines how Earth cooling strategies might alter critical rainfall patterns, including wet and dry spells, with implications for regional stability and food security. Utilizing advanced climate models, observational data, and scenarios from platforms like GeoMIP, the research addresses gaps in understanding interactions between cooling approaches and existing climate vulnerabilities, offering actionable insights to guide adaptation and risk mitigation in West Africa.

**Space Reflector Baseline Survey** [Planetary Sunshade Foundation | Cornell University | National Center for Atmospheric Research | University of Nottingham | Redwire Space | NASA Jet Propulsion Laboratory | Ethos Space]
To evaluate lesser-known climate cooling options such as space-based reflectors, this theoretical study unites top space engineering and climate modelling teams. Six conceptual space reflector designs will be modelled, followed by simulations of their potential climate impacts—including atmospheric dynamics, chemistry, and ocean/ice feedbacks. The goal is not deployment but to identify which concepts merit further research based on modeled efficiency, scalability, and side effects, fostering collaboration between engineering and climate science communities.

**Towards Robust and Unbiased Validation of SAI Simulations (TRUSS)** [Institut Teknologi Sepuluh Nopember]
Reliable data is essential for responsible decision-making about interventions like Stratospheric Aerosol Injection (SAI), yet current simulations carry significant uncertainties. This project uses advanced statistical and machine learning techniques to enhance the accuracy and impartiality of climate model outputs, especially regarding regional impacts. By improving simulation trustworthiness, this foundational work builds scientific confidence necessary for informed policymaking and public understanding

**Simulating Effects of Earth Cooling on Monsoon Dynamics and Precipitation Extremes** [Cochin University of Science and Technology | The Energy and Resources Institute (TERI)]
Stable rainfall patterns are vital for agriculture and water security in both India and the UK. This study explores how Earth cooling proposals could disrupt seasonal rains and precipitation extremes by analyzing climate simulations from GeoMIP and similar platforms. It aims to unravel the complex drivers behind potential changes, delivering region-specific evidence to assess risks to critical water cycles and resources.

**Defining the Minimum Scale of a SAI Test: A First Step Toward Outdoor Experiments** [Cornell University]
One key uncertainty in climate intervention science is how cooling aerosols behave when released into the stratosphere. This project tackles that gap through theoretical modelling, aiming to determine the smallest viable scale for an outdoor experiment that could provide real-world data to reduce uncertainty. Identifying this minimum scale is critical groundwork for responsible future research and for developing necessary governance and oversight frameworks.

#### 2.2.2.4.2 Planned outdoor monitoring activities

**De-risking Cirrus Modification** [Imperial College London | University of Leeds | University of Vienna | RIKEN]

Cirrus clouds at high altitudes generally warm the climate, but the role of atmospheric particles (like soot) in their formation is uncertain. This project combines modelling, satellite data analysis, and research aircraft flights to measure how natural and anthropogenic particles influence cirrus clouds. By improving understanding of these processes, it provides essential baseline knowledge for evaluating the safety and effectiveness of potential cirrus cloud thinning as a climate cooling strategy

**Ice-Nucleating Particles in the Upper Troposphere: Advancing Cirrus Control and Experimental Science Strength ("INPUT:ACCESS")** [University of Leeds | CIRES University of Colorado | Imperial College London]
Ice nucleating particles (INPs) are crucial for cirrus cloud formation but remain poorly characterized. This project develops balloon-borne collectors to sample INPs in the upper troposphere, followed by detailed lab analysis. These data will enhance climate models and improve monitoring of natural atmospheric processes, providing a critical baseline for climate science.

**StratoGuard – Global Monitoring of Climate Engineering Using Micro High-Altitude Balloons** [Voltitude | University of Hertfordshire | Imperial College London | NOAA Chemical Sciences Laboratory]
This project develops small, low-cost balloons equipped with sensors to navigate the stratosphere for up to 30 days, enabling sustained, affordable global climate data collection. StratoGuard aims to support detailed monitoring of natural climate phenomena and any future climate intervention activities, with test launches beginning in 2026 and full regulatory compliance assured.

**Monitoring Aerosol Climate Engineering (MACE)** [University of Bristol]
Natural volcanic eruptions offer opportunities to study aerosols relevant to climate science and interventions. This project develops advanced drones capable of high-altitude flights to sample emissions from active volcanoes in Guatemala, Montserrat, and Chile. By analysing natural aerosol-cloud interactions, the research seeks to establish a rapid-response capability for safely gathering crucial data from future eruptions.

#### 2.2.2.4.3 Planned controlled, small-scale outdoor experiments:

**Re-Thickening Arctic Sea Ice (RASi)** [University of Cambridge | University of Manchester | University College London | Nansen Center | Real Ice | Arctic Reflections | University of Washington | Arizona State University]
Accelerated Arctic warming threatens sea ice loss with serious global impacts. This project tests whether deliberately thickening winter sea ice by spraying seawater can reduce summer melt and Arctic warming. Small-scale experiments will take place in Canada over three winters, expanding coverage if ecological safety is confirmed. Conducted under strict governance and community collaboration, the research will deliver critical data on the intervention's feasibility and ecological effects.

**Marine Cloud Brightening in a Complex World** [Southern Cross University]
Marine Cloud Brightening (MCB) aims to cool vulnerable ecosystems by enhancing cloud reflectivity using seawater spray. Building on prior fieldwork near the Great Barrier Reef, this project combines advanced modelling and sea salt sprayer development. Subject to ARIA governance and community partnership, small-scale outdoor experiments are planned for years 3 and 4 over the reef. These will be carefully controlled and transparent, generating real-world data on MCB's effectiveness and risks.

**A Responsible Innovation Framework for Novel Spray Technology (REFLECT)** [University of Manchester | University of Cambridge | Archipelago Technology | University of Exeter | Finnish Meteorological Institute | University of Leeds]
This project develops and tests spray technologies critical for Marine Cloud and Sky Brightening (MCB/MSB). Through modelling, indoor tests, and community co-design, it aims to responsibly assess technical feasibility. Outdoor spray tests, if approved, will be very small and brief, replicating natural sea spray processes. The goal is to create a robust framework for evaluating and safely advancing spray technologies.

**BrightSpark – Cloud Brightening with Electric Charge** [University of Reading | Menapia Ltd | Celestial]
Exploring an alternative to seawater spraying, this project investigates using controlled electric charges

to enhance cloud reflectivity. It focuses on the fundamental science of how electrical charges affect cloud and fog droplets, aiming to determine whether this method could safely and effectively influence cloud properties.

## 2.3 Scientific Objectives and Observational Needs

This section lists the scientific objectives and observational needs of each SRM mechanism that will be investigated as part of *ACtIon4Cooling*

### 2.3.1 Stratospheric Aerosol Injection (SAI)

The injection of aerosol particles into the stratosphere may significantly alter the Earth's radiative budget and exert several effects on climate. On one hand aerosol droplets scatter part of solar radiation directly back into space resulting to a cooling effect. On the other hand, the emitted thermal radiation is absorbed in the stratosphere, resulting in warming of the upper atmosphere. The quantity and nature of the aerosols injected, determine the degree of cooling or warming and affect the course of important stratospheric chemical processes. A prominent example was the Mt. Pinatubo eruption which resulted in a long-lasting global temperature decrease (e.g. McCormick et al., 1995).

In this context, volcanic eruptions have been extensively investigated as a natural analog of SAI (Robock et al., 2013; Proctor et al., 2018) as they provide real-world test cases for understanding how large quantities of aerosols behave in the stratosphere. Although volcanic eruptions differ from intentional SAI employment (i.e. lack of control on injection location, altitude, duration, and aerosol composition), they allow direct observation of stratospheric aerosol evolution, chemical interactions, and climate response. Variability in eruption latitude and season further offers a framework for studying how transport pathways, residence time, and radiative effects depend on dynamical conditions. These observations form the physical basis for evaluating SAI strategies and their potential risks.

#### 2.3.1.1 Objectives

*ACtIon4Cooling* seeks to deepen our understanding on the climatic effects of volcanic eruptions focusing on events occurring at different times of the year (i.e. seasonality) and originating from diverse latitudes, such as tropical and high-latitude regions, in order to assess how transport pathways, lifetime and radiative effects may vary under different conditions These observations will provide a physically based framework for SAI, which may be used to increase its' effectiveness and avoid possible side-effects.

#### 2.3.1.2 Target regions and periods of interest

Based on results of previous studies, eruptions at tropical, high northern and southern latitudes can interact in distinct ways with climate phenomena such as the El Niño which would in turn affect the Pacific ocean surface temperature (SST) in a different way (e.g. Zuo et al., 2018). Seasonal variation is also expected to affect the dispersion of the volcanic air masses due to changes in wind motions, atmospheric stability and stratospheric circulation. Therefore, within *ACtIon4Cooling* , observations acquired at variable locations (i.e., mid latitude (Europe), tropical, and sub-Antarctic regions) and seasons (i.e., winter, spring and summer), will be targeted depending also on data availability for each eruption case. This approach will facilitate the need to study the long-term SAI effects like rainfall distribution and ozone layer dynamics as a function of space and time of the year of the eruption.

#### 2.3.1.3 Observational requirements

To achieve the objectives for SAI, comprehensive monitoring of volcanic aerosols using space-borne and ground-based observations is required. To this end remote sensing measurements with advanced capabilities, as well as state of the art optical models will be utilized to properly characterize the volcanic particles injected in the stratosphere in terms of their microphysical and optical properties, as well as to track their temporal evolution post injection. Special focus will be given to the use of lidar observations such as those provided from EarthCARE and CALIPSO missions or ACTRIS/EARLINET networks, in combination with their passive remote sensing data including AERONET photometers and satellite polarimetric sensors like POLDER, HARP2 and SPEXone). The synergistic use of the observations is crucial in order to acquire valuable information on the particle vertical distribution and injection height, along with their microphysical and optical properties, to accurately classify the aerosol types injected into the stratosphere from the volcanic eruptions and properly characterize their chemical and radiative impacts within the Earth system. Whenever available, airborne in-situ data (e.g. from balloon borne measurements) will be also utilized

to help constrain the aerosol microphysical properties like their size distribution (e.g. see Ansmann et al., 1996).

### 2.3.2 Marine Cloud Brightening (MCB)

The key cloud microphysical and optical properties essential for MCB studies are identified based on the state-of-the-art needs of Aerosol-Cloud Interactions (ACI). Important parameters include cloud droplet number concentrations, which vary with latitude and longitude, as they are critical inputs for Earth system models. Additionally, a dependence on cloud type may be required for more accurate characterization. However, deriving cloud microphysics from space remains challenging due to several assumptions inherent in remote sensing retrievals. For example, the cloud liquid water path, which is influenced by perturbations in cloud droplet number concentrations, may be assumed invariant in some Earth Observation (EO) datasets. The scientific objectives of what *ACtIon4Cooling* aims to understand, detect, evaluate, or develop is listed below:

#### 2.3.2.1 Objectives

**1. Understand the contribution of maritime emissions to MCB-like brightening**

Analyze how aerosols emitted by marine traffic act as CCN, modify cloud droplet populations, and enhance cloud reflectivity—using ship-track analogues as a real-world proxy for MCB.

**2. Detect ship-track-induced cloud perturbations using spaceborne observations**

Develop detection approaches based on trace gas/aerosol/cloud properties derived from operational EO datasets. A particular focus lies on evaluating spectral sensitivity by comparing the $O_2$ A-band (~760 nm) with broader multispectral windows such as those from VIIRS, in order to determine preferable spectral regions for identifying MCB-like signals.

**3. Evaluate detectability using single-instrument versus multi-instrument approaches**

Assess to what extent individual EO sensors can detect MCB-like events and identify the limitations when observations rely on a single instrument. Determine which complementary datasets might enhance detection skill. Radiative transfer simulations support these analyses by testing sensor sensitivity across spectral windows.

**4. Evaluate climatic impacts of MCB-like perturbations**

Using observationally constrained datasets, the regional climatic impacts associated with ship-track-induced brightening are quantified. This includes analyzing temperature anomalies and changes in precipitation patterns in regions with variant cloud covers.

**5. Develop classification models for detecting and predicting MCB-like events**

Build and train machine-learning models capable of identifying MCB events from ship emissions. These models form the basis for an observable-signature framework for marine cloud brightening within *ACtIon4Cooling*.

#### 2.3.2.2 Scientific and Technical Requirements

Scientific Requirements

To evaluate MCB feasibility and impacts, *ACtIon4Cooling* requires:

- Accurate retrievals of cloud microphysical and/or optical properties (COD, LWP, CDNC).
- Characterization of aerosol sources and composition along major shipping corridors.
- Ability to distinguish natural variability from anthropogenic aerosol perturbations.
- Sufficient temporal coverage to analyze any seasonal trends.

Earth Observation / Data Requirements

- High SNR: Many EO sensors suffer from limited signal-to-noise over bright marine clouds; assessing detectability therefore requires careful consideration of SNR limitations.
- Consistent gridding: All datasets used for MCB analysis must be aggregated onto a common spatial grid, particularly for integrating ship-track information with the native resolution of the sensor under investigation (e.g., TROPOMI).

- Multi-sensor synergy: Combining TOA reflectance, aerosol optical properties, cloud microphysics, and polarimetric information cloud be essential to detect subtle MCB-like signals.

Modelling Requirements

- Radiative Transfer Modelling:
  1. Ability to test detection in broader spectral windows.
  2. Adequate representation of marine low-cloud layers
- Global / Regional Climate Modelling:
  1. Finer spatial resolution to capture mesoscale cloud structures
  2. Improved representation of marine boundary layer processes and susceptibility metrics

#### 2.3.2.3 Regions of interest

The geographic focus includes marine regions where low-level clouds (cloud-top height < 3 km) form over ocean surfaces and where aerosol perturbations are significant. *ACtIon4Cooling* concentrates on:

Ship-Track Analogues

Regions along major global shipping corridors, where ship emissions regularly produce detectable cloud perturbations. These serve as the primary natural analogue for MCB. Sulfate aerosols have a well-documented cooling effect through cloud brightening mechanisms—particularly over stratocumulus cloud decks—by increasing cloud droplet number concentration and cloud albedo. Their reduction may lead to less reflective clouds (Gryspeerdt et al., 2021) and a corresponding increase in surface solar absorption, potentially contributing to amplified warming (Yuan et al., 2024) in high-traffic regions. The focus is in the Northern hemisphere in the mid-latitudes. The geographical grids of interest are:

1. **NorthEastern Atlantic (NEA)** (−35° to −8° W and 15° to 45° N)**:** Marine stratocumulus clouds, the amount of which decreases with increasing sea surface temperatures (Devasthale et al., 2025), or with decreasing sulfur emissions of ships (Benas et al., 2025).
2. **Mediterranean Sea (Med)** (−5° W to 35° E and 30° to 45° N)**:** Large shipping corridor with less cloudy scenes, making ship pollution plumes easily detected (Georgoulias et al, 2020; Kurchaba et al., 2023) .The Mediterranean region (even if it is not considered as one of the major cloud decks for MCB studies) is highlighted in particular due to the exceptionally high sea surface temperatures (SSTs) recorded in 2023. According to the European State of the Climate 2024 (ESOTC 2024) report, released in April 2025 by the Copernicus Climate Change Service (C3S) and the WMO [RD01], the Mediterranean experienced the most intense marine heat anomalies ever observed, underscoring the escalating impacts of climate change on this region.

### 2.3.3 Cirrus Cloud Thinning (CCT)

Global aviation exhaust emissions, primarily composed of greenhouse gases, aerosol particles, and water vapor, are injected into the atmosphere at high altitudes, which may lead to the formation of linear contrails and contrail cirrus. They increase global cloudiness and modify the existing cirrus properties indirectly. During the ML-CIRRUS campaign, the particle linear depolarization ratios (PLDR) of cirrus clouds have been measured with the WALES lidar of DLR. A backward trajectory analysis reveals that cirrus clouds with enhanced PLDR formed and evolved in the regions with high aviation emissions and those with smaller PLDR from rather pristine regions (smaller impact of aviation) (Urbanek et al., 2018). Furthermore, cirrus clouds with larger PLDR are characterized by larger ice crystals with smaller number concentration (Groß et al., 2023). The changes in cirrus cloud properties depending on aviation emissions have also been seen in the satellite observations (Li and Groß, 2021, 2022; Zhu et al., 2023).

#### 2.3.3.1 Objectives

There are several potential natural analogues for CCT. Dust episode, wildfire, and volcanic eruptions usually inject a large amount of mineral dust, smoke particles, and sulphate aerosols into the atmosphere which may act as INPs. The processes can shift cirrus cloud formation towards fewer and larger crystals. The consequent transport and spread of those particles under favorable meteorological conditions will induce changes in cirrus cloud properties in larger scales. But the induced aerosol perturbations are sporadic, localized and often lower in altitudes than cirrus layers. The microphysical impacts on cirrus cloud properties are difficult to control and track. Aviation-relevant cirrus cloud may not be a perfect natural analogue for

CCT, but they form in the same thermodynamic environment in the upper troposphere as natural cirrus and perturb cirrus cloud properties in ways comparable to CCT strategies (Urbanek et al., 2018; Groß et al., 2023). The involved processes provide helps for us to understand how CCT might work in the real atmosphere.

#### 2.3.3.2 Target regions and periods of interest

Cirrus clouds exhibit different microphysical, optical, and radiative properties depending on variable thermodynamic environments of different regions and seasons (e.g. Li and Groß, 2022, 2025a). Midlatitude cirrus clouds are of particular importance, not only because they significantly influence the Earth's radiation budget, but also they interact with the atmospheric dynamic and weather patterns. Furthermore, civil aviation takes place mainly in the northern midlatitudes and, hence, aviation-induced perturbations in cirrus clouds are the strongest in this area. Civil aviation over Europe grew strongly in the past years until the COVID-19 pandemic in 2020, when civil aviation was significantly reduced. This provides a great opportunity study the aviation impacts on cirrus cloud properties in a temporal domain. For this part of study, an area of the whole range of midlatitudes spanning from 35 to 60° N and from the Atlantic ocean (15° W) to Central Europe (15° E) will be investigated, which covers a large fraction of the North Atlantic flight corridor connecting Europe with North America (see the cyan rectangle shown in the map in Figure 2). Furthermore, cirrus clouds in the high-latitude regions which are more pristine with less aviation impact are characterized for a contrast with those at midlatitudes for studying CCT (the regions of research are indicated in red and blue in Figure 2). In addition, there is a distinct seasonal cycle in cirrus cloud appearance and properties. And aviation impacts on cirrus clouds also reveal seasonal variations with a stronger effect in other seasons than in summer. For the purpose of studying CCT, cirrus cloud observations will be analyzed covering the full annual cycle in the high- and mid-latitude regions.

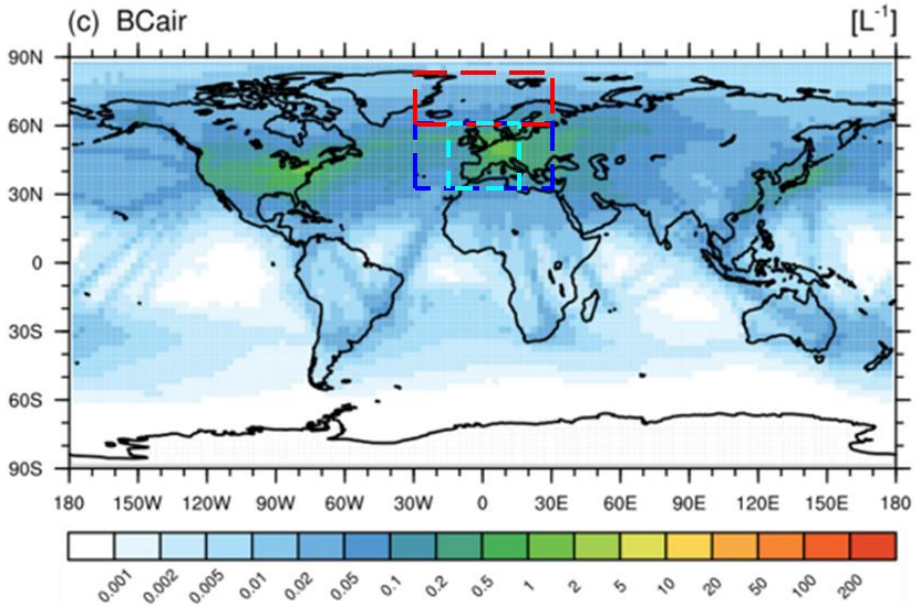


**Figure 2** Global distribution of the simulated number concentration of black carbon from aviation acting as INPs (L-1) inside cirrus clouds (reproduced from Beer et al., 2024). For long-term analysis of CCT-like effects, the observations are determined in the area indicated in cyan rectangle (35–60° N; 15° W–15° E), which covers a large fraction of Northern Atlantic flight corridor connecting Europe and North America. The red rectangle indicates the high-latitude regions of research (35–60° N; 30° W–30° E) and the blue one the midlatitude regions (60–80° N; 30° W–30° E) for comparison.

#### 2.3.3.3 Objectives and requirements

Within *ACtIon4Cooling*, existing airborne observations will be used to focus on specific clouds that may form in the regions with either dense aviation emissions or not and further derive the optical thicknesses, ice water content, and ice crystal number concentrations. From a statistical perspective, also satellite data will be used to determine the optical and microphysical properties of cirrus clouds as a function of latitude and longitude as input for Earth system model studies. During the ML-CIRRUS and CIRRUS-HL campaigns, there were in-situ instruments mounted under the wings of the HALO aircraft. Small particles in the size

range from 3 to 50 µm were detected by the CAS (Voigt et al., 2017; Kleine et al., 2018). Larger particles were detected by the CIP (Cloud Imaging Probe, in the size range from 15 to 960 µm) as part of the CCP (Cloud Combination Probe) and the PIP (Precipitation Imaging Probe, in the size range from 100 to 6400 µm) instrument (Weigel et al., 2016). With these instruments, the microphysical properties of cirrus clouds, like ice crystal effective diameter (De) and number concentrations (Ni), can be derived. However, the in-situ instruments can only provide 1-D measurements along the flight track, e.g., no vertical structure. WALES is a multi-wavelength lidar system including DIAL and HRSL capability. So it can measure water vapor mixing ratio and aerosol extinction, backscatter coefficients, and depolarization. With the lidar observations, the cloud top height will be identified and derive the optical thicknesses. From the satellite observations of CALIPSO, the extinction coefficients of cirrus clouds will be estimated and their optical depth calculated. The ice crystal De and Ni can be derived from the DARDAR data (with the synergy of CLOUDSAT and CALIPSO), which, however, are limited only for certain periods. In addition, the data products of IIR-CALIOP retrievals (Ni, De, and IWC) in 17 years (2006.06–2023.07) will be publicly available soon (Mitchell et al., 2018, 2025), which provide us the opportunity to determine the long-term evolution of microphysical properties of cirrus clouds responding to aviation emissions. EarthCARE will further provide the microphysical properties of cirrus clouds with the radar-lidar synergy as a successor in near future (Wehr et al., 2023). The determined microphysical and optical properties of cirrus clouds as a function of latitude and longitude will be provided for RF calculations to ICON model and PyDOME RT code. Especially, the perturbations in ice crystal number concentrations of cirrus clouds responding to aviation-induced impacts will be highly investigated.

### 2.3.4 Radiative Transfer Modelling (RTM) for SRM Monitoring

#### 2.3.4.1 Objectives

A radiative-transfer model (RTM) such as pyDOME (Efremenko et al., 2017) links the micro-physical properties of atmospheric constituents such as gases, aerosol particles, cloud water/ice particles as well as surface properties to the radiative quantities that govern climate response. By converting profiles of gases, aerosols, clouds and surface reflectance into wavelength-dependent optical properties, the RTM solves the radiative transfer equation for a specified solar and viewing geometry. From the resulting radiance field, the up-welling irradiance at the top of the atmosphere can be derived, yielding the change in reflected energy - or instantaneous radiative forcing - that determines whether the planet experiences cooling or warming. The same solution decomposes the down-welling irradiance at the surface, revealing how much sunlight actually reaches the ground or ocean. Irradiance convergence between layers provides heating-rate profiles, showing where the atmosphere itself is warmed or cooled and how circulation might respond.

#### 2.3.4.2 Requirements for input data (aerosol/cloud profiles, surface reflectance)

To perform radiative transfer simulations, the atmospheric model containing the temperature and gaseous profiles should be provided. In pyDOME, aerosol optical properties are normally derived from micro-physical inputs - namely the parameters of the particle-size distribution and the complex refractive index - through Mie computations that assume spherical particles. The code offers direct interfaces to the OPAC and MODTRAN aerosol libraries, so users can select mixtures representative of specific environments such as urban, continental, marine or polluted regions without having to build each distribution from scratch. The same Mie routine is applied to cloud droplets when spherical geometry is adequate. If desired, however, optical properties for any aerosol or cloud layer can be supplied explicitly by specifying its spectral optical thickness, single-scattering albedo and phase function. The phase function may be given either as Legendre coefficients or, more simply, via an asymmetry parameter; in the latter case pyDOME adopts a Henyey–Greenstein representation by default.

### 2.3.5 Global Climate Modelling

**Need for coupling observational constraints with climate model scenarios**

Set up of simulations with the atmospheric general circulation model (GCM), the ICOsahedral Non-hydrostatic (ICON) model (Hohenegger et al., 2023) for present-day boundary conditions (sea surface temperature and sea ice concentration distributions, land surface conditions, greenhouse gas and aerosol concentrations). The model will be prepared such that it can digest the relevant perturbations

- to the stratospheric aerosol layer, in terms of a distribution in aerosol optical depth as a function of altitude, with specified optical properties (single scattering albedo, asymmetry parameter)

- to boundary-layer clouds, in terms of a perturbation of the cloud droplet number concentration and potentially of the cloud liquid water path, for specified longitude-latitude boxes and potentially time periods,
- to cirrus, in terms of a perturbation to the ice crystal number concentration and potentially the ice water path, for specified longitude-latitude boxes and potentially time periods,

**Key outputs needed from climate models (e.g., temperature anomalies, precipitation shifts, radiative forcing changes)**

The model output will involve surface temperature and precipitation patterns for statistical analysis of extreme and mean values resolved by region, and of top-of-atmosphere and surface energy budgets to monitor the effects of the perturbations.

**Compatibility with major global models**

Similar quantities will be gathered from simulations from available model intercomparison projects (parts of the CMIP6).

## 2.4 Gaps in Existing Observational and Modelling Infrastructure

### 2.4.1 Summary of current capabilities and their limitations

The role of RTMs on simulating the SRM scenarios should be considered with some limitations as there are several assumptions to be made in each mechanism. For **MCB**, the limitations are bounded to the radiative properties of clouds which do not always align well with the microphysical and macro-physical properties used in those RTM simulations. The major uncertainties for MCB will be introduced due to the rapid adjustments of clouds during the spraying process. The biggest challenges for the global and regional climate models to study the impacts of MCB are the large uncertainties in cloud microphysics and prevailing turbulence.

Limitations related to **SAI** research partly arise from the incomplete characterization of the microphysical and optical properties of volcanic aerosols, since to date there is no extensive observational dataset for volcanic eruptions from both remote sensing and in-situ instruments. The associated uncertainties propagate in RTM calculations and further increase when attempting to track changes in particle properties over time. In addition, accurately representing aerosol interactions and removal processes in the stratosphere, remains challenging for global models, which still lack detailed processes descriptors of key mechanisms. To model SAI scenarios requires a robust representation of the chemical interactions in the stratosphere, as well as descriptions of the possible interactions between the injected particles and other aerosol types present in the stratosphere (e.g. smoke). Failing to reproduce these processes may lead to substantial uncertainties.

**CCT** effects remain difficult to quantify because there are many limitations in observational and modelling efforts. Active satellite probing has a poor coverage in space and time due to the narrow swaths. They likely miss the small-scale variabilities in cirrus cloud formation, which, however, are important for CCT processes. Airborne measurements on a campaign-basis, on the other hand, are episodic and localized. Current instruments are suffering from detection limit and retrieval uncertainty, especially, for very thin ice layers and sub-visual cirrus. It's almost impossible to distinguish ice nucleation pathways and operationally track the contribution of additional INPs to the changes in cirrus cloud properties. Modelling efforts are constrained by large uncertainties in ice nucleation physics and INP representation. The biggest GCM challenges to study CCT are in cirrus formation and dissipation mechanisms. High-fidelity LES and microphysical models are expensive and computationally limited to small domains and short periods.

The **RTMs** have limited capabilities due to the large uncertainties in cirrus microphysical and turbulent processes.

### 2.4.2 Relevance of satellite-based, airborne, and ground-based observations

To investigate **SAI** approaches, *ACtIon4Cooling* will rely on volcanic eruptions as the natural analogues for stratospheric aerosol injection. Satellite observations such as those provided from polar orbiting or limb sounding missions like SAGE, CALIPSO, EarthCARE and PACE , and potentially from geostationary satellites (e.g. MSG, MTG), are crucial for monitoring stratospheric perturbations including changes in the stratospheric aerosol load and changes in particle properties Moreover, ground-based lidar and photometer

observations, such as those provided from large-scale monitoring networks like ACTRIS and AERONET are valuable for cases when satellite data are sparse. Finally, any available in-situ measurements from high altitude tethered balloons can be exploited for validation purposes.

The detection and monitor capabilities of potential **MCB** activities can be examined by natural (non-perfect) analogues like cloud tracks observed from ship tracks. Spaceborne measurements are crucial for studying the changes in sunlight reflectivity caused by MCB, while ground-based observations (e.g., ACTRIS network) are valuable for characterizing the aerosols beneath the cloud base.

Aircraft-induced contrails form in the same thermodynamic environment in the upper troposphere as natural cirrus and can lead to perturbations in cirrus cloud properties indirectly. Further, cirrus clouds that form and develop under aerosol indirect effects from aviation emissions may exhibit different properties compared with those from pristine regions, which mimics the **CCT** strategies. The changes in cirrus cloud properties (optical, microphysical, and radiative) can be monitored responding to aviation emissions to understand the effects of CCT. For this purpose, all possible airborne measurements (both in-situ and remote sensing techniques) will be made use of during the ML-CIRRUS and CIRRUS-HL campaigns and satellite measurements of CALIPSO, EarthCARE, and MSG/MTG.

Table 6 represents the outcome of our assessment of currently available satellite sensors suitable for SRM studies. These sensors are considered relevant for quantifying intervention efficiency and evaluating associated risks in both ongoing and future projects.

**Table 6** List of EO datasets suitable for MCB, CCT and SAI development and validation studies in the context of (but not limited to) *ACtIon4Cooling*

| Sensor | Platform | Type | Spectral Range | Spatial Resolution | Temporal Resolution | Key Capabilities for MCB | Key Capabilities for CCT | Key Capabilities for SAI |
|---|---|---|---|---|---|---|---|---|
| **TROPOMI** | Sentinel-5P | Spectro-meter | UV–VIS–NIR–SWIR | ~5.5 × 3.5 km² | Daily (global) | Aerosol layer height, UVAI, absorbing aerosols, limited cloud properties | N/A | Stratospheric and tropospheric ozone profile, total column density |
| **CALIOP** | CALIPSO | Lidar | 532 & 1064 nm | ~30 m vertical, ~333 m horizontal | 16-day repeat (narrow swath) | Vertical aerosol/cloud profiles, layer typing, depolarization | Cloud profiling, aerosol extinction and depolarization | Profiles of aerosol and cloud backscatter coefficient and depolarization<br>Target classification<br>Mass concentration profiles |
| **CPR** | CloudSat | Cloud Profiling Radar | 94 GHz, W-band | 500 m vertical, /1.4 km horizontal | 16-day repeat | N/A | Partical size and number concentration with synergic CALIOP and CPR | N/A |
| **IIRS** | Suomi-NPP | Radio-meter | VIS–NIR–SWIR–TIR | 370 m (I-band), 740 m (M-band) | Daily (global) | Cloud optical thickness, cloud top properties, AOD | N/A | N/A |
| **MODIS** | Terra/Aqua | Radio-meter | 36 bands (VIS–TIR) | 250 m (bands 1–2), 500/1000 m (others) | 1–2 days (global) | Aerosol/cloud properties, cloud phase, droplet radius, optical depth | Cloud top properties, COT, cloud fraction | Aerosol spatial distribution in 2D, AOD |
| **ATLID** | EARTHCARE | High-spectral Resolution Lidar | 355 nm | ~100/500 m vertical (below/above 20km), /~100 m horizontal | 25-day repeat | Profiles of aerosol/cloud extinction, backscatter and depolarization, | Aerosol and cloud profiling, lidar ratio, aerosol extinction and depolarization | Profiles of aerosol and cloud backscatterand extinction coefficients, and depolarization<br>Target classification<br>Cloud top height |
| **CPR** | EarthCARE | Cloud profiling radar | 94 GHz W-band | 100/500 m vertical and 750 horizontal | Twice per day | N/A | Thick cloud profiling, Particle size and number concentration with synergic ATLID and CPR | N/A |
| **MSI** | EARTHCARE | Imager | 4 channels (VIS - SWIR)<br>3 channels (TIR) | 500 * 500 m (VIS–SWIR), 1 km (TIR) | 25-day repeat | Scene context for ATLID, cloud top height, aerosol optical depth, cloud masking | Cloud top properties, COT, cloud fraction, ice crystal size | Aerosol optical thickness at 0.67 and 0.865 um<br>Cloud masking<br>(up to 4) Aerosol types vertical distribution, AOD, SSA, CRI (in synergy with ATLID) |
| **OCI** | PACE | Spectro-radiometer | 340–885 nm (hyperspectral), | ~1 km | 1–2 days (global) | Ocean color, AOD over water, large-scale aerosol monitoring | N/A | N/A |

| | | | | | | | | |
|---|---|---|---|---|---|---|---|---|
| | | | NIR–SWIR bands | | | | | |
| **SPEXone** | PACE | Multi-angle Polarimeter | 400–770 nm (spectral resolution of 2-5nm for intensity, 10-40nm for DoLP, 5 viewing angles) | ~2.5*2.5 km | 1–2 days (narrow swath) | Fine-mode aerosol size/composition, CCN proxy, aerosol–cloud interaction metrics | N/A | For fine and coarse mode aerosols:<br>AOD, AE, CRI, SSA, Sphericity fraction, ALH, Volume density, reff, veff |
| **HARP2** | PACE | Wide-angle Polarimeter | 440, 550, 670, 870 nm (60 viewing angles for intensity and DoLP at 670nm, 20 in other wavelengths) | ~7 * 5 km | 1–2 days (broad swath) | Cloud droplet size, aerosol type, cloud thermodynamic phase | N/A | Similar to SpexONE<br>Cloud masking |
| **SLSTR** | Sentinel-3A/B | Radio-meter | VIS–SWIR–TIR (9 bands) | 500 m (VIS/SWIR), 1 km (TIR) | 2–3 days (global) | SST, cloud temperature, cloud mask, fire/aerosol detection | N/A | N/A |
| **OLCI** | Sentinel-3A/B | Spectro-meter | 400–1040 nm (21 bands) | 300 m | 2–3 days (global) | Ocean color, AOD, cloud optical thickness, water vapor | N/A | N/A |
| **FCI** | Meteosat Third Generation | Imager | VIS–IR (16 channels) | 0.5-1 km (VIS/NIR), 2 km (IR) | Every 2.5 minutes (Europe) / Every 10 minutes (full disk) | Rapid cloud/aerosol evolution, optical properties, nowcasting | Cloud top properties, COT, cloud fraction | Aerosol spatial distribution in 2D |
| **SEVIRI** | MSG, Meteosat Second Generation | Imager | 0.4 – 1.6 µm (4 visible/NIR channels), 3.9-13.4 µm (8 IR channels) | 3 km (narrowband), 1 km (HRV) | 5 min for rapid scanning,15 min for full disk scan | Cloud top properties, COT, cloud fraction | Cloud top properties, COT, cloud fraction | Aerosol spatial distribution in 2D |
| **POLDER** | PARASOL | Polari-meter | UV-NIR (7 channels between 443-1020nm) | 6 * 7 km | 16-day repeat | N/A | N/A | Similar to SpexONE and HARP |
| **AERONET** | Ground-based | Sun/Sky-radio-meters | UV-NIR (340-1020nm) | N/A | Direct sun measurements every 15min, solar almucantar every 1h | N/A | N/A | Column-effective AOD, AE, SSA, SD, phase function, calibrated radiances |
| **EARLINET** | Ground-based | Multi-wavelength polarization lidars | UV-NIR (355-1064nm) | N/A | Continuous | N/A | N/A | Extinction, Backscatter coefficient, Depolarization profiles (at least in 2 wavelengths) |

| | | | | | | | | |
|---|---|---|---|---|---|---|---|---|
| **OMPS/LP** | S-NPP | Limb profiler | VIS-NIR (510-997 nm) | (horizontal) 125km (vertical) 1km | | N/A | N/A | Ozone profile |
| **ACE-FTS** | ACE | high-resolution infrared spectro-meter ("solar occultation" technique ) | 750-4400 $cm^{-1}$ | 3km | | N/A | N/A | Ozone depletion |
| **MLS** | Aura | Limb sounder | Microwave (118-2500 GHz) | (horizontal) 200-500km (vertical) 0.5km in stratosphere | | N/A | N/A | Ozone and water vapor profiles (and other atmospheric gases) |
| **SAGE III** | ISS | Spectro-meter (solar and lunar occultation technique) | (UV-IR) | (vertical) 0.75-1.5km | | N/A | N/A | Upper-troposphere and strotosphere:<br>ozone, and water vapor<br>aerosol extinction coefficient 0.385-1.550 μm, AOD |
| **CERES** | TRMM, Terra, Aqua, S-NPP, NOAA-20 | Radiometer | SW (0.2–5 μm, Thermal (8–12 μm) Total (>0.2 μm) | 1 degree | | N/A | N/A | Radiation fluxes at TOA |
| **BBR** | EarthCARE | Radiometer | SW (0.25-4.0 μm) Total (< 0.25 to > 50 μm) | 10km | | N/A | N/A | Radiances and fluxes at TOA |

## 2.5 Inputs from the Scientific Community – ACtIon4Cooling Expert Survey

To ensure that the *ACtIon4Cooling* Requirements baseline reflects the broader expertise in the field of climate intervention and Earth Observation (EO), a targeted survey was conducted among members of the scientific community. The survey was distributed to experts in remote sensing, atmospheric modeling, and SRM research, including participants from international initiatives.

### 2.5.1 Survey Objectives

The survey aims to:

1. **Map expert expertise and ongoing engagement**, to understand the backgrounds contributing to SRM research and the operational contexts of respondents.
2. **Identify priority SRM strategies**, including interest and involvement in specific techniques such as Stratospheric Aerosol Injection (SAI), Marine Cloud Brightening (MCB), and Cirrus Cloud Thinning (CCT).
3. Catalog the EO data types and platforms most relevant for SRM monitoring—from cloud and water vapor measurements, to aerosol properties, atmospheric composition, surface indicators, and radiation fluxes, as well as specific instruments and missions.
4. Uncover current EO detection and attribution limitations, by soliciting expert assessments on methodological challenges and capability gaps.
5. Gauge the value of a centralized SRM EO data portal, to support potential coordination and sharing of observations and derived products.
6. Assess modeling practices and needs, including the use of global models (e.g., ICON, CESM, UKESM), preferred SRM scenarios or emissions pathways for future simulation efforts, and approaches for validating model outputs against observations or natural analogues.
7. Capture data requirements for model validation, spanning satellite, in-situ, airborne, and ground-based sources to address SRM-specific research needs.
8. **Surface unique research requirements**, by inviting input on elements of SRM science that require specialized attention beyond existing climate research frameworks.
9. **Understand justification strategies**, exploring how SRM research can be effectively communicated to funders, the public, and the media.
10. **Prioritize outdoor research problems**, through expert judgment on the most urgent field-level challenges requiring attention.
11. **Harvest strategy-specific insights**:
    - For **SAI**: focused data needs for detection and modeling, suitability of volcanic eruptions as analogues, and awareness of any SAI experiments.
    - For **MCB**: possible aerosol delivery technologies, field trial location priorities, and perceived mitigation benefits in regions with extreme weather threats (e.g., Mediterranean Europe).
    - For **CCT**: the applicability of aviation-induced cirrus modifications as analogues, candidate seeding materials and required densities, and approaches for distinguishing seeding effects from natural variability.
12. **Strengthen collaboration channels**, by inviting interest in workshops, data sharing, and expert input, and collecting suggestions on international SRM-related research initiatives to connect with.

### 2.5.2 Survey Participation

The following table lists the experts that participated in the survey. The participants were selected based on their expertise in various aspects of SRM, including SAI, CCT, MCB, as well as observational and modeling approaches.

This experts group represents a diverse international community of researchers and practitioners engaged in SRM research, encompassing academic institutions, research centers, and government agencies. Their contributions provide valuable insights into the scientific, technical, and governance considerations of SRM approaches.

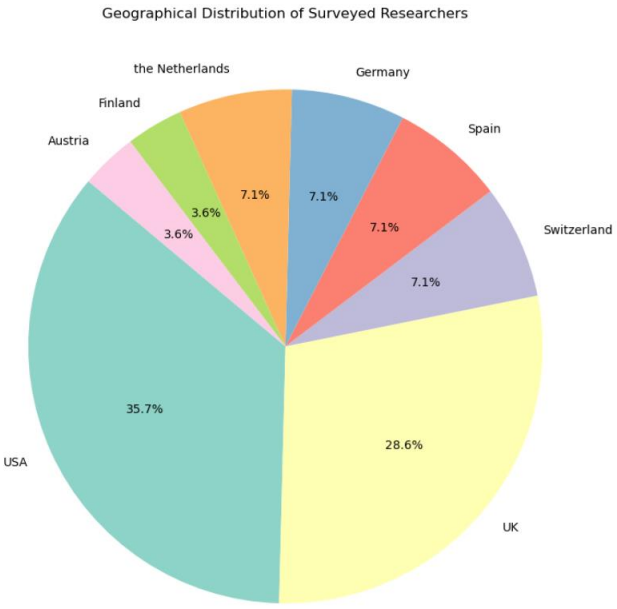


**Figure 3** Pie chart showing the geographical distribution of participants in the survey

Survey participants were asked to indicate their primary areas of expertise, with the option to select multiple fields. The responses highlight a broad and complementary set of skills across the international SRM research community. The distribution of SRM-relevant expertise (see Figure 4) showed that most of the surveyed experts cover quite uniformly the mechanisms that are investigated within the *ACtIon4Cooling* project. In addition, the majority of the surveyed experts declared that they are currently involved in SRM-relevant projects as Lead / Principal Investigator (PI) with a percentage of 64.3% or Collaborator with a percentage of 25% (see Figure 5). The surveyed experts are currently or planning to use global models like ICON, CESM or UKESM for SRM research (see Figure 6).

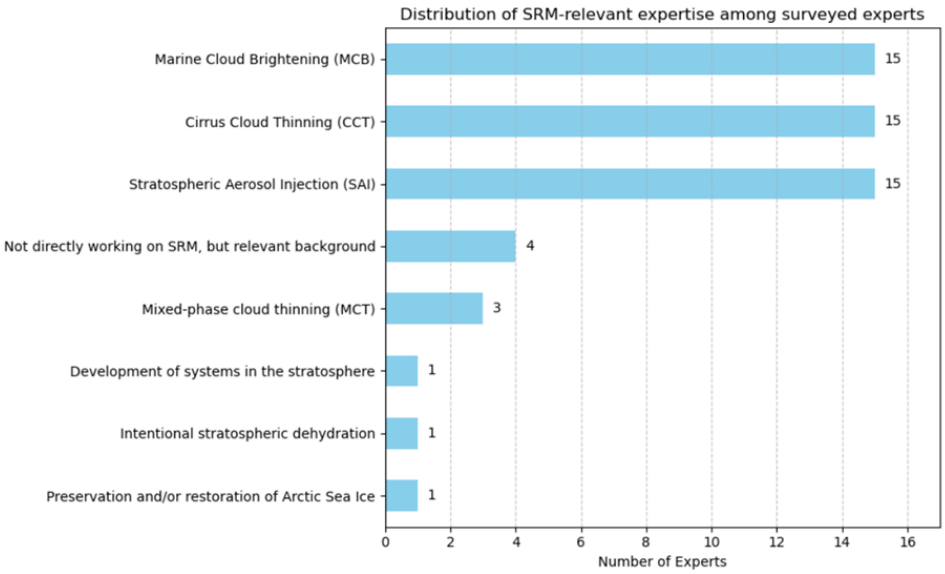


**Figure 4** Bar plot showing the type of SRM-relevant expertise of the surveyed scientists

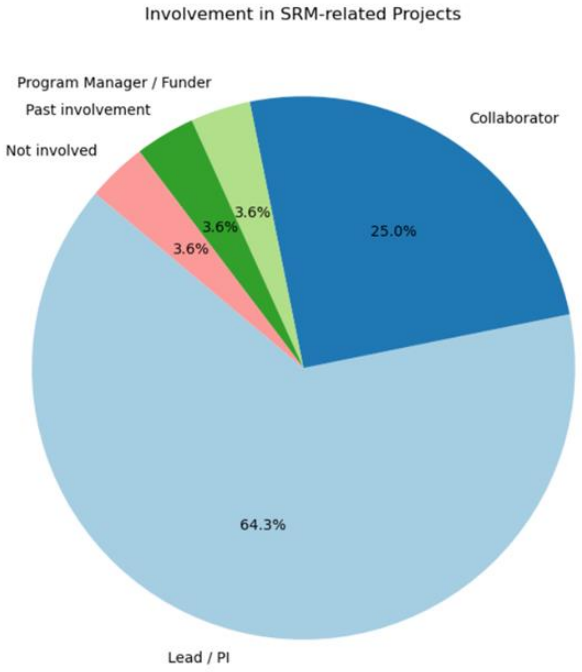


**Figure 5** Pie chart showing the involvement of the surveyed experts in SRM-relevant projects

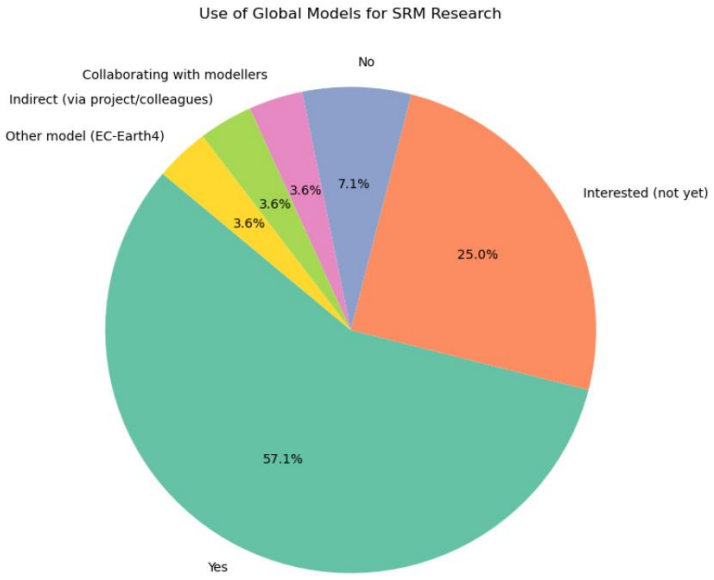


**Figure 6** Pie chart showing the knowledge/interest of the surveyed experts on Global Climate Models like ICON, CESM or UKESM

The survey participants identified several international SRM and related climate intervention research efforts that *ACtIon4Cooling* could connect with. Key programs and initiatives include:

- **United Kingdom:** ARIA, NERC-SRM.
- **United States:** NOAA Earth Radiation Budget (ERB) program, ERA, University of Washington, University of Chicago, SIMONS SRM program.
- **Germany:** Ongoing research activities (specifics not detailed).

- **International/Multilateral:** WCRP Lighthouse Activity on Climate Intervention, GeoMIP (model intercomparisons for SAI/MCB/CCT), DEGREES modeling initiative, UNEP and WMO SRM assessments.
- **Other initiatives/NGOs:** Ocean Visions, SilverLining, Arctic Climate Emergency Response (ACER) Initiative, ACTRIS/NDACC (observational networks).

Overall, respondents emphasized the value of connecting with both governmental research programs and NGO-led initiatives, as well as multilateral modeling and observational efforts, to foster collaboration and knowledge exchange in SRM research.

Below a bar chart (see Figure 7) visualizing the number of mentions for each international SRM research effort depicts the recommendations for *ACtIon4Cooling* collaboration. ARIA (UK) and DEGREES received the highest mentions. WCRP Lighthouse Activity, GeoMIP and NOAA (USA) are also commonly recommended. This chart provides a clear overview of priority connections for international collaboration.

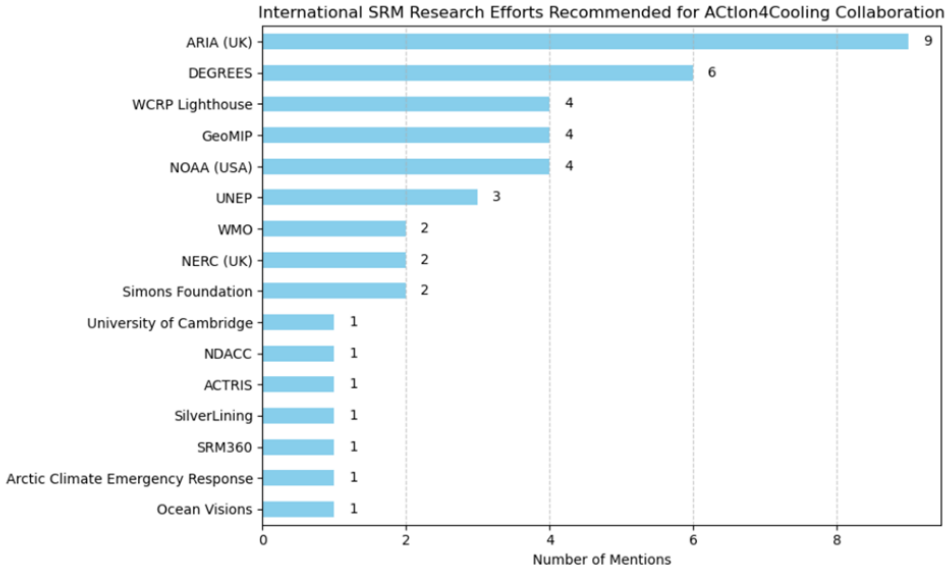


**Figure 7** International SRM Research Efforts which the surveyed experts recommended to *ACtIon4Cooling* to connect with

Over 90 % indicated willingness to contribute to *ACtIon4Cooling* through workshops, data sharing, or expert input. Overall, the majority of respondents are highly motivated to engage, with many emphasizing their interest in contributing to cloud and SAI research, as well as participating in WCRP and GeoMIP workshops.

### 2.5.3 Survey Outcomes

#### 2.5.3.1 General outcomes

The surveyed experts voted that all relevant EO data of cloud properties, water vapor, aerosol and trace gases as well as radiation and energy balance measurements as equally important for monitoring the SRM effects (see Figure 8).

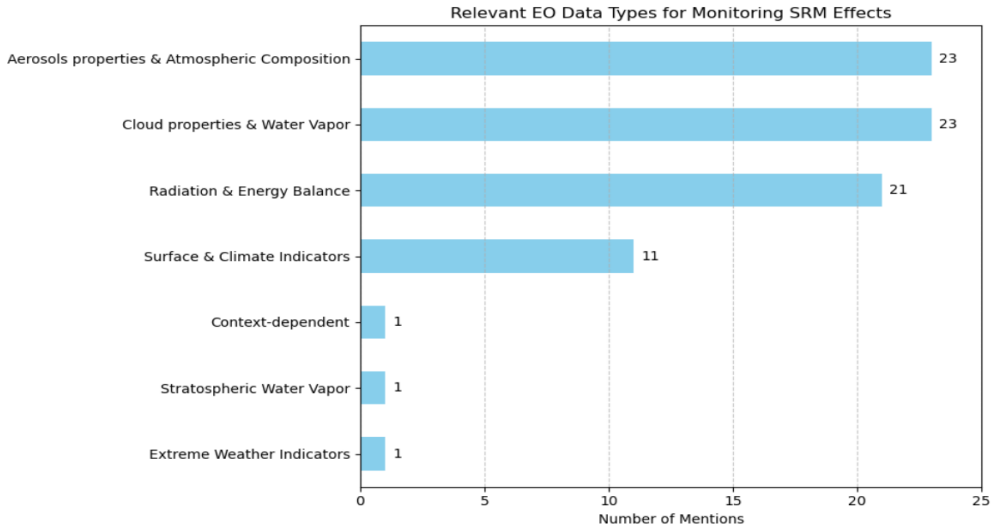


**Figure 8** Bar plot showing which types of Earth Observation (EO) data are most relevant for monitoring SRM effects

**Q: Which satellite instruments or missions do you consider most valuable for monitoring SRM-related effects?**

The table below summarizes the most frequently mentioned missions/instruments by the surveyed experts.

**Table 7** List of instruments and missions which are valuable for SRM monitoring

| Mission / Instrument | Role / Value |
|---|---|
| **EarthCARE (ATLID lidar, CPR radar, MSI, BBR)** | Successor to CALIPSO/CloudSat; cloud vertical profiling, radiation budget |
| **CALIPSO (CALIOP lidar)** | Historic reference for cirrus/CCT (Mitchell and Garnier, 2025) and cloud-aerosol structure |
| **MODIS (Terra/Aqua)** | Long record of cloud and aerosol properties |
| **CERES** | TOA radiation fluxes, albedo changes |
| **MLS (Aura)** | Stratospheric composition; data continuity concerns |
| **SAGE (SAGE-III, historic SAGE-II)** | Stratospheric aerosols/ozone records |
| **OMPS (Limb & Nadir)** | Stratospheric aerosol profiles |
| **AVHRR** | Very long time series of cloud/aerosol data |
| **OMI / TROPOMI** | $SO_2$ and UV Aerosol Index monitoring |

The responses highlighted a wide range of instruments and missions, reflecting both the diversity of SRM research needs and the complexity of monitoring requirements. Several experts emphasized the importance of long-term continuity in datasets such as MODIS, AVHRR, VIIRS, and Sentinel-3 SLSTR for detecting climate-relevant trends. For cloud and aerosol vertical profiling, CALIPSO, CloudSat, and the ESA EarthCARE mission were repeatedly mentioned as critical, especially for cirrus characterization in the context of Cirrus Cloud Thinning (CCT). Stratospheric aerosol and composition monitoring emerged as a central need, with strong support for limb-sounding instruments such as SAGE-III, OMPS-LP, MLS, ACE, SABRE, and the proposed CAIRT mission. OMI and TROPOMI were also noted as valuable for monitoring $SO_2$ and the UV Aerosol Index. Many participants stressed concern over the potential loss of key instruments (e.g., MLS, MODIS, CALIPSO), alongside anticipation for continuity and future missions such as STRIVE and PACE.

For the radiation budget, CERES was frequently cited, with EarthCARE's Broadband Radiometer (BBR) expected to provide valuable complementary information. Some experts also pointed to the importance of geostationary imagers (e.g., SEVIRI, ABI on GOES) for Marine Cloud Brightening (MCB), due

to their ability to capture diurnal cloud variability. In addition, specific mentions were made of datasets like GloSSAC (for stratospheric aerosol properties) and heritage missions such as HALOE and ILAS for stratospheric composition.

Several respondents cautioned that, given the small scale of SRM-related signals relative to natural variability, proxy measurements such as temperature trends and albedo changes may be essential for early detection. Others emphasized the importance of co-located observations to better capture aerosol–cloud–meteorology interactions. Finally, it was noted that ground-based and in situ networks (e.g., ACTRIS, AERONET, NDACC, BSRN, targeted aircraft campaigns) remain critical complements to satellite monitoring, ensuring robust detection and attribution of SRM signals.

Overall, the responses underscore the importance of an integrated, multi-platform observing system that combines heritage records, continuity missions, and innovative future instruments to meet SRM monitoring needs.

**Q: What are the current limitations of EO for detecting or attributing SRM effects?**

Experts highlighted multiple technical and conceptual limitations of current EO capabilities for SRM detection and attribution.

***1. Resolution constraints***

- Insufficient spatial and temporal resolution to capture small-scale or transient SRM signals.
- Limited vertical profiling of aerosols and clouds, especially in the stratosphere.
- Difficulty in quantifying 3D cloud structures and linking them to radiative fluxes.
- Lack of ability to capture the diurnal cycle with polar-orbiting satellites; geostationary observations or high-frequency active sensors could help.

***2. Sensitivity and signal-to-noise***

- SRM signals are often too small compared to natural variability, making attribution difficult.
- Low signal-to-noise ratio for key climate indicators (temperature, radiation budget, cloud microphysics).
- Retrieval uncertainties in cloud microphysical properties (liquid water content, particle size).

***3. Data continuity and consistency***

- Concerns about the loss of long-term high-quality datasets (e.g., MODIS, CERES, CALIPSO).
- Need for long-term, stable, cross-mission calibration and harmonized data records.
- Short mission lifespans limit the availability of consistent time series for attribution.

***4. Gaps in measurements***

- Lack of detailed aerosol composition and size distribution data from satellites.
- Insufficient in situ measurements to complement and validate EO datasets.
- Limited ability to measure the base state of the stratosphere against which SRM signals must be detected.

***5. Attribution challenges***

- Difficult to distinguish SRM signals from natural variability (e.g., recent temperature anomalies).
- Requires co-located observations of clouds, aerosols, radiation, and meteorology for robust attribution.
- Need for better integration with models to quantify fine-scale processes and bridge observational gaps.

***6. Accessibility and usability***

- Data platforms remain fragmented; expertise is required to locate, access, and use EO products.
- Calls for an international, harmonized platform with quick visualization tools (similar to NASA Worldview) to support the SRM and wider climate research community.

---

**Summary:** The main bottlenecks are resolution (spatial, temporal, vertical), sensitivity vs. natural variability, continuity of datasets, gaps in aerosol/cloud microphysics, insufficient in situ data, and fragmented data access. Future improvements should focus on long-term continuity, co-located observations, integration with models, and better user access to EO data.

**Q: What SRM scenarios or emissions pathways should be prioritized for modeling in the next 3–5 years?**

**1.** Stratospheric Aerosol Injection (SAI)

- Most frequently cited as the top priority, seen as more feasible and scientifically less risky than alternatives.
- Interest in peak-shaving scenarios (limiting peak warming or avoiding threshold exceedance).
- Specific references to GeoMIP scenarios such as G6-1.5K-SAI and to high-latitude small-scale deployments (potentially relevant to near-term field trial simulations).
- Calls for scenarios aligned with realistic emissions pathways (e.g., SSPs, RCPs) and exploring both idealized and non-ideal deployment strategies.

2. Marine Cloud Brightening (MCB)

- Highlighted as underexplored relative to SAI.
- Recommendations to model MCB across scales from LES (large-eddy simulations) to global climate models, with improved aerosol–cloud interaction representation.
- Suggested as a complementary priority alongside SAI, with possible focus on regional applications (e.g., subtropical marine stratocumulus).
- Mention of G6-1.5K-MCB as a benchmark scenario.

3. Cirrus Cloud Thinning (CCT) and Mixed-Phase Cloud Thinning (MCT)

- Several respondents pointed to CCT and MCT as important areas for fundamental research, though requiring significant model development.
- Emphasis on better representation of cloud microphysics in regional and global models before robust SRM scenario studies are possible.

4. Emissions pathways and baselines

- Need to anchor SRM scenarios to plausible socio-economic emission pathways (e.g., SSP2-4.5, SSP5-8.5/RCP8.5).
- Importance of considering worst-case emission pathways (in light of current fossil fuel trajectories) as well as middle-of-the-road mitigation cases.
- Recognition that short-term impacts may be relatively scenario-independent, but longer-term runs and integration with IAMs require robust emissions-linked scenarios.

5. Coordination and standardization

- Multiple comments on the need for community coordination across CMIP, ScenarioMIP, and GeoMIP to ensure consistency.
- Current SRM scenarios are often “reactions” to SSP/CMIP design rather than purpose-built; a call for more dedicated SRM scenario design.

6. General points

- Some participants stressed uncertainty in models, especially global ones, and suggested prioritizing regional optimization (e.g., LES-based approaches for MCB).
- Others highlighted the importance of proof-of-concept studies and sensitivity experiments to explore the parameter space rather than focusing only on one pathway.

---

**Summary**: SAI is seen as the immediate modeling priority (especially peak-shaving and GeoMIP scenarios), followed by MCB (currently underexplored), with CCT/MCT requiring more fundamental model development. Scenarios should be tied to plausible emissions pathways (SSPs, RCPs), coordinated across modeling intercomparison projects, and designed to test both idealized and realistic deployment strategies.

**Q: How do you evaluate SRM model outputs (e.g., against observations, historical analogues)?**

*Observations as the primary benchmark*

- Most experts emphasized evaluating SRM model outputs against observational datasets, including:
  - Satellite data (e.g., CALIPSO retrievals for cirrus/cloud microphysics).
  - In situ aircraft campaigns.
  - Ground-based measurements.
- Observations are used across different spatial and temporal scales to assess model fidelity.

*Historical and natural analogues*

- Volcanic eruptions (e.g., Mt. Pinatubo, smaller explosive/effusive events, smoke plumes) are the most frequently cited analogues for SAI.
- Ship tracks and natural aerosol perturbations are used as analogues for MCB.
- Seasonal and hemispheric contrasts also provide limited evaluation opportunities.
- However, many noted the limitations of analogues: incomplete input data, differences from deliberate SRM forcing, and difficulty transferring results to controlled SRM scenarios.

*Model–model comparisons*

- In the absence of robust observations, inter-model agreement is often used to build confidence in results.
- Multi-scale modeling approaches (LES, regional, global) can be compared to verify behavior across scales.
- Some highlighted the need for better microphysical process representation in models, especially for SAI and CCT, to improve trust in simulations.

*Idealized and constrained simulations*

- Some researchers run idealized simulations where outputs can be compared to a well-defined unperturbed baseline.
- Others use constrained modeling where models (e.g., CAM5/CAM6) are forced to match retrievals of cirrus cloud properties, enabling targeted evaluation of CCT effects.

*Current limitations and future needs*

- Many acknowledged that direct SRM-relevant observational data is lacking, particularly for MCB and CCT.
- Without dedicated field experiments, validation remains indirect.

- Calls for future field trials, targeted SRM experiments, and expanded satellite/in situ observations to test model predictions.
- Ultimately, robust evaluation requires both observational benchmarks and process-based validation of how well models capture the physical mechanisms (e.g., monsoonal circulation, stratospheric aerosol microphysics).

---

**Summary**: SRM model evaluation today relies on a mix of observational datasets, historical analogues (volcanoes, ship tracks), and model intercomparison, but each has significant limitations. While volcanic analogues and constrained simulations offer partial validation, the field ultimately needs dedicated observations and potential small-scale field trials to build confidence in SRM model outputs.

**Q: What data (satellite, ground-based, aircraft, etc.) would be most helpful for model validation in SRM studies?**

The responses emphasized that no single observational platform can adequately support SRM model validation; instead, a **synergistic, multi-platform approach** is required. Satellites, aircraft, and ground-based systems were consistently identified as complementary, each addressing different scales and aspects of the problem.

Satellite observations were highlighted as essential for providing a global, integrated perspective on aerosol–cloud–radiation interactions. Long-term, trustworthy datasets with global coverage are considered indispensable for capturing radiative effects and large-scale variability. Instruments capable of vertical profiling and synergy, such as those provided by EarthCARE (ATLID, CPR, MSI, BBR), and geostationary imagers like SEVIRI for diurnal cloud tracking, were frequently mentioned. Satellite products of cloud properties, aerosol optical depth (AOD), and radiative fluxes (e.g., CERES) were considered central to model evaluation.

Aircraft and in situ observations were recognized as critical for process-level understanding, particularly in areas where satellites face retrieval challenges. Key needs include aerosol composition and size distribution, cloud microphysics (droplet number closure, INP/CCN concentrations), and radiation closure measurements. Long-endurance aircraft systems and balloon-borne platforms were viewed as especially important for sampling the upper troposphere and lower stratosphere.

Ground-based networks such as ACTRIS, ARM, and BSRN were identified as indispensable complements, providing continuous, high-quality observations to constrain models and reanalyses. Lidar, radar, and ozonesonde data were noted for their ability to deliver vertical structure and long-term monitoring.

Several respondents also stressed the importance of event-based observations of natural analogues, including volcanic eruptions, large wildfires, and ship tracks, as they offer rare opportunities to evaluate SRM-relevant processes such as stratospheric aerosol evolution and cloud-aerosol interactions under perturbed conditions.

Overall, the expert consensus points to a smart integration of satellite, aircraft, and ground-based datasets, where satellites provide global context, aircraft and in situ measurements capture detailed processes, and ground-based systems ensure continuous monitoring. Such a combined strategy is seen as essential for robust evaluation of SRM model performance and for building confidence in predictions of potential climate impacts.

**Q: Can you identify any specific requirements for SRM research that are unique and not commonly addressed in other areas of climate research?**

Based on the collected responses, several specific requirements for SRM research emerge that are unique compared to other areas of climate research. These can be grouped into scientific, technical, governance, and societal categories:

**1. Scientific & Technical Requirements**

- *Stratospheric processes and aerosol evolution*
    - Long-term behavior of the stratosphere under continuous aerosol heating.

- Evolution of aerosols in stratospheric plumes (composition, size, and lifetime).
- Stratosphere-troposphere coupling, which is usually ignored in standard climate research.

- *SRM-specific climate response*
  - Differential climate response to shortwave dimming (SAI) vs. longwave changes.
  - Signal detection against high natural meteorological variability.
  - Regional impacts (monsoons, hydrological sensitivity, extremes).
- *Aerosol-cloud interactions for MCB/SAI*
  - Microphysical uncertainties in aerosol size, composition, and interactions.
  - Cloud-aerosol-precipitation feedbacks, particularly for marine cloud brightening.
  - Optimization of aerosol properties depending on environmental conditions.
  - Potential interactions between different SRM approaches (SAI vs. CCT).
- *Data and observation needs*
  - Combination of in-situ and remote sensing measurements.
  - Need for new lab experiments to test “designer aerosols” and cloud responses.

**2. Governance & Ethical Requirements**

- *Oversight and regulation*
  - Governance structures to oversee SRM implementations.
  - Consideration of deployment scenarios: IF, HOW, WHEN, and WHO.
  - Outdoor research requires careful governance, dual-badging, and adherence to ethical standards.
- *Transparency and public engagement*
  - Necessity of proactive public engagement and communication.
  - Total transparency to policymakers and the public, given the intentional climate intervention.
  - Framing of research messaging to avoid misinterpretation.

**3. Risk & Uncertainty Management**

- *Attribution and risk assessment*
  - Attribution of potential side effects is uniquely challenging due to novelty.
  - Risk-risk assessments are still underdeveloped for SRM deployment.
  - Understanding and quantifying front-loaded uncertainties (deployment timing, method, actors).
- *Interdisciplinary and ecological considerations*
  - Interactions with ecosystems, emissions, deposition, and other environmental impacts.
  - Ethical, social, and legal implications intersect strongly with the scientific research.

**Summary**: SRM research is distinct from typical climate science because it combines: (a) Novel physical processes (stratospheric aerosols, targeted cloud manipulation). (b) High uncertainty in both science and policy. (c) Direct societal, governance, and ethical implications requiring communication and oversight.

Essentially, SRM research cannot focus solely on understanding the climate system; it requires integrated, multidisciplinary approaches bridging climate science, technology, governance, and public engagement.

**Q: How would SRM research approaches be effectively justified both to potential funders and to (skeptical) public or media?**

Participants emphasized that SRM research must be justified not as an alternative to emissions reductions, but as a temporary, complementary, and risk-management measure to inform future decisions. The central argument is that knowing is better than not knowing: without research, society risks facing a future where SRM might be deployed under crisis conditions, "flying blind" about its impacts.

**Key justifications to funders and the public include:**

1. *Risk–risk framing*
    - SRM may represent the lesser of two evils compared to unmitigated climate change.
    - Research helps quantify risks and avoid unintended consequences if SRM were ever considered.

2. *Learning from nature and co-benefits*
    - Natural analogues (e.g., volcanic eruptions, ship tracks, wildfires) provide entry points for public understanding.
    - SRM studies also improve fundamental knowledge of aerosols, clouds, and climate systems, which benefits wider climate science and disaster preparedness.

3. *Transparency and governance*
    - Open data, independent ethics reviews, pre-registered experiments, and community engagement are vital to build trust.
    - Public funding ensures transparency and reduces the risk of unregulated or opaque private initiatives.

4. *Future preparedness*
    - With rising climate risks and Paris targets slipping out of reach, communities may one day call for emergency cooling. Having a scientific evidence base ready is an "insurance policy."
    - SRM research is not advocacy for deployment but preparation for informed, ethical decision-making.

5. *Communication strategies*
    - Use clear narratives: SRM research is about safety, precaution, and informed choices, not promoting deployment.
    - Highlight intergenerational responsibility ("what will our children think in 30 years if we chose not to investigate?").
    - Frame small-scale experiments as safe, limited, and non-climate-altering.

**Q: What would be the most urgent problem to be addressed by outdoor research?**

Respondents identified two broad categories of urgent issues for outdoor SRM research:

1. *Governance and ethical considerations*
    - Many highlighted that before any outdoor research, clear governance mechanisms and international oversight must be established.
    - Public trust, transparency, and ethical safeguards are prerequisites for legitimacy.

2. *Scientific and technical priorities*
    - Aerosol processes: How injected particles (SAI) evolve, age, disperse, and interact chemically in the stratosphere.
    - Aerosol–cloud interactions: Especially for MCB and CCT, where cloud microphysics, droplet activation, precipitation onset, and cirrus responses are poorly constrained.
    - Engineering feasibility: Demonstrating whether delivery systems (sprayers, nucleation methods) can generate and disperse particles of the required size and distribution.
    - Process validation: Moving beyond a “model world” by designing small, carefully governed outdoor tests to validate model predictions and improve microphysical schemes.
    - Background conditions: Better sampling of natural variability and volcanic analogues to provide reference states.
    - Measurement infrastructure: Developing sustainable, affordable, and globally deployable in-situ and remote-sensing systems for small-scale perturbation detection.
3. *Control and predictability*
    - Several stressed the need to test whether SRM interventions can be controlled and whether clouds or aerosols behave as expected under outdoor perturbations.
    - Small-scale, well-monitored experiments (e.g., sea-salt CCN closure studies, tracer-aided dispersion trials) were seen as the most realistic near-term step.

---

**Summary:** Outdoor SRM research must first establish governance frameworks, then focus on small-scale, carefully monitored studies to address the biggest scientific unknowns: aerosol microphysics, cloud responses, and delivery feasibility.

**Q: Would a centralized SRM EO data portal be useful to your research?**

Most respondents indicated that a centralized SRM EO data portal would be very useful, with an average score of ~7.6/10 and a median of 8/10. The majority of answers fall in the high range (7–10), and several participants gave the maximum score of 10, reflecting strong enthusiasm for such a resource.

At the same time, a few lower scores (1–5) suggest that not all researchers see direct value for their work, possibly because of specific research focuses, existing data access routes, or skepticism about centralization.

In summary, there is broad support for developing a centralized SRM EO data portal, with most researchers considering it highly useful for their activities, while a small minority remain uncertain about its relevance to their needs.

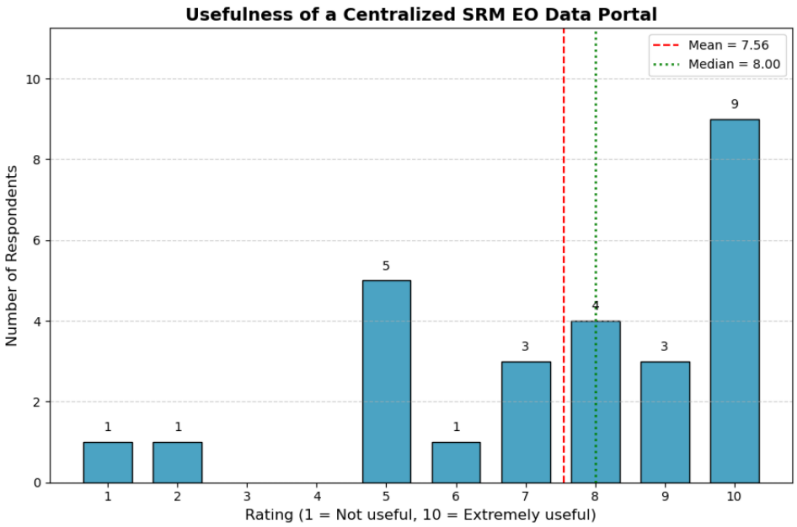


**Figure 9** Bar plot showing if a centralized SRM EO data portal would be useful to the research of the experts. The scale extends from 1 “Not useful” to 10 “Extremely useful”.

#### 2.5.3.2 SAI-relevant outcomes

**Q: Which existing EO datasets (captured by spaceborne, airborne, ground-based and in-situ sensors) can be used to detect, monitor and model the effects of SAI?**

A wide range of existing Earth Observation datasets from spaceborne, airborne, ground-based, and in-situ platforms could, in principle, be used to detect, monitor, and model the effects of SAI. These datasets include, but are not limited to:

1. **Spaceborne sensors**
   - Lidar and radar missions: e.g., *EarthCARE* (ATLID lidar, CPR radar) to observe aerosol plumes and cloud-aerosol interactions.
   - Aerosol and trace gas sensors: e.g., *OMI*, *TROPOMI*, *CALIPSO*, *MODIS* for monitoring $SO_2$, sulfate aerosols, and plume evolution.
   - Temperature and radiation sensors: to track stratospheric heating and radiative effects of aerosols.
2. **Airborne platforms**
   - Research aircraft such as *FAAM* (UK) or DLR sub-orbital platforms equipped with aerosol spectrometers, lidars, and trace gas instruments.
   - Can provide targeted high-resolution observations of stratospheric plumes and validate satellite measurements.
3. **Ground-based networks**
   - AERONET: aerosol optical depth, size distribution, and spectral properties.
   - Surface-based lidars: vertical profiling of aerosol layers and optical properties.
   - Volcano monitoring networks: provide insight into plume transport and chemical transformations (analogous to SAI injections).
4. **In-situ measurements**
   - Balloon or aircraft-borne aerosol collectors, optical particle counters, and chemical samplers to measure particle size, composition, and radiative properties.
   - Trace gas measurements for $SO_2$ and sulfate precursors.

**Key considerations for best use**:

- *Integration across platforms:* Combining datasets provides spatial and temporal coverage, reduces uncertainties, and allows cross-validation (e.g., satellite + airborne + ground).
- *Advanced data interpretation:* AI and machine learning methods can enhance detection, tracking, and modeling of SAI plumes, especially for differentiating natural from anthropogenic aerosol sources.
- *Analogy to volcanic eruptions:* Many existing datasets have been successfully used to monitor volcanic $SO_2$ and sulfate aerosol plumes, offering a proof-of-concept for SAI monitoring.
- *Accessibility and coordination:* Increasing open access to relevant EO datasets and fostering collaboration between space agencies, universities, and research centers is crucial.

**References / Examples**: *NOAA* B2SAP *project* [URL23]*, EO datasets for radiation and aerosol monitoring* [URL24]

All existing EO datasets are potentially useful, but their full utility depends on coordinated, multi-platform use and innovative analysis approaches. Current infrastructure is not designed specifically for SAI, highlighting the need to adapt existing systems and methods for future geoengineering research.

**Q: When using volcanic eruptions as natural analogues for SAI, do you think the immediate post-eruption phase (when volcanic ash is still present in the stratosphere) should be included in radiative impact assessments, or should the analysis focus primarily on the longer-term effects from sulfate aerosols?**

When using volcanic eruptions as natural analogues for SAI, it is important to consider both the immediate post-eruption phase, when volcanic ash is still present in the stratosphere, and the longer-term phase dominated by sulfate aerosols. The early ash-rich phase affects $SO_2$ oxidation, aerosol microphysics, plume transport, and radiative interactions, and can even prolong the lifetime of sulfate aerosols (Wells et al., 2023). While ash fallout typically occurs faster than the conversion of $SO_2$ to sulfate, it influences rainout, plume self-lofting, and early-stage radiative impacts, making it a valuable signal despite observational noise.

The longer-term sulfate aerosol phase represents the persistent radiative forcing that is more directly analogous to SAI injections. Both phases are necessary because focusing only on the long-term ignores critical early-stage processes, while the ash phase alone does not fully capture the sustained climate effects. Different eruptions produce different co-emitted species—e.g., Hunga Tonga emitted significant $H_2O$—which change aerosol microphysics and subsequent evolution, highlighting the need to assess all stages and types of eruptions.

While volcanic eruptions are not perfect analogues for sustained SAI, studying both immediate and long-term effects provides essential insights into aerosol lifetimes, transport, and radiative forcing. Using the full eruption record, even with noisy early observations, helps constrain models and improves understanding of uncertainties, including how a single pulse eruption may represent or deviate from long-term SAI deployment.

**Q: Are you aware of any SAI experiments (including indoor research)?**

The respondents are aware of few SAI research experiments, primarily conducted in indoor or laboratory settings. These experiments focus on studying the chemistry, microphysics, and behavior of solid or sulfate particles under stratospheric conditions, including their interactions with stratospheric gases and radiation. Examples include ARIA-funded projects led by Cambridge and Harvard, as well as related efforts in the US and other international research groups. Some studies also involve testing prototypes, such as nozzles or particle delivery systems, and observing naturally occurring emissions to validate measurement techniques. To date, no real outdoor deployment or active atmospheric injection experiments have been conducted by the scientific community, although some private companies and non-profits have explored small-scale tests in non-public settings. These controlled studies provide crucial insights into the physical and chemical processes relevant to SAI while maintaining zero risk to the environment.

**Table 8** List of SAI-relevant activities

| Initiative / Group | Type of Activity | Notes |
|---|---|---|
| **ARIA (Cambridge, Harvard, others)** | Laboratory experiments; chamber studies of particle chemistry/microphysics; nozzle testing | Publicly funded; focus on processes, not deployment |
| **Harvard & Cambridge collaborations** | Indoor experiments on stratospheric particle behavior | Part of ARIA-funded projects |
| **Stardust (Israel–US company)** | Reported small-scale outdoor release tests | Private, not transparent; credibility questioned |
| **Reflective (US non-profit)** | Planning small outdoor tests; involved in SRM advocacy and research | No deployment yet; exploratory phase |
| **NOAA (US)** | Laboratory and observational studies; monitoring volcanic analogues | Focus on understanding stratospheric processes |
| **SRM360 (NGO registry)** | Database of proposed/planned outdoor experiments | Transparency initiative; no deployment-scale work |
| **Other academic groups (US, EU)** | Chamber studies, sensor prototyping, testing with natural emissions (e.g., volcanoes) | Often linked to aerosol-cloud-radiation process research |

#### 2.5.3.3 MCB-relevant outcomes

**Q: Are you aware of any efficient technologies that could be used to deliver appropriate aerosols to clouds within the Planetary Boundary Layer (PBL)?**

The respondents are aware of several technologies that could potentially deliver aerosols to clouds within the Planetary Boundary Layer (PBL), although all are still under development. Proposed approaches include sea water spraying vessels propelled by wind power, spray systems mounted on tall towers or off-shore platforms, aircraft-based seeding at low altitudes, balloon-assisted low-altitude dispersion, and mod-ification of ship exhaust (e.g., rerouting or engineering emissions). Emerging concepts, such as electrifying plumes to produce droplets, have also been suggested as promising approaches. A key technical challenge is the design of nozzles capable of delivering droplets within a relatively narrow size range, which is crucial for efficient cloud seeding. Overall, these methods remain in experimental or conceptual stages and have not yet been deployed operationally.

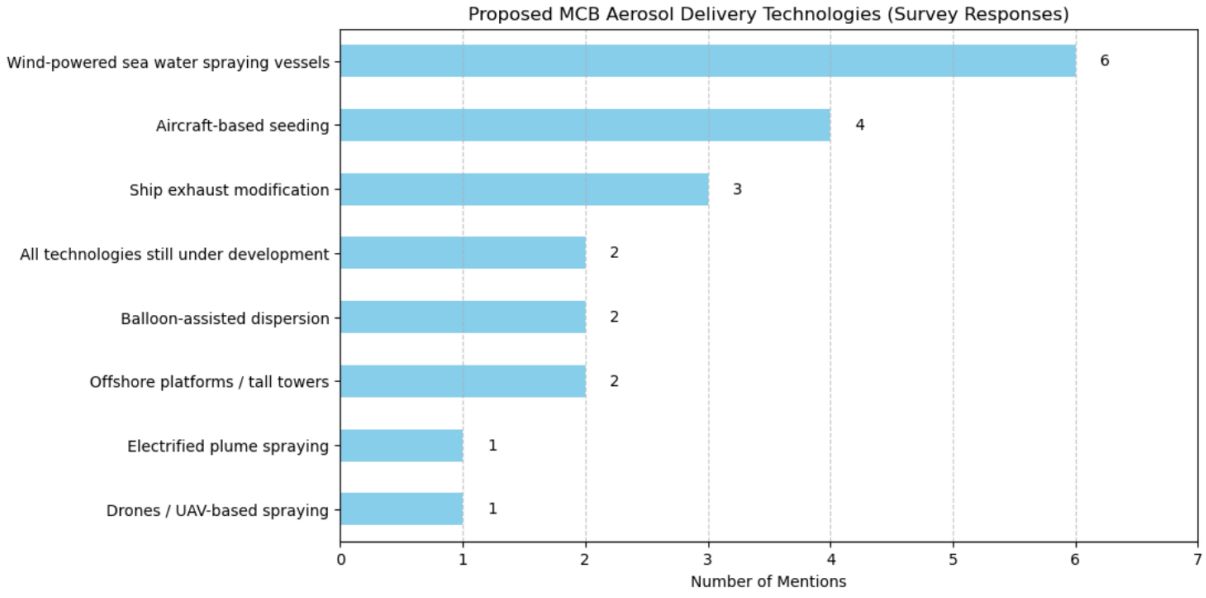


**Figure 10** Bar plot showing which technologies can be efficient to deliver aerosols at the cloud level for MCB studies

**Q: Field trials for MCB are currently underway near Australia's coral reefs, aiming to reduce coral bleaching. In your view, which other regions should be prioritized for MCB field research — and why?**

Most respondents emphasized that persistent stratocumulus regions should be prioritized for MCB trials, as they provide the most favorable meteorological conditions for testing cloud brightening and maximizing radiative effects (Feingold et al., 2024). Suggested locations included:

- Eastern subtropical ocean basins (e.g., off the coasts of California, Namibia/Angola, and Portugal/Canary Islands) where stratocumulus decks are climatologically extensive and sensitive to aerosol perturbations.
- Remote islands such as Ascension Island or Saint Helena, which offer logistical bases for field studies while minimizing confounding influences from continental pollution.

Several experts noted that the Great Barrier Reef (GBR) is not an ideal meteorological testbed—despite its ecological importance—because cloud conditions there are less conducive to robust MCB assessment. Instead, GBR trials serve mainly as ecosystem-protection pilots rather than optimal sites for understanding MCB processes.

Other priorities mentioned included:

- Arctic regions, where field trials could help assess the potential of MCB to slow sea-ice melt.
- Regions with diverse meteorological conditions, to test how cloud susceptibility varies across climates.

Finally, some highlighted that small-scale technology development trials (e.g., on generation/delivery systems and closure experiments) could be conducted in multiple locations, irrespective of ecological rationale, to improve process-level understanding before considering larger-scale climate impacts.

**Q: Recent years have been the warmest on record for many parts of Europe, with the Mediterranean Sea showing exceptionally high Sea Surface Temperatures (SSTs). Extended heatwaves and extreme weather — including increased occurrence of Medicanes — are among the observed climate impacts. In your view, could MCB offer any potential benefits for Europe in mitigating such effects? If yes, in which regions and through which mechanisms?**

The respondents consider that MCB could offer limited potential benefits for Europe, but there are significant uncertainties and constraints. Direct marine cloud brightening over the Mediterranean is unlikely to be effective due to sparse and patchy low-level cloud cover. Marine sky brightening—creating diffuse haze rather than brightening clouds—might offer some cooling potential in regions with limited clouds, but the trade-offs, such as reduced blue-sky conditions affecting tourism and local quality of life, would need to be carefully considered.

Potential mechanisms for indirect cooling include leveraging persistent stratocumulus decks in the NE Atlantic or other nearby regions to modulate sea surface temperature (SST) gradients, storm-track baroclinicity, and teleconnected climate patterns that influence Europe. Global MCB or SRM approaches could reduce mean temperatures and partially mitigate heatwaves, extreme weather, and Medicanes, but there is substantial uncertainty about unintended consequences, side-effects, or impacts on regional precipitation and circulation. High dust loads and existing cloud condensation nuclei (CCN) could also limit the effectiveness of regional interventions.

Overall, the respondent emphasizes that the feasibility and potential benefits of MCB for Europe remain a research question. Targeted process studies, high-resolution coupled modeling, and careful consideration of societal and economic impacts are essential before evaluating MCB as a climate mitigation strategy in this region.

#### 2.5.3.4 CCT-relevant outcomes

**Q: Observational evidence suggests that cirrus clouds affected by aviation often exhibit larger ice crystals and lower number concentration — a behavior which mimics somehow aspects of CCT. In your view, could aviation emissions be considered a natural analogue for CCT, by introducing ice-nucleating particles (INPs) that increase crystal size and reduce optical depth? Please elaborate on the mechanisms and limitations.**

There is broad agreement that aviation emissions may provide *some* insights into Cirrus Cloud Thinning, but most respondents emphasized significant limitations. Some experts suggested that aviation-induced cirrus, which often shows larger ice crystals and reduced number concentrations, could mimic aspects of CCT. Aviation soot could in principle act as an ice-nucleating particle (INP), but it is generally considered a very inefficient INP (Righi et al., 2020). While this inefficiency might prevent dramatic overseeding — given the enormous number of particles emitted (~10^14 per kg fuel) — it also limits its utility as a true analogue for intentional CCT interventions.

Several respondents noted that more targeted observations are needed to clarify the role of aviation. For example, long-term aircraft-based measurements (e.g., Lufthansa in-situ programs) and balloon-borne particle counters could provide valuable evidence of how aviation emissions interact with cirrus under different regimes. A few pointed to ongoing projects (e.g., ARIA initiatives) that explicitly examine aviation–CCT links.

Others stressed caution: cirrus cloud processes are highly uncertain, and overshooting with seeding could lead to warming rather than cooling. Some argued that, given the lack of consistent cooling signals in both models and observations, CCT may not be a viable SRM approach.

Finally, it was highlighted that aviation is not necessarily the best analogue, since the types of particles emitted differ from those envisioned for CCT. More natural analogues may be provided by dust outflow regions, where observations (e.g., CALIPSO, Mitchell and Garnier 2025) show reduced homogeneous cirrus when dust is abundant. A recent study by Erfani and Mitchell (2024), using CALIPSO cirrus cloud retrievals, estimated the surface cooling potential of CCT in polar regions. While the direct cooling impact appeared substantial, an estimated 20% increase in new cirrus clouds nearly offset this effect, resulting in only weak net surface cooling. Villanueva et al. (2022) showed that thinning of mixed-phase regime clouds can induce substantial cooling.

In summary, while aviation emissions may provide partial and opportunistic analogues for CCT, the evidence remains weak, highly regime-dependent, and not directly transferable. Aviation studies should be pursued to improve understanding, but they cannot substitute for targeted CCT research.

**Q: Which materials have been proposed in the literature as most effective for CCT studies? What is the threshold seeding density required to achieve a net radiative cooling effect?**

A range of materials has been proposed in the literature for Cirrus Cloud Thinning (CCT), though there is no consensus on the most effective candidate. Commonly discussed options include:

- **Silver iodide (AgI):** Historically used in cloud seeding and considered an effective ice-nucleating particle (INP) at cirrus temperatures.
- **Bismuth triiodide ($BiI_3$):** Highlighted in Mitchell & Finnegan (2009, *ERL*) as a promising candidate. It was reported to be comparably effective to AgI at < –25 °C, with lower cost, though concerns about toxicity remain and published evidence is limited.
- **K-feldspar and other silicates:** Proposed as naturally abundant INPs, though their efficiency under stratospheric conditions is still under investigation.
- **Soot/black carbon:** While aviation studies suggest that soot can sometimes act as an INP, it is generally considered inefficient for CCT and unsuitable due to associated warming effects.

Other materials (e.g., silver nitrate) have also been mentioned in the literature, but all candidates raise questions of toxicity, availability, and side-effects. Respondents emphasized that material safety and ecological impacts are as important as nucleating efficiency.

On the second part of the question — the threshold seeding density — no clear value is established. The most cited modeling study (Storelvmo et al., 2013, *GRL*) suggests an optimal concentration of ~10–70 INP per liter of air could induce a cooling effect by reducing cirrus optical depth. Other rough estimates suggest ~1 INP per $cm^3$, but respondents stressed that this remains highly uncertain because it depends on natural INP background concentrations, microphysical regimes, and interactions with underlying mixed-phase clouds.

Overall, while materials like AgI, $BiI_3$, and feldspar have been proposed, there is *no agreed-upon candidate* and *no robustly quantified seeding density* to guarantee net radiative cooling. Further laboratory, observational, and modeling work is needed before CCT can be evaluated as a viable SRM technique.

**Q: How could we separate seeding effects from natural variability?**

Separating potential seeding effects from the strong natural variability of cirrus clouds is one of the biggest challenges for CCT research. Respondents highlighted several complementary approaches:

- **Large observational datasets:** Long-term, high-resolution satellite and in-situ observations are needed to detect statistical signals of seeding against natural variability (Eastham et al., 2025). Reanalysis products will be essential to provide context.
- **Targeted field campaigns:** Projects such as *CloudLab* and *De-risking Cirrus Modification* were mentioned as promising, combining aircraft, balloon, and satellite observations in regions where cirrus formation is dominated by homogeneous nucleation (e.g., over mountains or the Southern Ocean). These locations may provide clearer signals of CCT interventions.
- **Understanding background INP variability:** Several respondents stressed the need to establish a robust baseline of natural upper-tropospheric INP concentrations. The *INPUT:ACCESS* project was highlighted as an effort to develop balloon-based technologies to measure INPs in situ at high temporal resolution. These measurements are expected to improve knowledge of variability and thereby enable attribution of seeding effects.
- **Experimental design:** Carefully controlled seeding experiments — for example, in geographically "locked" cirrus regions or in the lower stratosphere where seeded INPs can disperse more uniformly — could help isolate effects.
- **Modeling and tracers:** High-resolution models with ice tracers that can track contributions from seeded versus natural INPs are critical to interpret observations and quantify potential impacts.
- **Long-term perspective:** On short time and space scales, localized changes (analogous to shiptracks in MCB) may be detectable. But at larger spatial or temporal scales, natural variability dominates, so multi-year records and carefully designed before–after comparisons are required.

Overall, a combination of dedicated field tests, improved observational infrastructure, and advanced modeling frameworks will be required. Without establishing the baseline variability of natural cirrus-forming processes, it will remain nearly impossible to reliably separate a CCT signal from background fluctuations.

## 2.6 Summary of requirements

Stratospheric Aerosol Injection (SAI), Marine Cloud Brightening (MCB), and Cirrus Cloud Thinning (CCT) all show potential, substantial uncertainties remain regarding their effectiveness, side effects, and feasibility.

- **SAI** has been consistently shown in models to reduce global mean temperatures; however, the magnitude, spatial distribution, persistence, and regional climate impacts remain uncertain. Potential side effects include alterations to atmospheric circulation, ozone depletion, precipitation patterns, and ecosystem responses, with regional droughts and changes in monsoon systems poorly quantified. The effectiveness of SAI is sensitive to injection latitude, altitude, and aerosol type, and research on alternative materials remains limited. Abrupt termination of SAI could lead to rapid warming. Limited model capabilities and sparse observational data reduce confidence in predicted outcomes, and no operational platforms currently exist for stratospheric aerosol deployment, leaving energy, logistical, and cost requirements unclear.
- **MCB** aims to enhance the reflectivity of marine clouds to influence regional temperatures and mitigate climate extremes. Key uncertainties include optimal droplet size, spray flux, deployment locations, and cloud-aerosol interactions, which are highly non-linear and regime-dependent. Regional impacts on precipitation, circulation, and heat fluxes remain poorly quantified. Global models often inadequately resolve low-cloud microphysics and feedbacks, limiting confidence in regional predictions. Scalable spray technologies are experimental, and operational and energy challenges

remain unresolved. Detecting MCB-induced changes is difficult due to their subtle and localized nature, and ethical and governance issues arise from region-specific interventions.

- **CCT** targets high-altitude cirrus clouds to reduce longwave radiation trapping. Its climate efficacy is uncertain because the net radiative impact depends on cloud properties and may lead to unintended warming if deployed inappropriately. The effectiveness of seeding depends on aerosol type, background conditions, ice nucleation pathways, and cloud microphysical processes, all of which are poorly understood. No proven technology exists to deliver ice-nucleating particles to the upper troposphere, and candidate materials require further characterization. Few models adequately represent cirrus microphysics, and observational detection is challenging due to the thin and transient nature of cirrus clouds. Injecting artificial ice-nucleating particles introduces unknown chemical and ecological risks.

Overall, all three SRM approaches face substantial uncertainties in climate response, material properties, delivery methods, environmental impacts, modeling, observational constraints, and technological readiness. Addressing these knowledge gaps through coordinated research is critical before considering any deployment.

## 2.7 Conclusions from the STATISTICS / ACtIon4Cooling workshop on SRM techniques

On 17th June 2025 a workshop with SRM experts was organized by the co-funded ESA STATISTICS and *ACtIon4Cooling* project concluded on the following main conclusions:

**Support for Open-Ended Research**

The workshop participants expressed clear support for open-ended research on Solar Radiation Modification (SRM) techniques, particularly through publicly funded mechanisms. Given the deep uncertainties and the high stakes involved with climate mitigation and adaptation, a robust scientific understanding of potential processes, impacts, risks and unintended consequences of SRM must be constrained by neither narrow policy frames nor prematurely operational agendas. Public funding can ensure independence, transparency, and broad stakeholder engagement in setting research priorities. European funding for research explicitly labelled as SRM would build a basis for an independent stance on the topic.

**Enhanced Use of Natural Analogues and Existing Observations**

Great scientific potential exists in studying natural (and anthropogenic) analogues of SRM, such as explosive volcanic eruptions, low-level degassing volcanoes, changes or variability in traffic (ship) and industry emissions, dust events in the upper troposphere, or contrail cirrus. These opportunities remain underexploited. In particular, satellite datasets—some of which contain relevant but as-yet-unanalysed observations—offer a valuable resource for improving our understanding of aerosol–cloud–radiation interactions. A coordinated effort to mine and integrate such datasets is recommended. In particular, harmonizing assumptions made in models and satellite retrievals would help to better integrate observations and models (e.g. through digital twins). New observing capabilities should also be mobilized.

**Field experiments: Clarity of Rationale and Participatory Design Are Crucial**

While small-scale field experiments may eventually become necessary to resolve key scientific uncertainties that cannot be addressed by model experiments, natural analogues or laboratory studies alone, their justification and design must be articulated with great clarity. This includes defining specific scientific and/or technical objectives, ensuring transparent public communication, and co-developing experimental plans with a diverse range of stakeholders to maximise legitimacy, scientific and/or technical value, and ethical integrity. An assessment on potential impacts on weather and climate should be provided as part of the planning. It should be noted that field experiments relevant to SRM techniques may also be motivated by process understanding, regardless of SRM objectives.

**Improved Observing System with Distinction Between Monitoring and Detection**

The current global observing system is insufficient for monitoring key parameters relevant to SRM techniques, especially for Stratospheric Aerosol Injection (SAI), and for detecting SRM experiments below a certain size or uncoordinated deployment. There remain major observational gaps in trace gases, aerosol

and cloud properties, vertical distribution, radiative effects, and troposphere-stratosphere coupling. Further risks are associated with the downscaling, or lack of open access availability to European research, of US current and future observing programmes and satellite missions. A dedicated effort is required to document monitoring priorities in order to enhance these capabilities. The ongoing effort to produce long-term homogenised climate data records relevant to SRM processes should be continued. Observing systems designed to study natural analogues and assess the impacts of planned field experiments may not necessarily be the same as those needed for early detection and attribution of uncoordinated SRM field experiments or deployment.

**Improved Modelling Capabilities for Prediction and Attribution**

Earth System Models are improving through resolution increase and more comprehensive representation of aerosol and cloud processes, but different models continue to disagree on some key aspects of the climate response to SRM. Moreover, the predictions at subseasonal, seasonal and decadal scales are insufficient to reliably anticipate the impacts of field experiments and potential deployment. Similarly, it is necessary to establish confidence in counterfactual simulations that would be required to quantify intended and unintended impacts of SRM field experiments or deployment. Research is thus required on how trust in counterfactual simulations may be established. Further model improvements may build on insights from natural analogues and hypothetical future field experiments.

# 3. Development methods and validation mechanisms

This chapter describes the development and assessment of the methods, algorithms, models, and procedures employed in *ACtIon4Cooling*.

## 3.1 SAI

### 3.1.1 Overview

For SAI, volcanic aerosol detection and information on their vertical distribution, and injection heights is obtained from space-borne sensors, primarily the single-wavelength, HSRL, polarization lidar ATLID on board EarthCARE.

More specifically, to identify the aerosol layers of volcanic origin, the ATLID L2 optical property profiles and target classification product (EBD and A-TC; Donovan et al., 2024) are utilized. EBD relies on optimal estimation to derive particle linear depolarization ratio (PLDR), extinction ($a_p$) and backscatter ($b_p$) coefficient profiles at 0.355 um. A-TC uses the EBD output together with auxiliary model data to attribute the detected targets into distinct categories including ice/water clouds, different aerosol types and aerosol mixtures. Since ATLID is an HSRL system, $a_p$ profiles are derived directly without the need to rely on climatology data or other assumptions to estimate the lidar ratio (LR) values, thus resulting in an improved classification compared to its' predecessor elastic lidar CALIOP on board CALIPSO v4.5 (Tackett et al, 2023) incorporates new thresholds to enable efficient discrimination between volcanic ash, sulfates, wild-fire smoke and polar stratospheric aerosols. By applying this algorithm for recent volcanic eruptions in Southern America, Tackett et al. (2023) demonstrated that it is possible to derive a decay rate of the PLDR; a very useful parameter to describe particle aging and removal of ash particles from the stratosphere. CALIOP data are openly available through the Aeris database [URL17].

The main method to characterize the volcanic particles in the stratosphere for SAI, leverages also synergies between the lidar measurements and observations provided from passive remote sensing sensors. The latter are derived primarily from the Hyper-Angular Rainbow Polarimeter (HARP2) on board PACE mission (Petro et al., 2020) but also the Multi-Spectral Imager (MSI) of EarthCARE. HARP2 is a multi-spectral, multi-angle polarimeter that operates in four spectral bands from the ultraviolet to the near-infrared. It features a wide 2600 km swath (94° cross-track; ±57° along-track) and 10 viewing angles for each spectral band (i.e. each ground target is observed 10 times from unique views), except for the 0.67 um band, which offers hyper-angular sampling at 60 views, and is therefore employed for cloud property retrievals, as it enables detailed sampling of the liquid cloud bow (Mc Bride et al., 2024). Herein, L1C georectified HARP2 radiances are utilized along with HARP2 L2 cloud property retrievals, including cloud optical thickness (COT), cloud-top height (CTH), and cloud droplets effective radius ($r_{eff\_c}$). MSI is a seven-band, push-broom scanner that provides images at 500 m ground sampling distance over a 150 km wide swath, asymmetrically tilted (in roll direction) away from the sun and covering 35 km (-) to the west side and 115 km (+) to the east side of the nadir in order to minimize sun-glint (east/west refer to the descending (daytime) part of the EarthCARE orbit). The L2 MSI derived cloud optical properties (COT, CTH, $r_{eff\_c}$) are used for SAI.

Openly available EarthCARE L1 and L2 products can be downloaded through [URL18], while all products are currently being mitigated in ESA's Multi-mission Algorithm and Analysis Platform (MAAP, [URL28]). Openly available PACE data can be downloaded through the NASA Earthdata portal [URL19]. Table 8 summarizes the instruments currently used in the project regarding SAI and their characteristics.

To follow the same methodology for stratospheric particle characterization, in cases when ATLID and HARP2 data are not available, CALIOP (2006 – 2023; Winker et al., 2009) and POLDER (2006 – 2013; Deschamps et al., 1994) observations may be used in future. The latest version of CALIOP stratospheric particle classification (v4.5) incorporates new thresholds to enable efficient discrimination between volcanic ash, sulfates, wild-fire smoke and polar stratospheric aerosols which can be particularly useful for SAI studies assuming natural analogues as they help to disentangle the effects of different aerosol species to stratospheric radiative forcing and dynamics. Indicatively, by applying this algorithm for recent volcanic eruptions in Southern America, Tackett et al. (2023) demonstrated that it is possible to derive a *decay rate of the PLDR*; a useful parameter to describe particle aging and removal of ash particles from the stratosphere. CALIOP and POLDER L1C data are openly available through the Aeris database [URL17], while POLDER L2 grided product retrievals using GRASP algorithm [URL20] can be found under [URL21].

If applicable, the dataset for volcanic aerosol properties can be further complemented with ground-based data from multi-wavelength, polarization lidars of the European Aerosol Research Lidar Network (EARLINET; Pappalardo et al., 2014) and AERONET radiometric measurements. Ground-based lidar systems like those employed in EARLINET are commonly of additional capabilities compared to space-borne instruments (e.g. can be used to derive PLDR and LR in multiple spectral bands), and thus can be utilized for enhanced aerosol characterization. EARLINET data are distributed to registered users through the EARLINET database [URL25] while AERONET daily products can be found under [URL29]. Airborne in-situ measurements, when available, can further support validation activities and constrain optical modeling simulations.

**Table 9** Characteristics of the instruments used to derived particle properties for SAI in the context of *ACtIon4Cooling*

| Platform | Instrument | Spectral bands [µm] | Spatial/Temporal resolution | Measurement Capabilities |
|---|---|---|---|---|
| EarthCARE | ATLID | 0.355 | Vertical: 100 – 500 m<br>Horizontal: ~1 km<br>Temporal: 25 d | Polarization HSRL |
| | MSI | 0.670, 0.865, 1.670, 2.210 | Vertical: n/a<br>Horizontal: 0.5 km<br>Temporal: 8 d | Multi-spectral imager |
| PACE | HARP2 | 0.440, 0.550, 0.670, 0.865 | Vertical: n/a<br>Horizontal: 2.5 km<br>Temporal: 2 d | Multi-spectral, multi-angular polarimeter |

In addition to the satellite observations, optical modelling simulations are performed to support the characterization of stratospheric aerosol particles. These are performed using the EarthCARE *Modeled optical properties of ensembles of aerosol particles* (MOPSMAP) scattering database (Gasteiger and Wiegner, 2018).

In particular, the optical properties of particles representative of those injected into the stratosphere following a volcanic eruption, are pre-calculated and stored in tabulated forms using MOPSMAP. The required micro-physical input parameters (i.e., size, shape and composition in the form of complex refractive index) are derived either from the literature (e.g. the OPAC scattering database; Hess et al., Koepke et al., 2015) or from available observational data, e.g. [URL22]

In the context of *ACtIon4Cooling* :

1. bi-modal and mono-modal size distributions, with variable effective radii ($r_{eff}$) and variances ($v_{eff}$),
2. CRIs that reflect different ash minerals in the atmosphere (e.g. Vogel et al., 2017), their mixtures with sulfates, and pure sulfate particles
3. different particle shapes (including spheres and spheroids),

are used to cover the range of realistic micro-physical properties of volcanic particles that can be found in the stratosphere (see for example Table 10 and Figure 11).

**Table 10** The microphysical properties used to calculate optical properties of volcanic ash and sulfate particles with MOPSMAP database.

| **Volcanic Ash** | | |
|---|---|---|
| **Parameter [step]** | **Range** | |
| $r_{eff}$ (µm) | 0.8, 1.0, 1.2, 1.5, 2.0, 3.0 | Mono/Bi-modal log-normals |
| $v_{eff}$ | 1.8, 2.4 | |
| Real Refr. Index (0.4 – 1.5 µm) | 1.4 – 1.6 taken from Vogel et al., 2017 for 6 different types of ash minerals and extrapolated to 2.5 µm | |
| Imag. Refr. Index (0.4 – 1.5 µm) | 0.0005 – 0.002 taken from Vogel et al., 2017 for 6 different types of ash minerals and extrapolated to 2.5 µm | |
| Shape: Spheroids | Aspect ratio: 1.3 – 1.6 [0.05] | Mono-modal log-normals |
| $v_{eff\_s}$ (shape distr. aspect ratio) | 1.65 | |
| **Sulfates** | | |
| $r_{eff}$ (µm) | 0.1-0.5 [0.05] | |
| $v_{eff}$ | 1.6, 1.8, 2.4 | |

| | | |
|---|---|---|
| Real Refr. Index (0.4 – 2.5 µm) | OPAC database for sulfates at 0% relative humidity | |
| Imag. Refr. Index (0.4 – 2.5 µm) | OPAC database for sulfates at 0% relative humidity | |
| Shape: Spheres | n/a | |

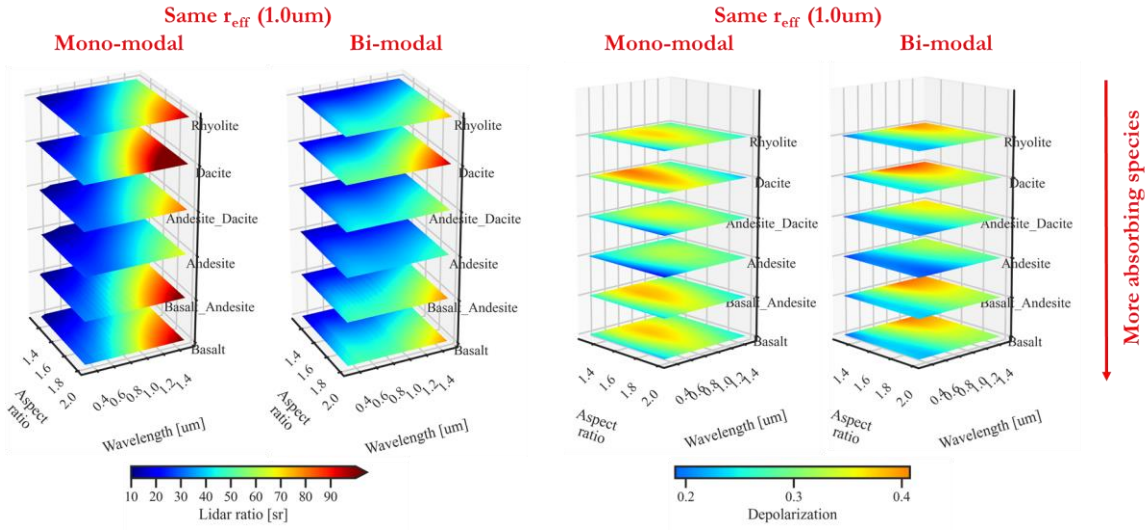


**Figure 11** Variations of lidar relevant parameters: the LR (left) and PLDR (right), for the different properties of ash minerals presented in Table 10.

### 3.1.2 Method

To detect and characterize stratospheric aerosol layers, simultaneous collocated (not coincident) lidar and polarimeter measurements are used. The methodology builds on the approach introduced by Wanquet et al. (2009, 2013), which exploits aerosol-induced modifications of liquid cloud signatures, specifically the alteration of the polarized light signal emerging from the underlying clouds at the top of the atmosphere (TOA). Originally the method was applied to A-train observations of POLDER, CALIPSO and MODIS for biomass burning and dust above clouds. Unlike the near-simultaneous observations of A-train sensors, PACE and EarthCARE overpasses can be up to 2 hours apart, depending on the latitude of the observations. Thus, since a direct temporal collocation of the two datasets is not possible, any possible changes in stratospheric AOD at 0.355 µm and vertical distribution are derived using ATLID data from consequent EarthCARE overpasses (within less than 2h close to the equator), while information on other particle optical (i.e. SSA, asymmetry factor etc.) and micro-physical properties ($r_{eff}$) are derived from HARP2 observations, using also MOPSMAP (see Section 3.1.1) and radiative transfer simulations (Mayer and Kylling, 2005; Emde et al.,2016).

More specifically, the following properties are directly derived from the ATLID EBD product per latitude and longitude point along the EarthCARE footprint:

- $a_p$, PLDR and LR profiles at 0.355 µm, which are used to calculate the layer integrated AOD, layer top/bottom, layer mean PLDR and LR

And from HARP2 polarimeter:

- COT, CTH, and $r_{eff\_c}$, which are used together with optical modeling to derive the AOD at 0.67 µm and aerosol $r_{eff}$.

The underlying principle of the applied method is that the presence of aerosols above a liquid cloud modifies the total polarized radiances ($L_p$) observed at the cloud top. Specifically, aerosols are expected to reduce the intensity of the primary cloud bow, and increase the intensity in the scattering angle range approximately between 80 and 120 degrees. The difference between the polarized radiances of a cloud-only scene ($L_{pc}$) and those of a cloud-aerosol scene ($L_p$) can therefore be used to constrain the properties of aerosols located above the cloud layer. Figure 12 demonstrates the above: for an example scene of HARP2, for every pixel the measurement geometry (i.e. viewing zenith, solar zenith and relative azimuth angles) and the measured *Q* polarized radiance component of the Stokes vector (shown with blue symbols) was

extracted. The characteristic liquid cloud bow is clearly visible between 135° and 145°. A critical aspect here is that apart from the liquid cloud droplets, the stratospheric volcanic aerosols which are above the clouds, also affect the HARP2 measurements across all the selected pixels, and this influence forms the basis of the methodology employed to retrieve the particle properties. To illustrate the differences, for the same measurement geometry, radiative transfer calculations were utilized to simulate the corresponding polarized radiances if there was only liquid clouds present in the scene (red symbols) and if a stratospheric layer is located above the liquid clouds assuming an $AOD_{670}$ of ~0.05, aerosol particles $r_{eff}$ = 0.3 µm and the CRI of sulfate particles at 0% relative humidity taken from OPAC database (pink symbols).

The effect is more pronounced at shorter wavelengths and can be detected at high angular resolution measurements where enough information are available to efficiently resolve the cloud bow that is sensitive to cloud droplet $r_{eff}$ and $v_{eff}$ (Breon and Goloub, 1998; Alexandrov et al., 2015; Di Noia et al., 2019). For this reason, the analysis is limited to the 0.67 µm HARP2 spectral band. The retrieved aerosol $r_{eff}$ are subsequently utilized in MOPSMAP to provide the properties needed for PyDOME simulations in the spectral range of 0.4 – 2.5 µm, assuming literature values for the CRI.

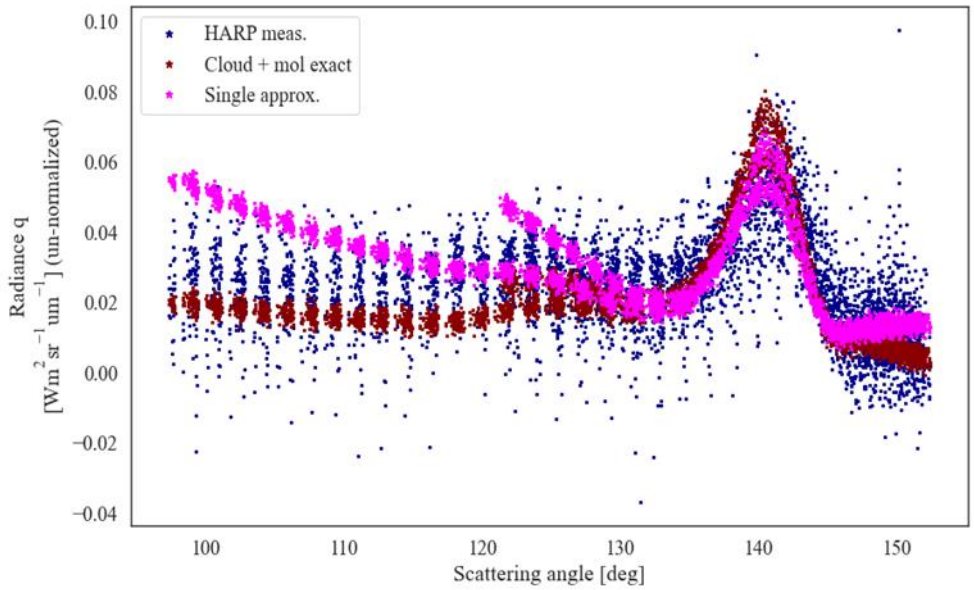


**Figure 12** Polarized radiances (Q component of the Stokes vector) measured by HARP2 at 0.67 µm as a function of the scattering angle (blue symbols), for the selected pixels shown in the red box on Figure 21 to Figure 24. For the same measurement geometry, the red symbols illustrate what would be the Q values in case only liquid clouds where present in the scene, and when fine mode stratospheric aerosol particles at low AOD (~0.05 at 0.67 µm) are located above (pink symbols).

Due to the overpass time differences between EarthCARE an PACE, a direct temporal collocation is not possible in this case as differences in the observed atmospheric scenes may occur due to temporal evolution. Nevertheless, ATLID and MSI cloud products can be compared to HARP2 cloud products to assess the temporal stability of the observed scenes in between the two satellite overpasses, with respect to cloud properties. ATLID observations can also help verify, as far as possible, the absence of any other aerosol layers between the liquid clouds and the stratosphere (e.g. long-range transported lofted dust or smoke plumes), as well as the absence of polar stratospheric clouds (PSCs). For this purpose, collocated ATLID/HARP2 observations are sought for in the initial steps of the analysis. In any case, stratospheric aerosol properties are not expected to vary rapidly due to the lack of efficient removal processes, and are therefore assumed to remain relatively stable and representative over extended time periods.

***Products***

The EarthCARE and PACE products used are described in Section 5.1.1 and specific steps followed herein are summarized below:

***Step 1: identify the volcanic aerosol layers and extract relevant values from ATLID***

The volcanic layers in the stratosphere are identified using the ATLID A-TC target classification product, the corresponding AOD and vertical distribution, as in layer top/bottom and thickness, is derived from the $a_p$ profile at 355nm (A-EBD product). Herein, layer bottom/top correspond to the lowest/highest valid extinction value per profile. Small discontinuities spanning only 2–3 height bins are ignored.

The main steps are summarized in the following flowchart (Figure 13) and visualized in Figure 14 to Figure 17.

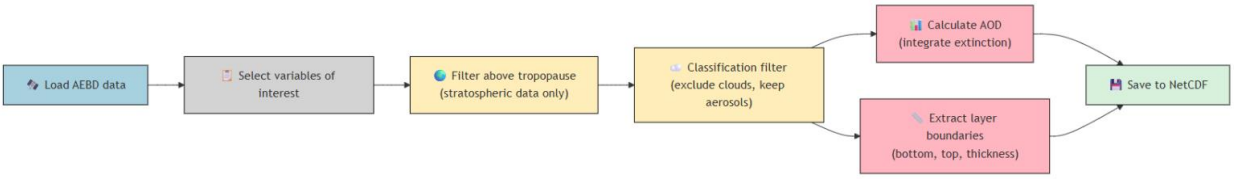


**Figure 13** Flowchart of the steps followed to filter EBD products for stratospheric particles

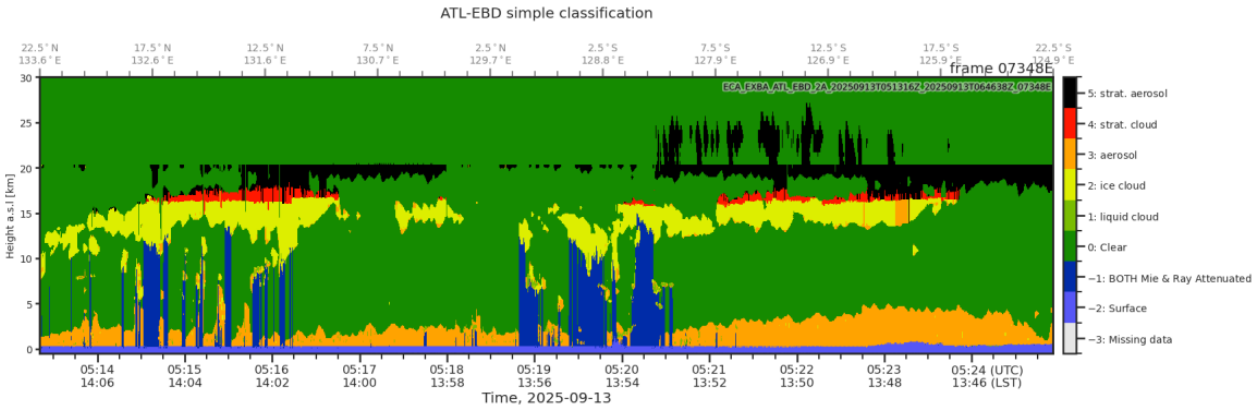


**Figure 14** The original ATLID EBD scene, showing the vertical distribution of classified features (aerosol, cloud, surface, etc.)

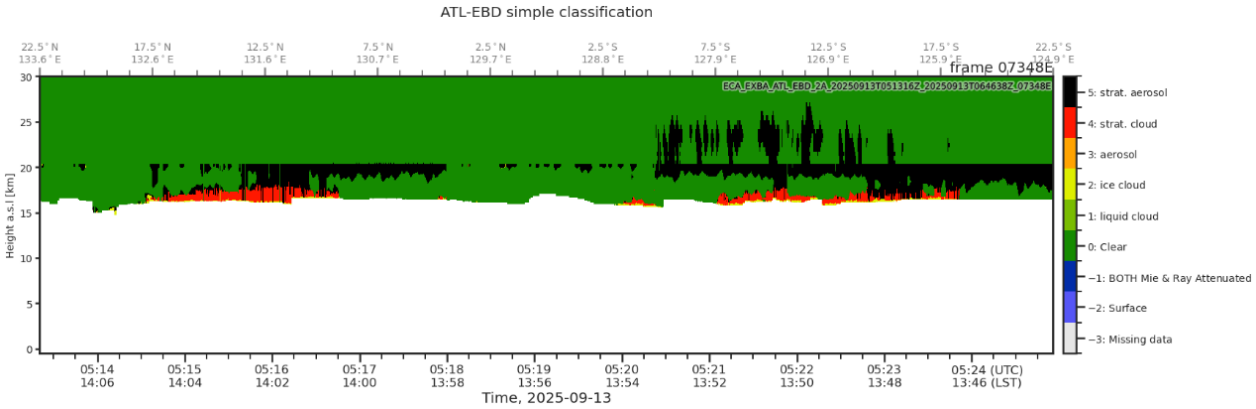


**Figure 15** Data below the tropopause are removed to retain only stratospheric features.

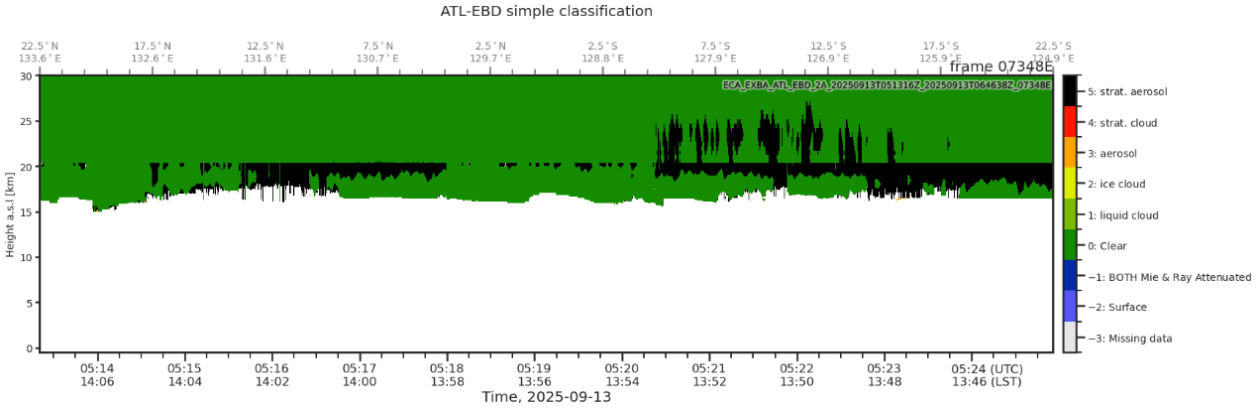


**Figure 16** Remove remaining non-aerosol elements. After filtering, only profiles corresponding to aerosol layers above the tropopause are preserved. Any remaining cloud and surface signals are masked out.

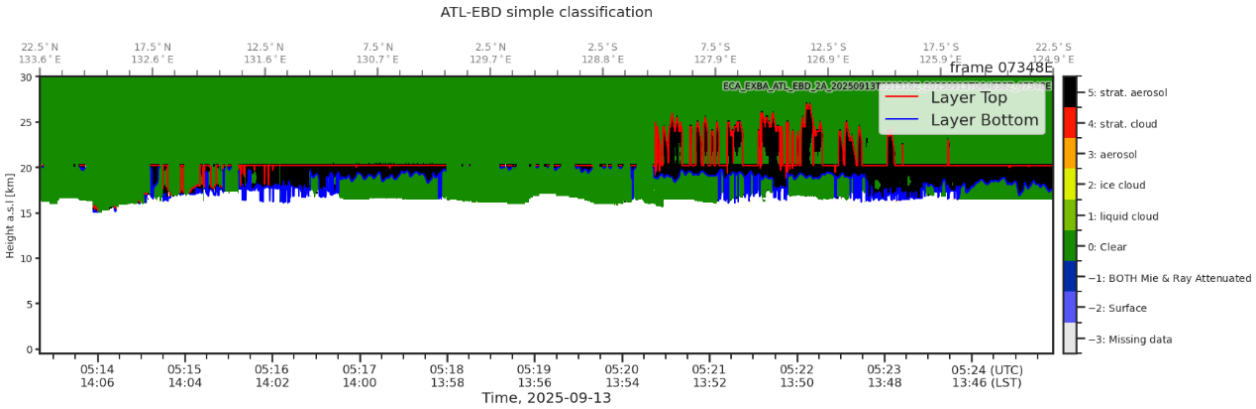


**Figure 17** The AOD, as well as layer top and bottom heights, are computed from the filtered extinction values

The outputs are stored in monthly NetCDF files (EarthCARE/ATLID revisit time is 25 days) including the following variables per latitude, longitude point along the ATLID track:

- lidar_ratio_355nm
- particle_extinction_coefficient_355nm
- particle_linear_depol_ratio_355nm
- aod_355nm
- layer_top
- layer_bottom
- layer_thickness

The LR, $a_p$ and PLDR correspond to the low-resolution variables (i.e. their horizontal resolution is ~40 km) provided in the ATL-EBD 2A product at the selected points of interest.

***Step 2: EarthCARE–PACE synergistic implementation and scene selection***

Collocated (not coincident) EarthCARE and PACE scenes are selected based on the following requirements:

- The scene must have a total water cloud fraction above 90%
- Above 15km, only aerosol layers should be present (e.g. no Polar Stratospheric Clouds (PSCs))

For the scenes that satisfy these requirements, it was assumed that the stratospheric layer can be found above every HARP2 pixel at the latitude band considered. Since the vertical distribution of the atmospheric scene is not available from ATLID at the time of the PACE overpass, a selection criterion to use only

HARP2 pixels with CTH > 5km is applied. This criterion is intended to maximize the likelihood that no other aerosol types are present between the stratospheric aerosol layers and the underlying clouds (e.g. long-range transported, lofted dust or biomass burning plumes), relying also on the fact that aerosol fields are not expected to change so rapidly (Mona et al., 2009). Further, HARP2 data are filtered so as only pixels with COT > 5 remain in the atmospheric scene. This ensures that the polarization signal emerging from the liquid cloud will be saturated and thus mainly sensitive to cloud droplet effective radius and variance (Waquet et al., 2009; 2013). Finally, the strength of the primary cloud rainbow is quantified using the liquid index (L1) introduced in (Van Diedenhoven et al., 2012). Values of L1 < 0.3 suggest ice contamination at the observed cloud tops and are excluded from this analysis.

***Step 3: Retrieval of stratospheric aerosol properties from polarized radiances***

Following the approach of Waquet et al. (2009), the total polarized radiance ($L_{p\lambda}$) emerging from a plane-parallel system consisting of an atmosphere overlying a thick cloud can be expressed as follows in Eq. (1):

$$L_{p\lambda}(\theta_s,\theta_v,\varphi_r) = \frac{q^m(\Theta)\tau_\lambda^m}{4\mu_v} + \frac{\omega_{0,\lambda}^a q_\lambda^a(\Theta)\tau_\lambda^a}{4\mu_v} exp(-m\gamma\tau_\lambda^m) + L_{p\lambda}^c(\theta_s,\theta_v,\varphi_r)exp[-m(\gamma\tau_\lambda^m + \beta\tau_\lambda^a)] \quad (1)$$

where:

- $\theta_S, \theta_v, \varphi_r$ and $\Theta$ represent the solar zenith, the viewing zenith, the relative azimuth between the sun and the sensor and the scattering angle, respectively. These information are currently taken from HARP2 measurements per pixel.

First term of the equation on the right hand-side is the molecular term, second term represents the aerosol contribution and third is the cloud term.

- Molecular term contains the molecular phase function $q^m(\Theta)$, the molecular optical depth above the cloud $\tau^m_\lambda$ and the cosine of the viewing zenith angle $\mu_v$.
- The aerosol term contains the SSA ($\omega_{0,\lambda}{}^a$), the polarized phase function $q_\lambda{}^a(\Theta)$ (element $F_{12}$ of the scattering matrix), the AOD ($\tau^a_\lambda$) and the air mass factor m.
- The cloud term contains the cloud polarized reflectance $L^c_{p\lambda}$ and two empirical factors $\gamma$ and $\beta$ which depend on the choice of the aerosol model.

For the *aerosol term*, the volcanic aerosol properties (sulfates, ash or mixtures) are calculated using MOPSMAP scattering database as described in Section 3.1.1. The $\tau^a_\lambda$ at 0.67 µm varies between predefined values of 0.00009 - 1 (with a step 0.005) for every pixel. For the *cloud term*, the $L^c_{p\lambda}$ is calculated using libRatran radiative transfer code. Similar to the aerosol term, several water cloud models are developed with $r_{eff\_c}$ in a predefined range of 5 – 20 µm and following a gamma type size distribution. Then the appropriate cloud model per pixel is selected based on CTH, COT and $r_{eff\_c}$ of HARP2 retrievals. Retrieval of the stratospheric aerosol properties is based on the minimization of the cost function between the measured and the simulated polarized radiances $L_{p\lambda}$. The state vector contains the $r_{eff}$ of the aerosol particles and their AOD at 0.67 µm.

### 3.1.3 Case studies

#### 3.1.3.1 Mt. Ruang volcanic eruption

To illustrate the processing steps described above, the April 2024 eruption of Ruang volcano, observed by both EarthCARE and PACE, is used as a case study. The Indonesian volcano (2.30° N, 125.37° E) experienced a series of explosive eruptions between mid- and late April 2024, one month prior to the EarthCARE launch. The changes in stratospheric AOD between August 2025 and September 2025 are monitored using ATLID as explained in ***Step 1***. For the analysis only latitudes between +/-25 degrees are considered. This selection is motivated by the fact that at higher northern latitudes, additional stratospheric injections (i.e. smoke from Canadian wildfires) may be present and thus could obscure the isolated effect of volcanic particles on the stratospheric AOD perturbation.

Examples of monthly AOD values calculated from EarthCARE data between +/-25 degrees in latitude, are shown in Figure 18 and Figure 19 for August 2024 and September 2025 respectively. Figures in the left columns present the AOD values at 0.355 µm, while figures on the right present the perturbation as in the increase in AOD induced due to Mt. Ruang eruption. Since the mean stratospheric AOD during the last

month of the analysis remains close to 0.04 and therefore above background levels as these are reported in the literature, the perturbation is calculated assuming a stratospheric background AOD of 0.008 at 0.355 μm based on the results of previous studies (Friberg et al., 2018; Li et al., 2022; Schmidt et al., 2022; Vernier et al, 2011).

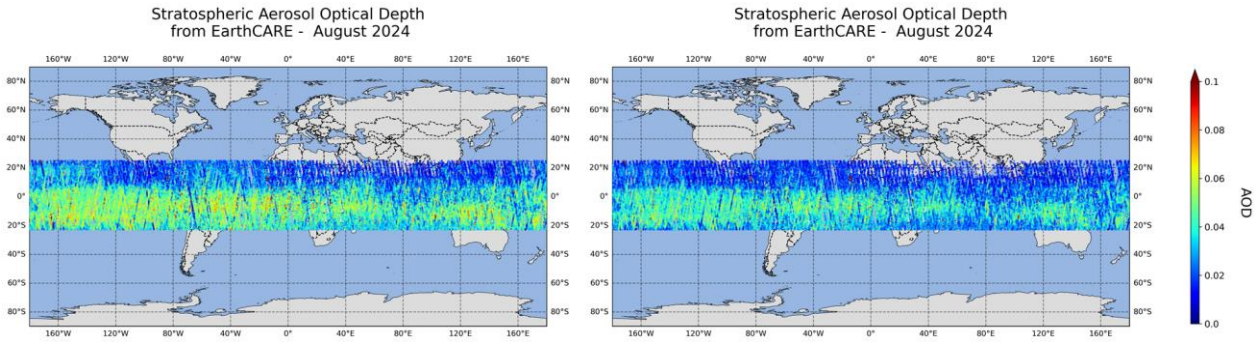


**Figure 18** The stratospheric AOD at 0.355 μm for the month of August 2024, as derived from ATLID data (left) and the perturbation (absolute difference) in AOD, assuming a background stratospheric value of 0.01 at 0.355 μm (right).

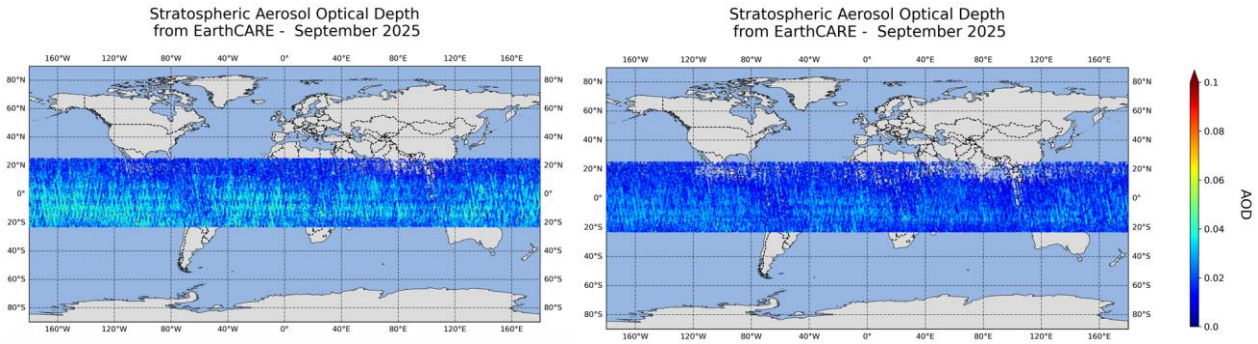


**Figure 19** Same as Figure 18 but for September 2025

To demonstrate the rest of the analysis steps, the day of August 25, 2024 was selected. The scene presented in Figure 20 shows for this case the ATLID time-height A-TC plot with the Ruang stratospheric layer detected between ~17 and 22 km (in yellow) in the left panel, while the total intensity (radiance component *I* of the Stokes vector), at 0.67 μm measured by HARP2 for a viewing angle close to 100 degrees is shown on the right. The EarthCARE overpass is superimposed on HARP2 observations on the right panel; note that for the specific scene, the two measurements are separated by 1 hour (EarthCARE overpass is at 16:00 UTC and PACE overpass at 15:00 UTC).

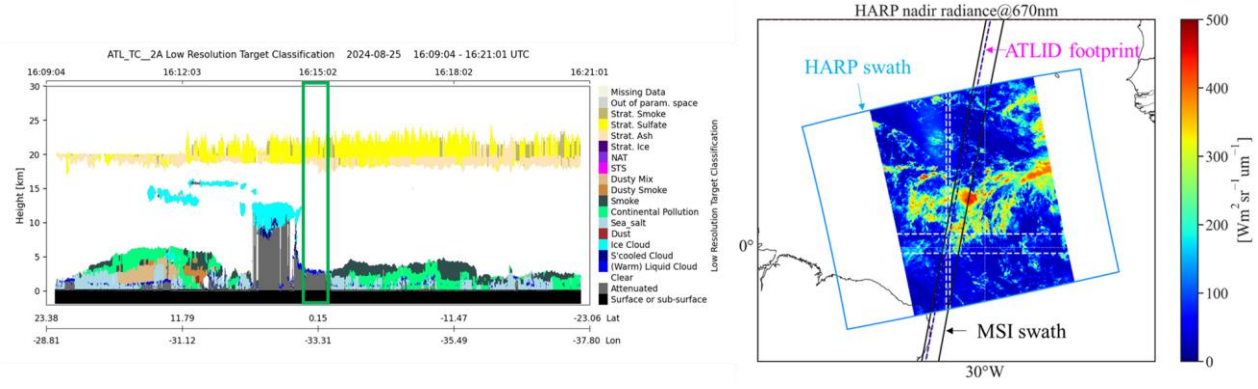


**Figure 20** ATLID target classification (left), HARP total intensity at 670 at a viewing angle close to nadir(right).

Figure 21 demonstrates the corresponding Q component of the Stokes vector (left) and the resulting pixels after the different filters applied to HARP2 data (right) as explained in ***Step 2.*** For a selected pixel inside the red box shown in Figure 21, Figure 22 demonstrates the normalized $L_p$ values at all scattering angles sampled by HARP2 (green line) and the fitting line used to calculate the liquid cloud (L1) index with the red dashes. It should be noted that HARP2 polarized radiances are affected by relatively high noise levels, while the expected stratospheric AOD values in this case are low (of the order of 0.05 – 0.1); therefore a reduced sampling of HARP2 data is performed as part of the analysis as a quick approach to improve the signal-to-noise ratio. The reduced angular resolution is illustrated with the blue curve.

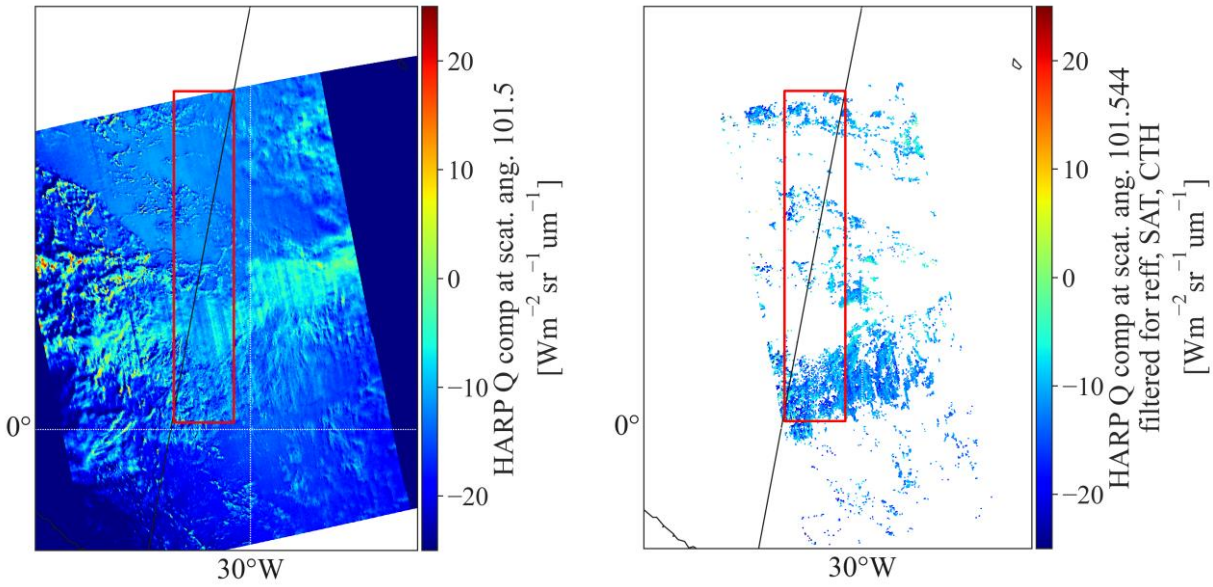


**Figure 21** (left) Original HARP2 Q polarization component measurements at 0.67 μm for a selected scene, at scattering angle ~100°. The black line indicates the ATLID footprint and the red box the area of focus for the stratospheric aerosol retrievals. (right) same as left, filtered to satisfy the requirements: CTH > 5 km, COT > 5 and L1 > 0.3.

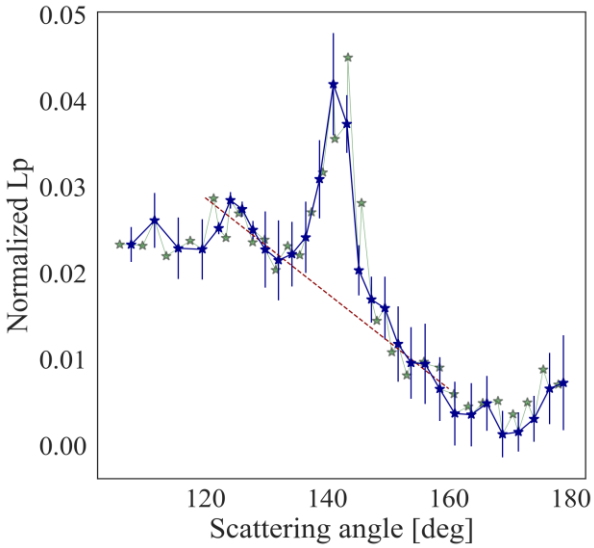


**Figure 22** Normalised $L_p$ values at all HARP2 scattering angles (green line) and re-sampled to minimise instrumental noise (blue line). Fitting line (red dashed) used to calculate the L1 index (~3.04). For this pixel, the CTH is ~5.5 km) and COT ~5, as extracted from HARP L2 data.

The area highlighted with the red box shown in Figure 21, is used to demonstrate the evaluation of the temporal homogeneity of the scene in terms of cloud properties, given the time difference between the two overpasses. It has to be noted that for this analysis, MSI, HARP2, and PACE/OCI measurements are used as the CTH and COT values presented are currently derived from PACE/OCI data and provided as ancillary data at the HARP2 resolution (HARP2/OCI from here on), while $r_{eff\_c}$ is directly derived from HARP2. The first row of Figure 23, displays the water CTH derived from the MSI (left) and HARP2 (right) instruments, for all the pixels with the cloud boundaries outlined in the box. For this region, histograms of the CTH distributions are provided in the second row. It should be noted that the spatial resolution differs significantly between the two datasets: MSI product comes at a 500 m × 500 m resolution, while HARP2 and HARP2/OCI product comes at a 10 km × 10 km resolution. Similarly, Figure 24 presents the water cloud COT and Figure 25 the $r_{eff\_c}$ of water cloud droplets.

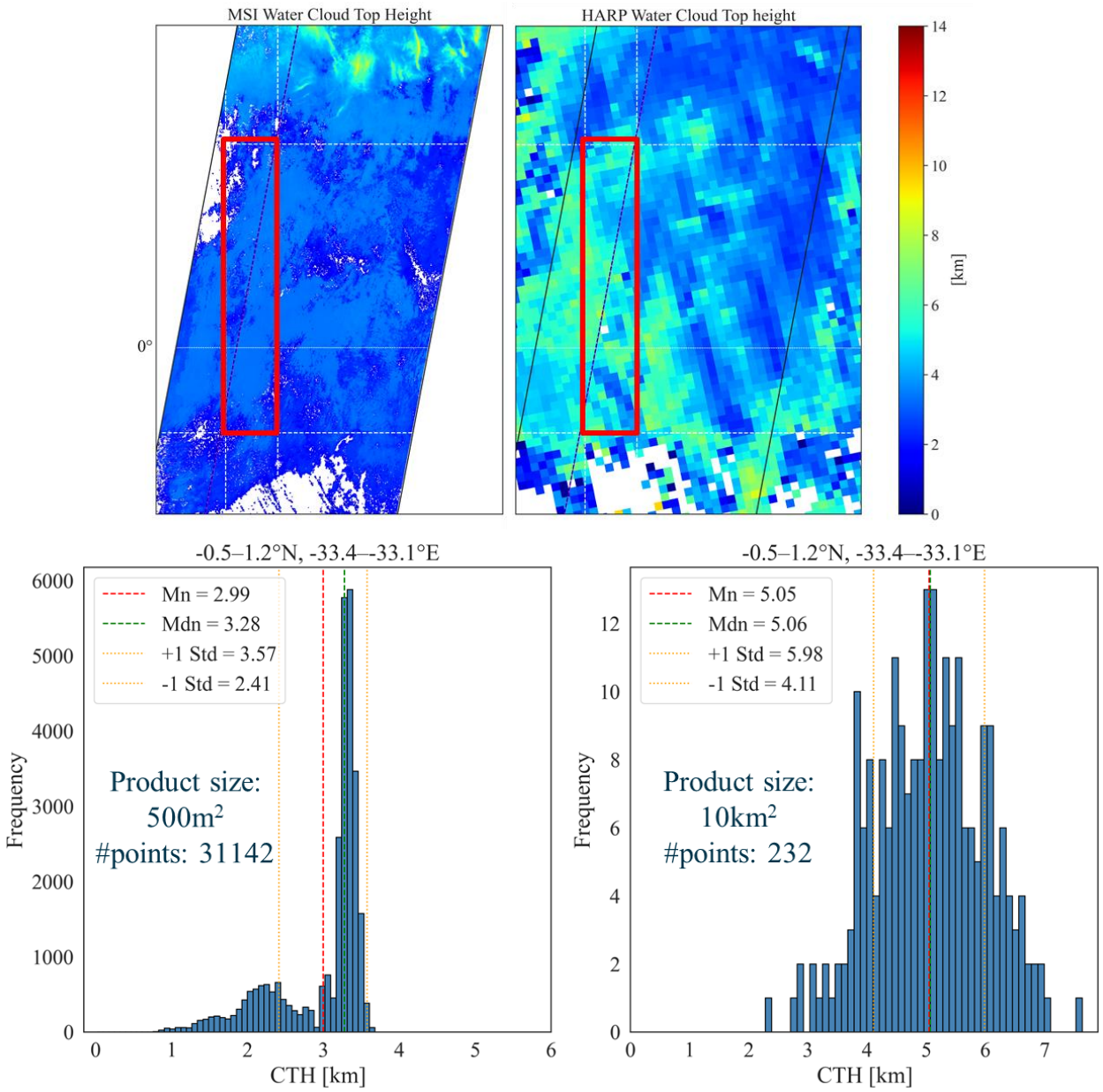


**Figure 23** (top panel) Water CTH retrievals from MSI (left column) and HARP2 (right column). (bottom panel) Histogram of the retrieved values extracted from the region highlighted with the red box in both plots.

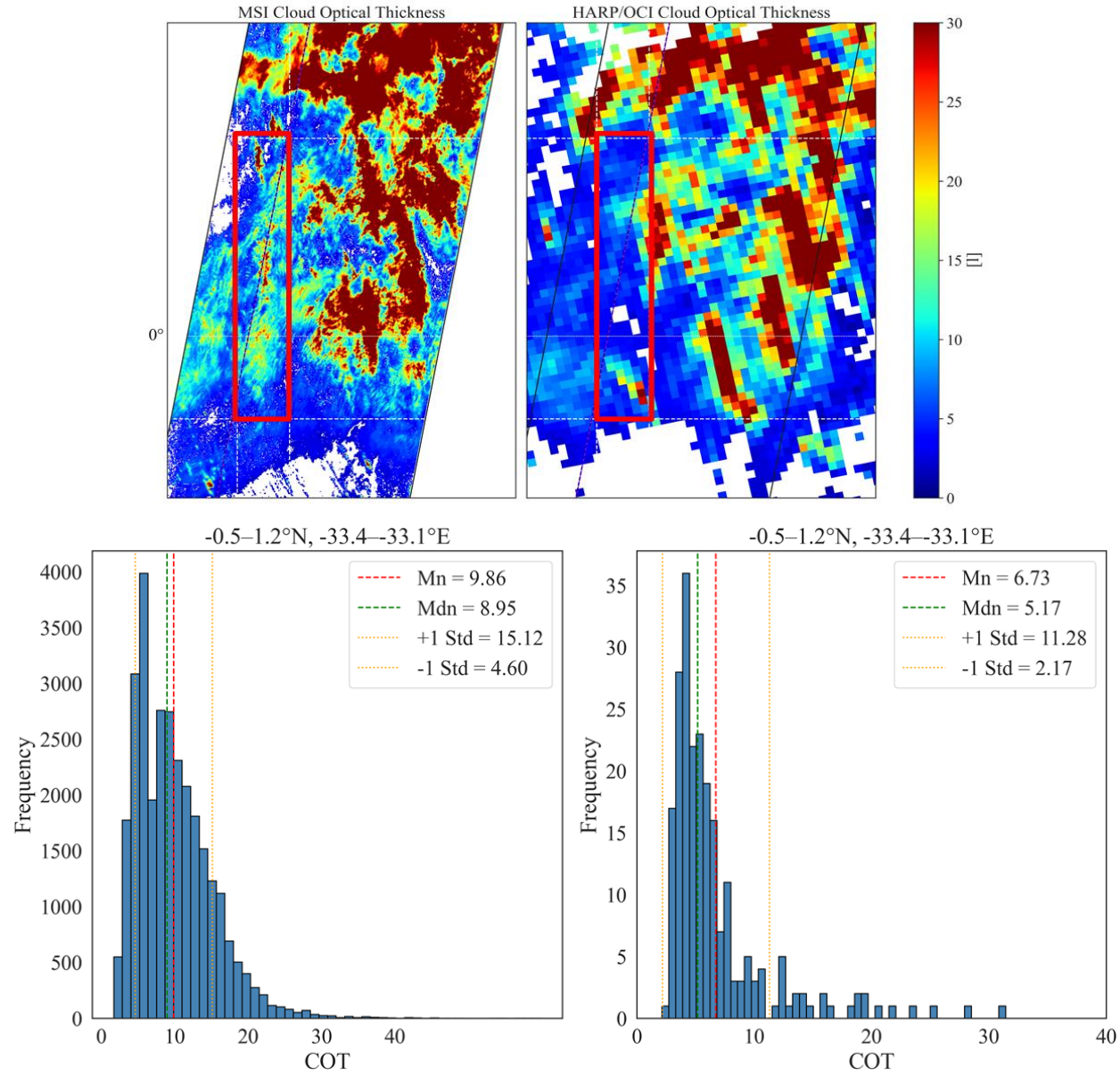


**Figure 24** Same as Figure 23 but for the COT

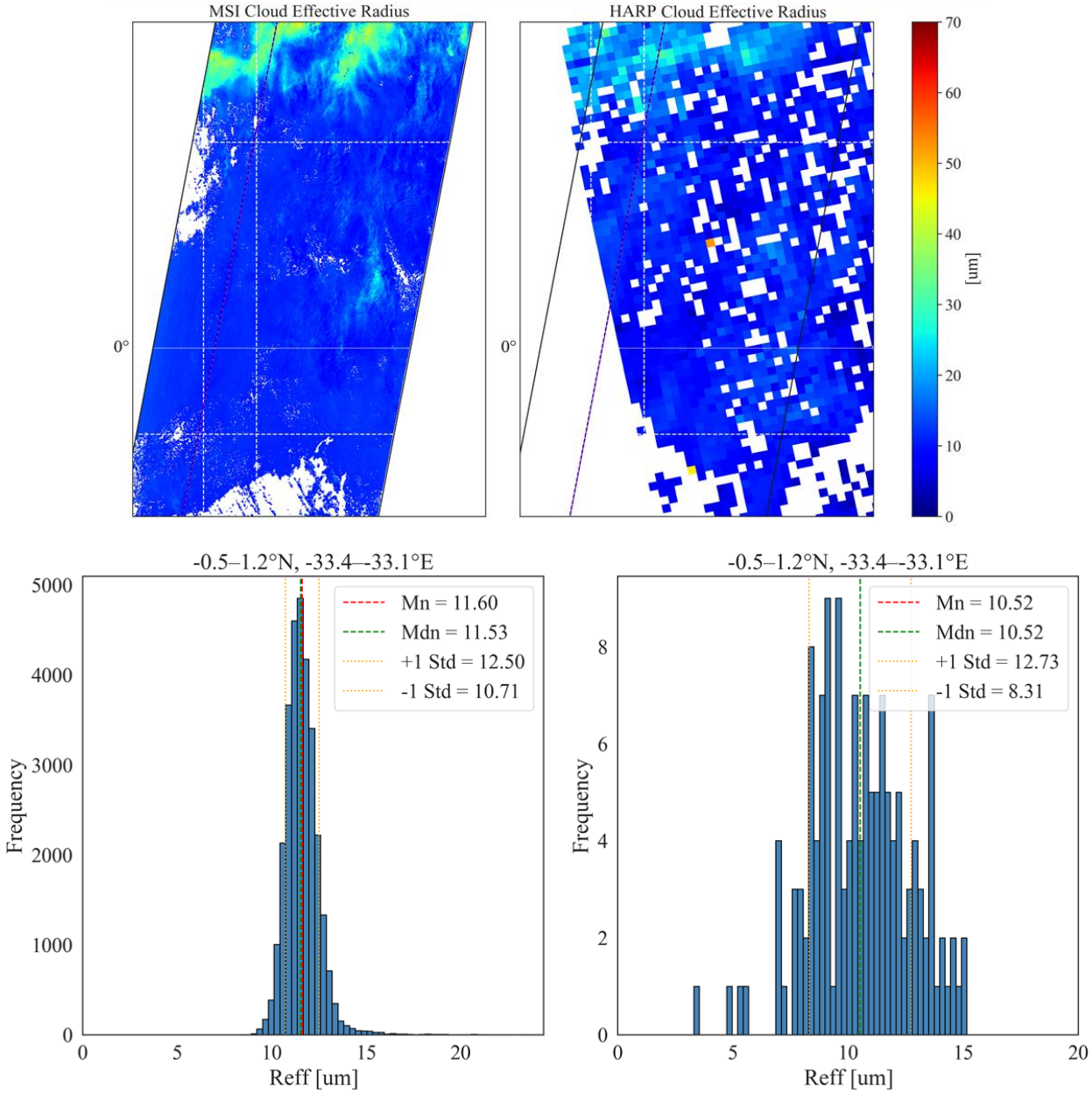


**Figure 25** Same as Figure 23 but for the cloud effective radii

MSI scene exhibits greater homogeneity in terms of water CTH and COT with mean values of ~3 km and 10, respectively. In contrast, the HARP2/OCI retrievals indicate higher values for the CTH with mean around ~5 km and mean COT around 7. Nevertheless, for the $r_{eff\_c}$ retrievals which are derived directly from HARP2, the mean values derived are close to 11-11.5 µm from both instruments. Given the fact that HARP2 measurements are of higher information content compared to OCI (due to the additional polarimetric measurements), these differences may reflect discrepancies between the measurement information content, retrieval algorithms or genuine variability caused by the 1-hour measurement time offset.

***Results***

The retrieval described above was performed for all the pixels of HARP2 inside the red box in Figure 21 and only a few qualified (~150 pixels) based on the strict selection criteria (see Figure 25, squares). Concerning aerosol properties, from the MOPSMAP database constructed (see Section 3.1.1), monomodal, log-normal size distributions of spherical particles with a refractive index corresponding to sulfates at 0% relative humidity (from OPAC) in the stratosphere where considered. To account also for the potential

presence of residual ash, bimodal, log-normal size distributions were also examined, combining sulfates (fine mode) and ash (coarse mode) particles. Volcanic ash was modeled as spheroids with a mean aspect ratio of 1.4 and a refractive index corresponding to Basalt-Andesite, consistent with Ruang ash as reported by Suhendro et al. (2025). All properties are summarized in Table 10. It is noteworthy that none of the bimodal size distributions was found to successfully reproduce the HARP2 L1C radiances for the selected scene; therefore, the analysis was restricted to mono-modal sulfate-only distributions. Considering the time elapsed between the initial eruption (April 2024) and the analysis period (August 2024), the absence of coarse mode volcanic ash in the stratosphere is consistent with its removal through gravitational settling.

Figure 26 presents the HARP2 derived AOD at 0.67 µm (squares) and as a comparison, the ATLID-derived stratospheric AOD at 0.355 µm (circles). Mean and maximum AOD, standard deviation, and the corresponding ATLID values are summarized in Table 11, along with derived mean $r_{eff}$ and $v_{eff}$. Overall the agreement between HARP2 and ATLID is satisfactory. The derived mean value of $r_{eff}$ of 0.3 µm could indicate either residual super-micron ash in the stratosphere or sulfate deposition on ash (e.g. Zhu et al., 2020), which would result in larger particles than expected for purely fine-mode sulfuric aerosols (see for example the values provided from the OPAC database). These first results demonstrate the potential of passive polarimetric observations to complement lidar data for monitoring volcanic aerosol layers in the stratosphere, however further analysis is imperative.

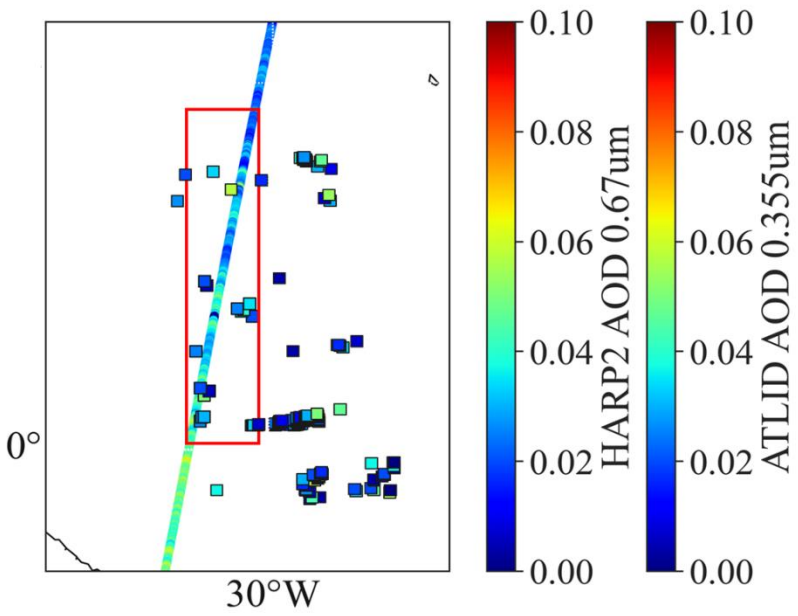


**Figure 26** AOD at 0.355 µm along the ATLID track (circle markers) and at 0.67 µm from HARP2 (square markers)

**Table 11** Derived AOD at 0.355 and 0.67 µm , and particle size ($r_{eff}$, $v_{eff}$) for the example scene selected

| | **HARP2 0.67 µm** | **ATLID 0.355 µm** |
|---|---|---|
| **AOD** | | |
| Mean: | 0.03764 | 0.036632 |
| StDev: | 0.02575 | 0.012009 |
| Max: | 0.09509 | 0.079349 |
| **Size** | | |
| $r_{eff}$ (µm) | 0.3 | X |
| $v_{eff}$ (µm) | 1.2 | X |

#### 3.1.3.2 Mnt. Pinatubo eruption

For the Mnt. Pinatubo case study, volcanic aerosol size distributions approximately one year post the eruption were constrained by combining ground based lidar observations from Germany (Ansmann et al. 1996) with in-situ balloon-borne optical particle counter (OPC) measurements from Laramie, Wyoming (Deshler et al., 1993). As presented in Wandinger et al. (1995), microphysical stratospheric particle properties such as surface-area concentration, volume concentration, and effective radius can be derived from Raman lidar extinction and backscatter observations using Mie scattering calculations. These retrievals were evaluated against long-term OPC measurements, which provided independent constraints on particle size distributions. The reported effective radii derived from the balloon borne in-situ data in the period mid-1991 to mid-1992 (~0.4–0.55 µm) were used as the primary constraint for constructing representative volcanic aerosol size distributions utilizing the lidar data.

Similar to the methodology followed for the Ruang eruption, a comprehensive sensitivity analysis was performed using mono-modal and bi-modal log-normal size distributions composed of sulfate (fine mode) and ash (coarse mode) particles, with optical properties calculated using the MOPSMAP scattering database and refractive indices from OPAC and laboratory measurements. Mono-modal distributions were rejected because they produced effective radii inconsistent with the lidar and ballon-borne observations, whereas selected bi-modal distributions reproduced the lidar-constrained effective radius when integration was limited to particles ≤1.5 µm (cut-off radius of the OPC instrument), consistent also with lidar sensitivity to smaller particles (ground based lidar measurements performed at 0.355 µm). The fine mode radius ($r_n$ = 0.0775) of the final selected distribution was found to agree well with OPAC sulfate aerosols Figure 27.

Nevertheless, the derived data for Mnt. Pinatubo eruption where not further utilized for SAI studies in the context of *ACtIon4Cooling* due to the limited information content of the available data compared to the advanced observations of EarthCARE and PACE synergy.

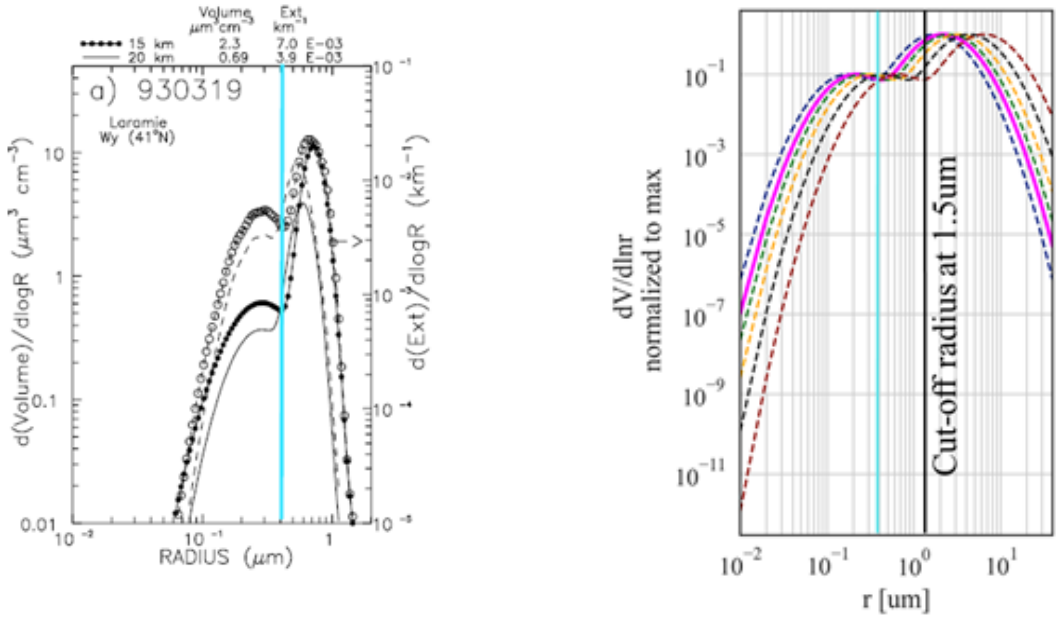


**Figure 27** Rough comparison of the form of the volume size distribution derived from Wyoming in-situ data (left; March 1993), with the volume size distribution from the simulations (right). For the simulated data, the cut-off radius (1.5 µm) is shown with black line to visualize the contribution of the coarse mode.

### 3.1.4 Synthetic materials as alternative approach for SAI

Although the release of volcanic aerosols in the stratosphere after major eruptions, is widely used as a natural analogue of SAI, it may not be the optimum solution due to its adverse effects (e.g. depletion of stratospheric ozone). For this reason, simulated cases of SAI using artificial particles should be investigated.

In the context of the *ACtIon4Cooling* project, apart from the properties provided for particles released after Ruang volcanic eruption, the corresponding properties of theoretically-constructed artificial particles, with varying microphysical characteristics are provided. The size distributions used are similar to those of volcanic aerosols, but also take into account larger and smaller particles (in order to also investigate the effects of quicker or slower deposition, respectively). The CRI of calcite particles is utilized, since these particles have been reported to contribute to ozone depletion by a lesser degree (e.g. Tilmes et al., 2022). For the calculation of the corresponding optical properties, MOPSMAP code is used.

It should be emphasized that the goal of this dataset is to provide the baseline for the appropriate microphysical and optical properties of theoretically-constructed artificial particles, not to be confused with existing particles, as for example calcite particles. The main reason is that the latter have been also associated with negative effects, since for example the ozone depletion risk remains, although smaller than the depletion caused by sulphate particles (Dai et al., 2020). It remains unclear how durable the calcite's "beneficial" surface properties are under real stratospheric conditions: temperature, pressure, mixing, coating by other species, etc., causing particle chemical aging and changing their reactivity (Vattioni et al., 2025). Moreover, solid particles like calcite may clump or aggregate after dispersion, which can alter their size distribution, optical scattering properties, and "residence time". Their aggregation complicates the logistical details of their proper dispersion in the stratosphere, increasing also the deployment cost (e.g. Hack et al., 2025).

## 3.2 MCB

In this section, the proposed methodology establishes a systematic monitoring approach to assess shipping-induced cloud perturbations as an observational analogue for MCB within the *ACtIon4Cooling* project. Monitoring and understanding of aerosol–cloud–trace gas interactions can contribute to mitigation strategies addressing the negative effects of strong extended heatwaves and droughts on human health, agriculture, and ecosystems (Jones et al., 2022).

### 3.2.1 Overview

Marine vessels inadvertently contribute to MCB by releasing sulphate aerosols into the atmosphere, which act as CCN and form ship tracks – a terminology used to describe the type of cloud associated with shipping activity (Hobbs et al., 2000).

From the current existing EO datasets, the detection capabilities of identifying which marine clouds appear with enhanced brightness due to the presence of exhausted particles from the ship engines will be examined. The vessel density and route density maps which are created since the 2019 by Cogea for the European Marine Observation and Data Network (EMODnet) can be used for defining where the ships are located. The Route Density Map at 1 km resolution was created by EMSA in 2019 and made available on EMODnet Human Activities, an initiative funded by the EU Commission. The dataset is updated every year and is available for viewing and download on EMODnet Human Activities web portal [URL14]). The maps are based on AIS data monthly aggregated and show shipping density in 1x1km grid covering all EU waters and some neighboring areas. Density is expressed as hours per square kilometer per month.

If available, *ACtIon4Cooling* aims to collocate the considered EO datasets with the ship tracks originating from the AIS (Automatic Identification System) data at the ship level (high temporal resolution of 5-6 minutes), which contain the exact geographical location of the vessel with the registered MMSI tracker number, as long as other type of complimentary information, like the type of the vessel (e.g., Cargo, Tanker, Pleasure Craft, Passenger Ship and more types), destination, vessel dimensions and speed. The AIS datasets are ideal for building ship-track cloud datasets but are not publicly available and thus, they need to be purchased.

For MCB, the primary information on cloud properties will be acquired from the space-borne spectrometer TROPOMI on Sentinel-5 Precursor (Veefkind et al., 2012). The operational algorithms for the retrieval of cloud parameters from the atmospheric Sentinel missions make use of Earth-shine reflectance measurements in the spectral windows of UV, VIS and NIR. The TROPOMI operational cloud algorithms OCRA/ROCINN (Loyola et al., 2018) have a long-standing heritage and they were applied operationally to several instruments starting with GOME (Global Ozone Monitoring Experiment) on ERS-2 (European Remote Sensing Satellite) (Loyola et al., 2010), SCIAMACHY (SCanning Imaging Absorption spectroMeter for Atmospheric CartograpHY) on ENVISAT (ENVIromental SATellite) (Loyola et al., 2004), the GOME-2 instruments on board MetOp-A/B/C (Meteorological Operational satellite) (Lutz et al. 2016), and the EPIC

(Earth Polychromatic Imaging Camera) instrument on the DSCOVR (Deep Space Climate Observatory) satellite, located at the Lagrangian point L1 (Molina García, 2022).

The existing satellite records of cloud-aerosol properties have been so far derived either from measurements in the optical range of MERIS (Mei et al., 2017a,b, 2018) and near infrared (NIR) from passive sensor (as in Lelli et al. 2012, 2014 for clouds and Lelli et al., 2015, Sanders et al. 2015, Kylling et al. 2018 for aerosols) of the GOME/GOME-2 and SCIAMACHY sensor family or from signal returns of the active sensors CALIOP on CALIPSO (Winker et al., 2009) or CPR on CloudSAT (Stephens et al., 2002). Despite their operation dates back in time, being commendable for long-term global climatological and trend studies, the coarse footprint of the NIR passive sensors inherently favors the detection of high clouds over low clouds, which have higher probability of being shielded in multi-layered cloud systems. When an instrument with higher spatial resolution is used such as TROPOMI, it must be expected that the derived cloud retrievals will improve the representativeness of tropospheric low-level cloud structures. Due to the vertical structure of the troposphere, low-altitude cloud textures, that are the manifestation of the manifold pathways aerosols influence their microphysics, will be better captured. Complementary information for the clouds captured by TROPOMI instrument will be exploited from VIIRS on Suomi-NPP.

The low-level clouds with maximum cloud top height at 3km over the water surfaces will be studied. The marine clouds with ship-track signature over the Mediterranean Sea and North Eastern Atlantic, could function as the cloud brightening geoengineering experiment within the *ACtIon4Cooling* project. Already in 1966, ship-tracks were observed as anomalous cloud lines from weather satellites. Those lines have been attributed to the aerosol emissions of ships, mainly referring to sulphates and black carbon (Conover et al, 1966).

The aerosol information is captured by the TROPOMI sensor in the Oxygen absorption bands (i.e., Aerosol Layer Height), and in the UV spectral window as well. In particular, the ultraviolet (UV) Absorbing Aerosol Index (AAI) is widely used as an indicator for the presence of absorbing aerosols in the atmosphere (Kooreman et al., 2020; Torres et al., 1998a). The ship-track signature of aerosols in the TROPOMI cloud retrievals will be investigated via the scientific NASA TropOMAER (TROPOMI aerosol algorithm), which simultaneously retrieves aerosol optical depth (AOD), Single-Scattering Albedo (SSA), and the qualitative UV aerosol index (UVAI) (Torres et al., 2020).

In addition, the TROPOMI $NO_2$ Tropospheric Vertical Column Densities (VCDs) will be analysed to quantify shipping-related nitrogen dioxide enhancements along major maritime corridors in the Mediterranean Sea and North Eastern Atlantic. Elevated $NO_2$ VCDs provide an independent proxy for combustion-related emissions from ships and can support the attribution of aerosol–cloud interactions observed in ship-track regions. The combined analysis of aerosol properties, cloud microphysical retrievals, and $NO_2$ TVCDs enables a more robust detection and characterization framework for MCB analogues.

Including tropospheric $NO_2$ column measurements from the TROPOMI instrument in the central Mediterranean showed that plume-like emission structures in tropospheric $NO_2$ columns when they were collocated to Automated Identification Signal (AIS) data of ship locations (Georgoulias et al., 2020). Aggregate traffic density metrics (number of ships, total vessel length, vessel-hours) by grid cell and time period (daily or weekly): Additional information about ship length and ship speed, combined with an analysis of ship tracks and ship position, reveal that nearly all emission plume-like tropospheric $NO_2$ structures can be attributed to the largest ships, mostly container ships and crude oil tankers. Georgoulias et al., (2020) via their pioneering approach proved that $NO_2$ emission plumes from ships can be detected and attributed to individual ships using satellite measurements with fine spatial resolution like the one of TROPOMI. During the COVID-19 period, Riess et al. (2022) conducted an analysis of the decreased $NO_x$ emissions over the European Seas by making use of the TROPOMI tropospheric $NO_2$ columns and demonstrated that the spatial resolution of TROPOMI allows for the detection of several lanes of $NO_2$ pollution ranging from the Aegean Sea near Greece to the Skagerrak in Scandinavia, which have not been detected with any other satellite instrument before. The observations showed a decreasing trend in $NO_2$ ship emissions, occurring at the beginning of the Pandemic (i.e., March–April 2020), and those reductions were correlated to the restrictions in shipping activity as inferred from the AIS data on ship location, speed, and engine. Later, Kurshaba et al. (2023) proposed an approach for a large-scale ship $NO_2$ estimation using TROPOMI measurements via a supervised machine learning-based segmentation of ship plumes.

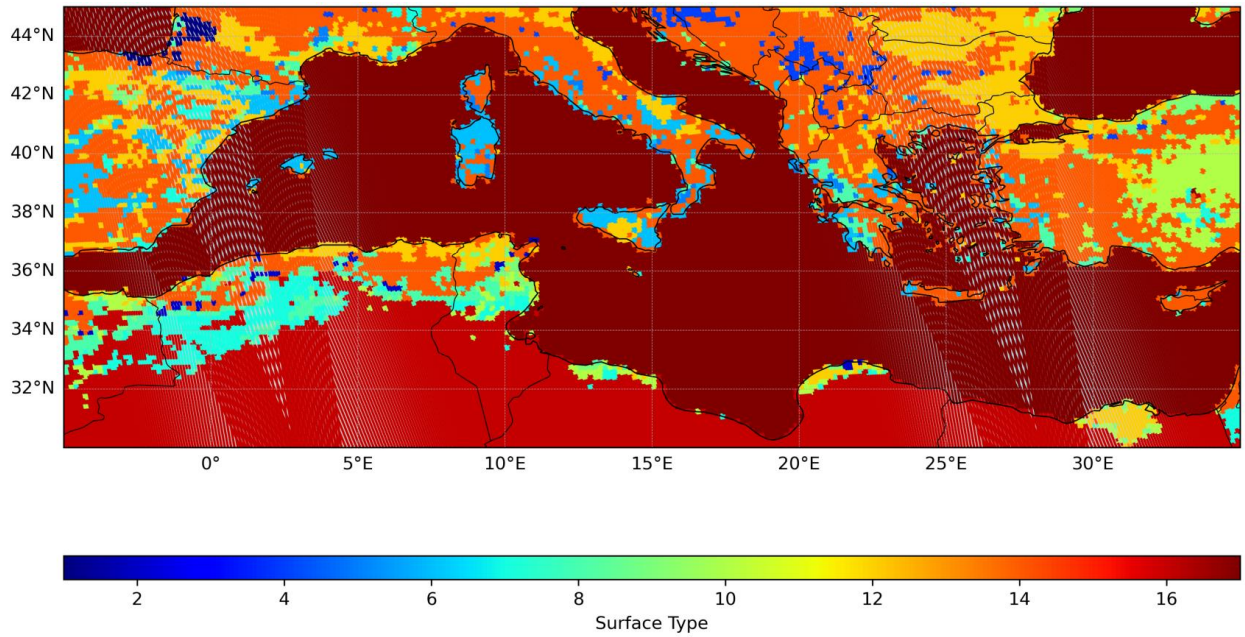


**Figure 28** Surface Type Classification: The low-level clouds over water (Surface Type = 17) are used for the analysis

### 3.2.2 Method

To quantify the cloud perturbations which are attributed to the ship-emissions as the natural analogue of the MCB-technique, the methodology on how this is achieved is described below:

**Step 1: Preprocessing and quality control of satellite datasets**

Prior to any aggregation or classification, all cloud, aerosol, and trace gas datasets are preprocessed to ensure consistency and relevance for marine low-level cloud analysis. The datasets are spatially masked using the latitude and longitude boundaries of the defined region of interest (e.g., Mediterranean Sea and North Eastern Atlantic).

To ensure that only marine low-level clouds are retained:

- Cloud Top Heights (CTH) from VIIRS and TROPOMI must be lower than 3 km.
- Surface type is restricted to water-only pixels (see Figure 28).

In addition, all Sentinel-5P (S5P) products are quality-filtered using the recommended Quality Assurance (QA) values as specified in the respective Product Readme Files (PRFs) provided by the algorithm developers. This ensures that only scientifically reliable retrievals of aerosol, cloud, and trace gas parameters are included in the analysis.

**Step 2: Aggregation of vessel data to satellite footprints**

The EMODnet vessel density data (hours per km²) are aggregated to the TROPOMI / Sentinel-5P footprints. The aggregation strategy aims to create spatial grids aligned with the native TROPOMI pixel geometry in order to ensure spatial consistency between shipping activity and atmospheric observations. The vessel density maps are ingested to the same grid with the S5P satellite observations using the nearest neighbor based on the distance between the EMODnet data against the central point of the S5P footprint.

When Automatic Identification System (AIS) data are available, additional parameters can be incorporated, including:

- Ship positions (latitude, longitude, timestamp)
- Vessel types (cargo, tanker, passenger vessel)
- Technical characteristics (vessel length, draught)

- Movement data (speed, course)

This enables a more refined characterization of emission strength and plume evolution.

**Step 3: Classification of ship-affected pixels**

Ship-affected pixels are separated from background pixels through a binary classification scheme. A flag is introduced to distinguish between impacted and non-impacted observations. The separation is based on the threshold criteria:

- vessel_density_threshold = 10 h $km^{-2}$
- distance_threshold = 10 km

These thresholds define pixels likely influenced by shipping emissions while minimizing contamination from unrelated sources.

**Step 4: Calculation of perturbations in atmospheric and cloud variables**

Perturbations are calculated for all TROPOMI/S5P variables (definitions provided in Section 3.2.4), including the $NO_2$ Tropospheric Vertical Column Densities (TVCDs) and cloud properties.

**Step 5: Development of an automatic ship-track detection algorithm**

The feasibility of implementing an automatic ship-track detection algorithm for TROPOMI will be evaluated. Such an algorithm would combine spatial gradients in aerosol indices, $NO_2$ TVCD enhancements, and cloud microphysical anomalies to detect linear plume structures.

A robust performance assessment across different spatial zones (e.g., Mediterranean Sea vs. North Eastern Atlantic) and seasons will require access to non-public AIS data and extended time series. Seasonal dependencies, meteorological variability, and regional background conditions will be explicitly investigated to ensure transferability and reliability of the detection framework.

**Validation strategy**

Matching cloud/aerosol measurements from CALIPSO, PACE and the EARTHCARE missions to the TROPOMI overpasses would be the strategy to minimize the knowledge gaps which are expected to appear at the cloud retrievals from Spectrometers, as some assumptions are required in the forward models used in retrieval algorithms accepting reflectance from passive remote sensing sensors.

### 3.2.3 Example of investigating cloud brightening events due to the presence of aerosols over the Mediterranean

The UV Aerosol Index (UVAI), also known as the Absorbing Aerosol Index (AAI), is a qualitative satellite product designed to indicate the presence of UV-absorbing aerosols in the atmosphere. It is derived from the difference between the UV radiation backscattered and measured by the TROPOMI instrument and the radiation expected from a purely molecular (Rayleigh) atmosphere without aerosols. A reduction in the backscattered signal, caused by the presence of absorbing aerosols such as smoke, desert dust, or volcanic ash, leads to positive UVAI values. In contrast, the presence of non-absorbing aerosols or clouds may result in values close to zero or even negative.

The interpretation of UVAI values follows a general scale. Positive values greater than one indicate the presence of UV-absorbing aerosols, with values between 1 and 2 corresponding to weak to moderate absorption, and values above 2 representing strong absorption, often associated with thick smoke plumes, Saharan dust outbreaks, or volcanic ash events. Values close to zero suggest the absence of significant absorbing aerosols, while negative values typically indicate dominance of non-absorbing aerosols or clouds, though they can also arise from retrieval artefacts.

The UVAI product is particularly valuable for detecting large-scale events. These include biomass burning plumes originating from regions such as the Amazon, central Africa, or Siberia; volcanic ash clouds that pose risks to aviation safety; and desert dust transport from the Sahara to Europe and beyond. The index is less sensitive to non-absorbing aerosol types, such as sulfate or sea salt particles.

Despite its usefulness, the UVAI has important limitations. It remains a qualitative indicator and does not provide direct information on aerosol concentration or optical depth. Its sensitivity is highest in the ultraviolet spectral range, which can limit its ability to detect aerosols at low altitudes when they are obscured by

cloud cover. Additionally, the retrieval can be influenced by variations in surface albedo and cloud contamination, which must be considered in data interpretation.

In summary, the UV Aerosol Index highlights the presence and strength of UV-absorbing aerosols such as smoke, dust, and volcanic ash. While qualitative, it is an effective tool for mapping and monitoring the occurrence and large-scale transport of absorbing aerosol events. In Figure 29 one can distinguish cloud structures with observed UVAI anomalies. Perturbations of the marine cloud parameters over a small region in the Easter Mediterranean have been calculated in the presence of absorbing/ non-absorbing particles by calculating to UVAI anomalies.

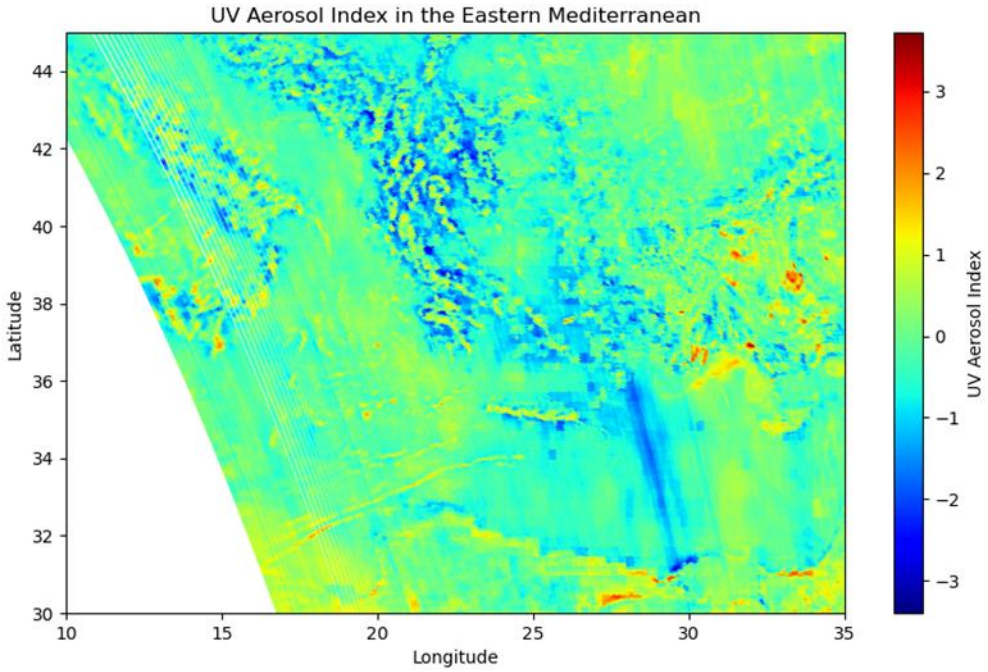


**Figure 29** The TROPOMAER UV Aerosol Index parameter for the Eastern Mediterranean on 21st August 2024

The correlations between UVAI and VIIRS cloud properties (see Figure 30) reveal several distinct patterns. Cloud optical depth shows a moderate to strong positive correlation ($r \approx 0.54$, $p \ll 0.001$), indicating that regions with higher absorbing aerosols tend to have optically thicker clouds. Similarly, liquid water path exhibits a positive correlation ($r \approx 0.47$, $p \ll 0.001$), suggesting that more absorbing aerosols are associated with clouds containing greater amounts of liquid water. Cloud top emissivity also shows a strong relationship ($r \approx 0.52$, $p \ll 0.001$), as absorbing aerosols coincide with clouds that appear more emissive at the top, consistent with optically denser or more developed systems. In contrast, the correlation with cloud effective radius is very weak ($r \approx 0.12$, $p < 1e\text{-}11$), implying that absorbing aerosols are not strongly linked to changes in droplet size, or that retrievals for this parameter may be noisy. Finally, cloud top height shows only a weak correlation ($r \approx 0.09$, $p < 1e\text{-}7$), indicating that absorbing aerosols do not strongly relate to higher cloud tops, though slight co-location effects may exist. In this context, the correlation coefficient r describes the strength and direction of the relationship, with values closer to 1 or –1 representing stronger associations, while values near zero indicate weak or no correlation. The accompanying *p*-values show the likelihood that the observed correlations occurred by chance, and the very low values reported here demonstrate that all of the relationships are statistically significant, even in cases where the correlations themselves are weak.

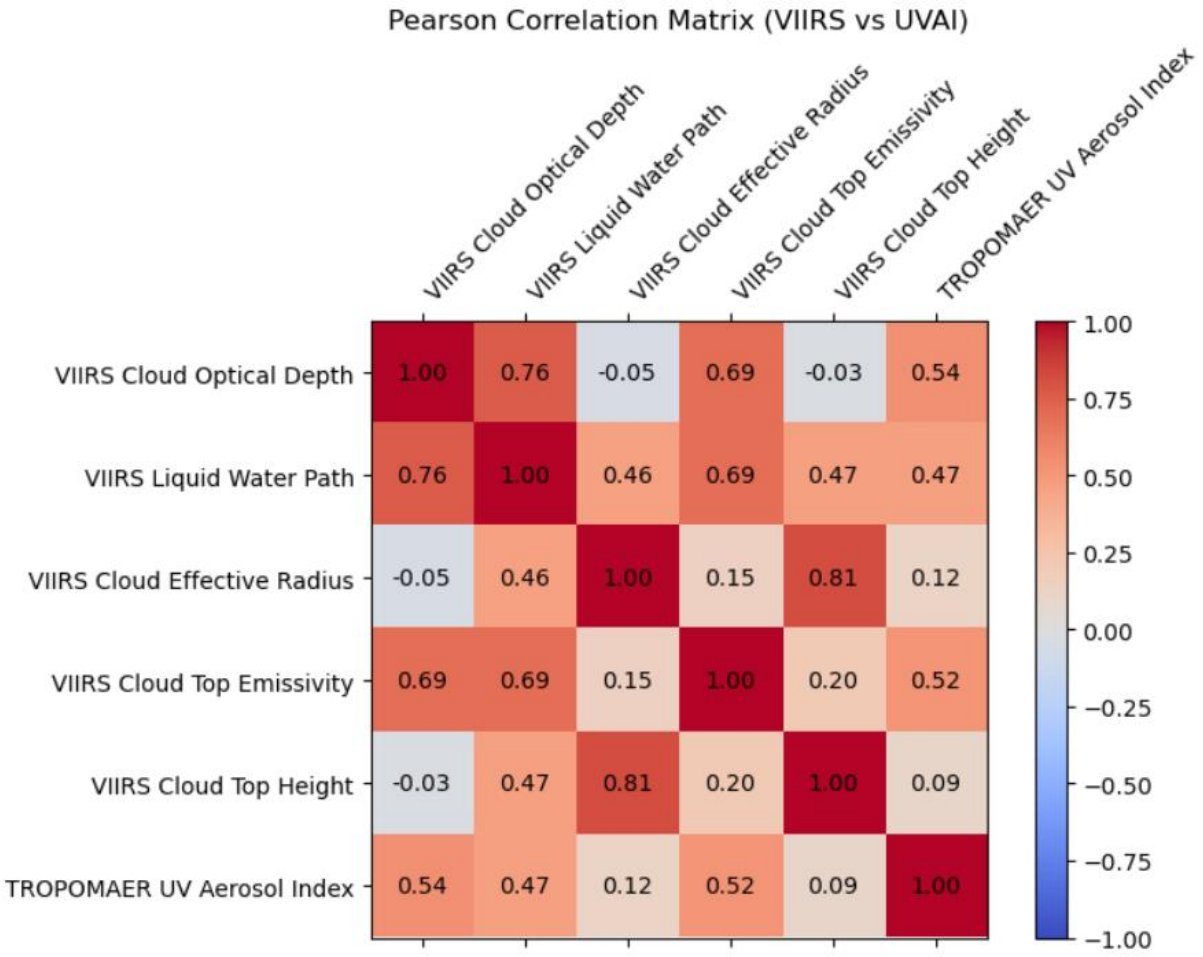


**Figure 30** Correlation Matrix between the S5P_NPP/VIIRS cloud properties and the TROPOMAER UVAI

### 3.2.4 AIS Data Exploration and Added Value for Ship-Track Detection

The original project plan foresaw the use of temporally collocated Automatic Identification System (AIS) data to construct a high-accuracy training dataset for the machine learning (ML) ship-track detection framework. Direct AIS observations provide precise vessel position, type, speed, and size information, which are essential for building a reliable ground truth dataset.

Although full AIS coverage for the analysis period was not ultimately made available, a daily sample dataset for 21 August 2024 (Eastern Mediterranean) was explored to assess the potential added value of AIS data. For the broader analysis, publicly available vessel density products from EMODnet were used as a proxy. Nevertheless, the AIS sample analysis demonstrates the significantly richer feature space that could be exploited if full AIS data access were ensured.

***Importance of AIS for ML Training***

The efficiency of any ML-based ship-track detection model depends critically on the quality and accuracy of the training set. Raw AIS data temporally collocated with satellite observations allow:

- Precise geolocation of vessel tracks
- Direct identification of ship type
- Access to vessel size (length) and operational characteristics
- Filtering by emission-relevant ship categories

Such information enables the model to learn realistic ship-track geometries rather than relying solely on indirect spatial proxies (e.g., density maps).

A statistical evaluation of a sample AIS data for the region of interest in the Eastern Mediterranean on 21st August 2024 was performed. The AIS dataset indicates that the global fleet is dominated by cargo (28.4%) and tanker vessels (15.8%), which together account for nearly half of all registered ships (see Figure 32). These vessel classes are the most relevant for ship emission studies, as they represent the bulk of long-range maritime transport and contribute significantly to aerosol precursor emissions that can lead to ship track formation. Passenger ships (8.3%) and tugs (7.0%) are also important contributors, particularly in coastal regions with high traffic density.

The latitudinal distribution (see Figure 33) further highlights that these emission-relevant vessel classes (cargo and tanker vessels) operate across a wide latitude band, around a mean of 38° N in the present dataset, corresponding to heavily trafficked routes in the Mediterranean. In contrast, vessel types such as pleasure craft, sailing vessels, and fishing vessels, while numerous, tend to cluster near coastal latitudes and contribute less to large-scale ship emission signatures detectable from space. Specialized vessel types (e.g., high-speed craft, search and rescue, or special craft) are limited in number and regional in operation, making them less relevant for large-scale aerosol–cloud interaction studies.

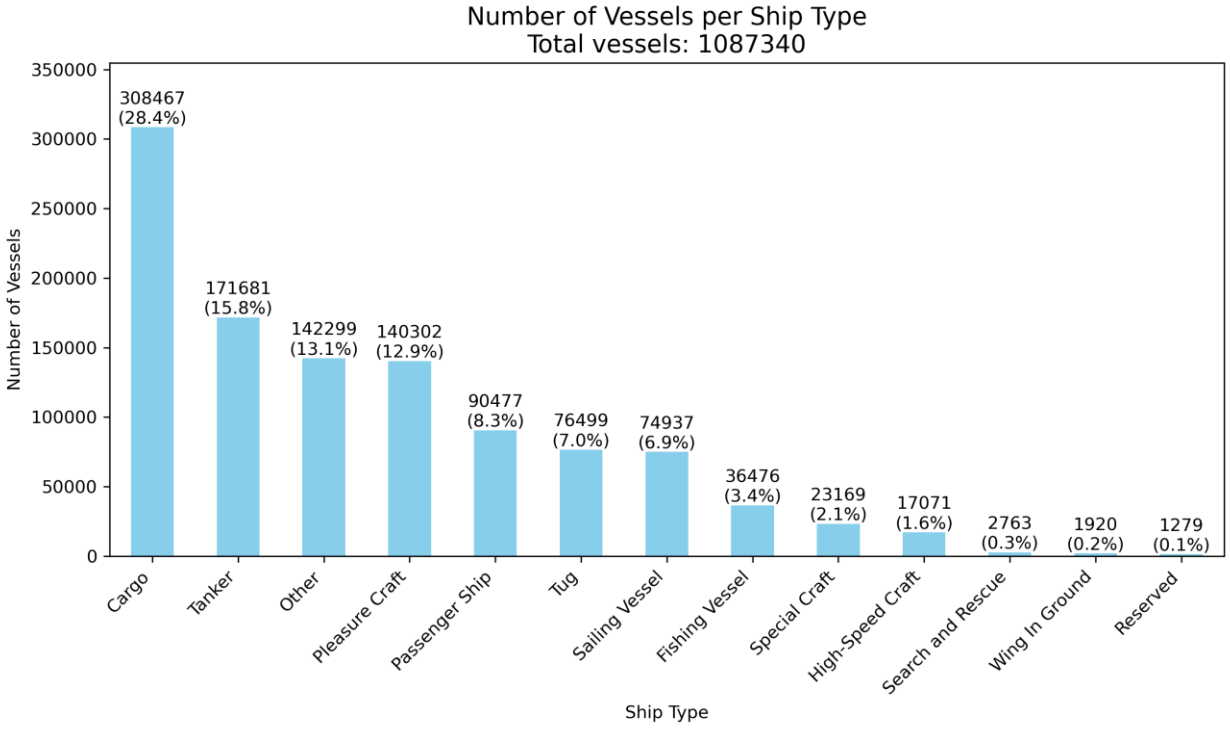


**Figure 31** Bar plot of number of vessels per ship type based on the sample AIS data from 21st August 2024

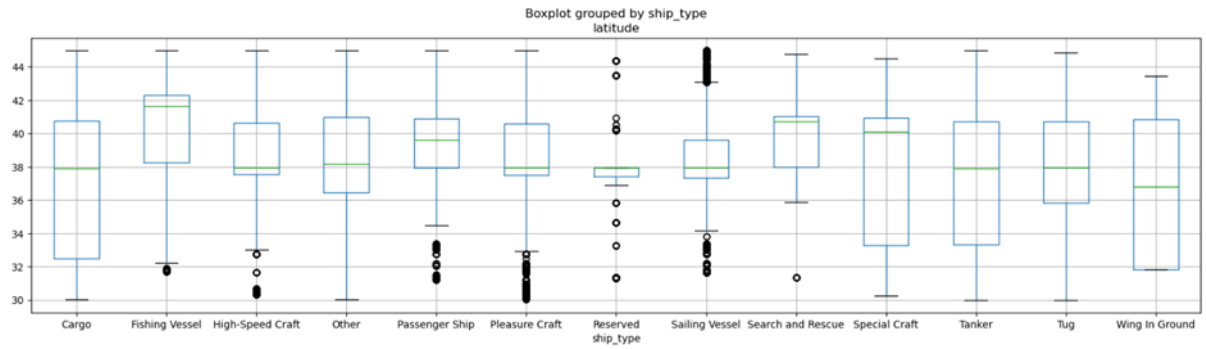


**Figure 32** Boxplot of the latitudinal distribution of the AIS data as grouped by ship_type

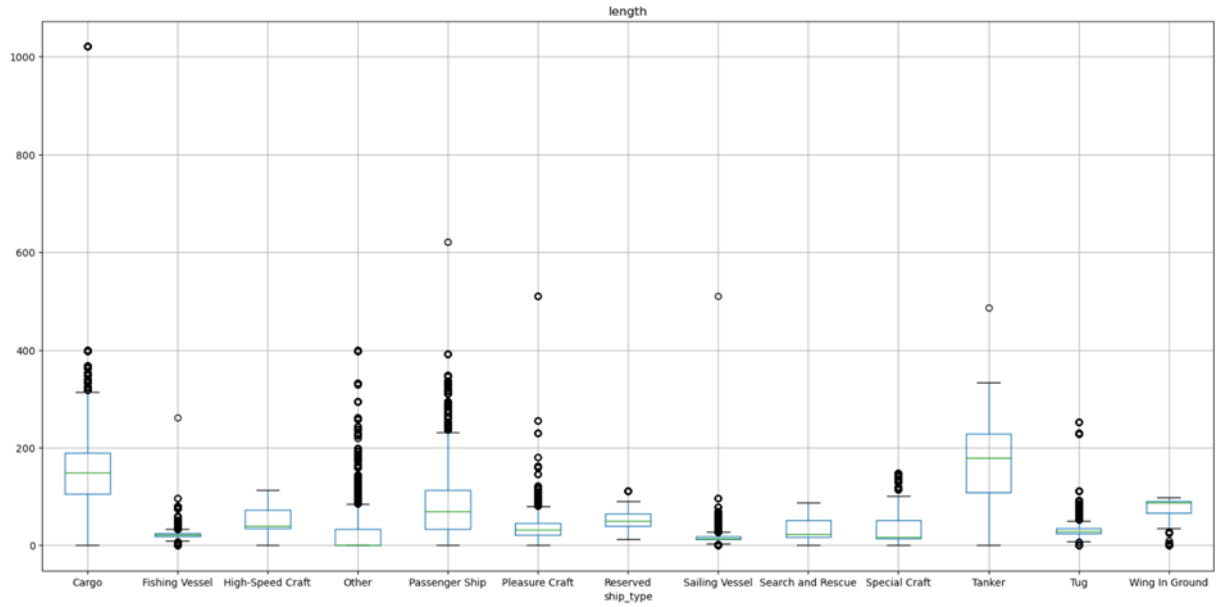


**Figure 33** Boxplot of the vessel length distribution of the AIS data as grouped by ship_type

The size distribution per vessel type (see Figure 33) highlights several insights relevant to emissions and ship tracks. Cargo and tanker ships dominate the upper range of ship lengths, often between 150 and 300 meters, with some exceeding 400 meters, while passenger ships also include very large vessels over 200 meters, corresponding to cruise liners. In contrast, fishing vessels, tugs, and pleasure craft are much smaller on average, typically below 100 meters, with outliers representing the largest ships in each class such as mega-container ships or large cruise ships. Since ship length serves as a proxy for vessel capacity and engine power, larger ships generally consume more fuel and emit greater amounts of aerosol precursors. As a result, cargo, tanker, and passenger ships are more important for atmospheric emissions and ship track formation, even though smaller vessels might be more numerous.

### 3.2.5 Definition of the perturbations

**Local Pixel-by-Pixel Perturbation** (Nearest-neighbor background reference)

This formulation quantifies the perturbation of a ship-affected pixel relative to its closest background pixel. Let

$X_i^{ship} = \text{value of variable X for ship} - \text{affected pixel } i$

$X_{NN(i)}^{bg} = \text{value of variable X for the nearest} - \text{neighbor background pixel}$

**Absolute perturbation**

$$\Delta X_i^{local} = X_i^{ship} - X_{NN(i)}^{bg} \quad (2)$$

**Relative perturbation (%)**

$$\Delta X_i^{local,\%} = \frac{X_i^{ship} - X_{NN(i)}^{bg}}{X_{NN(i)}^{bg}} \times 100 \quad (3)$$

The conceptual meaning of the local pixel-level perturbation is that it isolates the local microphysical/macrophysical modification under similar meteorological conditions.

***Regional Mean Perturbation*** *(Ship-mean vs background-mean per day and region)*

This formulation compares the aggregated ship-affected pixels to aggregated background pixels within a defined region and day.

Let

$$\overline{X}_{d,r}^{ship} = \text{mean of variable X for all ship} - \text{affected pixels on day d and region r}$$

$$\overline{X}_{d,r}^{bg} = m\text{ean of variable Xfor all background pixels on day d and region r}$$

- **Absolute perturbation**

$$\boldsymbol{\Delta X_{d,r}^{regional} = \overline{X}_{d,r}^{ship} - \overline{X}_{d,r}^{bg}} \qquad (4)$$

- **Relative perturbation (%)**

$$\boldsymbol{\Delta X_{d,r}^{regional} = \frac{\overline{X}_{d,r}^{ship} - \overline{X}_{d,r}^{bg}}{\overline{X}_{d,r}^{bg}} \times 100} \qquad (5)$$

Provided that the algorithm for detecting ship-tracks is limited to the shipping corridors, the latter coarser perturbation dataset can be used to detect the MCB-like signals. There, the mean values of the ship-affected pixels are compared to the mean background values. This definition yields one perturbation per day or scene, which may be less precise than the first definition that uses the nearest-neighbor background pixel. On the other hand, this coarser estimate of cloud perturbations is more stable in cases of failed detections. Therefore, it can be considered more robust than the pixel-by-pixel approach, at least until a proper validation scheme for the local perturbation method is implemented.

Few statistical measures for testing the statistical significance of the regional mean perturbations are estimated. Those are

- **Standard Error of the Difference**
  Standard error for two independent samples with unequal variances

$$\boldsymbol{SE = \sqrt{\frac{s_{ship}^2}{N_{ship}} + \frac{s_{bg}^2}{N_{bg}}}} \qquad (6)$$

where

$$\boldsymbol{s = \sqrt{\frac{1}{N-1}\sum\left(X_i - \overline{X}\right)^2}} \qquad (7)$$

- **Z-score (Standardized Mean Difference)**
  Expression on how many **standard errors** the observed difference is away from zero

$$\boldsymbol{z = \frac{\overline{X}_{ship} - \overline{X}_{bg}}{SE}} \qquad (8)$$

  Interpretation:
  - |z| ≈ 2 → significant at ~95% level
  - |z| ≈ 3 → very strong evidence

  When the number of observations N is large, z can often be large even for small differences.

- **Welch's t-test (p-value)**
  This is mathematically identical to the z-score formula, but the distribution used is Student's t.

$$\boldsymbol{t = \frac{\overline{X}_{ship} - \overline{X}_{bg}}{\sqrt{\frac{s_{ship}^2}{N_{ship}} + \frac{s_{bg}^2}{N_{bg}} +}}} \qquad (9)$$

The degrees of freedom are computed using the Welch–Satterthwaite equation:

$$df = \frac{\left(\frac{s_{ship}^2}{N_{ship}} + \frac{s_{bg}^2}{N_{bg}}\right)^2}{\frac{\left(\frac{s_{ship}^2}{N_{ship}}\right)^2}{N_{ship}-1} + \frac{\left(\frac{s_{bg}^2}{N_{bg}}\right)^2}{N_{bg}-1}} \quad (10)$$

The p-value is $p = P(|T| \geq |t_{obs}|)$ under the null hypothesis: $H_0 : \mu_{ship} = \mu_{bg}$. Thus, the test evaluates whether the true population means differ.

- **Cohen's d (Effect Size)**

$$d = \frac{\overline{X}_{ship} - \overline{X}_{ship}}{s_{pooled}} \quad (11)$$

where the pooled standard deviation is

$$s_{pooled} = \sqrt{\frac{s_{ship}^2 + s_{bg}^2}{2}} \quad (12)$$

Interpretation (following Cohen 1988 convention):

- 0.2 translates to small effect
- 0.5 translates to medium effect
- 0.8 translates to large effect

This measures the magnitude, independent of sample size.

## 3.3 CCT

### 3.3.1 Overview

There are several potentials for natural analogues of CCT. Volcanic eruptions inject sulfur dioxide and water vapor into the atmosphere, forming sulfate aerosols and affecting cirrus formation indirectly. During a mineral dust episode (like Saharan dust), a significant amount of mineral dust is lifted into the upper troposphere, which may act as INPs. The consequent transport of dust particles, depending on meteorological and dynamical conditions, from their source regions across large distance will spread the influence into larger scales. However, volcanic injections and mineral dust outbreak with sufficient number concentrations tend to produce more ice crystals and often have an opposite effect of CCT. Aircraft-emitted particles taking place at the cirrus levels may also act as INPs, causing heterogeneous nucleation in regions with a favorable atmospheric state. It leads to the formation of contrails and exerts indirect effects on the existing cirrus clouds. Aviation emissions may also not be a good candidate for CCT analogues since aviation soot is typically a moderately inefficient INP that it doesn't fully suppress homogeneous freezing and efficiently reduces ice number concentration. Recent studies proposed aviation decarbonization strategies with sustainable aviation fuels (SAF), which directly reduce aviation CO2 and soot emissions and indirectly prevent ice crystal formation in contrails and reduce contrail optical depth (Voigt et al., 2021; Märkl et al., 2024). In the frame of *ACtIon4Cooling*, it was focused on the changes of cirrus cloud properties responding to aviation impact as a natural analogue of CCT.

Previous studies indicated that the enhanced heterogeneous nucleation caused by aviation exhaust particles can be responsible for the enhanced values of PLDR of cirrus clouds (Urbanek et al., 2018; Li and Groß, 2021, 2022). Furthermore, cirrus clouds with enhanced PLDR exhibit larger effective ice particles and lower number concentrations (Groß et al., 2023). This indicates that there were more heterogeneous nucleation occurring due to aviation-induced emissions, as homogeneous nucleation is expected to be suppressed by heterogeneous nucleation (Gierens, 2003). The processes mimic the CCT strategies. During the COVID-19 pandemic, significant reductions in aviation led to fewer contrails and contrail cirrus revealed with experimental and modelling efforts (Schumann et al., 2021a, b) and there was a significant increase in

ice particle number concentration detected by CALIPSO, which indicates more homogeneous nucleation occurrence due to reduced aviation emitted soot acting as INPs (Zhu et al., 2023). Furthermore, a significant reduction in PLDR of cirrus clouds was found in both March and April 2020 compared with the corresponding periods in the pre-COVID years by analyzing lidar observations of CALIPSO (Li and Groß, 2021). The changes in the optical and microphysical properties of cirrus clouds responding to aviation emissions can act as natural analogue of CCT for further studies.

During the HALO missions (including ML-CIRRUS and CIRRUS-HL campaigns), a comprehensive suite of sophisticated in situ and remote sensing instruments were mounted onboard the aircraft for scientific aims. Within *ACtIon4Cooling* , the available airborne measurements during the ML-CIRRUS was used to trace specific clouds forming in the regions with either dense aviation emissions or not according to the distribution of PLDR of cirrus clouds. Furthermore the cloud optical thickness, ice water content, and ice crystal number concentrations was calculated with in situ instruments and lidar. From a statistical perspective, the available CAPLISO satellite data have also been exploited to determine the optical and microphysical properties of cirrus clouds temporally (e.g. during the pre-COVID years period and year-to-year variation) and spatially (comparison between midlatitudes and high latitudes). The derived microphysical and optical parameters of cirrus clouds as a function of latitude and longitude have been provided for model simulation of ICON and RF calculations with pyDOME RT code.

### 3.3.2 Available datasets

During the campaigns ML-CIRRUS in spring 2014, HALO was equipped with a suite of in situ and remote sensing instrumentation to investigate contrail cirrus as well as to observe differences between contrails and natural cirrus clouds in combination with satellites and models (Voigt et al., 2017). Small particles in the size range from 3 to 50 µm were detected by the CAS (Voigt et al., 2017; Kleine et al., 2018). Larger particles were detected by the CIP (Cloud Imaging Probe, in the size range from 15 to 960 µm) as part of the CCP (Cloud Combination Probe) and the PIP (Precipitation Imaging Probe, in the size range from 100 to 6400 µm) instrument (Weigel et al., 2016). With these instruments, ice crystal effective diameter (De), number concentrations (Ni), and ice water content (IWC) can be derived. WALES is a multi-wavelength lidar system including DIAL and HRSL capability. So it can measure water vapor mixing ratio and aerosol extinction, backscatter coefficients, and depolarization. The HALO data are available at the HALO database (HALO2025, last access: 02 December 2025).

The satellite observations of CALIPSO provides us depolarization and extinction coefficients that can be used to determine cloud top height and cloud optical thickness. For the relevant-study of the project, the Level 2 5 km cloud profile products are used. To distinguish cirrus clouds from other features including aerosols and non-cirrus clouds, the vertical feature mask (VFM) has been applied to yield information on feature types and subtypes by decoding the bit-mapped integers from VFM (e.g. Winker et al., 2009). Microphysical parameters, like De and Ni, can be derived from the DARDAR data (applying the radar-lidar synergy of CLOUDSAT and CALIPSO), which, however, are limited only for certain periods. In addition, the data products of IIR-CALIOP retrievals (Ni, De, and IWC) in 17 years (2006.06–2023.07) are publicly available (Mitchell et al., 2018, 2025) and the relevant analyses have been carried out. The CALIPSO data are available via [URL24] (login required). The post-processed datasets are partly uploaded to Li and Groß (2025b) and CEDA (see Datapool description in Chapter 5.3). Launched on 28 May 2024, EarthCARE provides the microphysical and optical parameters of cirrus clouds as a successor to CALIPSO (Wehr et al., 2023). The dataset of EarthCARE can be accessed at [URL19]. The analyses of them for relevant studies of CCT have been conducted.

### 3.3.3 Method

Previous studies on the enhanced cirrus PLDR and changes in ice crystal properties caused by aviation exhaust particles provide a strong support that changes in the microphysical properties of cirrus clouds depending on aviation emissions can serve as a natural analogue of CCT. Following the previous studies, we collected the in-situ measurements of IWC, De, and Ni during the ML-CIRRUS campaign and grouped them into high-PLDR-mode and low-PLDR-mode of cirrus clouds with the reference of coordinated lidar measurements of WALES. To derive the parameters for a defined region, we integrate the coordinates and altitudes from the coordinated BAHAMAS information to the dataset and derive one number in the defined region (i.e. a latitude-longitude-altitude box) and time period. and calculated the respective perturbations in the microphysical parameters with the background references from literatures.

EO instruments like CALIOP aboard CALIPSO and ATLID aboard EarthCARE are optimized for global profiling of the atmosphere, providing vertical structures and optical properties of aerosols and clouds. With the vertical feature mask (VFM) products, cirrus clouds can be distinguished from aerosols and non-cirrus clouds. Besides the measured cloud properties with lidar instruments, including cloud height, attenuated backscatter, and depolarization, temperatures are interpolated from the GEOS-5 analysis fields along the satellite tracks. Aiming to avoid misclassified mixed-phased clouds and noise-contaminated signals, only measurements at temperatures below -38 °C, above 6 km altitudes, and with geometric thickness larger than 0.1 km are considered. Furthermore, VFM can help to distinguish cirrus clouds due to deep convection. Moderately thick cirrus clouds have therefore been masked out, which have been classified as deep convective outflows and/or opaque clouds. With the measured depolarization of cirrus clouds, the horizontal distributions of cirrus optical properties have been identified, which have been compared with the density maps of aviation emissions (e.g., from EUROCONTROL), especially with the resulting formation of persistent contrails (Teoh et al., 2024).

Figure 34 presents the global spatial distribution of the simulated number concentration of black carbon (BC) particles emitted from aviation that are active as INPs (in units of $L^{-1}$) using the EMAC model (Beer et al., 2024). The rectangles in red and blue indicate the research areas in the high-latitude and mid-latitude regions, respectively. From the simulations, a hotspot of aviation-induced BC in the European part of the mid latitudes can be seen with a much higher number concentrations at midlatitudes than high latitudes. The distinct latitudinal differences in aviation-induced BC provide a natural laboratory to study the aviation-impact on cirrus cloud properties, i.e. CCT-like effects of aviation. Focusing more on the mid-latitude regions shown in the cyan rectangle with higher aviation emissions, the changes in cirrus cloud properties responding to aviation reduction in April 2020 due to the COVID-19 curfew are examined as well as to a long-term increase of aviation emissions in the period before COVID. In Figure 36, we show the changes in air traffic in terms of $CO_2$ emissions from aviation over Europe in 11 years from 2010 to 2020 covering the first lockdown period of COVID-19. From the plot, civil air traffic has been growing in the past years until the COVID-19 and presenting a strong reduction afterwards from March 2020. The temporal changes in aviation over Europe provide a good opportunity to study the evolution in cirrus cloud properties and their response to aviation impacts.

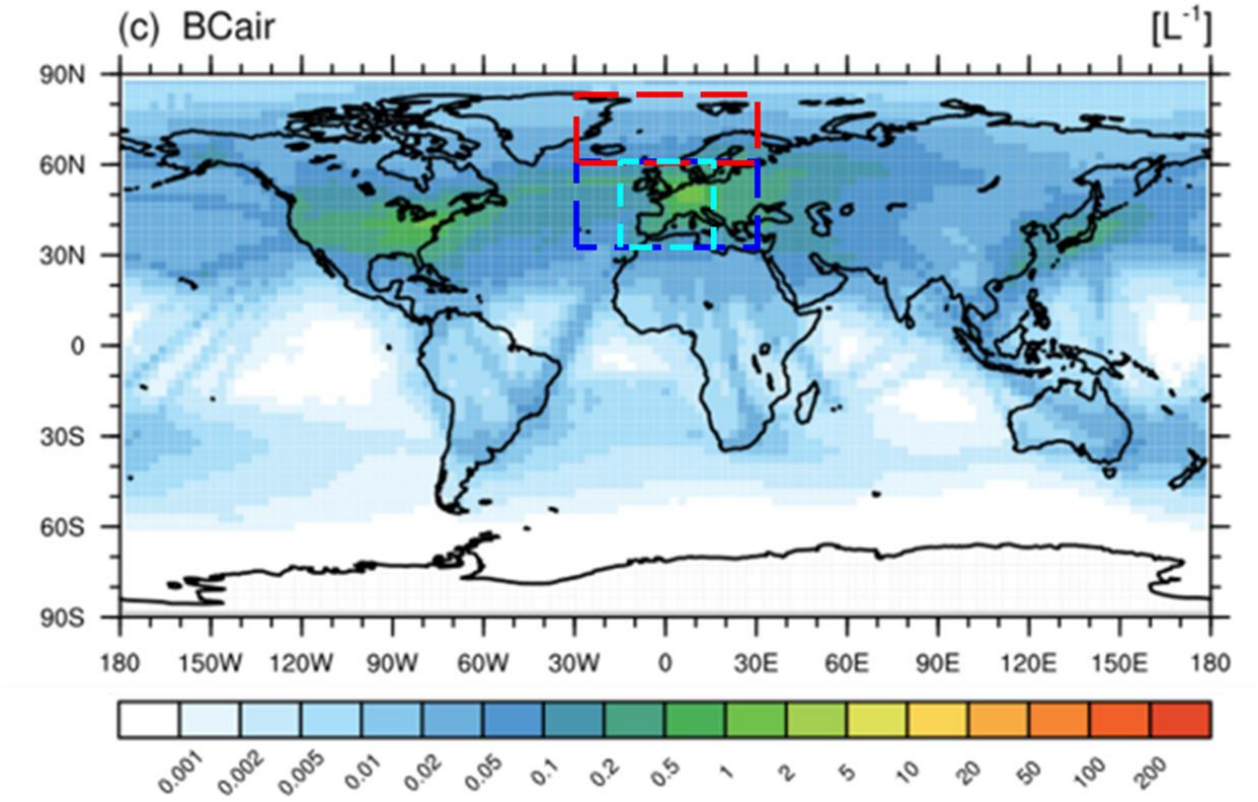


**Figure 34** Global distribution of the simulated number concentration of black carbon from aviation acting as INPs ($L^{-1}$) inside cirrus clouds (Beer et al., 2024). For long-term analysis of CCT-like effects, the EO observations are determined in the area indicated in cyan rectangle (35 – 60 $^{o}$N; 15 $^{o}$W – 15 $^{o}$E) which covers a large fraction of Northern Atlantic flight corridor. The red rectangle indicates the high-latitude regions of research (35 – 60 $^{o}$N; 30 $^{o}$W – 30 $^{o}$E) and the blue one the midlatitude regions (60 – 80 $^{o}$N; 30 $^{o}$W – 30 $^{o}$E) for comparison.

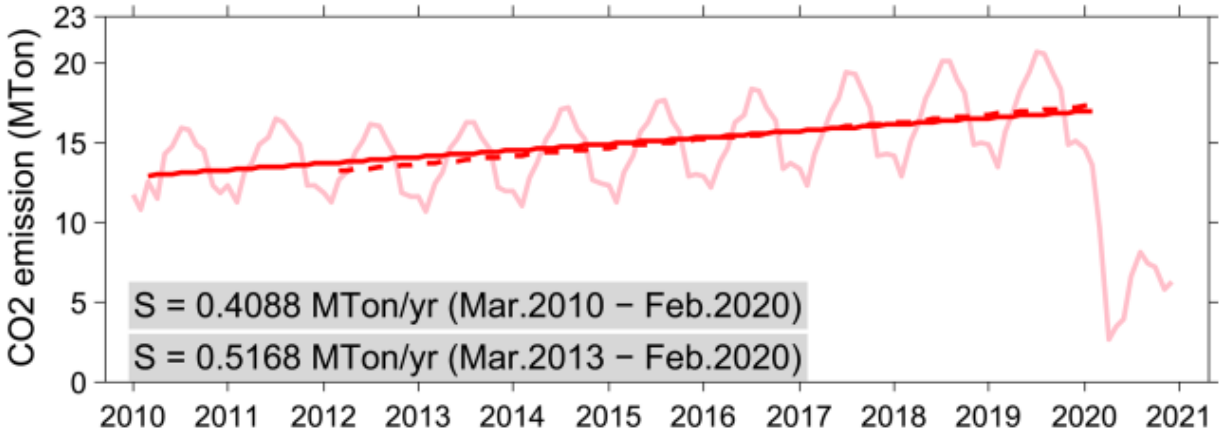


**Figure 35** $CO_2$ emissions from air traffic in different month over Europe including a total of 42 countries and regions in 11 years during 2010-2020. There is a clear seasonality in aviation showing more flights in summer than in winter. The aviation-emitted CO2 increased by about 3.2% per year in the last 10 years before the COVID-19 outbreak. During COVID starting in March 2020, however, air traffic was significantly reduced in Europe. The figure is generated based on the European historic data from the European Organization for the Safety of Air Navigation (EUROCONTROL, https://www.eurocontrol.int/our-data, last access: 18 February 2026).

To calculate the perturbation from the in-situ measurements, a clear baseline (background state) needs to be defined and deviations need to be quantified relative to that baseline, which including IWC and Ni are derived from Table 1 in Li et al., (2023). Furthermore, observations from the low-PLDR-mode cirrus clouds

are presumed to originate from more pristine regions and hence are used as the background state. The absolute and relative perturbations are calculated based on the following equations, respectively:

- Absolute perturbation $\Delta X = X_{observed} - X_{baseline}$
- Relative perturbation $\Delta X = \frac{X_{observed} - X_{baseline}}{X_{baseline}} * 100.$

where $X$ stands for IWC, Ni, depolarization, etc. "*observed*" stand for the observed parameters with respective instruments and "baseline" for the baseline as clean reference state.

The derived perturbations in Ni and De from the in-situ measurements during ML-CIRRUS are shown in Figure 36. Here the baseline values are chosen as the mean values calculated from all the observations of low-PLDR-mode cirrus clouds. From the comparison, it can be seen that cirrus clouds formed and evolved in the high-aviation regions are characterized by larger effective diameters and lower number concentrations. More details on the comparison can been found in Groß et al., (2023).

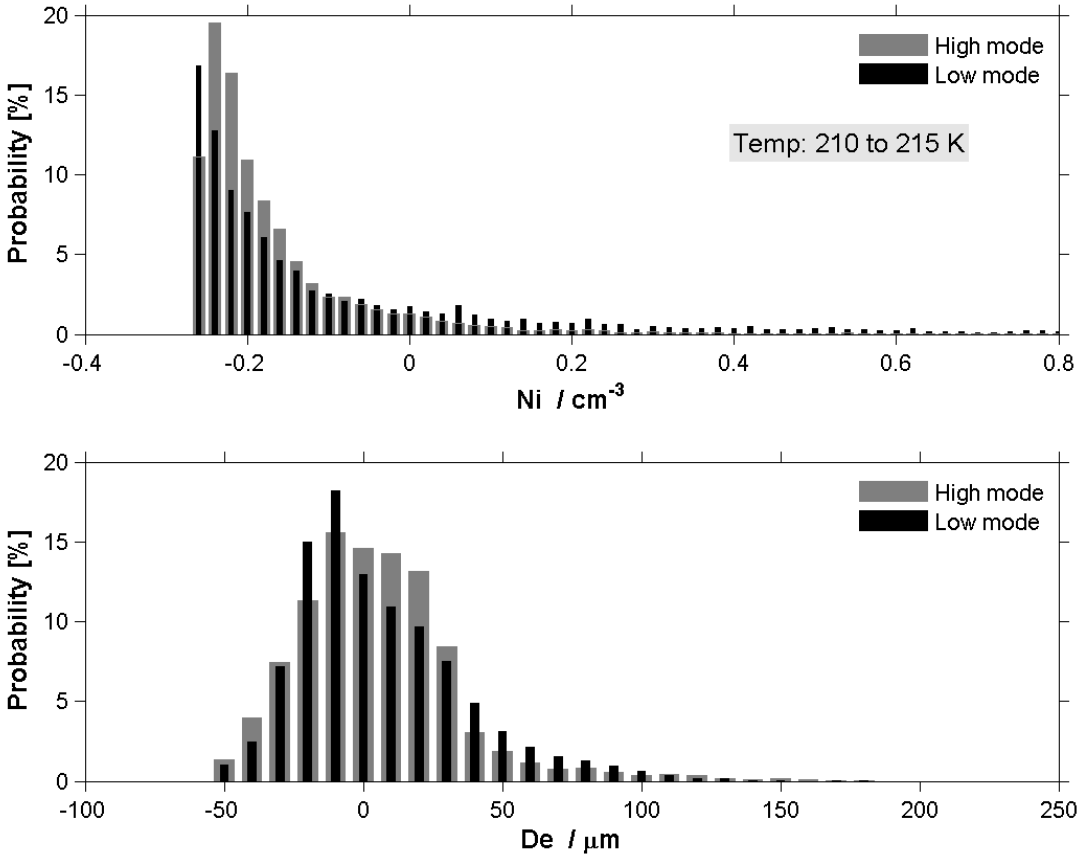


**Figure 36** Perturbations in Ni and De from the in-situ measurements during the ML-CIRRUS campaign in 2014 with the baseline values calculated from the medians of low-PLDR-mode cirrus clouds. The observations were chosen in the temperature range from 210 to 215 K for a reliable comparison.

For the satellite observations, the microphysical parameters (IWC, Ni, and De) from IIR-CALIOP retrievals (Mitchell et a., 2025) are mapped onto regular 1°x1° latitude-longitude grid boxes for subsequent analysis. The baseline values are calculated with the 10-year observations in 2010-2019. One example of mapped De of cirrus clouds in April from IIR-CALIOP retrievals is shown in Figure 37. The mean values are calculated from all the 10-year observations from 2010 to 2019, which are considered as the baseline values (in the left panel). The perturbations in De in 2019 and 2020 are calculated based on the above-mentioned equations for a comparison. For optical parameters (Extinction, backscatter, and depolarization) from only lidar observations of CALIOP, are derived from altitudes between 6 and 13 km and with occurrence rate of cirrus clouds larger than 1%. One example of the calculated geometric thickness in spring 2019 and 2020

is shown in Figure 38 for a comparison. The perturbations are calculated based on the above-mentioned equations with the baseline values calculated from the 10-year observations from 2010 to 2019.

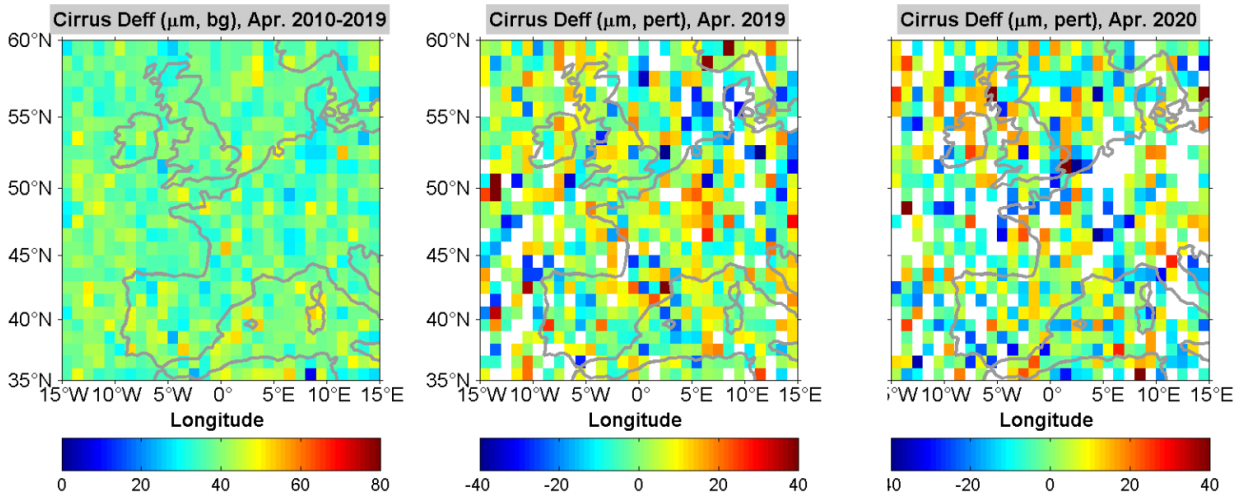


**Figure 37** Example of the De baseline and perturbations in April 2019 and 2020 from IIR-CALIOP retrievals in the midlatitude regions (35 – 60 ºN; 15 ºW – 15 ºE).

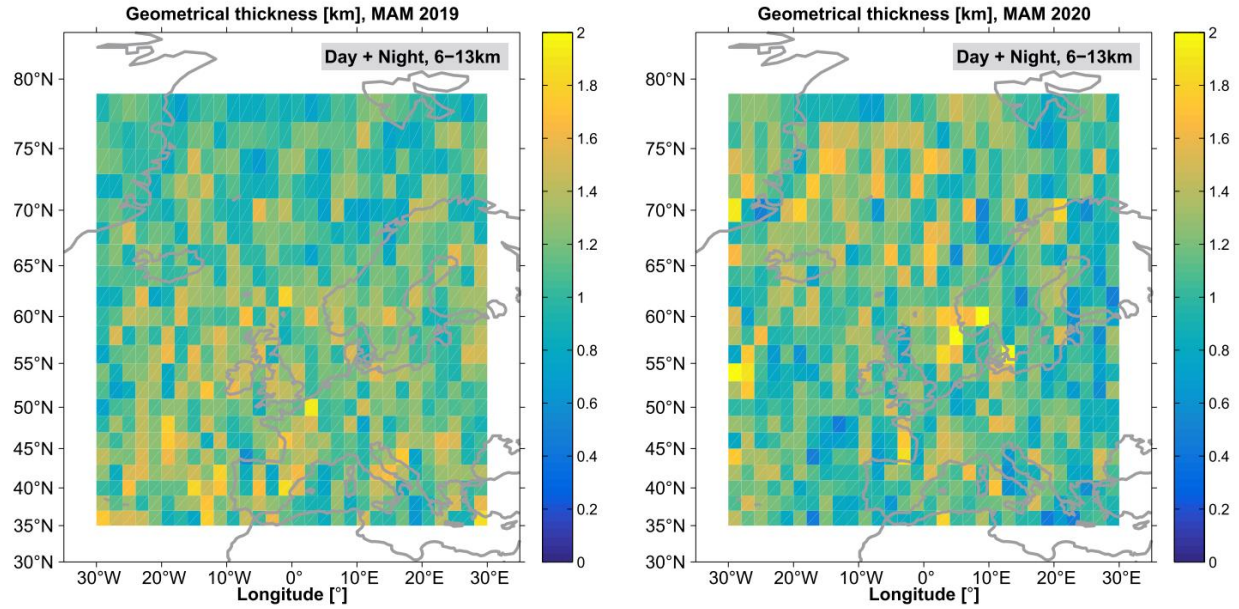


**Figure 38** Example of the calculated geometric thickness from lidar measurements of CALIOP in spring 2019 and 2020 in both midlatitude and high-latitude regions (35 – 80 ºN; 30 ºW – 30 ºE).

### 3.3.4 Overview

To assess the impact of different mechanisms from the perspective of radiative transfer, the DLR radiative transfer model pyDOME (Efremenko et al., 2017) is used. The model is designed for high-accuracy spectral simulations of solar radiation scattered and absorbed in the Earth's atmosphere. It provides a modular and physically consistent framework that combines spectroscopic absorption, molecular scattering, and particle scattering within a unified solver architecture. The overall computational workflow consists of several components. Molecular absorption cross-sections are derived from the HITRAN database using the Py4CATS interface (Schreier et al, 2019) integrated into pyDOME. This allows line-by-line cross-section calculations with full temperature and pressure dependence. Alternatively, precomputed absorption cross-sections can be read from external files, which is useful for efficient operational runs or when using externally

prepared spectroscopic datasets. Rayleigh scattering is modeled following the formulation of Bodhaine et al. 1999, including the wavelength-dependent scattering cross-sections, refractive index of air, and depolarization corrections. This ensures accurate representation of molecular scattering over the UV to near-infrared spectral range. For aerosol and cloud particles, pyDOME computes optical properties using Mie theory for spherical particles. Given a particle size distribution and a complex refractive index, the model calculates extinction and scattering coefficients, single scattering albedo, and phase function expansion coefficients. Alternatively, aerosol optical properties can be read from external sources. Several input formats are supported, including OPAC aerosol files and MODTRAN tp6 outputs. This flexibility allows consistent coupling with external aerosol models or observational datasets.

All these optical parameters form the input to the radiative transfer solver. The radiative transfer equation is solved using the discrete ordinate method with a matrix exponential formulation (DOME), implemented in Python. The theoretical description of the solution method used in the model is outlined in Efremenko et al. 2017.The solver treats a plane-parallel multilayer atmosphere and allows an arbitrary number of streams. The matrix exponential approach provides improved numerical stability, particularly in strongly scattering or optically thick layers, compared to classical eigenvalue-based implementations.

pyDOME can compute spectral radiances and irradiances at the top and bottom of the atmosphere as well as at intermediate levels. It allows separation into direct and diffuse components and supports both spectral and broadband integrations. Due to its modular structure and consistent treatment of atmospheric optics, the model is well suited for sensitivity studies of radiative fluxes with respect to aerosol optical thickness, particle size, refractive index, and surface albedo. The data pipeline in pyDOME is illustrated in Figure 39.

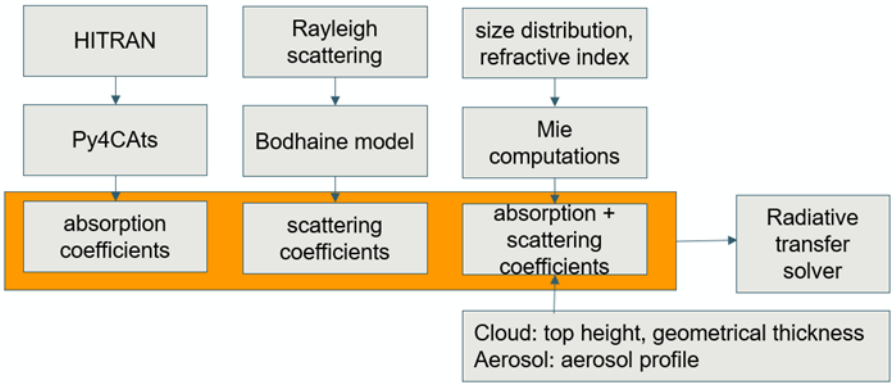


**Figure 39** The data pipeline of the radiative transfer model pyDOME.

For **SAI** studies, one of the major objectives is to perform sensitivity analysis on layer injection height and latitude. The changes in surface solar radiation and the diffuse-to-direct radiation ratio can be investigated with pyDOME. More specifically, the total radiance can be decomposed into direct and diffuse components and their ratios can be analyzed across different atmospheric conditions.

For **MCB** studies, one of the major objectives is to perform sensitivity analysis on the size distributions and the cloud water content of the studied marine clouds. For every SRM pathway a dedicated Python wrapper was built that sits “above” pyDOME, assembles the atmospheric state, perturbs the variables of interest, and then invokes the radiative transfer solver. Gas absorption coefficients from HITRAN are merged with Mie-derived aerosol and cloud optics, so that each atmospheric layer is characterized by its spectral optical thickness, single-scattering albedo and an effective phase function. These quantities are passed directly to pyDOME, which returns the full radiance field together with TOA forcing, surface irradiance and heating-rate profiles for every perturbation.

For **CCT** studies, one aspect to study with RTM simulations is to examine how ice crystals with irregular shapes, can be parameterized in a vectorized version of pyDOME as a pre-requisite to account for the depolarization effect.

## 3.4 Calculation of radiative properties

The radiance field is computed with a discrete-ordinate solver for the radiative-transfer equation. Accuracy increases with the number of angular streams, but so does cost, so an optimal stream count was determined that preserves sub-percent accuracy while keeping run times practical. The solver expands the radiance field in Fourier azimuth modes, solves the transfer equation for each mode independently, and then reconstructs the full field by summation. Across the solar spectrum, computational speed is boosted by applying a principal-component representation of optical properties; this reduces the number of monochromatic calculations required in each band by roughly an order of magnitude without compromising spectral fidelity.

### 3.4.1 Validation

Internally, the radiative transfer model consists of two main components: (i) the radiative transfer solver, which numerically solves the radiative transfer equation, and (ii) the preprocessing routines, which translate the physical properties of the atmosphere and the gaseous profiles into optical properties such as absorption coefficients, scattering phase functions, and single scattering albedos. These optical properties form the inputs to the radiative transfer solver.

The most challenging part of generating accurate optical parameters lies in the computation of absorption coefficients in gaseous absorption bands, where line mixing, pressure broadening, and high spectral resolution are required. Consequently, the validation of the radiative transfer model developed in the project follows a two-step strategy: first, validating the solver itself, and second, validating the generation of optical input data.

Following established benchmarking practices (Kokhanovsky et al. 2010), the most representative way to validate a radiative transfer solver is through the comparison of angular distributions of reflected radiances. As a first step, results from the in-house solver pyDOME are compared with those obtained from the well-established DISORT model, which serves as the numerical kernel for several widely used radiative transfer frameworks, including libRadtran.

As a benchmark exercise, a multilayered atmosphere consisting of 13 layers was considered. For each layer, the optical thickness, single scattering albedo, and phase function are prescribed (data provided by Robert Spurr). Both solvers were run using 20 discrete ordinates to ensure consistency of angular resolution.

Representative results are presented in Figure 40, illustrating the agreement between the two solvers under these benchmark conditions up to the sixth digit.

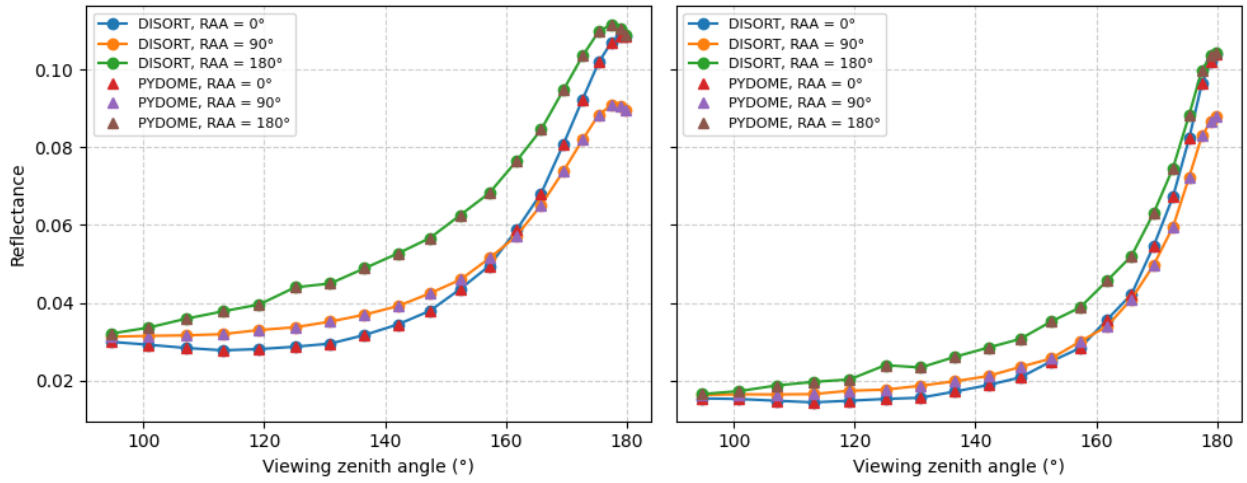


**Figure 40** Reflectance computed with the pyDOME and DISORT radiative transfer solvers for a 13-layer atmosphere for three values of the relative azimuth angle (RAA): at the top of the atmosphere (left) and at layer 10 (right). The solar zenith angle is 35 degrees.

In addition to simulations over a purely reflecting surface, pyDOME also includes the capability to represent the ocean surface, accounting for refraction and reflection at the atmosphere-ocean interface. This feature allows a more realistic treatment of oceanic scenes, which are of particular importance for satellite missions focusing on the retrieval of trace gases and aerosols over water. To assess this functionality, pyDOME results have been compared with those obtained using the LIDORT model, which includes a dedicated coupled ocean–atmosphere module. The comparison demonstrates very good agreement between the two solvers for angular distributions of reflected radiances. Representative results of these benchmark comparisons are shown in Figure 41.

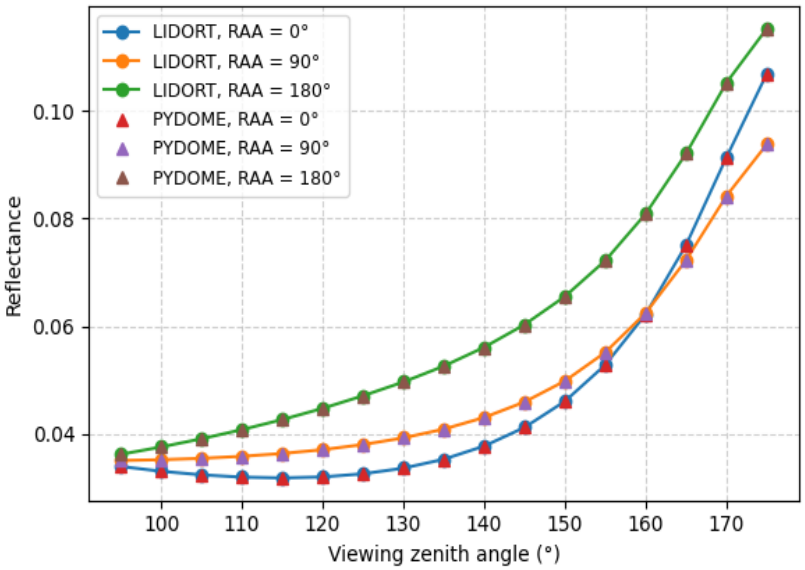


**Figure 41** Reflectance computed for a 13-layer atmosphere and 2 layered ocean with a flat interface. Comparison between pyDOME and LIDORT.

Below, a comparison of simulations in absorption bands was considered. Figure 42 presents the results for the diffuse transmittance in the spectral region 800–1000 nm, which includes a strong water vapor absorption band. The simulations were performed using three different radiative transfer models: libRadtran with a spectral resolution of 1 $cm^{-1}$, MODTRAN with 0.1 $cm^{-1}$, and pyDOME also with 0.1 $cm^{-1}$. To ensure comparability with typical instrument characteristics, all spectra were subsequently convolved with a Gaussian slit function with a full width at half maximum (FWHM) of 30 $cm^{-1}$. Similarly, Figure 43 shows results for radiance computations for the spectral region 1000-2500 nm. pyDOME is able to reproduce the band structure with high spectral resolution, showing consistency with the established reference models. Since pyDOME is an in-house model and demonstrates a good agreement with established tools such as libRadtran and MODTRAN, this model was chosen for the *ACtIon4Cooling* simulations.

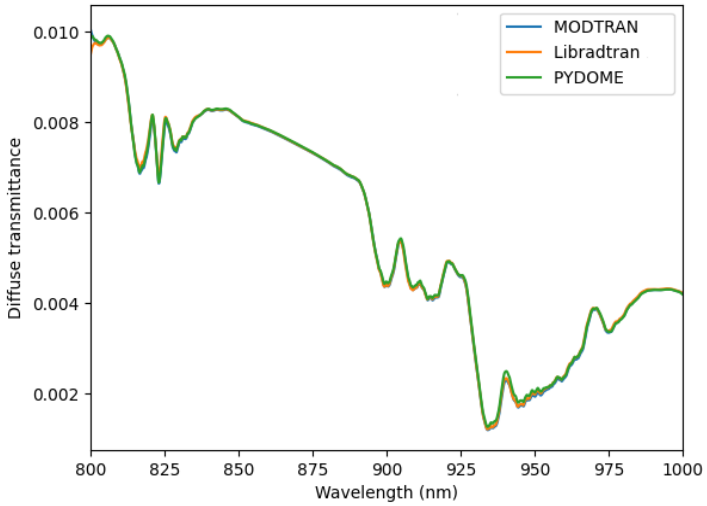


**Figure 42** Diffuse transmittance computed in the spectral domain 800-1000 nm, which includes a water vapor absorption band. Simulations are performed with MODTRAN, LibRadTran and pyDOME for the US standard atmosphere.

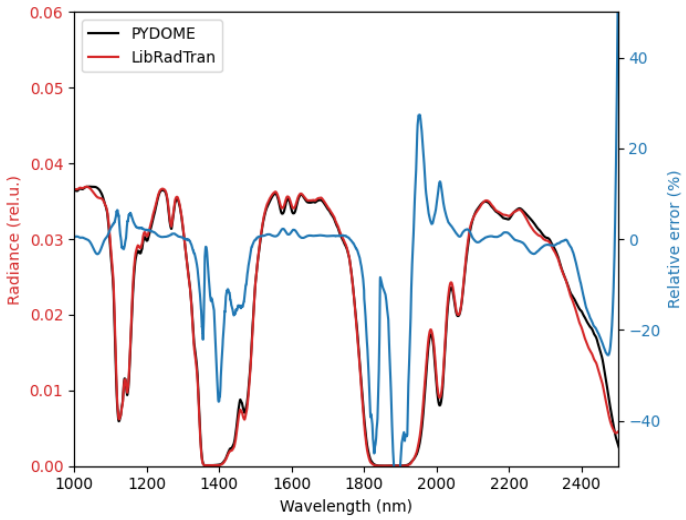


**Figure 43** Comparison of reflected spectra at the top of the atmosphere computed with pyDOME and libRadtran in the spectral domain 1000–2500 nm for the US Standard Atmosphere. The spectra were calculated with a spectral resolution of 1 $cm^{-1}$ for libRadtran and 0.1 $cm^{-1}$ for pyDOME, and subsequently convolved with a Gaussian slit function with a FWHM of 30 $cm^{-1}$.

### 3.4.2 SAI

To illustrate the application of pyDOME for SAI simulations, an aerosol case study was considered. In this example, a rural aerosol model is used, consistent with that implemented in MODTRAN. The aerosol model is specified by providing the wavelength and altitude dependence of the extinction and scattering coefficients, as well as the asymmetry parameter (see Figure 44 and Figure 45). Figure 46 presents examples of computations of BOA irradiance and TOA radiance for the described aerosol model. The simulations are performed over the spectral range 400–2500 nm for different values of aerosol optical thickness.

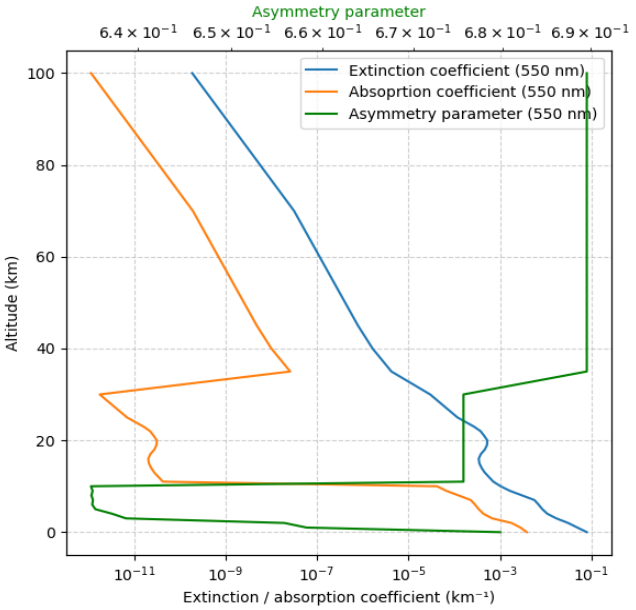


**Figure 44** Aerosol extinction and absorption coefficients as well as the asymmetry parameter at 550 nm as functions of the altitude

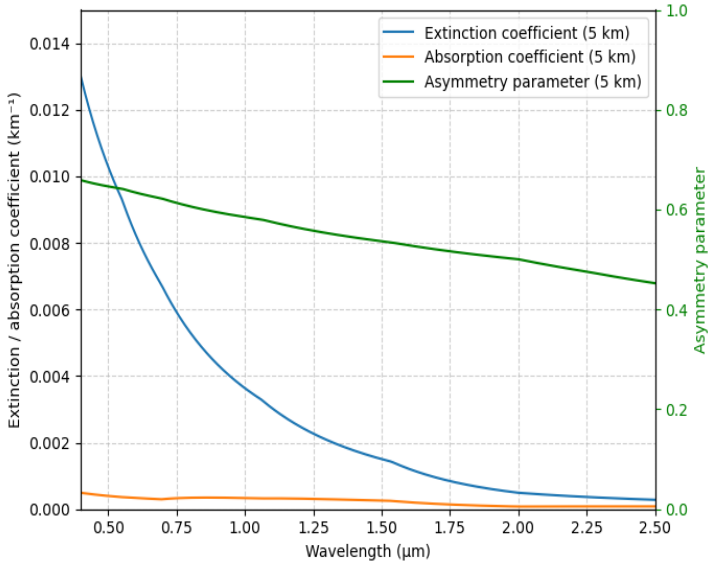


**Figure 45** Aerosol extinction and absorption coefficients as well as the asymmetry parameter at 5 km as functions of the wavelength

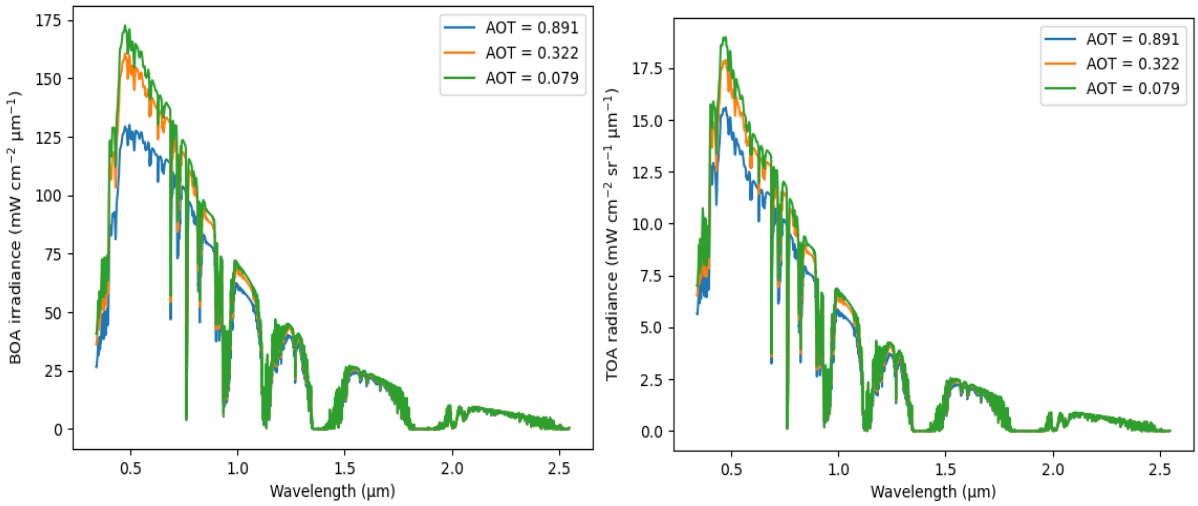


**Figure 46** Bottom-of-atmosphere (BOA) irradiance (left) and Top-of-atmosphere (TOA) radiance (right) simulations over the spectral range 400–2500 nm for different values of aerosol optical thickness

### 3.4.3 MCB

In the next example, a simulation of the downwelling transmitted radiance at the bottom of the atmosphere was performed. The cloud-top height, cloud optical thickness, and cloud effective radius are taken from VIIRS observations. The corresponding scene is shown in Figure 47. The simulations are performed in the spectral range 765–767 nm, and the resulting spectra are convolved with a rectangular slit function of 2 nm width.

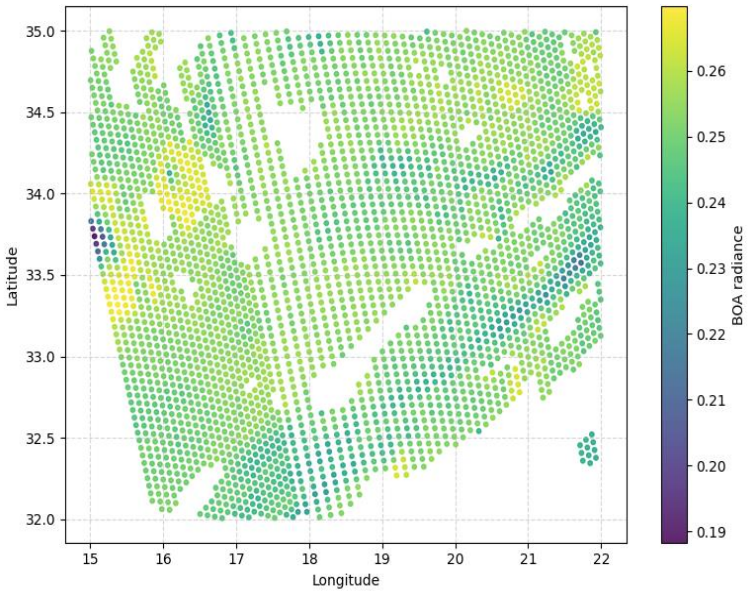


**Figure 47** Example of a map of downwelling radiance at BOA for a cloud scene. Cloud top height, cloud optical thickness and Cloud Effective Radius are provided by VIIRS.

### 3.4.4 CCT

Following Meyer et al. (2004), a cirrus cloud with a cloud-top height of 10 km and optical thicknesses of 0.5, 1, and 3 was modelled. The cirrus consists of hexagonal particles. The corresponding irradiance spectra within the $O_2$ A-band are shown in Figure 48. As the optical thickness increases, the downwelling irradiance at the surface decreases due to stronger extinction (enhanced scattering and, to a lesser extent, absorption) and increased reflection back to space.

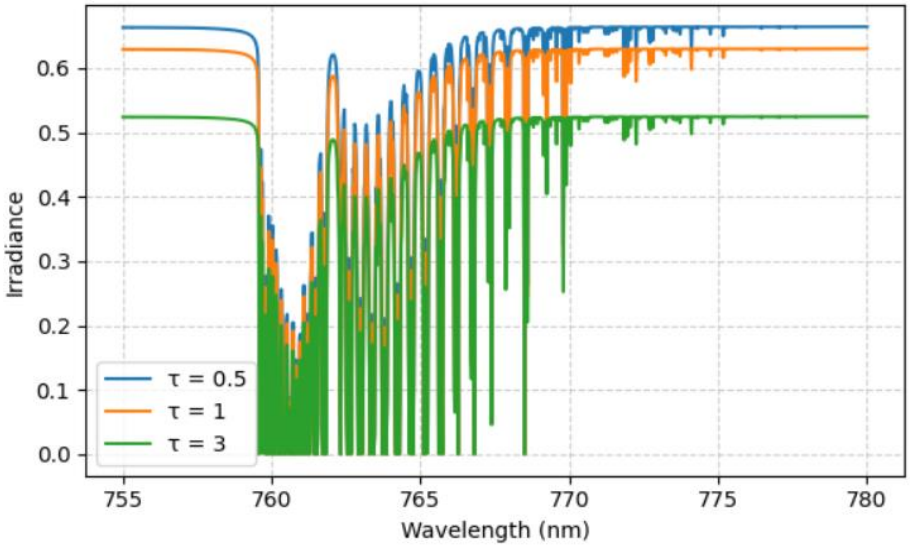


**Figure 48** $O_2$ A-band downwelling irradiance at the surface for different values of cirrus cloud optical thickness.

## 3.5 Climate Simulations

### 3.5.1 Overview

In order to synthesize the observations-based results and to explore the large-scale implications of the perturbations in stratospheric aerosol, in marine low-level clouds, and in cirrus, simulations are conducted with the state-of-the-art atmospheric general circulation model ICON (the ICOsahedral Non-hydrostatic model, Hohenegger et al., 2023).

While in principle, the science question of synthesis might be addressed by different atmospheric general circulation models as well (e.g. the Community Earth System Model, CESM), there is a strong rationale for choosing ICON. It is a model system that seamlessly allows to simulate limited-area and global domains, and that allows for resolutions between hectometers and order of 100 km (albeit with somewhat varying physics choices). In addition, the model has been used before to study the climate impacts of cloud- and aerosol perturbations (Dipu et al., 2021).

The aim is to quantify the implications of perturbations for case studies with perturbations to the aerosols and/or clouds at sub-seasonal to seasonal time scales. Sea surface temperatures (SST) and sea ice concentrations are pre-scribed to isolate the effects on atmospheric processes and land surfaces, consistent with an assessment of the effective radiative forcing, thus the radiative forcing as well as adjustment mechanisms (Quaas et al., 2024).

In the simulations, stratospheric aerosol concentrations and properties (for testing SAI), low-level cloud water content and droplet number concentrations (for testing MCB), as well as cirrus water content and ice number concentrations (to test CCT) were perturbed following the approaches developed by Dipu et al. (2021).

The model is set up for simulations at the German Climate Computing Centre (Deutsches Klima-Rechenzentrum, DKRZ) and prepared for the simulations.

### 3.5.2 SAI simulations

The satellite-observed stratospheric AOD perturbations for the case of the Ruang volcanic eruption (April 2024), were reproduced in the ICON simulation to evaluate the global impacts of SAI. The observed monthly area-averaged AOD perturbations over the tropical region between 20°S and the Equator, together with the corresponding aerosol layer top and bottom heights, from August 2024 to September 2025, were used as inputs to the ICON model (Figure 49). A pair of global simulations with a horizontal resolution of 160 km (R2B4 triangular grid refinement of the hexagonal grid) was performed for the period July 2024 – September 2025, with the first month used as spin-up time. The control simulation was initialized using current weather conditions obtained from the European Centre for Medium-Range Weather Forecasts (ECMWF) reanalysis. The perturbed simulation incorporates height-resolved AOD perturbations over the

region between 20°S and the Equator, using climatological single-scattering albedo and asymmetry parameters for sulfate particles calculated from the Optical Properties of Aerosols and Clouds (OPAC) database. Differences between the perturbed and control simulations are used to analyze the consequences of SAI.

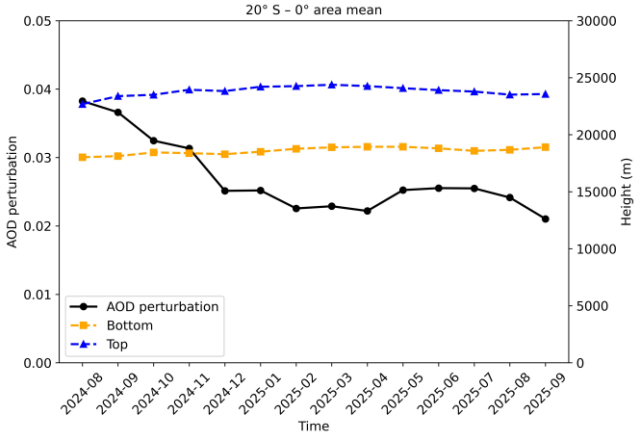


**Figure 49** Time series of the monthly satellite-observed area-averaged AOD perturbations (black line) over the tropical region between 20°S and the Equator, and the corresponding aerosol layer top (blue line) and bottom (yellow line) heights. The time is from August 2024 to September 2025.

### 3.5.3 MCB simulations

The satellite-observed ship-affected marine cloud perturbations were reproduced in the ICON simulation to evaluate the global impacts of MCB. Pairs of global simulations with a horizontal resolution of 160 km (R2B4 triangular grid refinement of the hexagonal grid) were performed. A control simulation was initialized using the current weather conditions, as obtained from the European Centre for Medium-Range Weather Forecasts (ECMWF) re-analysis. One perturbation area was defined in the Northeast Atlantic (24° to 45°N, 33° to 8°W, over ocean, see Figure 50) for the period from 6 August to 31 August 2024, after five days of as spin-up time. In the perturbed simulation, the liquid water path was increased by 1%, as suggested by observations over the region of interest. As discussed later in Section 4.2, this perturbation, which is inferred from the observations-based analysis, yields a signal that is small compared to the internal variability of clouds. In a second perturbation in the same setup, thus, the liquid water path was increased by a much stronger perturbation, a factor of 10. Also, a second perturbation area was defined in the Eastern Mediterranean (30° to 40°N, 10° to 30°E, over ocean), for a case study 21 – 31 August 2024, consistent with the observations analysis in the first step that lead to the initial perturbation simulations conducted after this first co-design of the simulations. The perturbed simulation increased the liquid water content of low-level clouds over the region of interest. This assumed again a strong increase in liquid water path, by a factor of 10, assuming an effective cloud seeding response.

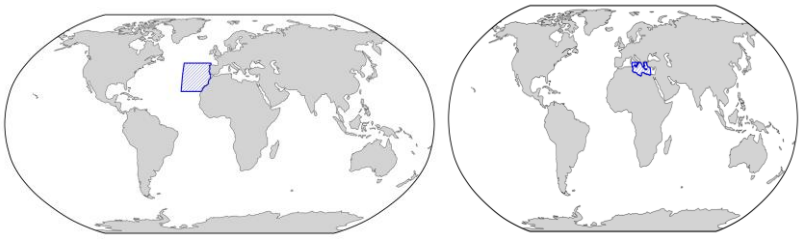

**Figure 50** Sensitivity study for MCB with the ICON model (left) perturbation domain in the Northeast Atlantic (blue outline), (right) perturbation domain in the Eastern Mediterranean.

### 3.5.4 CCT simulations

For the assessment of ICON simulation for CCT, making use of the analogue of the COVID lockdown, a perturbation in the region of Europe (latitude 35° – 60°N, longitude 15°W – 15°E; Figure 51) is defined. In this study area, ice crystal number were reduced by 12% in 2020 compared to 2019, as obtained from the observations delivered by the team at DLR. A pair of global simulations with a horizontal resolution of 160

km (R2B4 triangular grid refinement of the hexagonal grid) was performed. A control simulation was initialized using the current weather conditions, as obtained from the European Centre for Medium-Range Weather Forecasts (ECMWF) re-analysis.

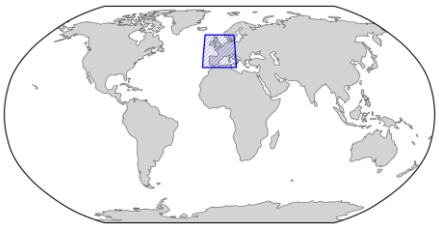

**Figure 51** Perturbation domain for the CCT case.

# 4. Scientific & Risk Assessment and Roadmap

This chapter provides the scientific analysis of all investigated SRM mechanisms, the radiative and climate impact assessment as well as a risk assessment .

## 4.1 SAI mechanism

### 4.1.1 Scientific Analysis

According to Suhedro et al. (2025), the eruption of Mount Ruang in April 2024, followed a 6.5 magnitude earthquake and unfolded in three eruptive phases. Phase 1 eruption (April 16–17) produced plumes that reached up to ~12 km in altitude, widespread fine ash dispersal; releasing approximately 0.1 Tg of $SO_2$. Phase 2 (April 18–28) consisted of smaller explosions with low plume heights (0.2–1.2 km) and minimal emissions. Phase 3 (April 30) was a stronger eruption, generating a ~19 km plume, intense lightning, fire fountains, and emitted approximately 0.3 Tg of $SO_2$, bringing the total sulfate emissions to ~0.4 Tg. Both major phases produced abundant very fine ash (median grain size ~26–29 um). The combined injection of fine ash and substantial $SO_2$ allowed for extensive dispersion, with sulfur dioxide reaching Africa by mid-May 2024. According to the Global Volcanism Program, the Volcanic Explosivity Index (VEI) assigned to the Mount Ruang eruption in April 2024 is VEI 4 ([URL31]). Khaykin et al. (2026) also document the evolution of the eruption an stratospheric perturbations in terms of the AOD, utilizing observations from ATLID, supplemented by limb-viewing sensors (e.g., OMPS-LP and SAGE III) and ground-based lidar measurements. According to their study, the enhancement in stratospheric AOD doubled the background tropical load and increased the values in extra-tropical regions by a factor of ~1.8 for several months. Dodangodage et al. (2025), determined the composition and size of the stratospheric sulfate aerosol particle using measurements of the Atmospheric Chemistry Experiment (ACE). According to retrievals performed by fitting the infrared transmission occultation spectra of ACE-FTS imager, Ruang emissions consisted of about 64 % (by weight) sulfuric acid, and the particles had an average median radius of 0.127 µm. Silicate features from volcanic ash were observed by ACE only in the very young plume and no indications for enhanced H2O mixing ratios were reported. As derived from ATLID data herein, but also shown in Khaykin et al. (2025), by the end of 2025, the stratospheric AOD had not yet returned to the pre-eruption levels, suggesting the lifetime of Ruang aerosol in the stratosphere of at least 16 months.

The analysis performed in the context of the *ACtIon4Cooling* project using ATLID lidar data, reveals that in the earlier months after the eruption (e.g. around August 2024 – four months after the eruption), the highest AOD recorded in the stratosphere between +/-25 degrees in latitude, was close to 0.06 at 0.355 nm, while linear depolarization values did not exceed 0.10 in most cases, with a mean value of ~0.07 (see Figure 52 Figure 53). This is consistent with the findings reported from previous studies, that the primary product of Ruang eruption were spherical particles of sulfuric nature that do not depolarize the lidar emitted radiation. Any depolarization signature must come from sub-micron ash particles remaining in the stratosphere or particles formed by coagulation of sulfates on ash. It is wort mentioning that throughout the period examined (August 2024 – September 2025), there seems to be negligible change in depolarization values while the maximum AOD slowly drops close to 0.04, revealing also a very slow removal of the particles from the stratosphere.

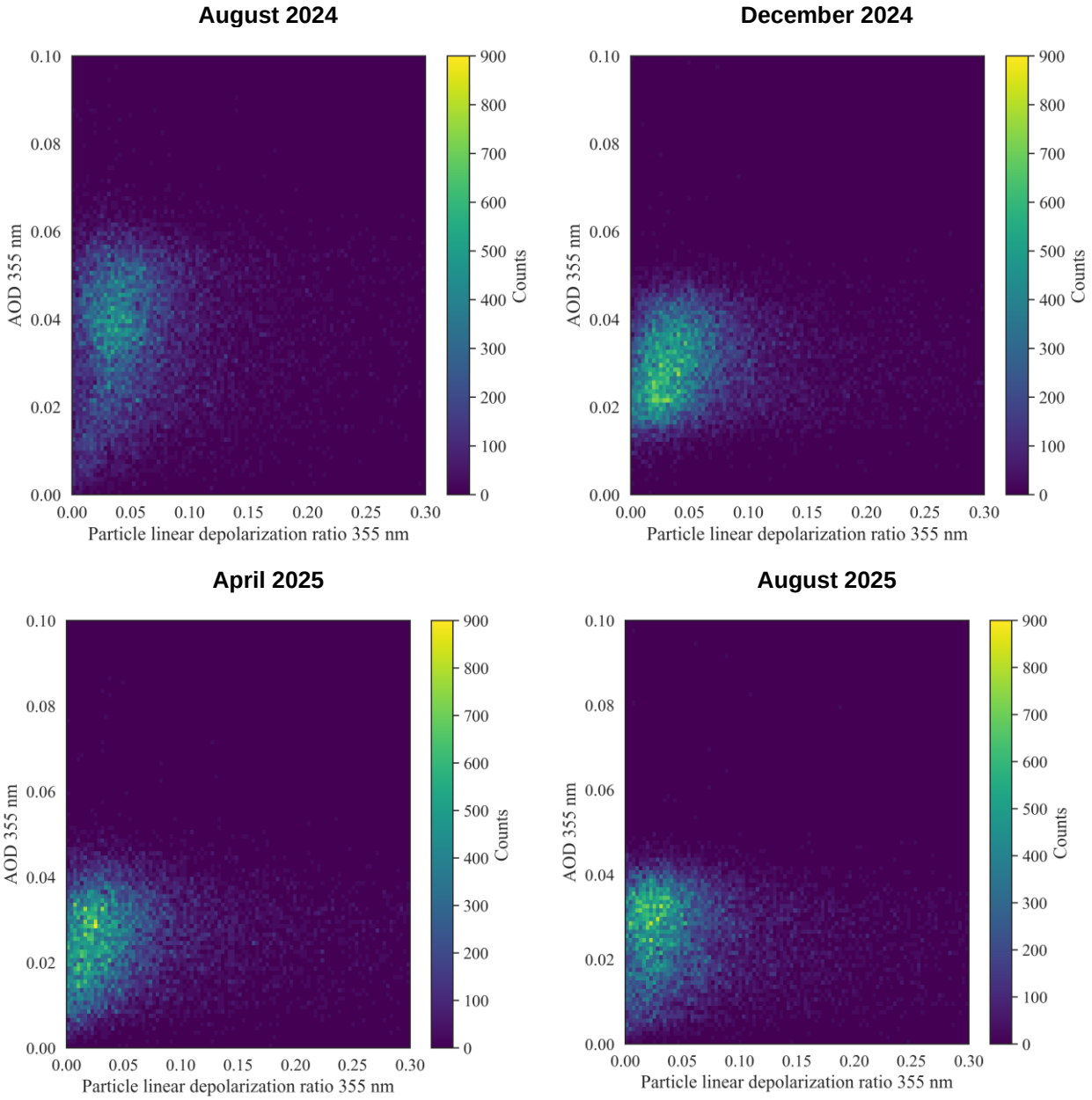


**Figure 52** Frequency distribution of AOD versus particle linear depolarization values at 0.355 um for August 2024 (upper left), December 2024 (upper right), April 2025 (bottom left) and August 2025 (bottom right).

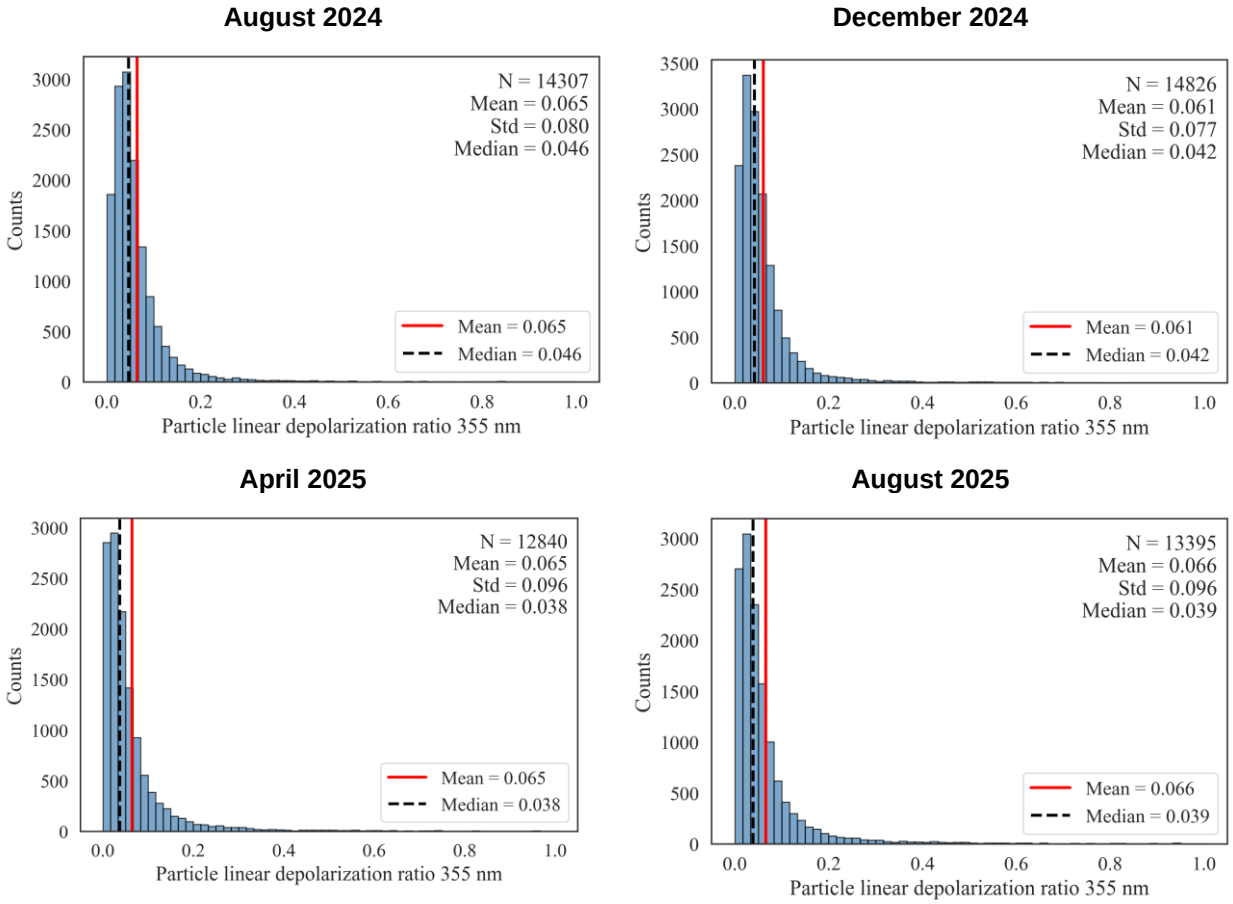


**Figure 53** Frequency distribution of the particle linear depolarization values at 0.355 um for August 2024 (upper left), December 2024 (upper right), April 2025 (bottom left) and August 2025 (bottom right). Depolarization is almost constant throughout the period of the study

Regarding the vertical distribution of the Ruang layers in the stratosphere, an ascending phase until April 2025 is observed, which is also consistent with the findings of Khaykin et al. (2025). After injection at ~19–25 km, the Ruang aerosol layer continued to ascend further within the tropical stratosphere over several months, likely driven by diabatic ascent through the Brewer-Dobson circulation (BDC); while aerosols advected poleward into extratropical regions underwent subsidence to lower stratospheric heights. Nevertheless, no hard conclusions can be drawn at this stage at least regarding the stratospheric layer top derived from ATLID L2 data, driven by an artifact that seems to be present close to 20 km in altitude, where the vertical resolution of the measurements changes from 100 to 500 m (see Figure 55).

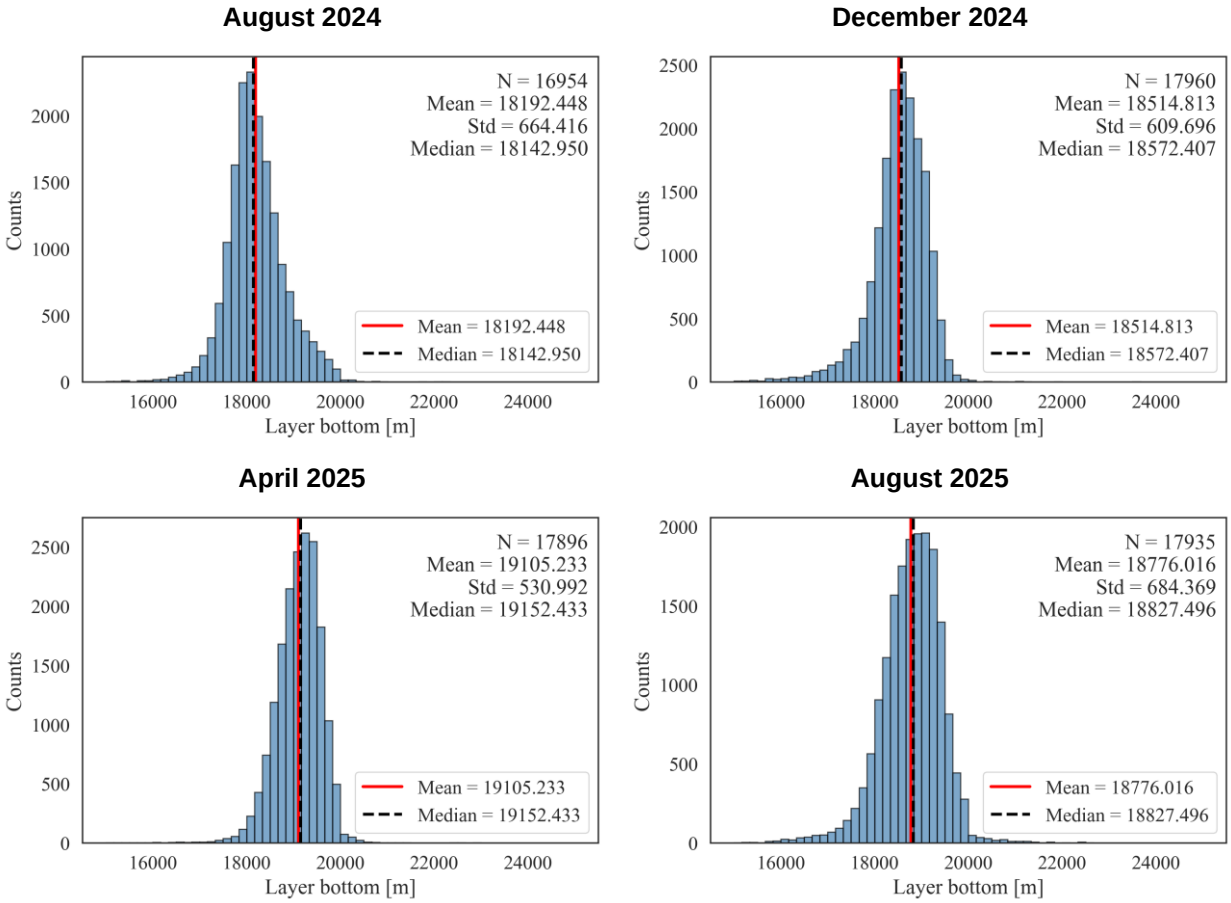


**Figure 54** Same as Figure 53, but for the stratospheric layer bottom

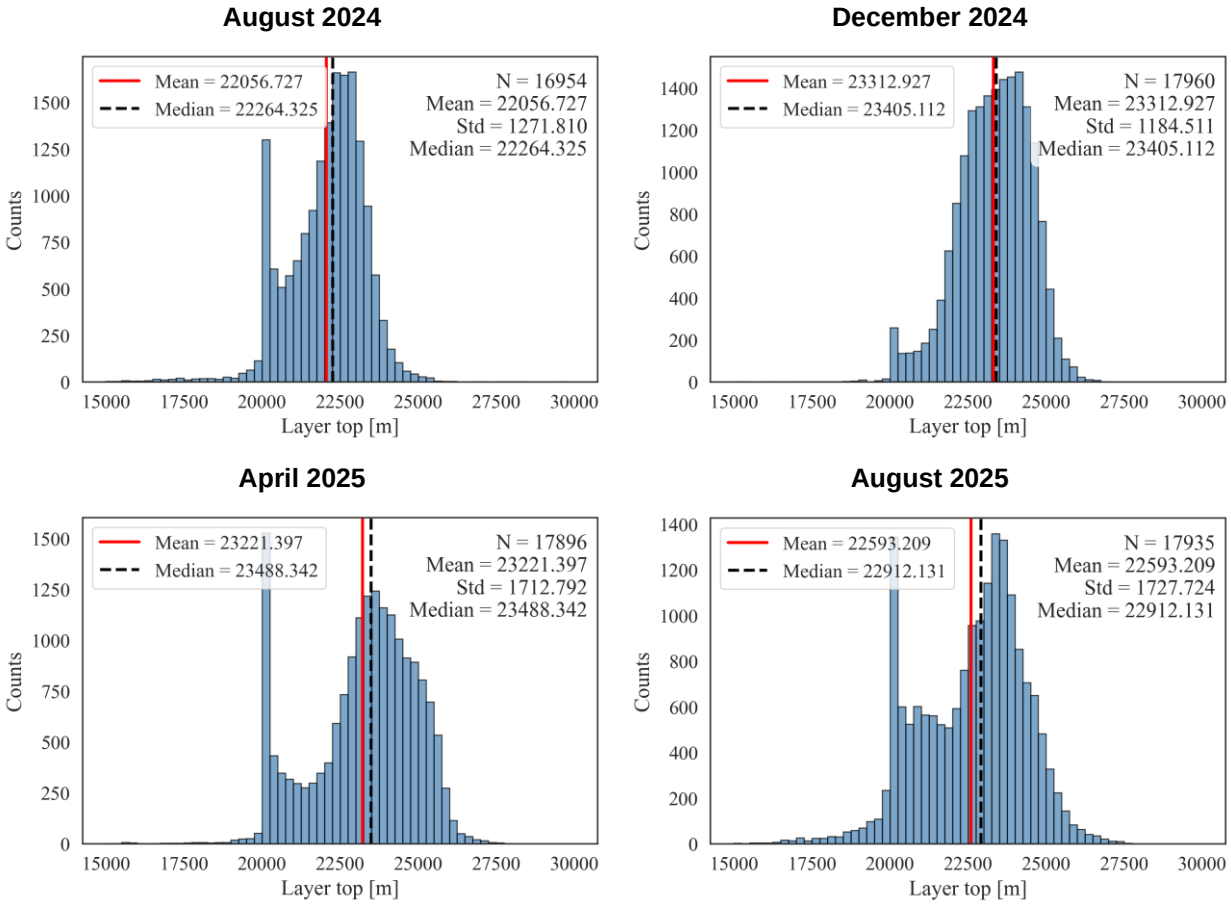


**Figure 55** Same as Figure 54, but for the stratospheric layer top

One key scientific and technical aspect highlighted within the *ACtIon4Cooling* project, is the advancement of stratospheric aerosol property retrievals above liquid clouds through the synergistic use of EarthCARE ATLID lidar and PACE HARP2 polarimetric observations, extending methodologies originally developed for tropospheric aerosols and coincident A train observations (Wanquet et al., 2009, 2013). Previous studies (e.g., Robock, 2015) indicate that the variability of stratospheric aerosol particle size following volcanic injections remains a major open question in current stratospheric-aerosol research. Given the substantial differences in particle size estimates reported across the limited number of available studies (McLinden et al., 1999; Bingen et al., 2003, 2004a, b; Deshler et al., 2003; Bourassa et al., 2008; Deshler, 2008; Malinina et al., 2018; Ugolnikov et al., 2018; Zalach et al., 2019), it is evident that particle size parameters of stratospheric aerosols, even under background conditions, remain poorly constrained. Cur-rent state of the art methods to derive particle size in the stratosphere include solar occultation measurements (e.g. Wrana et al. 2021), from which the median radius and mode width of the size distribution can be derived from multi wavelength extinction ratios. Although the technique benefits from the broad spectral coverage of the solar occultation data, it has been demonstrated that the particle size estimates have a tendency to be systematically overestimated compared to retrievals based on other methods like active remote sensing (e.g. aerosol size retrievals from backscatter lidar measurements. Overall, aerosol size retrievals from optical measurements are inherently sensitive to assumptions about the particle size distribution and measurement geometry, and systematic differences can arise when the assumed shape of the distribution is different compared to the reality (e.g. mono-modal assumptions versus bimodal real size distributions).

The method presented herein, derives aerosol optical depth (AOD) and effective radius of stratospheric particles, above liquid clouds by exploiting collocated, polarimetric active and passive remote sensing observations. This approach has the potential to provide spatially resolved retrievals that complement the high vertical resolution but limited horizontal sampling of solar occultation methods in the stratosphere.

Potential sources of uncertainty in the applied method include: (i) Instrumental noise: as HARP2 polarized radiances currently exhibit high noise levels, it was necessary to re-sample to retain only half of the original viewing angles. However, for future applications this needs to be performed with caution, as only certain viewing and scattering angles are informative for above cloud aerosol retrievals, particularly those sensitive to aerosol scattering effects. Insufficient angular sampling reduces the sensitivity of the method to certain aerosol features and contributes to retrieval error. (ii) Heterogeneity in cloud microphysical properties, which could unmask potential 3D cloud radiative effects that propagate into the aerosol retrievals. Indicatively, for homogeneous cloud scenes, comparisons of plane parallel with 3 D radiative transfer modeling indicate errors of the order of 4–8 %, introducing uncertainty into the simulated radiances used for the retrieval (Wanquet et al., 2013). (iii) Limited sensitivity of the polarized signal to certain aerosol species, particularly coarse-mode particles and non-spherical aerosols (i.e. volcanic ash in the stratosphere), whose scattering contributes weakly to the observed polarization, as well as uncertainties in the assumed refractive index; (iv) Uncertainties in cloud properties (e.g. droplet size distributions, optical thickness, or vertical variability) that propagate into the aerosol retrievals. Any mis-representation of the cloud component introduces additional uncertainty. (v) Dependence on a priori assumptions for aerosol size distribution and optical properties, which may not accurately represent the true aerosol population above clouds. (vi) Temporal mismatch between EarthCARE and PACE overpasses. Due to the fact no vertical information are available at the time of the PACE overpass, strict filtering of HARP2 data was re-quired to minimize the likelihood of other aerosol types being present in the column between the liquid clouds and stratospheric layers, resulting in only a few HARP2 pixels left in a certain scene to attempt the retrieval. Additional technical considerations include the operational use of a radiative transfer model to simulate cloud-polarized radiances, whereas, as demonstrated by Wanquet et al. (2013), off-line calculations across multiple observational geometries and cloud conditions improve retrieval performance. Taken together, these factors contribute to the overall retrieval uncertainty and must be quantitatively assessed to ensure robust estimation of stratospheric aerosol properties.

Despite the aforementioned challenges, the comparison between HARP2 and ATLID lidar derived AOD revealed satisfactory agreement for the case study of Ruang eruption, indicating that passive polarimetric retrievals can meaningfully enhance current knowledge of stratospheric aerosol size and optical properties. This enhancement is significant not only for validating radiative transfer models and quantifying aerosol radiative impacts but also for guiding future observational strategies, such as improved scattering property databases and joint active-passive retrieval frameworks that reduce uncertainty propagation and improve the characterization of volcanic aerosol layers relative to state-of-the-art methods.

### 4.1.2 Impact Assessment

#### 4.1.2.1 Radiative Impact

To assess the radiative impact of the SAI mechanism, a sensitivity analysis of TOA and BOA irradiances was performed with respect to perturbations in stratospheric AOT. As a case study, aerosol conditions representative of the Ruang eruption were considered.

The stratospheric AOT perturbations are prescribed from EarthCARE/ATLID lidar data as described in Section 3.1.1. Aerosol microphysical properties are defined consistently with volcanic sulfate aerosols. The stratospheric effective particle radius $r_{eff}$ was derived from EarthCARE and PACE collocated observations, in combination with optical modeling and radiative transfer simulations. The complex refractive index corresponds to sulfate particles at 0% relative humidity from the OPAC database (*suso00* dataset [URL30]). All radiative transfer calculations are performed spectrally over the wavelength range 0.4–2.5 µm with a spectral resolution of 0.01 µm. The solar zenith angle is fixed at SZA = 0 degrees in order to isolate intrinsic radiative sensitivity without geometrical modulation.

The computations are performed in two stages: At step 1, radiative transfer simulations are carried out on a coarse AOT grid to determine the dependence of irradiances ($E$) on AOT. At step 2 the resulting irradiance vs. AOT relationship is interpolated onto a finer AOT resolution, enabling accurate estimation of derivatives d$E$/dAOT. This approach reduces computational cost while preserving spectral accuracy.

For a perfectly absorbing surface (ground albedo = 0), increasing AOT increases the effects of multiple scattering and hence produces the expected redistribution between direct and diffuse components, namely, diffuse irradiance $E_{dif}$ increases, while direct beam irradiance $E_{dir}$ decreases. In particular,

- at BOA $dE_{dif}/dAOT \approx +350\ W\,m^{-2}$ per unit AOT, $dE_{dir}/dAOT \approx -500\ W\,m^{-2}$ per unit AOT. The strong negative sensitivity of the direct component reflects exponential attenuation of the solar beam. The diffuse increase is driven by enhanced multiple scattering.
- at TOA $dE_{dif}/dAOT \approx +63\ W\,m^{-2}$ per unit AOT. The positive TOA sensitivity indicates that additional scattering redirects radiation upward.

For a moderately reflective surface (albedo = 0.3), the BOA sensitivities remain nearly unchanged, namely,

- at BOA $dE_{dif}/dAOT \approx +350\ W\,m^{-2}$ per unit AOT and $dE_{dir}/dAOT \approx -460\ W\,m^{-2}$ per unit AOT. Thus, surface albedo does not significantly alter the perturbation of downwelling irradiance at the surface.
- at TOA $dE_{dif}/dAOT \approx -17\ W\,m^{-2}$ per unit AOT.

Here, the sign reverses relative to the zero-albedo case. This reflects the interplay between aerosol scattering and surface reflection.

The results indicate that the radiative impact of SAI is not uniform but strongly modulated by underlying surface albedo. Over dark surfaces (e.g., ocean) increasing AOT effectively masks a low-albedo surface. The enhanced aerosol scattering increases upward radiation at TOA. Over bright surfaces aerosol layers intercept radiation that would otherwise be reflected upward by the surface. Part of this radiation is absorbed or redirected downward, reducing TOA outgoing irradiance. That implies that there exists a ground albedo, such that aerosol-induced scattering and surface-reflection feedback compensate each other. This transition marks a regime shift in the aerosol radiative effect.

Figure 56 and Figure 57 show the irradiance values at BOA and TOA for ground albedo 0 and 0.3, respectively.

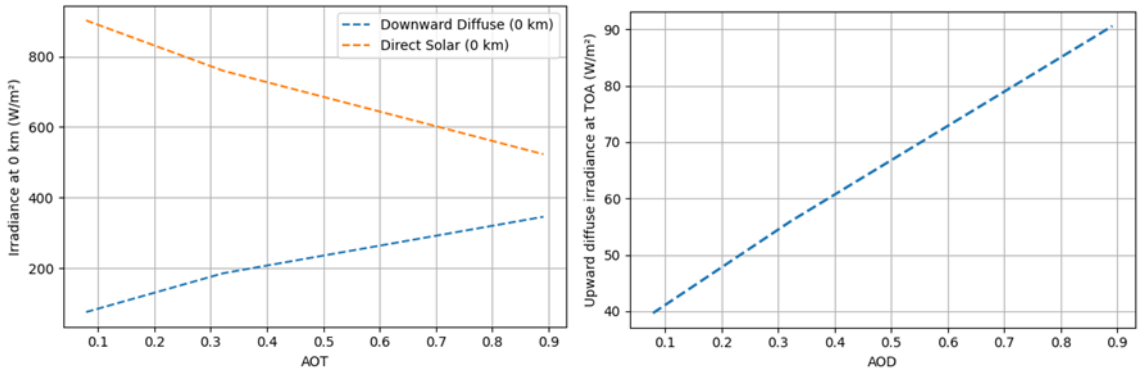


**Figure 56** Irradiances at BOA and TOA as functions of AOT. Gound albedo 0

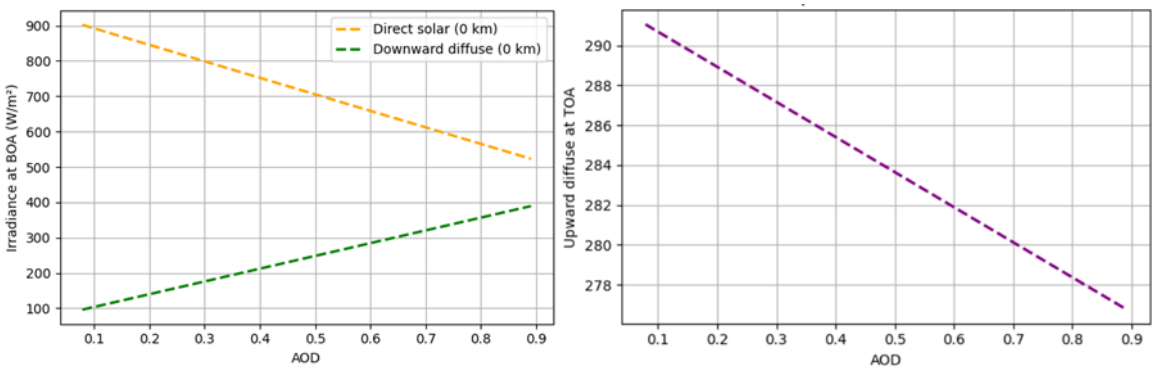


**Figure 57** Irradiances at BOA and TOA as functions of AOT. Ground albedo 0.3

Having such assessment, the perturbations in AOT can be transformed into related radiative forcing. Figure 58 shows examples of radiative forcing distributions at several months in 2024 and 2025 when the changes in stratospheric AOT and background particle properties are derived from EarthCARE and PACE data.

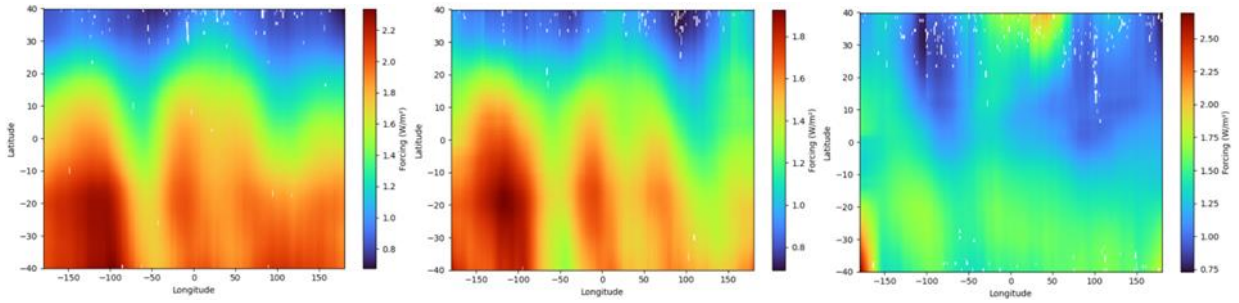

**Figure 58** Radiative forcing due to perturbation in AOT caused by Ruang eruption: November 2024, January 2025 and June 2025

#### 4.1.2.2 Modelling synergy: Results and consequences for ERF

A clear reduction in the clear-sky TOA downward radiative flux is found over the perturbed region (left panel of Figure 59), with a mean perturbation of −1.89 W m-2 between 20°S–0°, largely attributable to reflection by the implemented aerosol layer. Additional clear-sky TOA effective radiative forcing perturbations are observed outside the perturbed region, primarily over North America, Tibet Plateau, and the Arctic. These perturbations are mainly driven by changes in surface albedo associated with snowfall and sea ice, as evident from the surface albedo perturbations shown in the right panel of Figure 59.

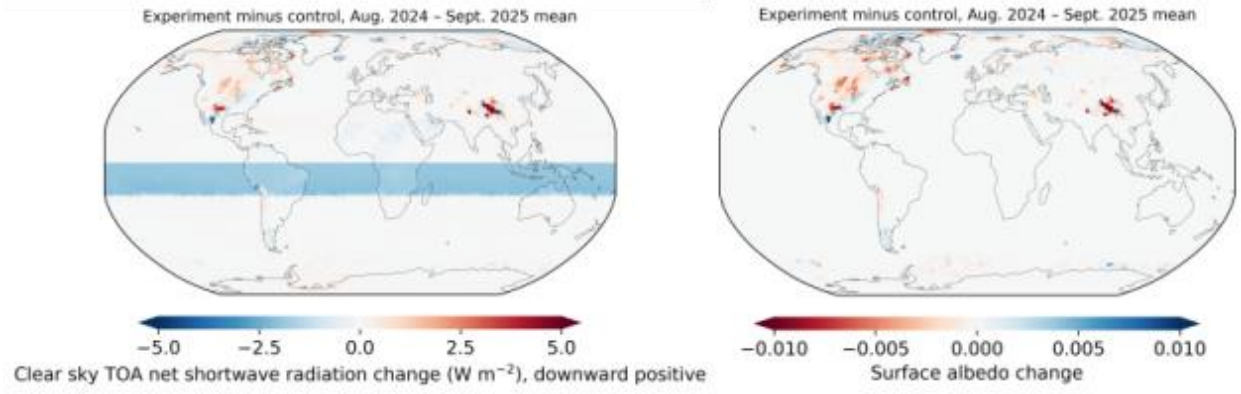


**Figure 59** Time-mean responses to SAI from August 2024 to September 2025. Left: perturbation of clear-sky top-of-atmosphere downward radiative flux. Right: surface albedo response.

The perturbation of the TOA radiative flux (effective radiative forcing) is influenced by cloud adjustments, with a global mean change of 0.11 W $m^{-2}$ and a 20° S – 0° regional mean change of 0.79 W $m^{-2}$ (left panel of Figure 60). Land surface air temperature shows a global mean response of –0.02 °C and a 20° S – 0° regional mean response of –0.07 °C. Besides the mean continental cooling, surface air warming is observed in regions such as Russia and Antarctica (middle panel of Figure 60). Surface precipitation shows pronounced responses both outside the northern and southern side of the perturbed region (right panel of Figure 60), implying dynamics and thermodynamics adjustments. The average precipitation perturbation within 20°S – 0° is −0.03 mm $day^{-1}$, while the global average shows a slight positive response of 0.003 mm $day^{-1}$.

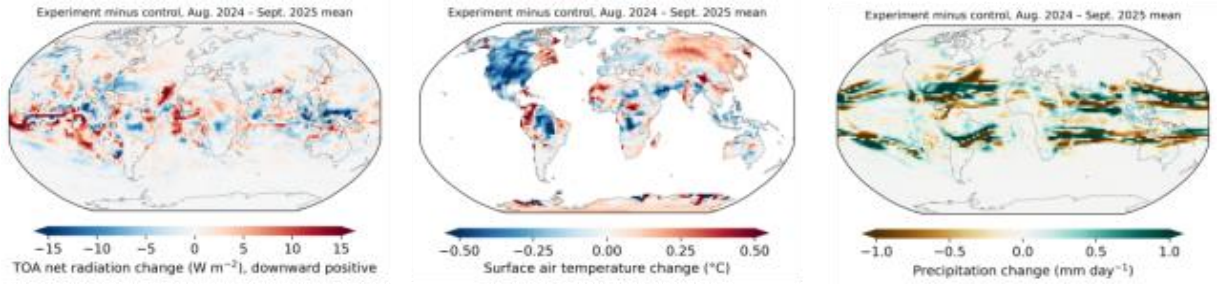


**Figure 60** Time-mean responses to SAI from August 2024 to September 2025. Left: perturbation of the top-of-atmosphere radiative flux (effective radiative forcing). Middle: response of land surface air temperature. Right: response of surface precipitation.

Global patterns of changes in cloud ice water path (IWP) tend to align more closely with precipitation changes because ice-phase clouds play a crucial role in precipitation formation (right panel of Figure 60). In contrast, changes in cloud liquid water path (LWP) are less correlated with precipitation, but LWP shows good agreement with effective radiative forcing (left panel of Figure 61). LWP represents the total liquid water content in clouds, this liquid water does not always directly convert into precipitation. Instead, LWP primarily influences cloud optical properties and radiative effects rather than precipitation process.

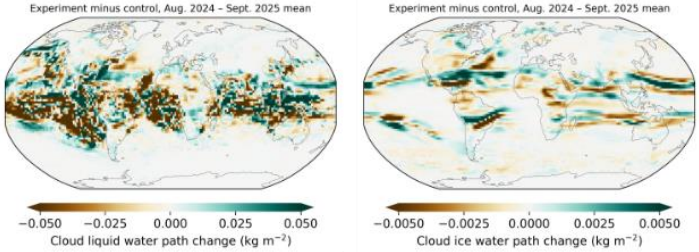


**Figure 61** Time-mean responses to SAI from August 2024 to September 2025. Left: response of cloud liquid water path (LWP). Right: response of cloud ice water path (IWP).

Figure 62 shows the response of atmospheric radiative heating, which is the difference between top-of-atmosphere and surface radiative fluxes. Atmospheric radiative heating or cooling alters the atmospheric internal energy, affecting temperature and humidity profiles, which in turn influence atmospheric stability and convection. Since precipitation is closely linked to convective processes and latent heat release, changes in the atmospheric radiative energy budget can partially explain the spatial and temporal changes in precipitation patterns. For example, an increase in net atmospheric radiative heating tends to enhance convection and precipitation, whereas a decrease can suppress them.

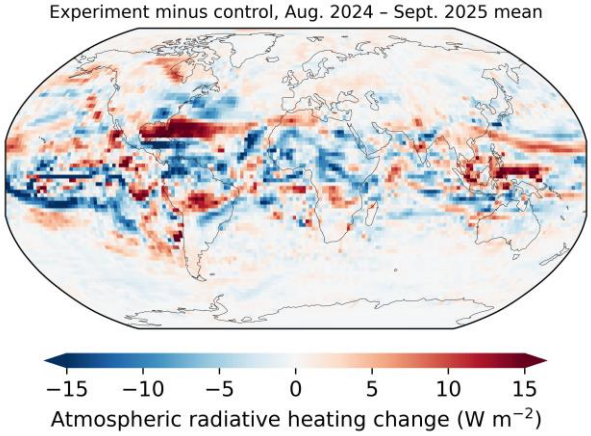


**Figure 62** Time-mean responses of atmospheric radiative heating (difference between top-of-atmosphere and surface radiative fluxes) to SAI from August 2024 to September 2025.

Precipitation response to SAI also shows some seasonal differences (Figure 63). During December-January-February (DJF), the impact is more pronounced outside the southern side of the perturbed region, whereas in June-July-August (JJA), it tends to impact the area outside the northern side more strongly. This is likely due to seasonal differences in circulation responses to SAI, warranting further detailed investigation.

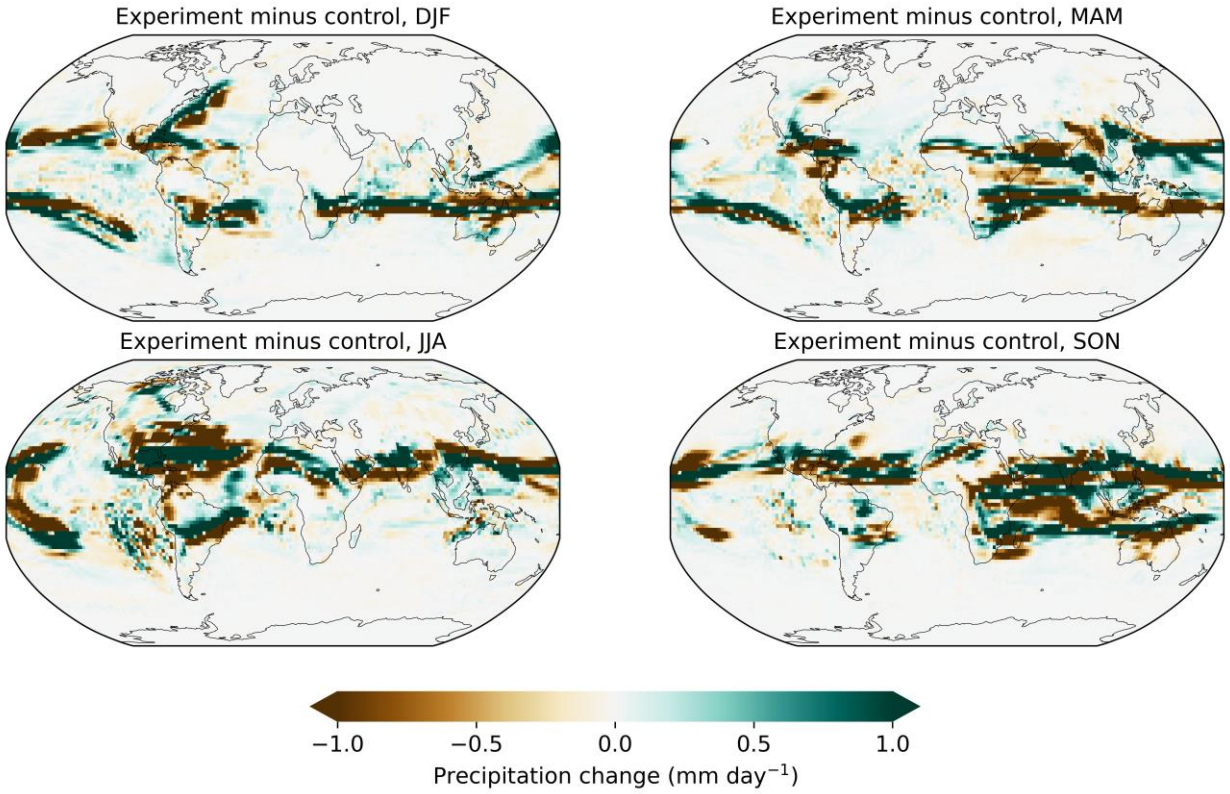


**Figure 63** Seasonal cycle of surface precipitation response to SAI for one year from October 2024 to September 2025. The four seasons are December-January-February (DJF), March-April-May (MAM), June-July--August (JJA), and September-October-November (SON).

### 4.1.3 Risks

The results presented in Section 4.1.2 highlight that the perturbations in stratospheric aerosol load due to the injection of volcanic particles (i.e. reflective aerosols of sulfuric nature) are spatially heterogeneous and show a clear correlation with surface albedo, cloud adjustments and dynamic circulation. This implies that the climate response to SAI would not be uniform, even if the changes in radiative forcing were negative on a global scale. Regional differences in ERF, temperature and precipitation patterns highlighted in Section 4.1.2.2 point to a redistribution of climate impacts rather than producing an overall global cooling, which is one of the main risks associated with SAI. In the perturbed tropical region, rainfall slightly decreases, while the global average change (positive) is very small. Such changes could disproportionately affect regions already vulnerable to drought extremes or monsoon variability (e.g. see Abiodun et al., 2021; Fu et al., 2025; Sun et al., 2020). Furthermore, the identified regime shift in TOA radiative response as a function of surface albedo (see Section 4.1.2.1) demonstrates that SAI impacts may reverse sign depending on underlying surface conditions, complicating predictability and governance.

Additional risks arise from uncertainties in the retrieval of aerosol microphysical properties and their evolution in the stratosphere. Retrieval uncertainties, limited sensitivity of the applied methodology and available measurements to coarse mode or non-spherical particles, and assumptions related to the particles' refractive index and size distributions propagate into radiative transfer simulations and radiative forcing estimates. If aerosol size or composition deviates from the assumed sulfate-dominated conditions (i.e. if in addition to sulfates, sub-micron ash particles, or smoke co-exists in the stratosphere) the radiative efficiency, lifetime, and heating rates could differ substantially from the case study examined. Any changes in stratospheric radiative balance can modify temperature gradients, potentially affecting circulation patterns, ozone

chemistry, and cloud formation. These uncertainties underscore that even modest misrepresentation of aerosol properties may lead to significant deviations in the predicted ERF and associated climate responses, thereby increasing the risk of unintended atmospheric and climatic consequences.

The ICON simulation, albeit short, shows a very strong precipitation response. A detailed analysis of the exact mechanisms has yet to be done, but it is evident that such very large consequences for precipitation patterns and intensity are a serious risk to be taken into account for SAI application, and even for any large-scale field experiments.

### 4.1.4 Outlook

Progress in SAI-related research will depend on consolidating process-level understanding through advances in observational capabilities, aerosol optical modeling, and coordinated model development. Of high priority would be the development of improved stratospheric aerosol characterization, explicitly accounting for the properties of sulfate, ash, increasing concentrations of stratospheric smoke particles due to large scale wildfire emissions, as well as their mixtures. This includes refined representations of particle size distributions, refractive indices, potential hygroscopic growth in case large amounts of water vapor injected into the stratosphere together with aerosol particles (Asher et al., 2023; Chen et al., 2025), aging processes, and absorption characteristics, ensuring that radiative transfer calculations more realistically capture stratospheric aerosol variability.

Also, the development of a joint ATLID-polarimeter operational retrieval scheme for the stratosphere, exploiting the synergy between EarthCARE's high-spectral-resolution lidar and multi-angle polarimetric observations (e.g., including also 3MI/MetOp-SG in future developments). Such synergistic retrieval frameworks will improve the discrimination between sulfate, ash and smoke layers, enhance the use of volcanic eruptions as natural analogues for SAI, and provide robust observational constraints for climate model evaluation. Together, these developments will enable more reliable assessment of SAI radiative impacts, reduce key uncertainties in aerosol-radiation interactions, establish a technically mature foundation for future research activities on stratospheric aerosol processes and provide the transparent, observation-based knowledge foundation required for informed international discussions on SRM-related risks and feasibility.

## 4.2 MCB mechanism

The MCB mechanism studied with the natural analogue of ship-tracks seems to have great potential. The ship-affected pixels are separated from the background pixels and a binary flag is introduced to classify them. The ship-affected pixels are separated from the background pixels using the threshold criteria {*vessel_density_threshold* = 10hkm$^{-2}$, *distance_threshold* = 10km}. The ship affected pixels are defined to be about 10 km far, which is comparable to the spatial resolution of TROPOMI footprints. The performance of the ML classifier is not sensitive to the distance threshold. The vessel density threshold is defined empirically based on the EMODnet histograms. The ship-track detection model has a poor performance if the vessel density threshold gets reduced too much, as the false negatives eventually increase. On the contrary, if the vessel density threshold increases that much, the imbalance of the training set for the ML classifier gets stronger.

The vessel density parameter illustrated in Figure 64, highlights the major shipping lines in the Mediterranean. It is clear that the shipping activity is maximum during the summer and decreases towards the winter with December being the month with the lower vessel density. Therefore, it is expected that most of the ship-tracks under this study are found in July-August-September where the vessel densities are large (see histograms of Figure 65).

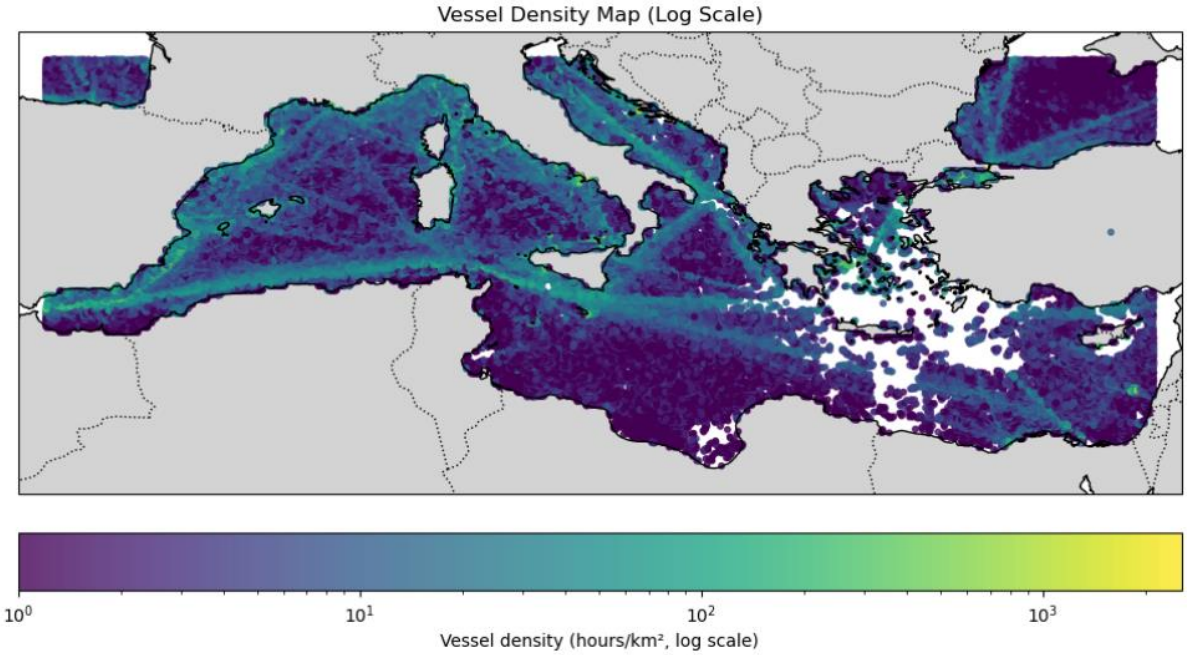


**Figure 64** EMODnet Vessel Density maps over the Mediterranean

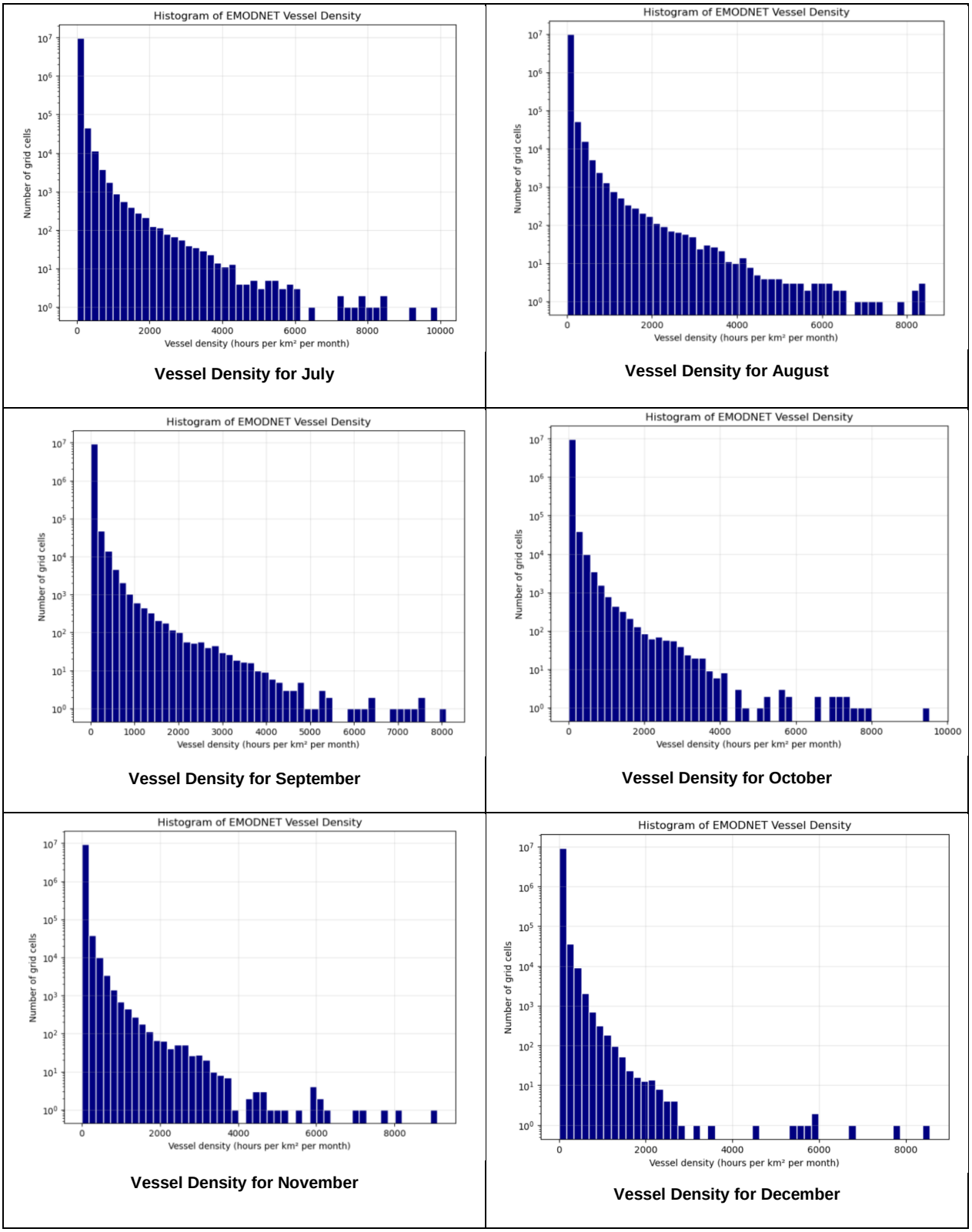


**Figure 65** Histograms of the EMODNET Vessel Density data per month in the period July-December 2024

The percentage of ship-contaminated pixels of Figure 66 verifies that ship-tracks are most probably detected during the summer months.

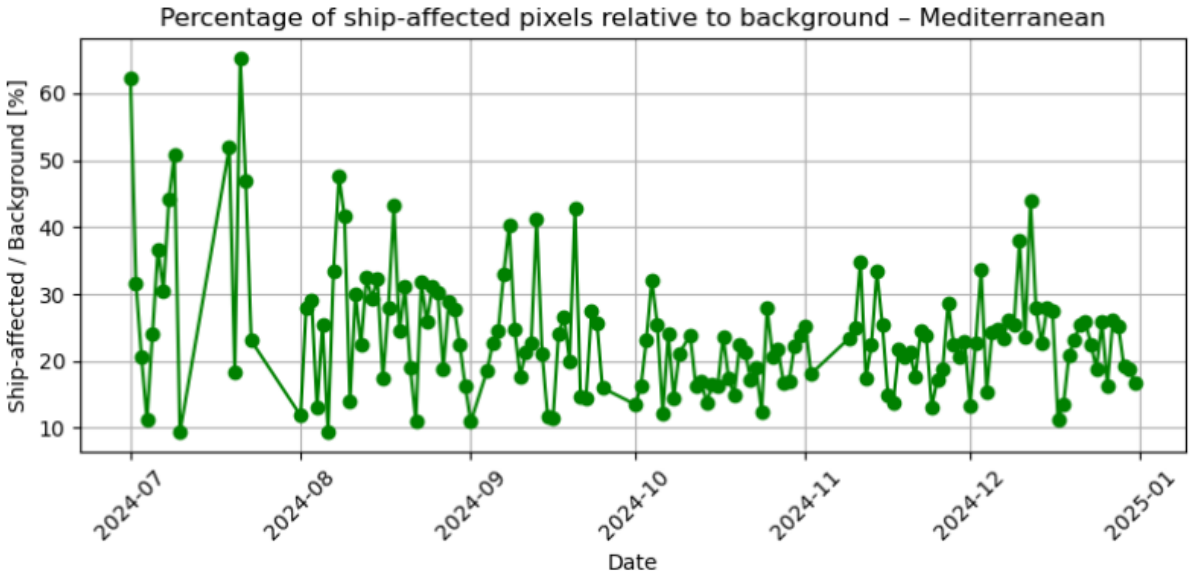


**Figure 66** Percentage of ship-affected pixels over the background pixels over the MED grid

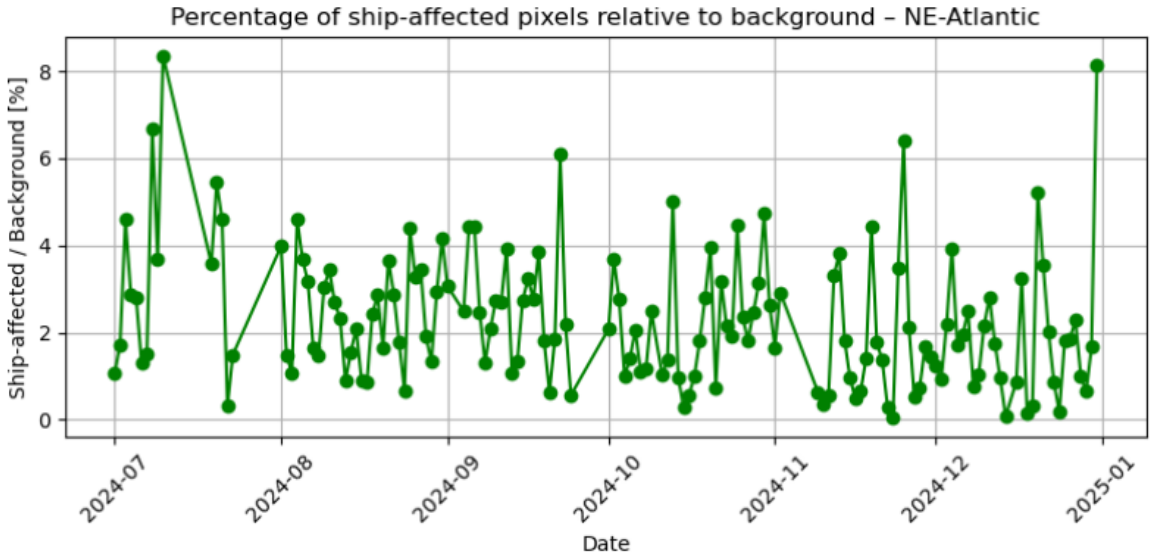


**Figure 67** Percentage of ship-affected pixels over the background pixels for the NEA grid

Based on the analysis for the 6 months of data (second half of 2024), the chances are higher to find ship-tracks over the Mediterranean than over NE-Atlantic (see Figure 67). This is quite expected as the EMODnet dataset refers to the European Seas and the Atlantic Ocean is only partly covered (and mainly near the coast). This limitation can be in future overcome if the actual AIS data are used instead of the aggregated monthly maps.

### 4.2.1 Scientific Analysis

#### 4.2.1.1 Analysis of the ship tracks over the NEA grid

The relative difference of the tropospheric $NO_2$ column is calculated as the regional mean perturbation for the ship-affected pixels over the background.

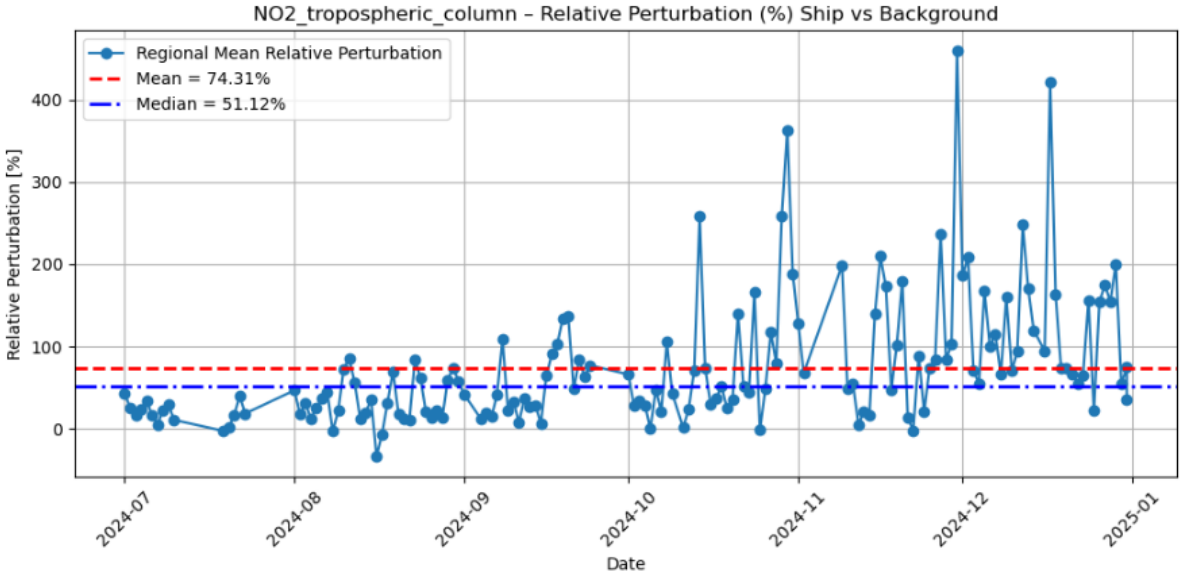


**Figure 68** Regional mean perturbations of the TROPOMI Tropospheric $NO_2$ columns for NEA grid

The daily perturbations of the tropospheric $NO_2$ column should be always seen together with the number of detected ship-tracks. As an example, the maximum perturbation for NEA seems to be on the 30-11-2024. However, when the actual number of ship-tracks is considered (which appears to be less than 2% from Figure 67), one could understand that the class “ship-affected” is underrepresented in this scene/day and no conclusions should be drawn. Another important aspect for this case is that the flagging of ship-affected pixels depends strongly on the threshold of vessel density (see Figure 69). Therefore, the detected ship-tracks do not lie on the most polluted shipping corridors and uncertainties are higher there. Such uncertainties can be minimized when actual AIS data are used.

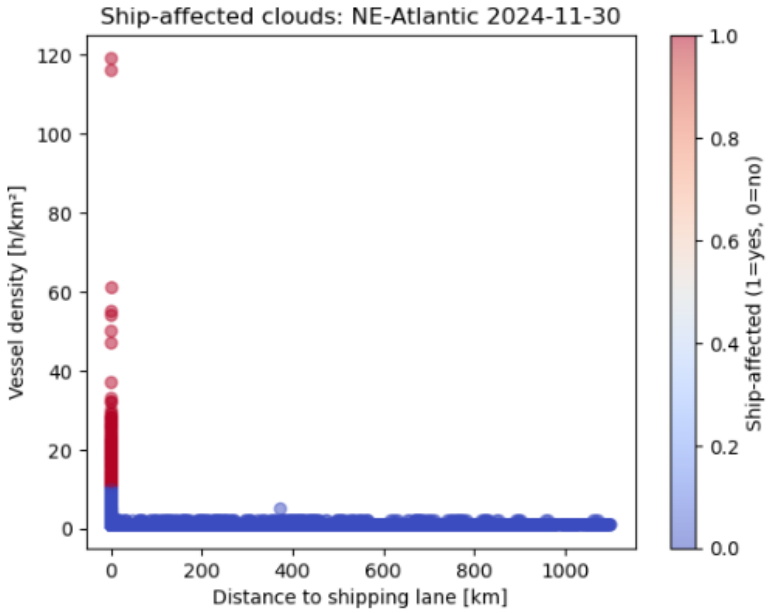


**Figure 69** Ship-track flagging for 30-11-2024 over NEA grid: the vessel density threshold strongly affects the classification

One more problematic issue is that many high-altitude clouds (Figure 70) are present in the scene and the ship-track clouds only appear far from the EMODnet shipping lines (see Figure 71).

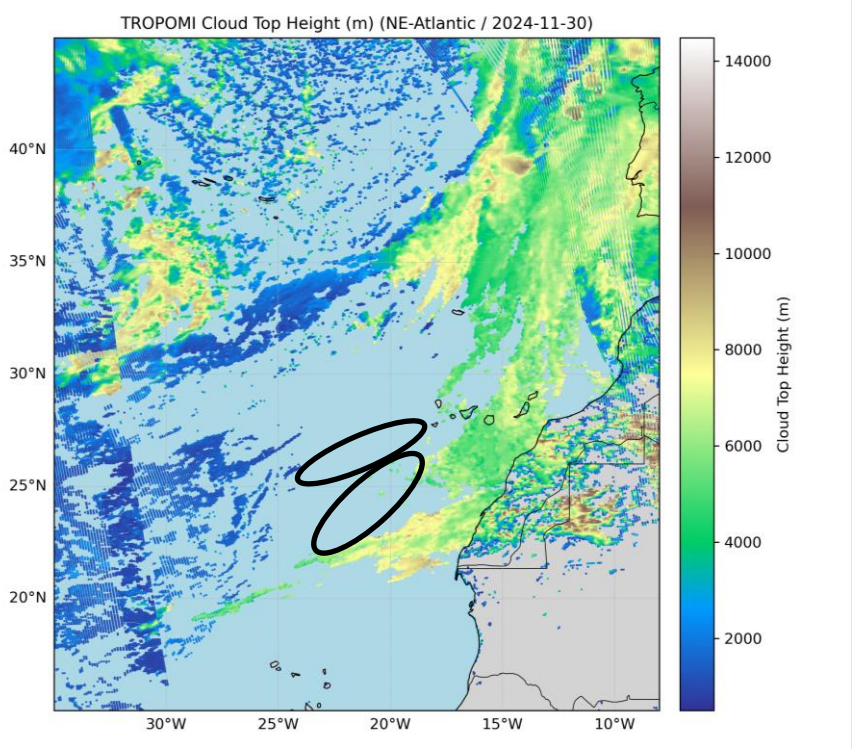


**Figure 70** TROPOMI Cloud Top Height for 30-11-2024 over NEA: the low clouds appear far from the shipping lines based on the EMODnet vessel density maps of Figure 71

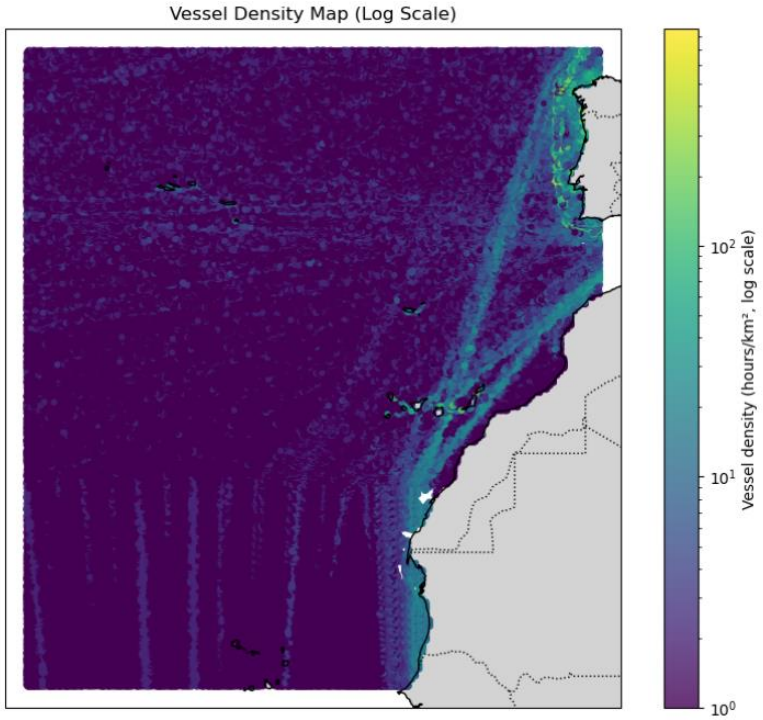


**Figure 71** EMODnet Vessel Density Map over NEA

Even though the capability to detect the ship-tracks in the NEA grid is limited due to the EMODnet vessel map restrictions, there are opportunistic occasions in which it is still possible to detect the ship-tracks with high confidence. Below is the scene of 18-09-2024 where the ship-tracks appear within the major

corridors for the NEA grid and a low background $NO_2$ pollution occurs. The increase of $NO_2$ tropospheric column due to ships is quantified to be about 100% (see Figure 68).

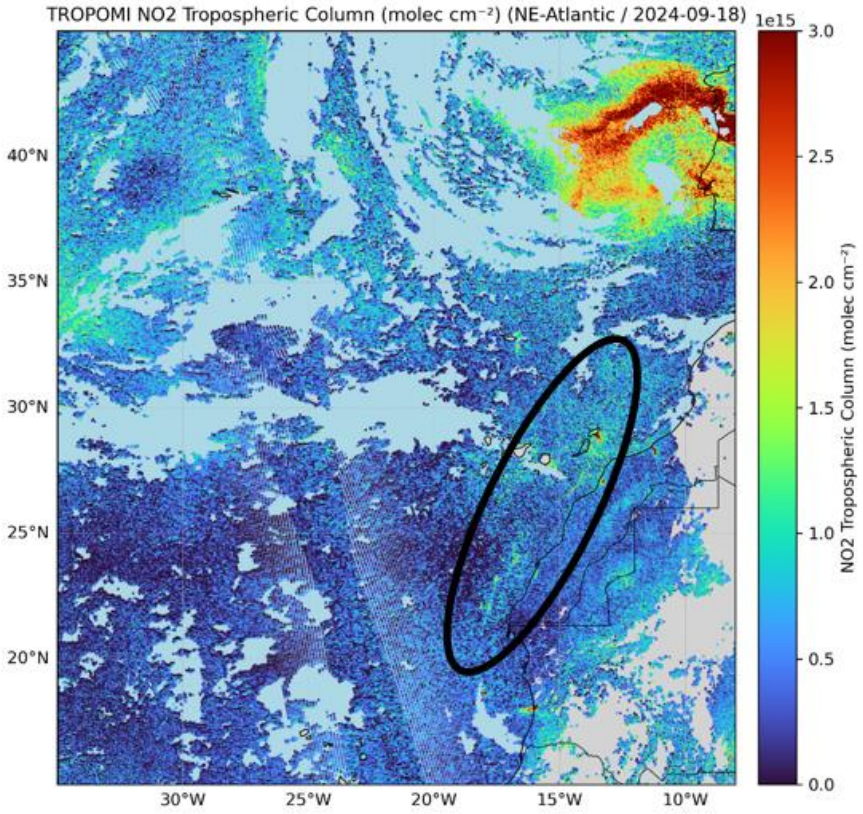


**Figure 72** TROPOMI $NO_2$ Tropospheric Column for 18-09-2024 over NEA

Detecting the individual ship tracks close to the shipping corridors in those conditions is possible. The retrieved cloud top heights from VIIRS agree quite well with the TROPOMI cloud top heights (see Figure 73). Both sensors capture the ship-affected cloud structure between 30–35°N. This is a cloud with a low cloud top height in the vicinity of likely terrestrial middle-level clouds. In such cloud inhomogeneous scenes, it is possible to detect the ship-tracks with higher confidence. Notice that the cloud structure does not appear at the $NO_2$ map as the retrieval of the $NO_2$ vertical column is not possible when there is a high cloud cover (i.e., for TROPOMI the threshold in the cloud fraction is 0.2). The TROPOMI cloud fraction map is presented in Figure 74, along with the VIIRS cloud top emissivity, which shows some spatial gradient within the cloud structure. The cloud perturbation is mostly captured at the liquid water content and cloud optical depth maps (see Figure 75). The ability to capture the cloud perturbation by VIIRS is advanced compared to TROPOMI alone, as the TROPOMI cloud optical thickness (see right panel of Figure 75) appears relative homogeneous within the cloud, with only some minor enhancement around 32°N.

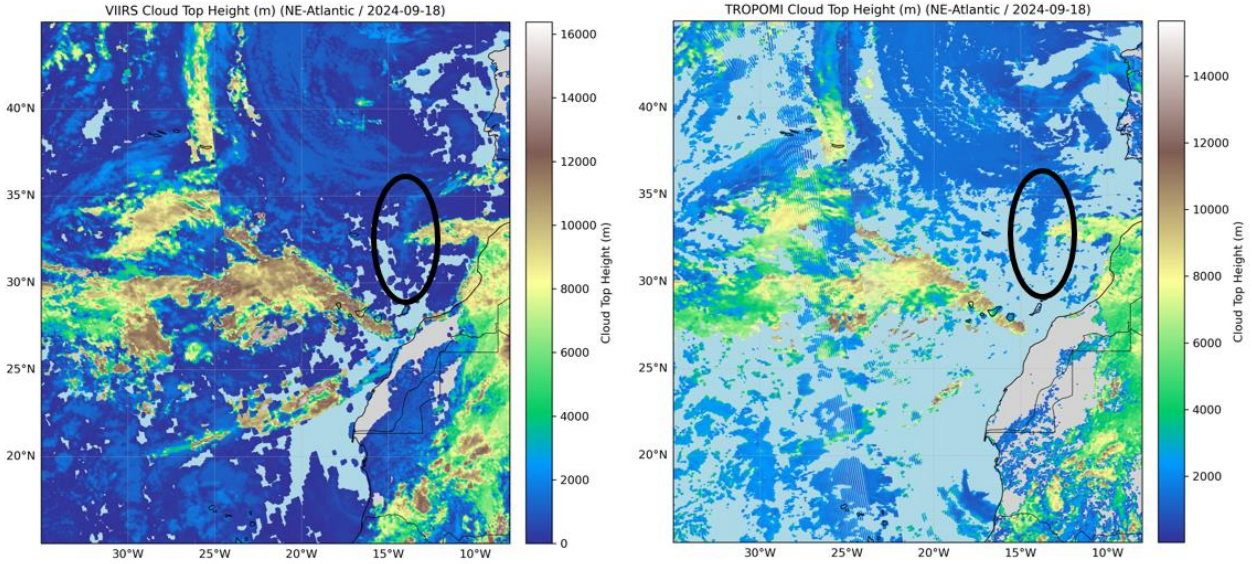


**Figure 73** VIIRS (left panel) and TROPOMI (right panel) Cloud Top Height for 18-09-2024 over NEA: ship-tracks appear with low cloud top heights (i.e., CTH < 2km)

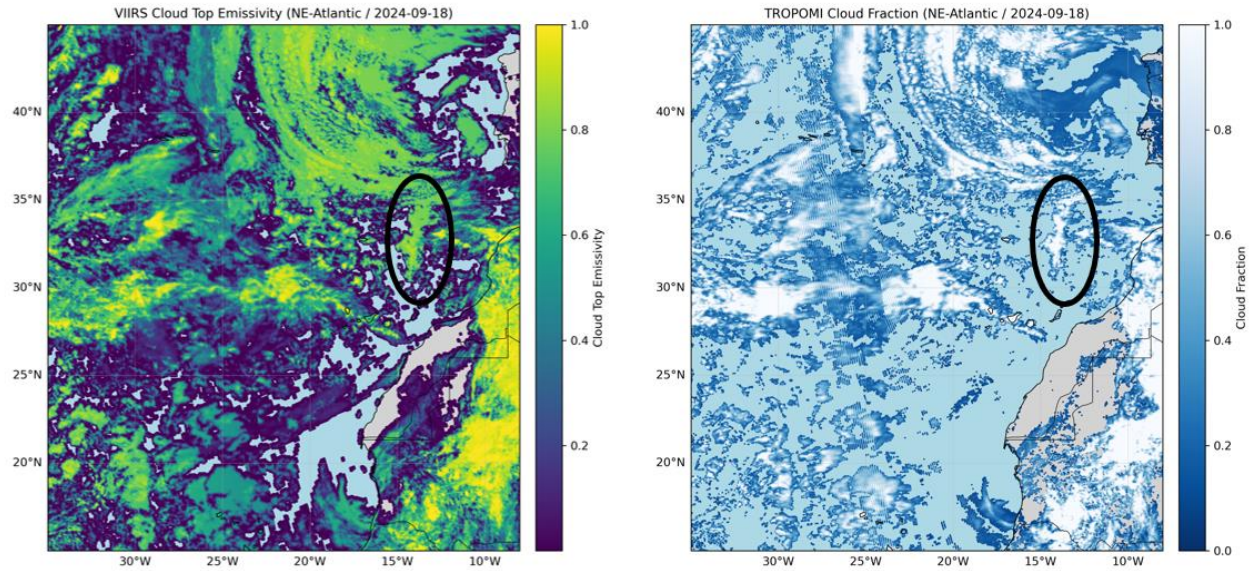


**Figure 74** VIIRS Cloud Top Emissivity (left panel) and TROPOMI Cloud Fraction (right panel) for 18-09-2024 over NEA

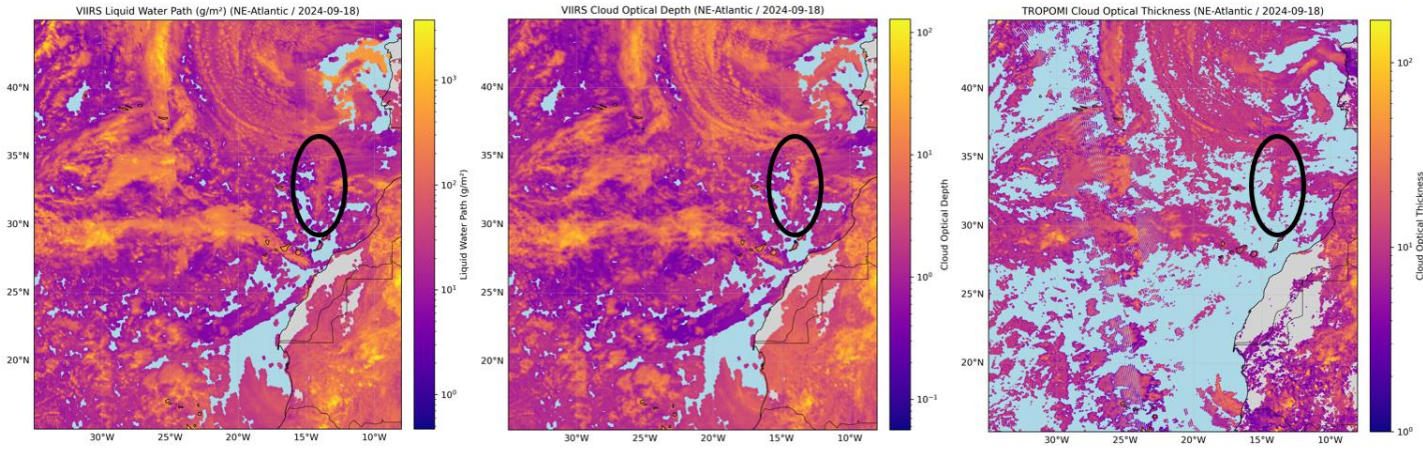


**Figure 75** VIIRS Liquid Water Path (left panel), VIIRS Cloud Optical Depth (middle panel) and TROPOMI Cloud Optical Thickness (right panel) for 18-09-2024 over NEA

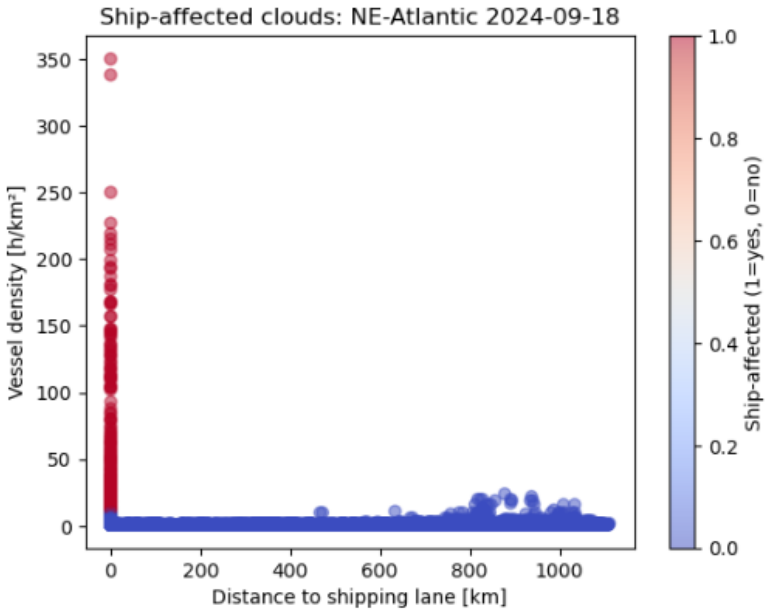


**Figure 76** Ship-track flagging for 18-09-2024 over NEA grid

On that day (18-09-2024), over NEA there are 715 ship-affected pixels over 18567 background pixels for the NEA grid box on that day (see Figure 76). The values of the $NO_2$ column at the ship-affected pixels were significantly elevated against the background pixels with a mean of 103% (see Figure 68). The regional mean cloud perturbations for ship-affected over background pixels is quite high, well above the average (see green circles of Figure 79 to Figure 81).

The local pixel-by-pixel perturbations of the liquid water path have in general a positive sign (see Figure 77) and the amplitude of the perturbation is pretty high on that day (18-09-2024). The ship-induced perturbations of the cloud optical depth (see Figure 78) are less systematically positive as few pixels appear with negative perturbations.

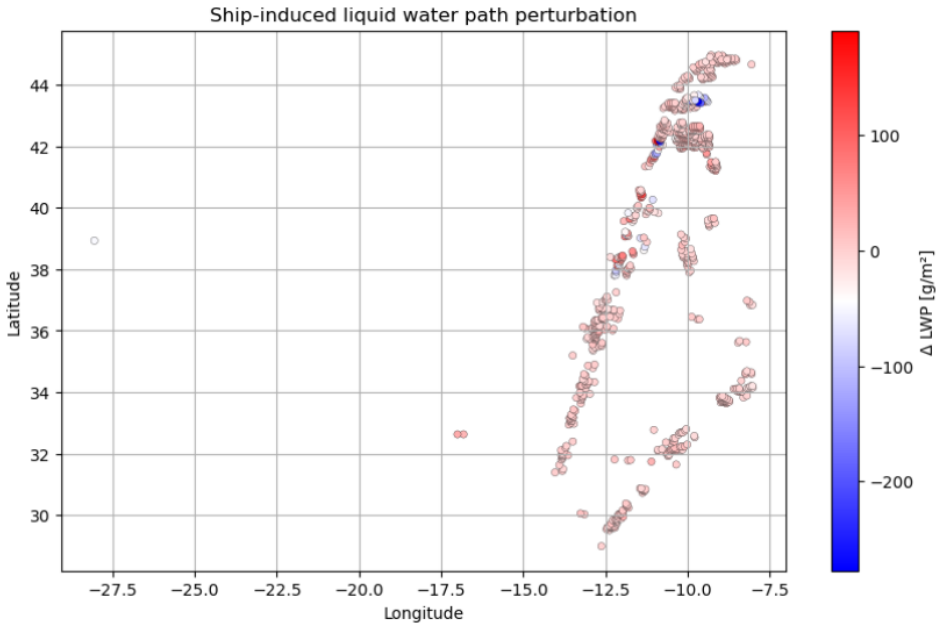


**Figure 77** Local Pixel-by-Pixel Perturbation in the VIIRS Liquid Water Path for the detected ship-tracks on over NEA 18-09-2024

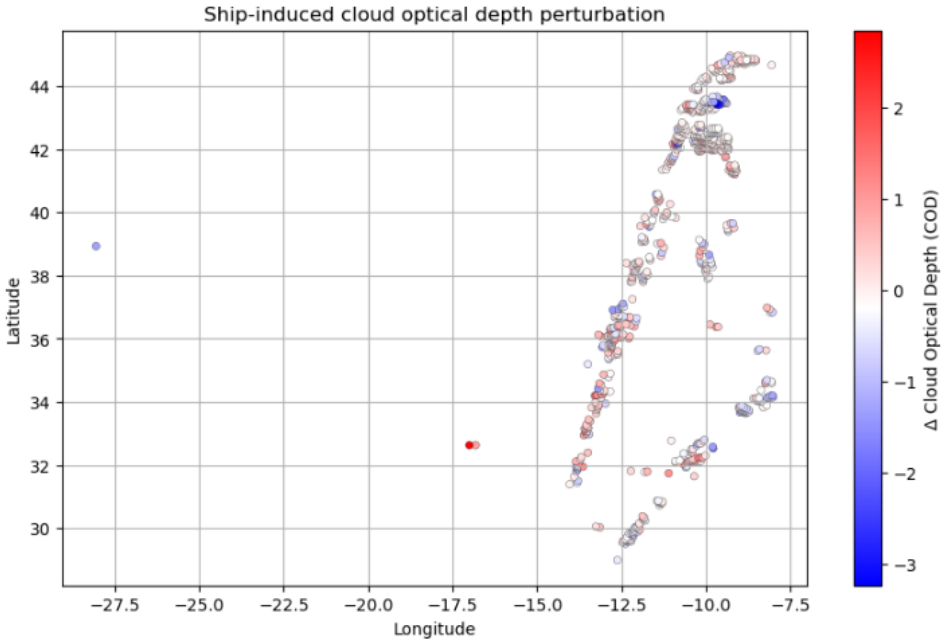


**Figure 78** Local Pixel-by-Pixel Perturbation in the VIIRS Cloud Optical Depth for the detected ship-tracks over NEA on 18-09-2024

For the whole period of the analysis over the NEA grid, the regional mean perturbations for the cloud parameters are presented in Figure 79 to Figure 81. One could see that the regional mean perturbation in the effective radius has an overall negative sign with a mean value of about -5% and a median of -9%. This is in line with literature referring to the Twomey effect (i.e., due to the activation of new particles into cloud droplets, the fresh CCNs added into the cloud base decrease the effective size of the cloud droplets). The regional mean perturbation of liquid water content has also a negative sign, which is not very well understood. This could be a cloud dynamical adjustment since the new aerosol particle population compete for water vapor to get activated into droplets. Finally, the regional mean perturbation of cloud optical depth has a positive sign, but a relatively small magnitude with a mean being +5% and the median +2%.

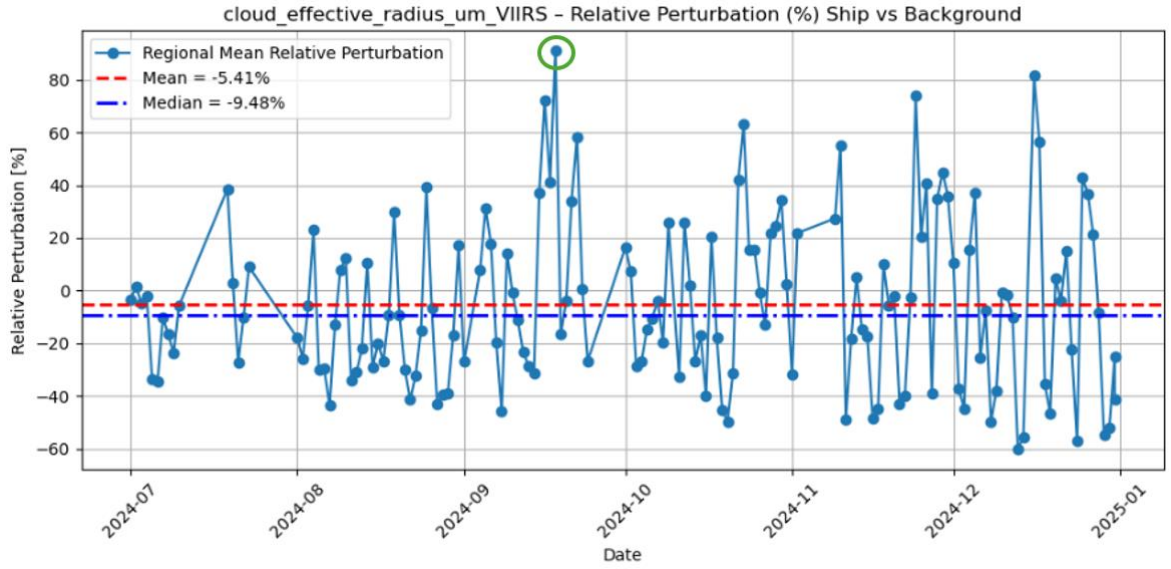


**Figure 79** Time series of the Regional Mean Perturbation of VIIRS cloud effective radius perturbations over NEA

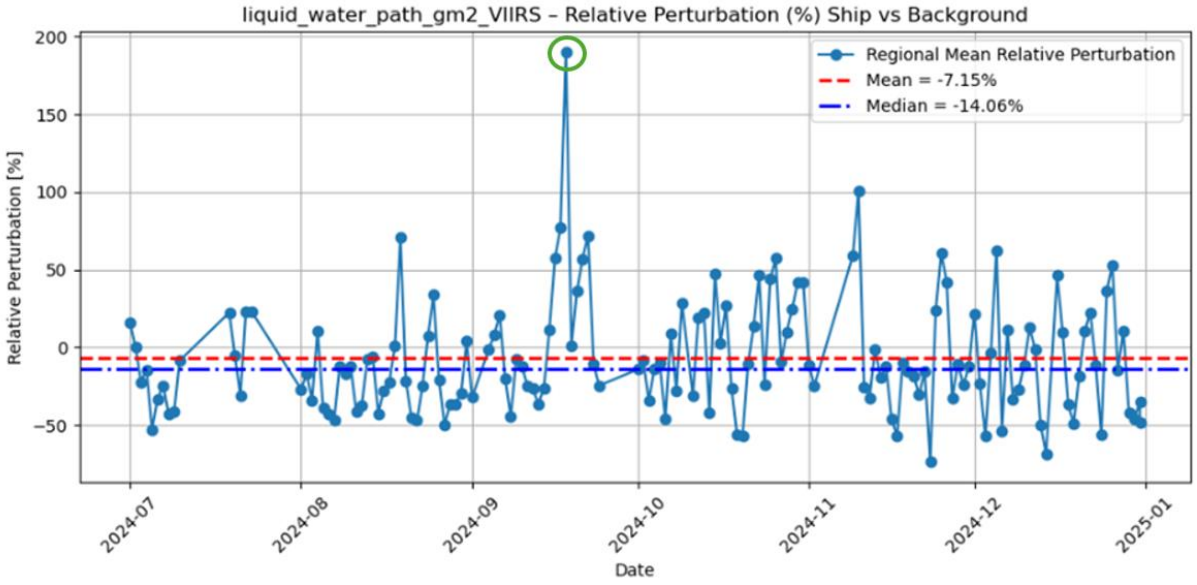


**Figure 80** Time series of the Regional Mean Perturbation of VIIRS cloud liquid water path over NEA

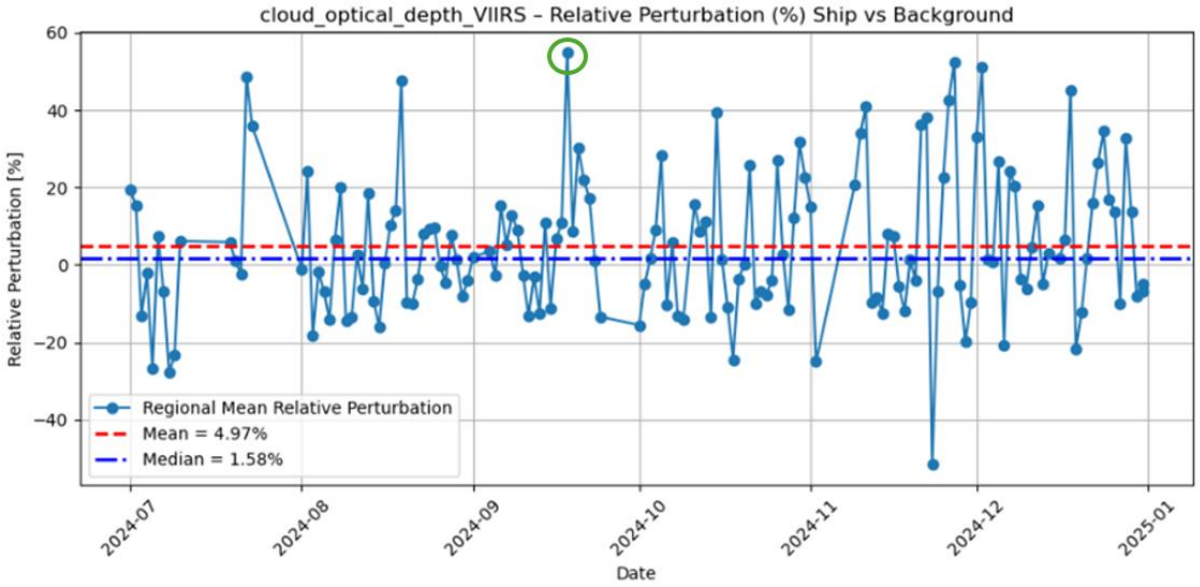


**Figure 81** Time series of the Regional Mean Perturbation of VIIRS cloud optical depth over NEA

#### 4.2.1.2 Analysis of the ship tracks over the MED grid

For the Mediterranean region, the $NO_2$ tropospheric column appears quite increased for the detected ship-tracks; ~30% enhancement as shown in Figure 82 (the mean is slightly above the median as it is more affected by the extreme values).

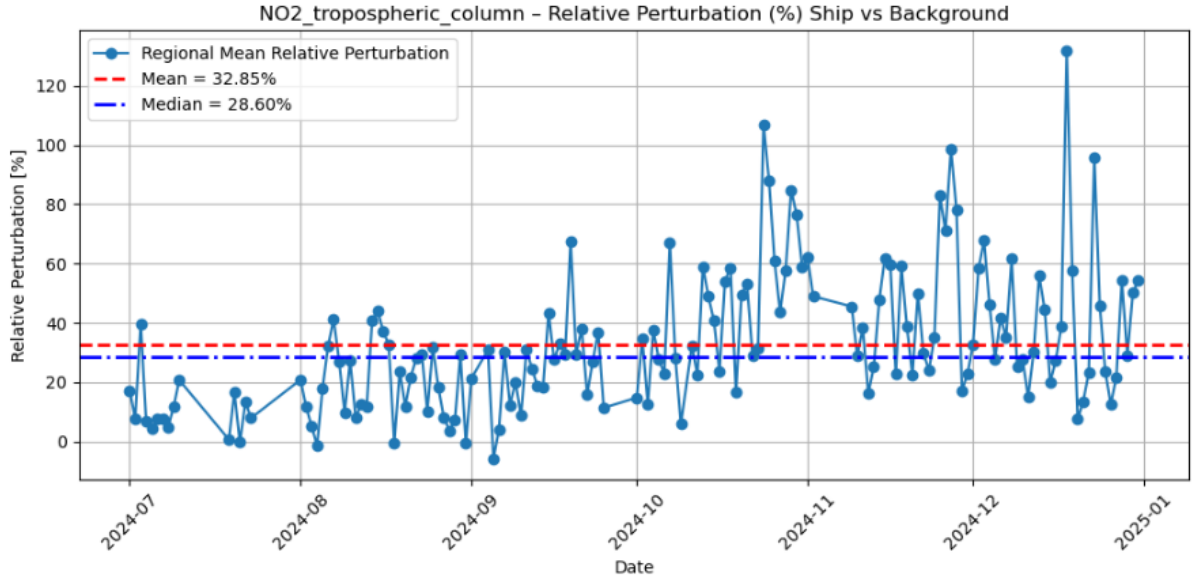


**Figure 82** Time series of the Regional Mean Perturbations of the $NO_2$ tropospheric column over MED

The mean perturbation for the cloud effective radius (see Figure 82) does not show any trend in this region. The mean perturbation of the liquid water path has a positive sign in this region (see Figure 83 with median/mean ~4-5%). Similarly to the NEA region, the cloud optical thickness shows a systematic positive mean perturbation of about 6% as illustrated in Figure 84.

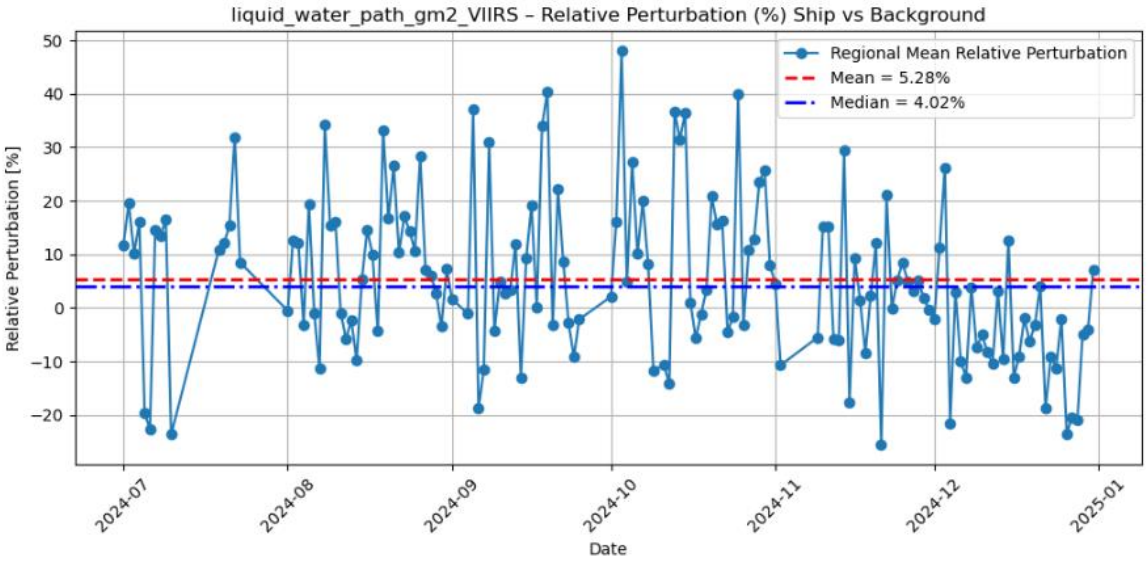


**Figure 83** Time Series of the Regional Mean Perturbations of VIIRS liquid water path over MED

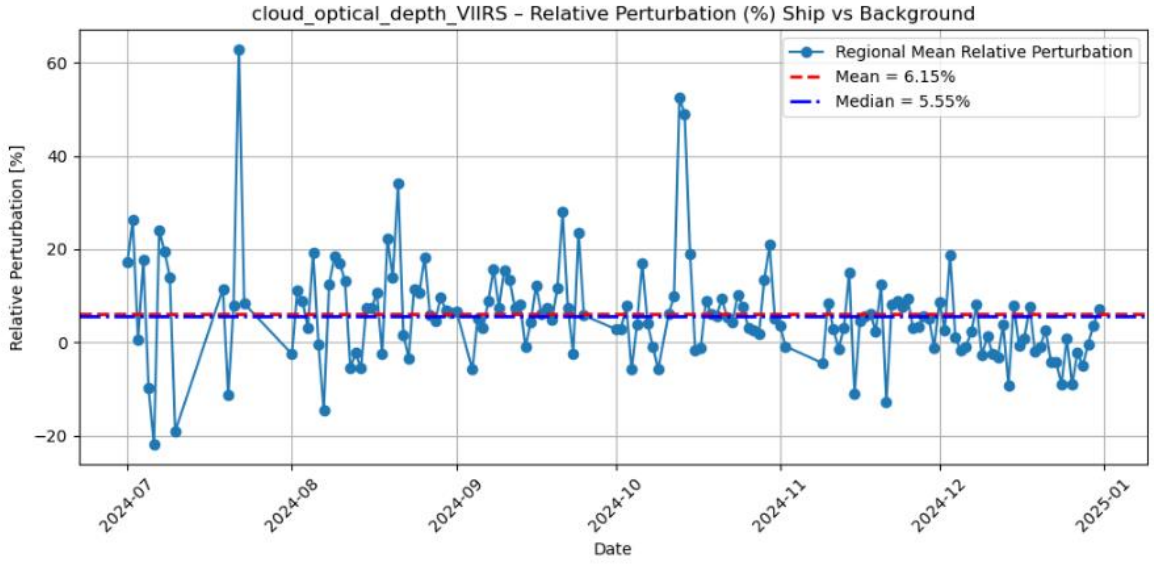


**Figure 84** Time Series of the Regional Mean Perturbations of VIIRS cloud optical depth over MED

In the MED grid, it gets more challenging to identify the ship tracks because the background $NO_2$ is not that low as the NEA grid. Many other sources of pollution can contribute to the elevated NO2 VCDs. On the other hand, with the limited data points on the ship information from EMODnet, where only the European Seas are included in the dataset, the MED grid is much better represented than the NEA grid.

#### 4.2.1.3 The case study of 14-08-2024 over the Mediterranean

Ship emissions are found on the 14 August 2024 at the TROPOMI $NO_2$ maps: mostly visible between Italy and Greece around 36.0° N and North of Africa at 0° E – 5° E. The clouds appear only at the second area though (i.e., missing values/gaps at the $NO_2$ maps imply that there are clouds in the region).

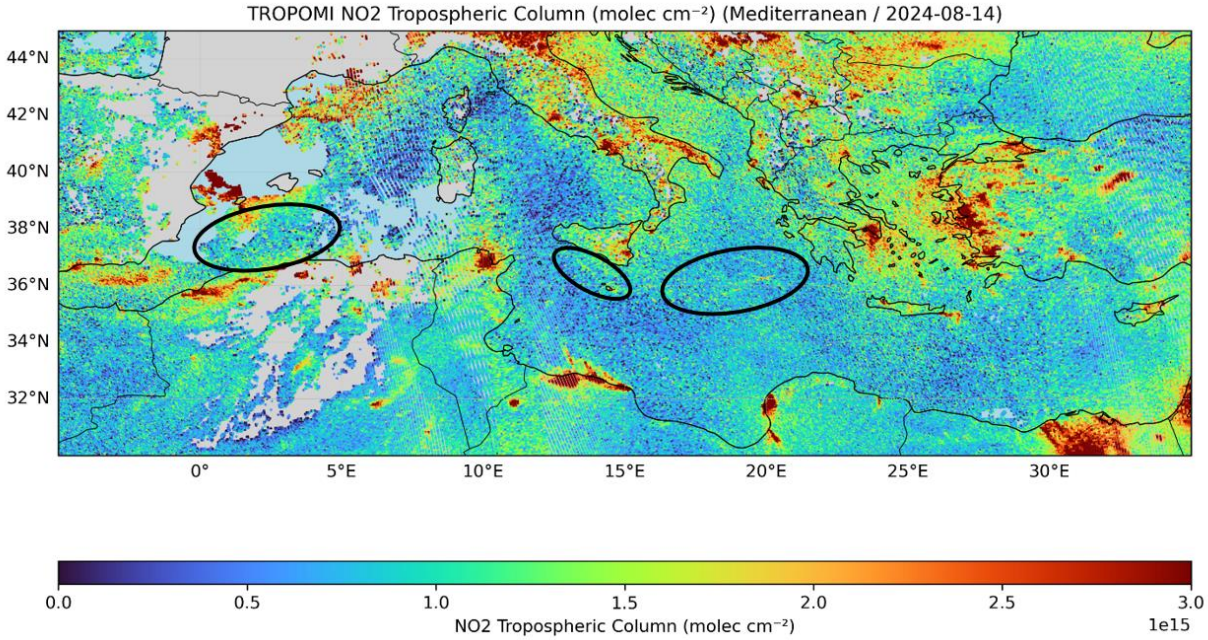


**Figure 85** TROPOMI $NO_2$ Tropospheric Column for 14-08-2024 over MED: the ship emissions are visible directly on the maps

This is an interesting case where the TROPOMI sensor can directly see the ship-tracks as they appear at a different cloud height (see TROPOMI cloud top height of Figure 86) with respect to the neighboring cloudy pixels. This is also confirmed by the VIIRS cloud top height map of Figure 87. Therefore, in that case, the ship-tracks are well captured at the Oxygen A-band (~758–770 nm) where TROPOMI retrieves the cloud properties.

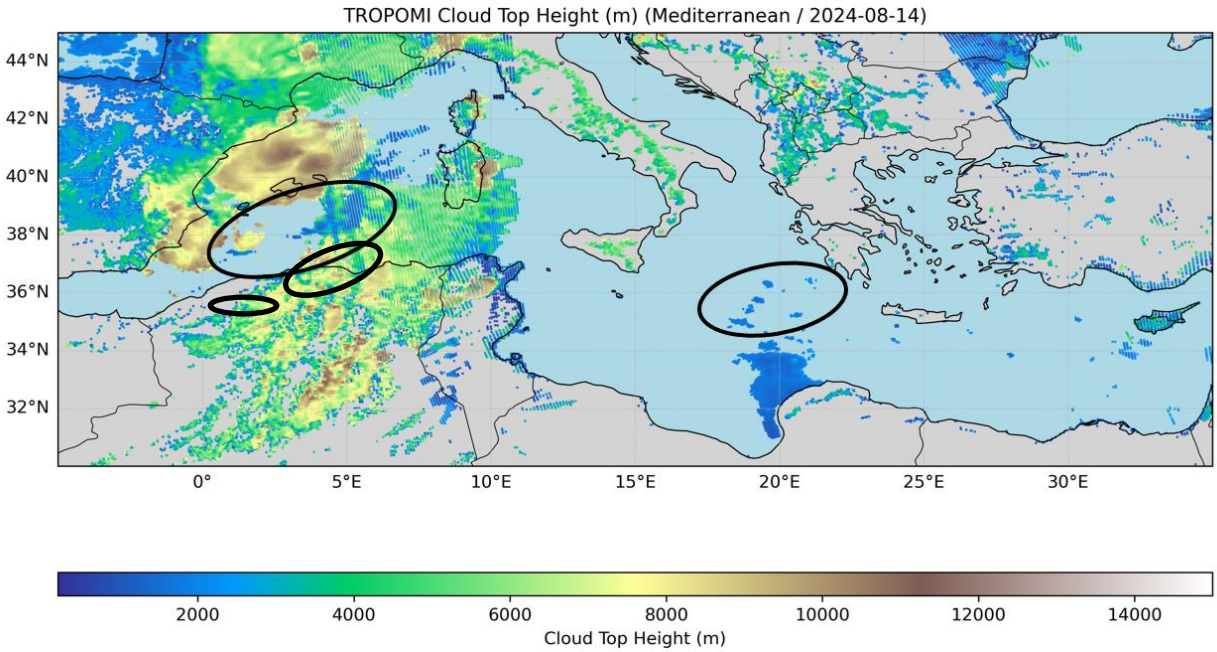


**Figure 86** TROPOMI Cloud Top Height for 14-08-2024 over MED: the ship tracks appear with a lower cloud top height

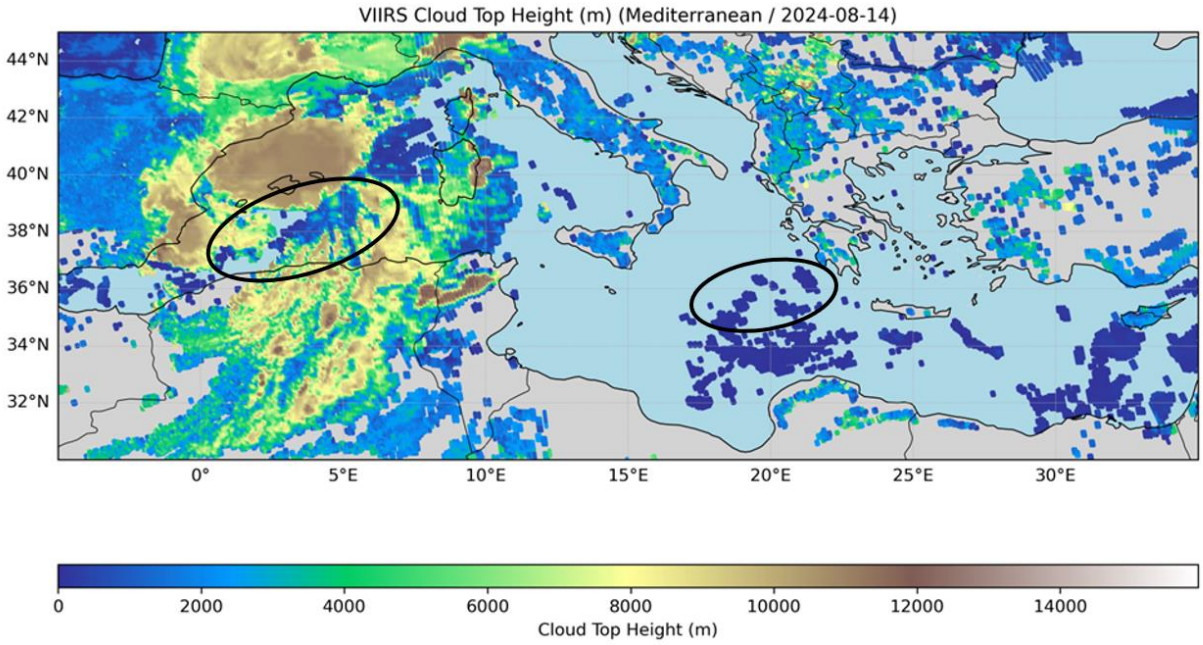


**Figure 87** VIIRS Cloud Top Height for 14-08-2024 over MED: the ship tracks appear with a lower cloud top height but not that strong difference like for TROPOMI

The ship-tracks appear with an increased value in the TROPOMI Aerosol Absorbing Index maps, which at first seem independent of the wavelength ratio used (see Figure 88 - Figure 91). TROPOMAER AAI (Figure 91) makes use of the 340/380 wavelength ratio. The 335 nm wavelength band is closer to strong ozone absorption (Hartley–Huggins bands) and the retrieval might become more sensitive to ozone contamination. The Rayleigh scattering is weaker at 388 nm; stronger spectral contrast should be expected for this reflectance. Therefore, the detection capability to ship tracks is optimized for the 354/388nm wavelength ratio, while the noisiest signal should be for the 335/367nm wavelength ratio.

**Technical Restriction**: In the ellipse between Italy and Greece ship-tracks cannot be seen. The reasoning should be due to sun glint; an optical phenomenon that occurs when sunlight reflects off a water surface directly into a satellite or airborne sensor. That is a potential reason of suffering signal-to-noise ratio over bright water surfaces. Moreover, one other technical issue of ship-track detection capability appears at the edges of the swath with a twofold possible explanation:

- the binning changes and the footprint become much larger; the instrument loses partly the detection capability due to its spatial resolution decrease. In general, the TROPOMI NIR ground pixels appear shifted towards the east with regard to the UV ground pixels. The spatial misalignment in the across-track direction is not a fixed number, but instead it depends on the position in the swath since the ground pixels at nadir are different in size than those at the swath edges. The ground pixel size is 3.5 km in the center of the swath and in a large area around it, but it becomes larger towards the edges of the swath due to the Earth's curvature and the instrument's large swath angle. The so-called binning factors are selected to optimize the signal-to-noise ratio per pixel with the aim of minimizing the difference in ground pixel sizes in the across-track direction. For the TROPOMI L1 radiance measurements, a binning factor of 2 is used in the center and in a large region around it, resulting in a ground pixel size of 3.5 km. At the edges of the swath, the binning factor is reduced from 2 to 1 in order to keep the ground pixel size at a reasonable value. Due to optical limitations of the instrument and the curvature of the Earth, the ground pixel size at the edges of the swath is about 15 km. The spatial resolution inhomogeneity along the swath could result to co-registration issues (Argyrouli et al., 2024).
- some atmospheric products from passive spectrometers might suffer of low accuracy far from the nadir position as their viewing-angle-dependent correction scheme could be imperfect. Special algorithmic treatments are usually needed at the edges of the swath to calculate the reflectance ratio for a pure Rayleigh molecular atmosphere, like applying viewing-angle-dependent correction, which is fundamentally tied to the solar zenith angle and viewing zenith angle geometry.

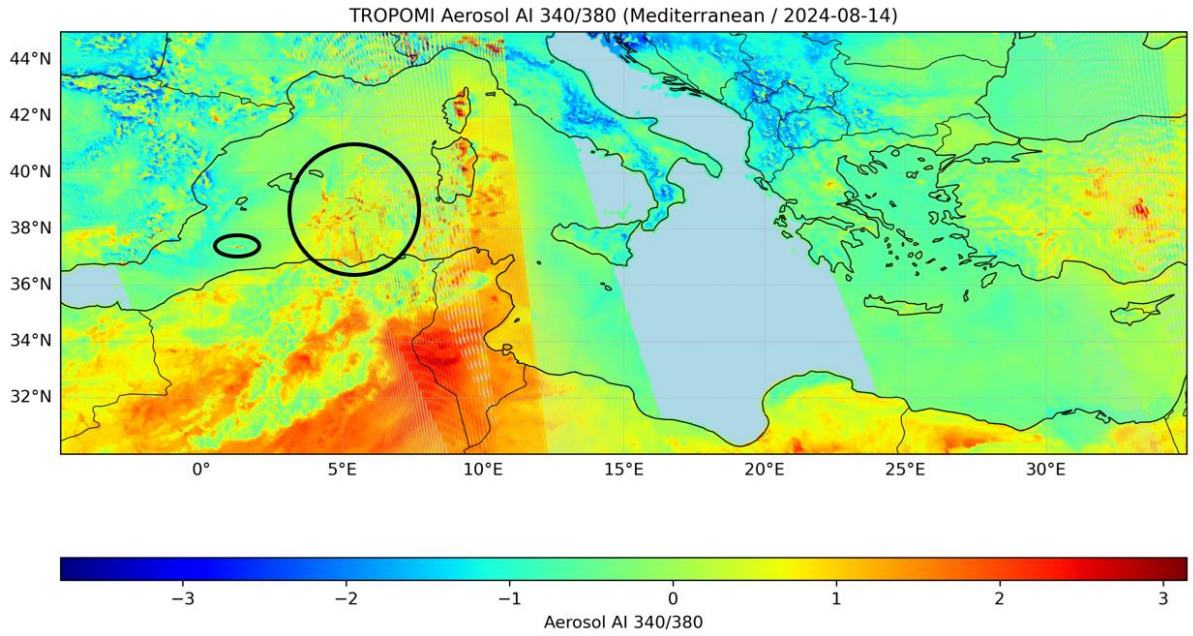


**Figure 88** TROPOMI AAI at 340/380nm for 14-08-2024 over MED: the ship tracks appear with elevated values

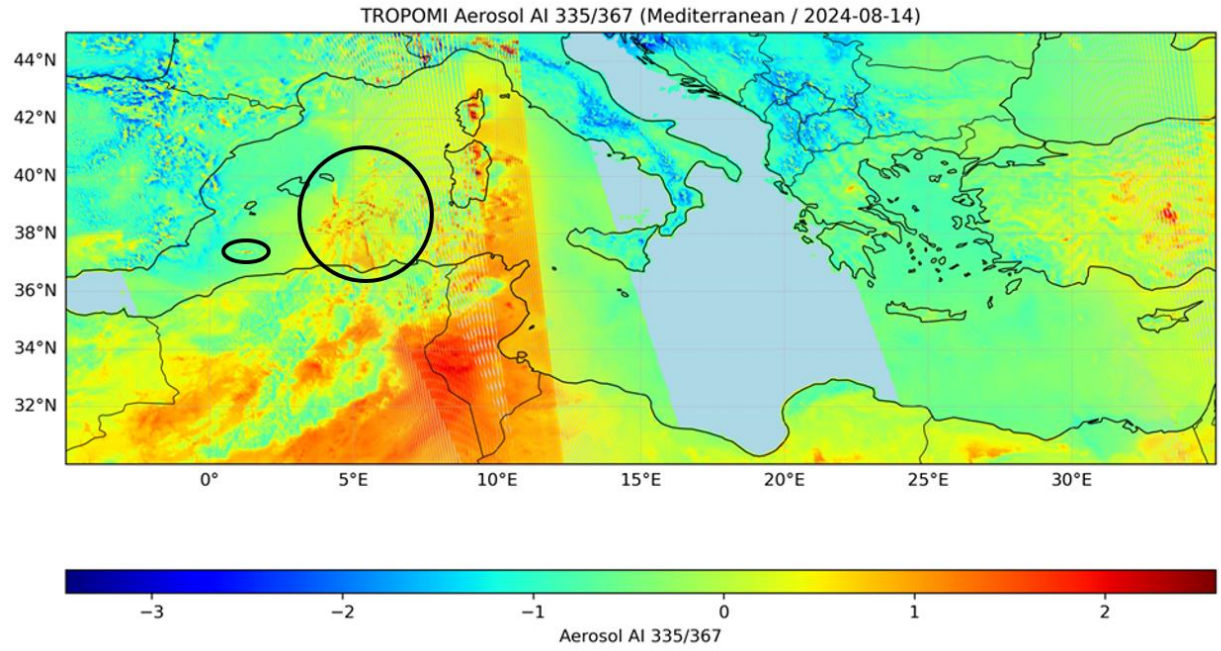


**Figure 89** TROPOMI AAI at 335/367nm for 14-08-2024 over MED: the ship tracks appear with elevated values

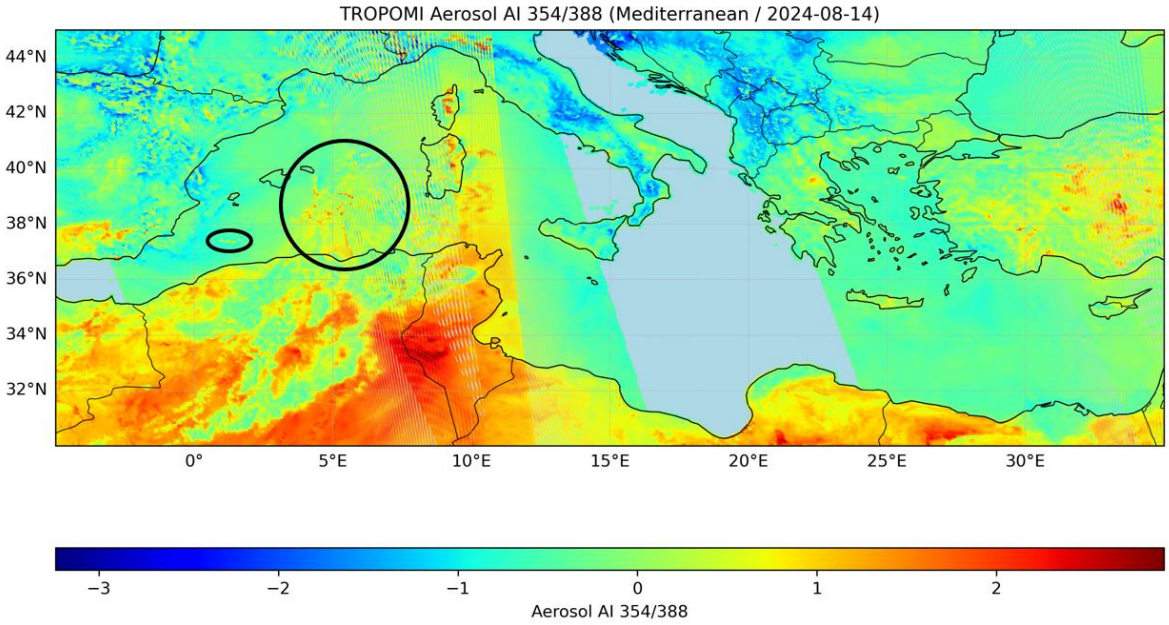


**Figure 90** TROPOMI AAI wavelengths 354/388 for 14-08-2024 over MED: the ship tracks appear with elevated values

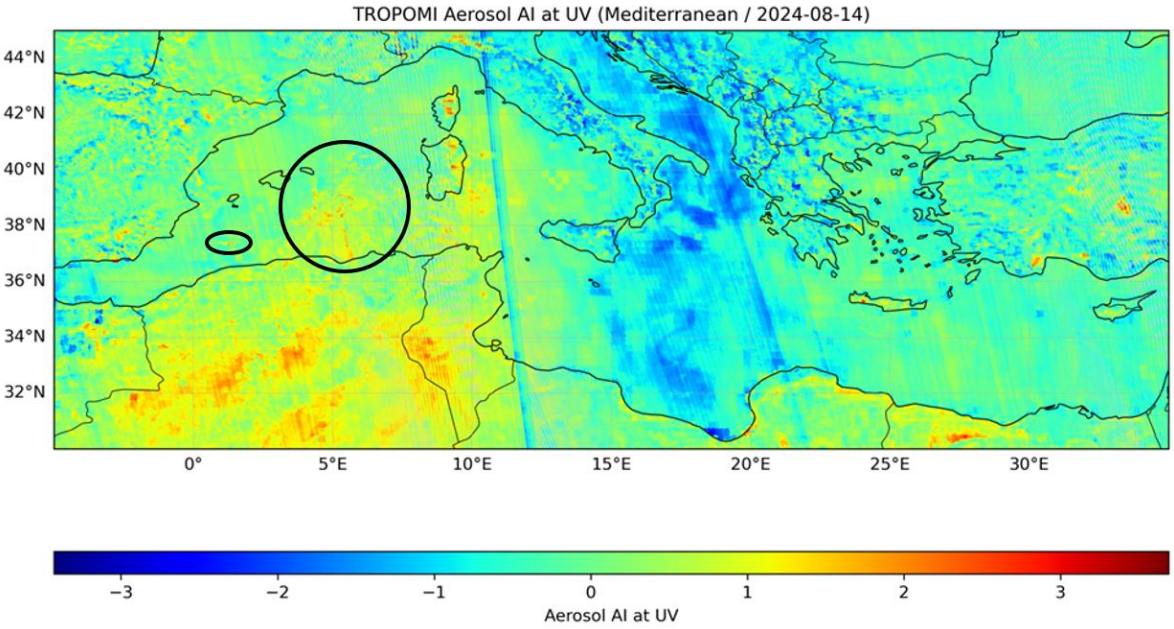


**Figure 91** TROPOMI AAI at UV for 14-08-2024 over MED: the ship tracks appear with elevated values

On that day (14-08-2024), the absolute number of ship-affected pixels is 375 compared to the 1278 that compose the background (see Figure 92). Local pixel-by-pixel perturbations in the liquid water path have an overall negative sign (see Figure 93), as well as a negative sign appears for the cloud optical depth perturbations (see Figure 94). It is noticeable that only the cloud structure at 44°N, 8°E has the shape of a ship-track straight line pattern.

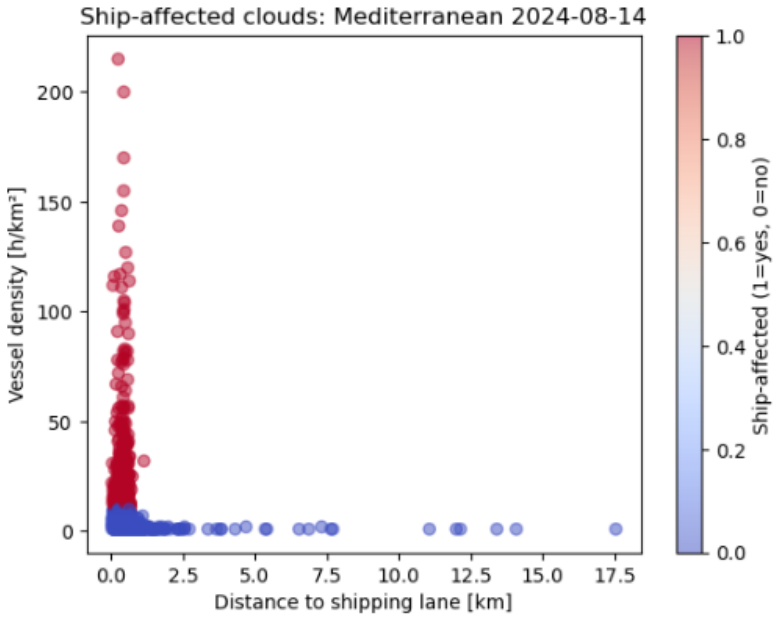


**Figure 92** Ship-affected pixels flagging over MED on the 14-08-2024

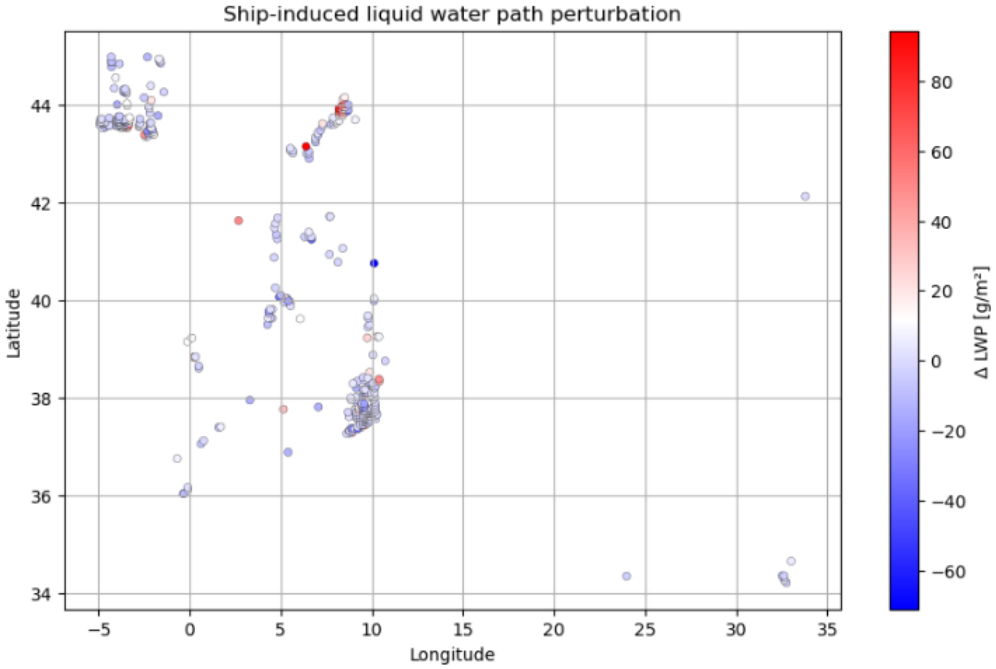


**Figure 93** Ship-induced perturbation in the liquid water path over MED for the 14-08-2024

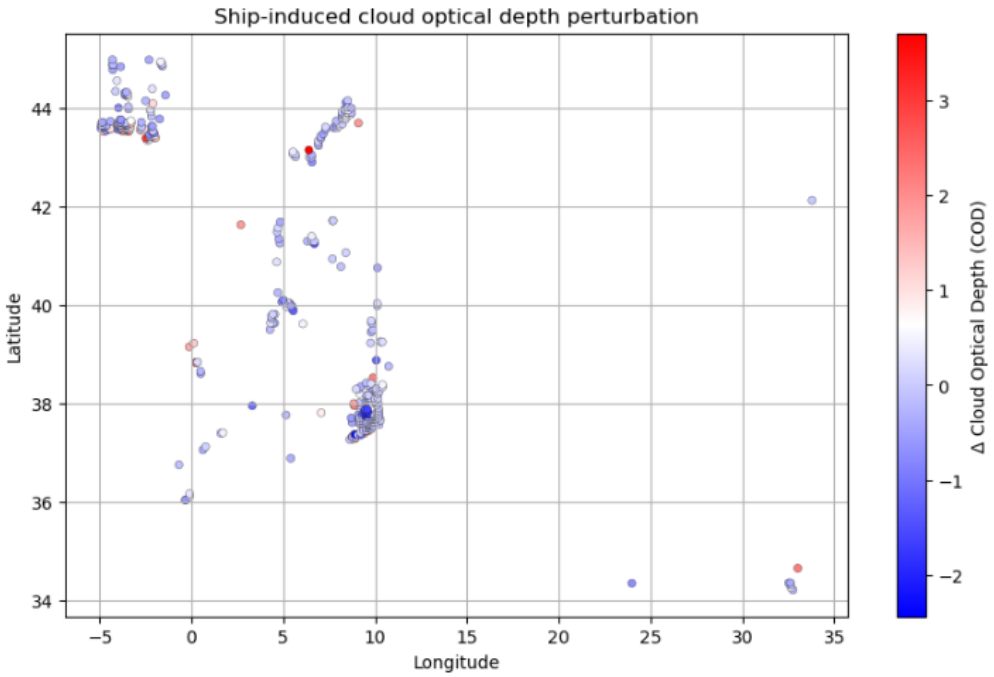


**Figure 94** Ship-induced perturbation in the cloud optical depth over MED for the 14-08-2024

#### 4.2.1.4 The case study of 15-08-2024 over the Mediterranean

Often the ship tracks are detected over the Mediterranean close to the Gibraltar Strait (Latitude: 36° N – 37.0° N). This is the narrow waterway between southern Spain and northern Morocco, connecting the Atlantic Ocean to the Mediterranean Sea. The Gibraltar Strait itself is a critical shipping corridor, so it's highly relevant to the ship-affected cloud analysis. The TROPOMI VCDs (see Figure 95) are elevated and the cloud top height (Figure 96) detects the clouds at low altitudes.

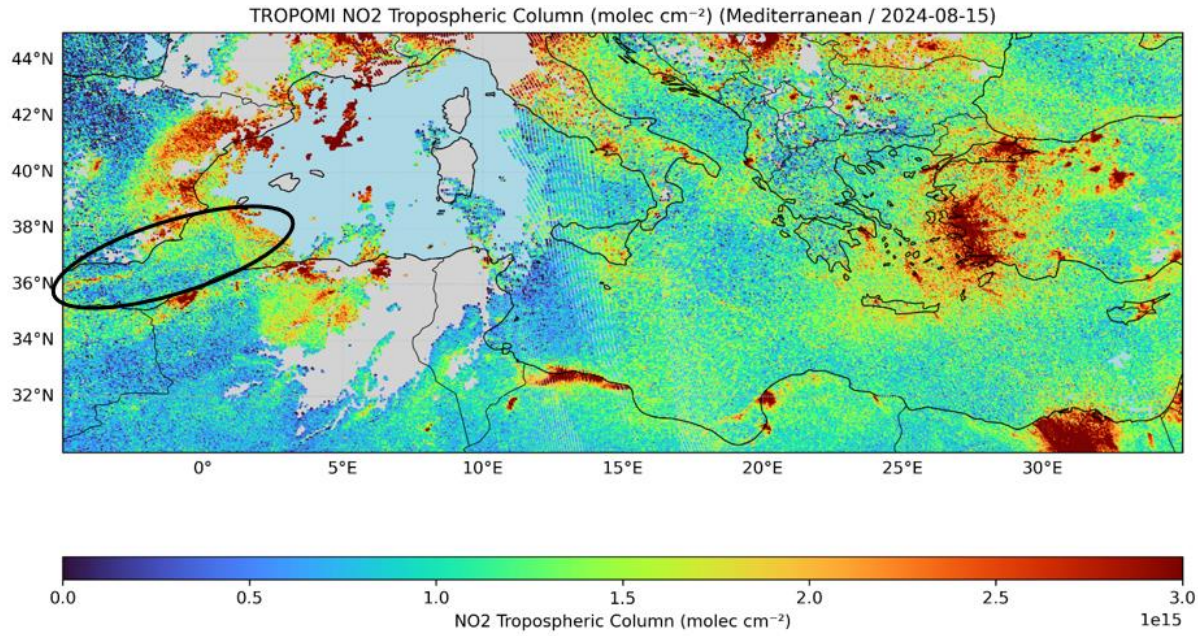


Figure 95 TROPOMI Tropospheric $NO_2$ columns for 15-08-2024 over MED: ship tracks are captured close to the Gibraltar Strait

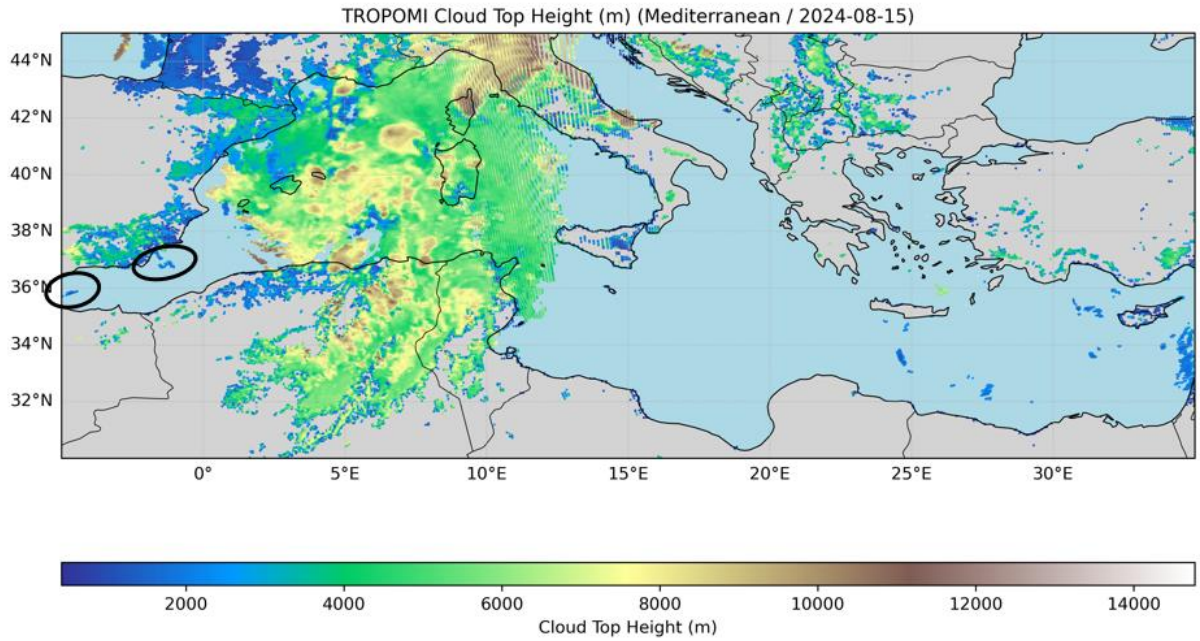


**Figure 96** TROPOMI cloud top height for 15-08-2024 over MED: ship tracks are captured close to the Gibraltar Strait

#### 4.2.1.5 The case study of 16-08-2024 over the Mediterranean

Another interesting case where the $NO_2$ maps appear with elevated values in the west part of the Mediterranean (Figure 97). It is hard to conclude whether the elevated VCDs are due to actual pollution from shipping (or other pollution sources in the vicinity) or just the impact of saturation at the raw signal. From the shape of the missing data over the water surfaces in the Aerosol AAI map (see Figure 99), it appears that the satellite viewing geometry favors sun glint. In both cases, the ship emissions cannot be quantified on that day since the pixels used as the background contains large amounts of $NO_2$. Therefore, in days where the background NO2 pollution is that much, the detection capability is very limited. Few ship-tracks are captured at the VIIRS Cloud Top Emissivity map (Figure 98).

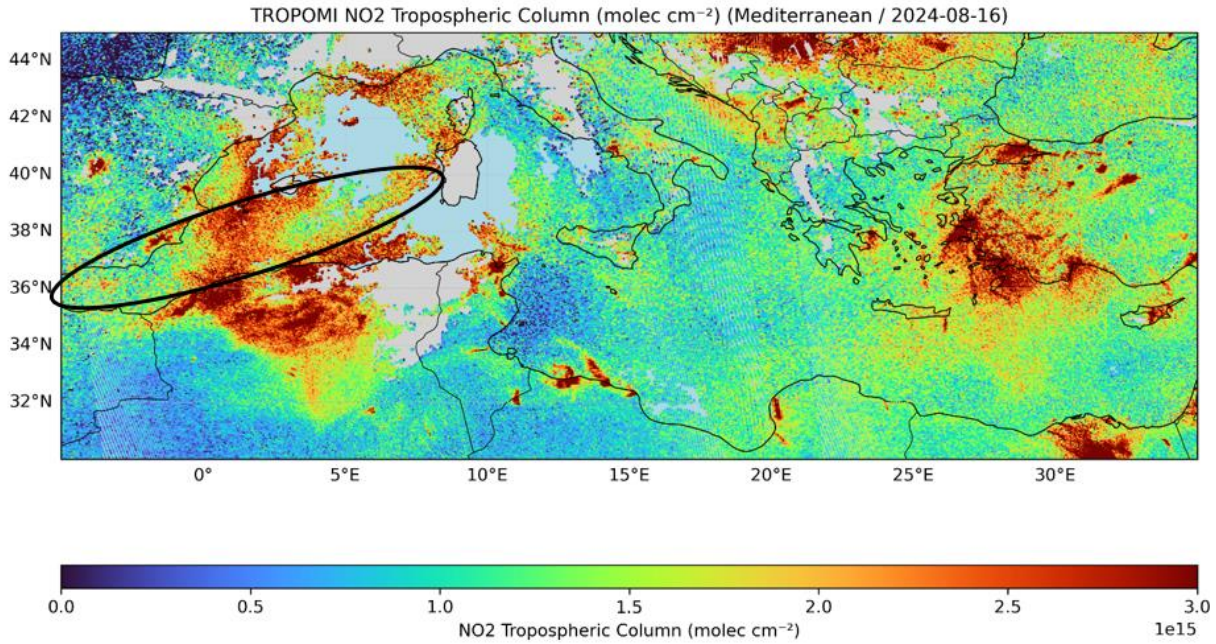


**Figure 97** TROPOMI $NO_2$ Tropospheric Column for 16-08-2024 over MED: ship tracks appear at region with extremely high $NO_2$ Tropospheric Column; could be actually a very polluted region/day but also the raw signal might be saturated due to sun glint

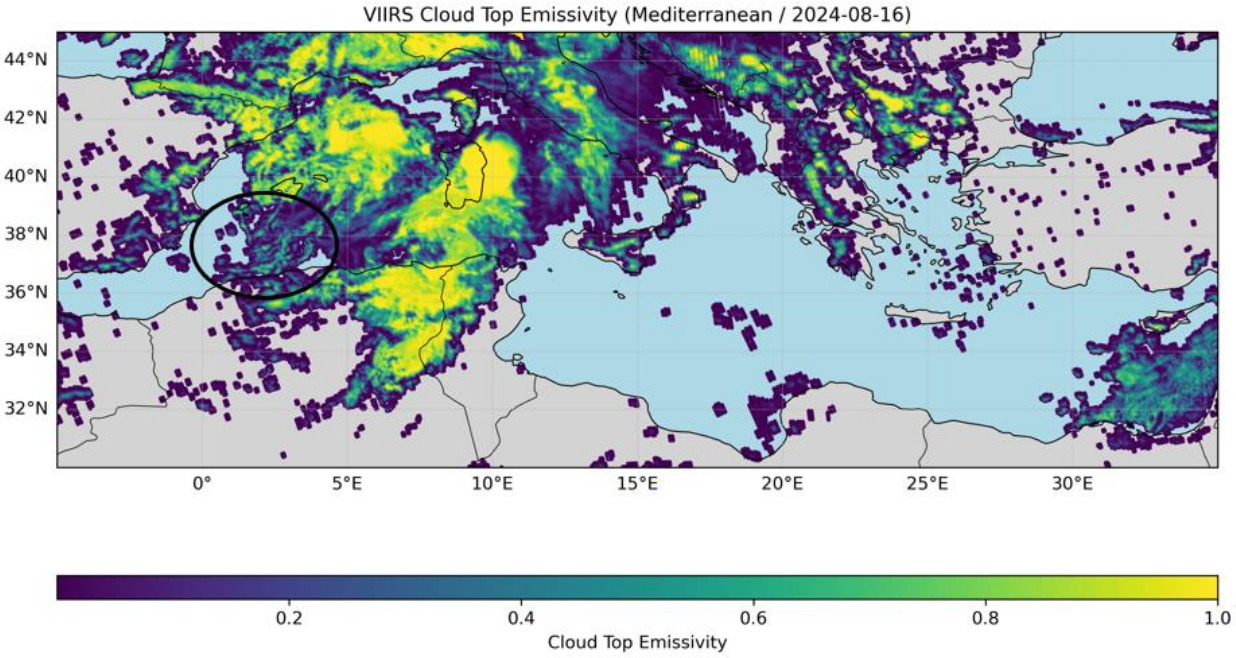


**Figure 98** VIIRS Cloud Top Emissivity for 16-08-2024 over MED: ship tracks are captured

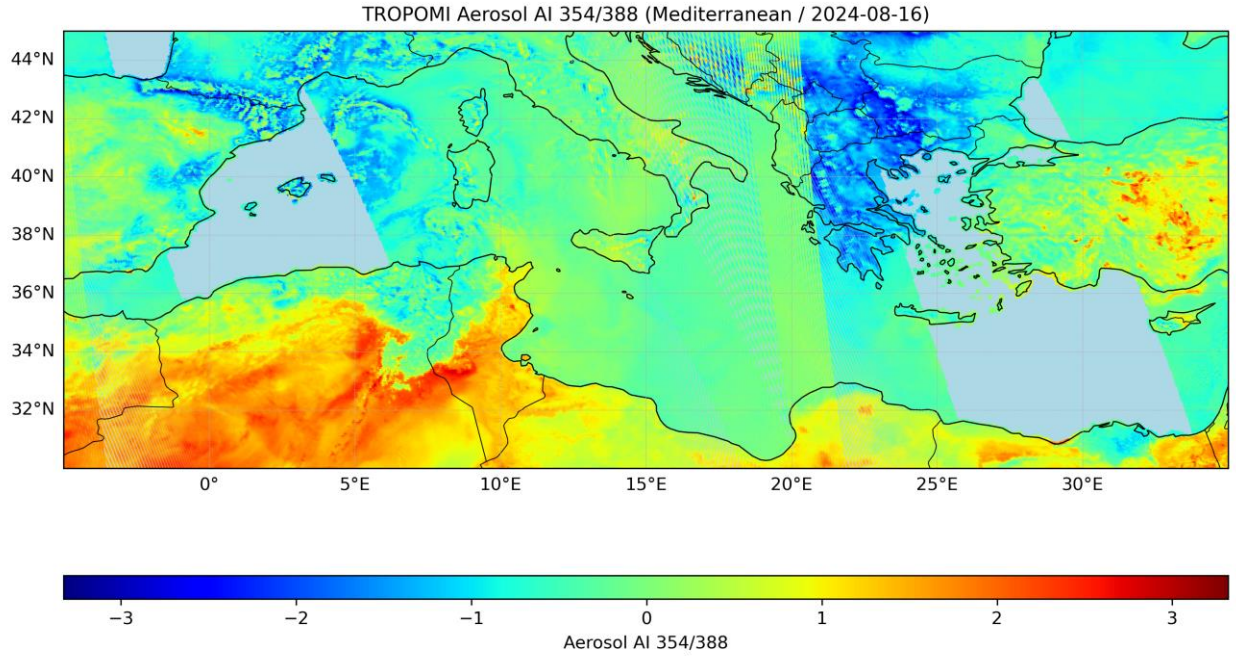


**Figure 99** TROPOMI AAI for 16-08-2024 over MED: the missing data appear where sun glint occurs

#### 4.2.1.6 Statistical Significance of the $NO_2$ and cloud signals

Cohen's *d* quantifies the standardized effect size between ship-affected and background pixels, expressed in units of pooled standard deviation. Unlike the p-value, which is strongly influenced by sample size, Cohen's *d* provides a measure of the magnitude of the perturbation and is therefore more suitable for assessing physical relevance in large satellite datasets. Following the conventional thresholds (Cohen, 1988), effect sizes can be interpreted as:

- |d| ≈ 0.2 means small effect
- |d| ≈ 0.5 means medium effect
- |d| ≥ 0.8 means large effect

In the context of ship-tracks detectability, values around |d| ≥ 0.2 indicate a measurable but subtle perturbation, whereas |d| ≥ 0.5 suggests a physically meaningful signal that may be robust under operational monitoring conditions. Very large values (|d| ≥ 0.8) imply strong separability between ship-affected and background cloud properties.

Because Cohen's *d* is independent of the sample size, it provides a more appropriate metric than p-values for evaluating the practical detectability of $NO_2$ and cloud perturbations in large-scale satellite analyses.

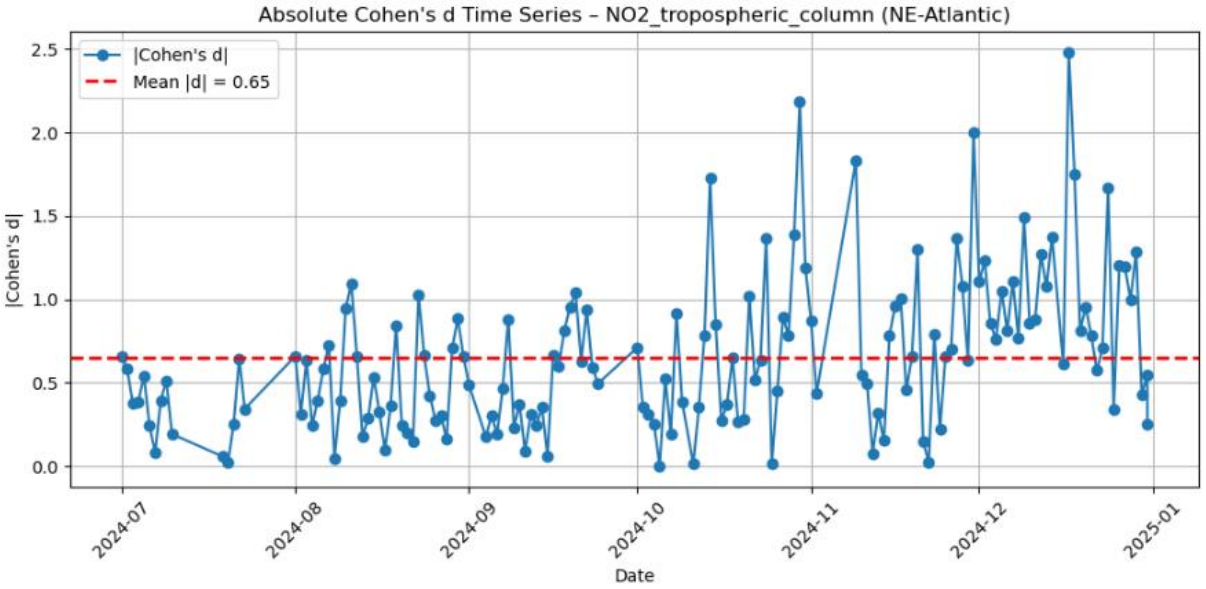


**Figure 100** Cohen's *d* absolute value Time Series for the TROPOMI $NO_2$ signals over NE-Atlantic

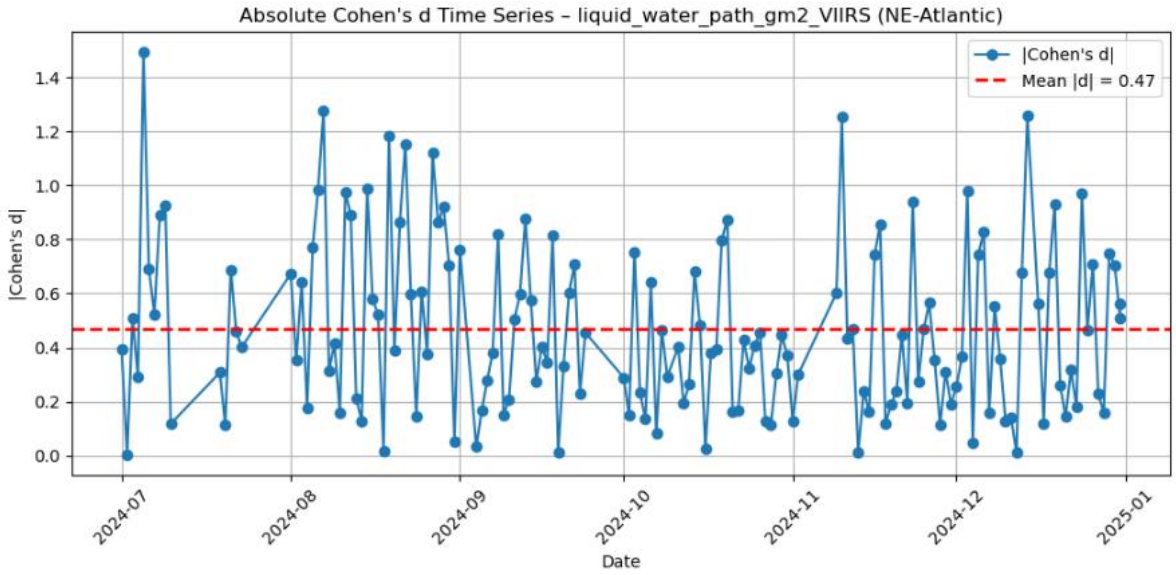


**Figure 101** Cohen's *d* absolute value Time Series for the VIIRS LWP signals over NE-Atlantic

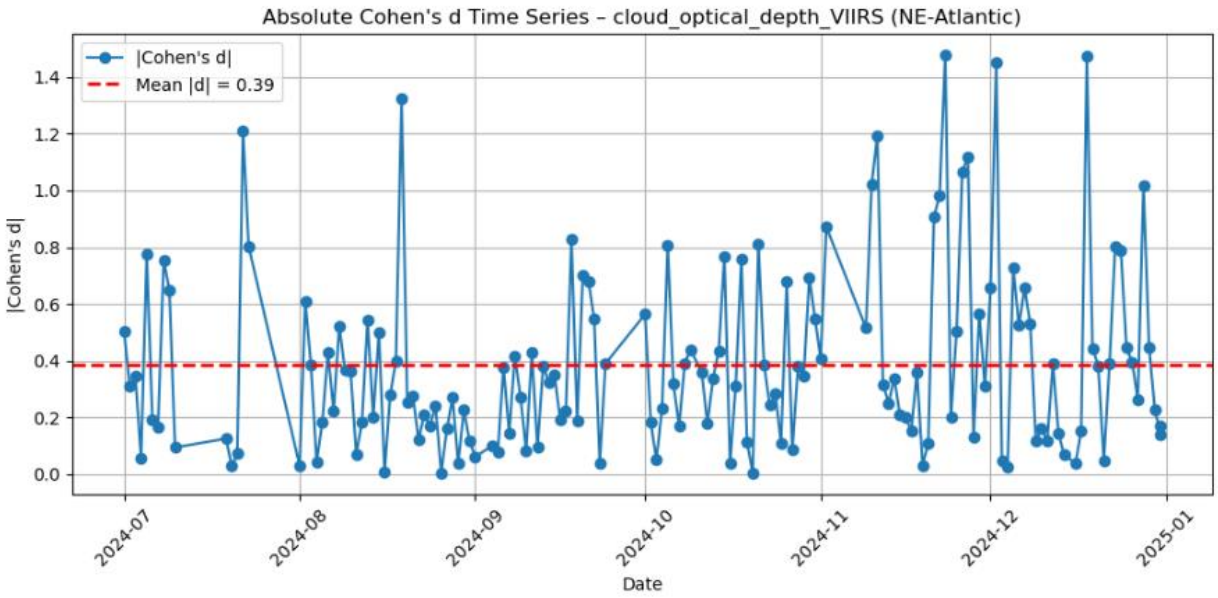


**Figure 102** Cohen's *d* absolute value Time Series for the VIIRS COD signals over NE-Atlantic

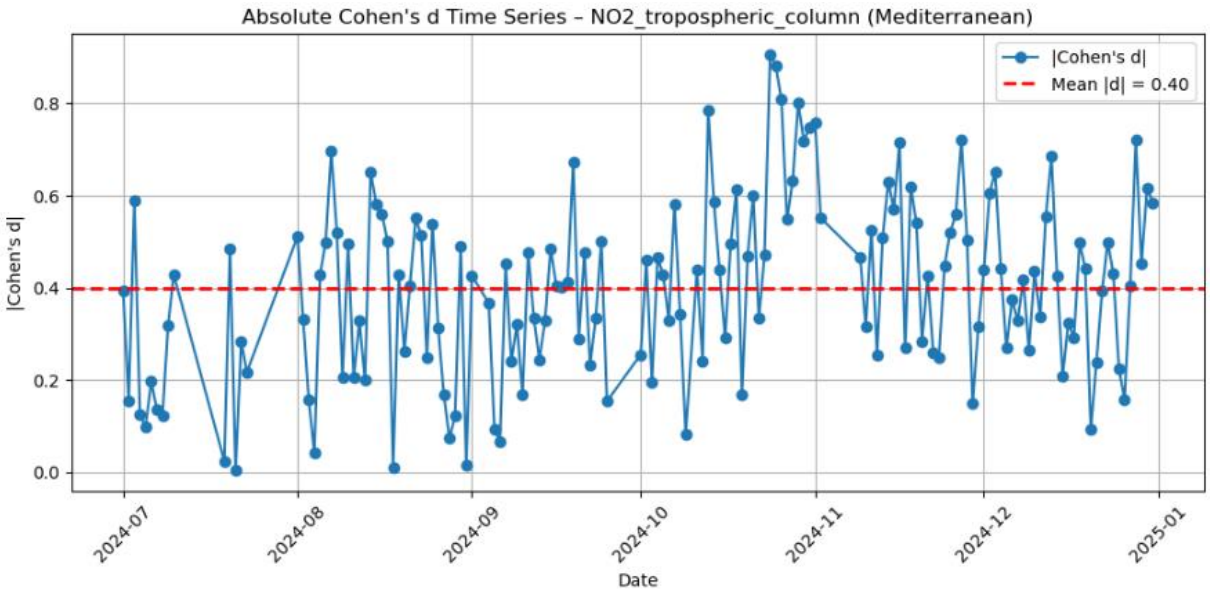


**Figure 103** Cohen's *d* absolute value Time Series for the TROPOMI NO2 signals over the Mediterranean

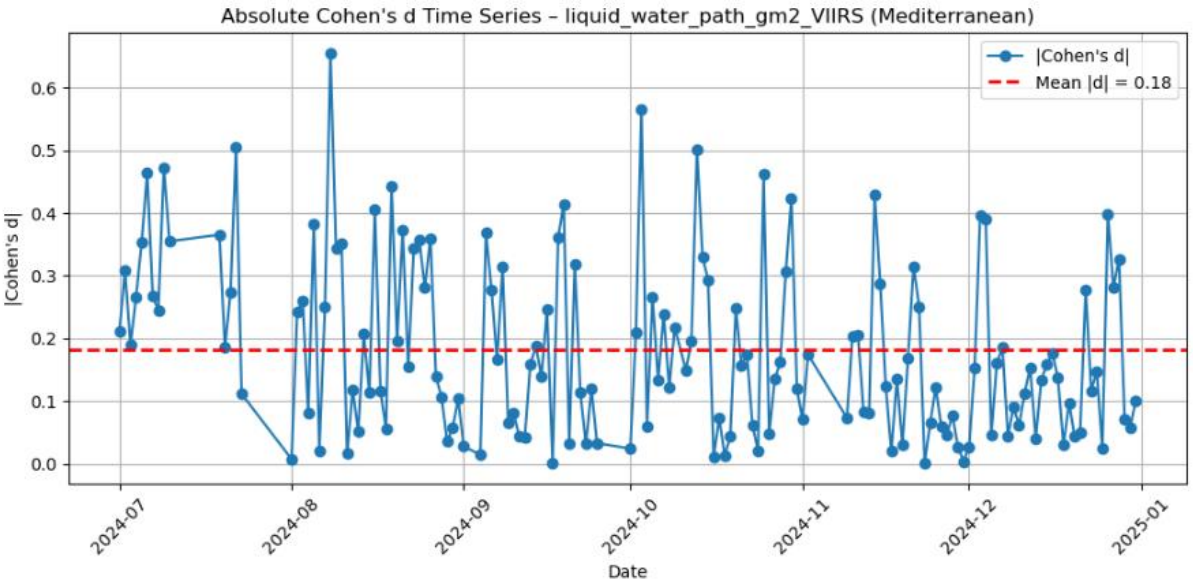


**Figure 104** Cohen's *d* absolute value Time Series for the VIIRS LWP signals over the Mediterranean

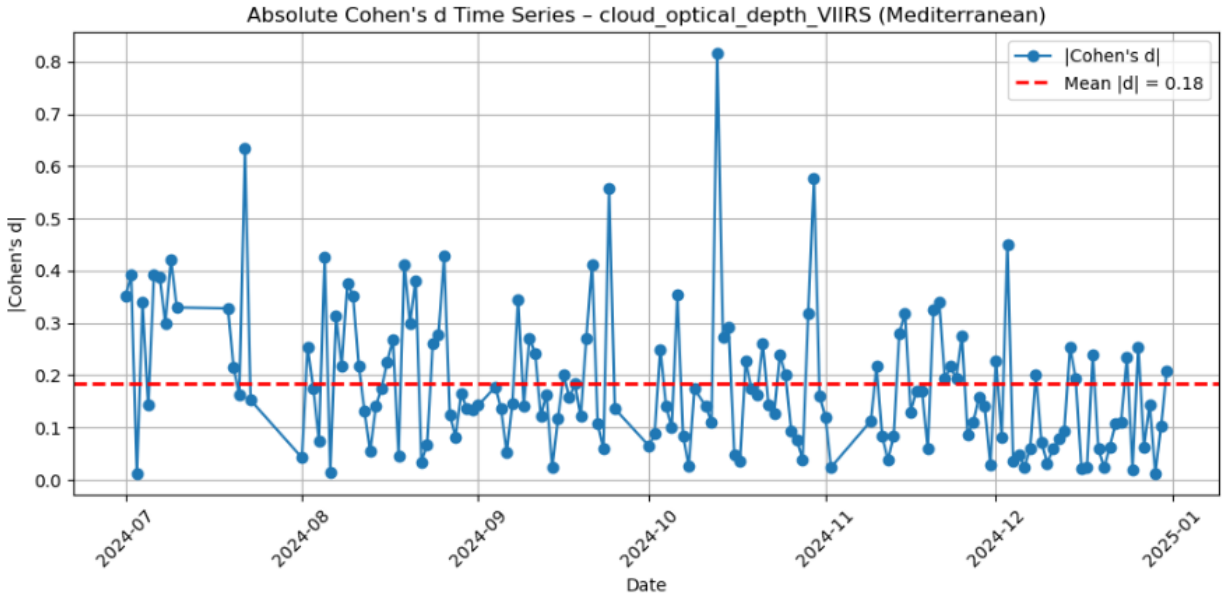


**Figure 105** Cohen's *d* absolute value Time Series for the VIIRS COD signals over the Mediterranean

#### 4.2.1.7 Accurate Detection of the ship-tracks from Space

Machine Learning Classifiers can be used for accurate/semi-automatic detection of the ship-tracks from spaceborne instruments. The limitation with the current merged dataset is that the location of the ships do not match temporally with the satellite overpasses. Moreover, training of ML classifiers is limited in space as the vessel maps are available at the major shipping corridors of the European Seas in EMODnet. Due to less imbalance at the two classes "ship-affected" versus "background" for the MED grid, the detection accuracy has been compared using a baseline Logistic Regression classifier and a Random Forest classifier, see Table 12 for the MED grid. Actual AIS data at the ship level is expected to improve significantly the performance of the ML techniques by bringing less imbalance at the two classes "ship-affected" versus "background".

**Table 12** Results of detection models

| Model | Accuracy | Precision (ships) | Recall (ships) | F1 (ships) | ROC-AUC |
|---|---|---|---|---|---|
| Logistic Regression | 0.66 | 0.26 | 0.51 | 0.35 | 0.635 |
| Random Forest | 0.74 | 0.32 | 0.42 | 0.36 | 0.673 |

**Logistic Regression** detection model has been implemented for the second half of the year 2024 (6 months in total)

- Class 0 refers to the background pixels without the effect of ships: 353771 observations without ship signature.
- Class 1 refers to the ship-affected pixels where the ship-tracks are detected: 76864 observations with ship signature.

The training is built on a relative imbalanced dataset as it contains few ship-affected cloud data with a ratio of 18% against the background cloud data. That is moderate imbalance; not extreme, but enough to bias logistic regression toward Class 0. We also notice that the feature space separating ship vs non-ship is region-dependent.

**Random Forest** improves the overall accuracy from 66% to 74%. Precision for ships increased slightly from 0.26 to 0.32. Recall decreased slightly for ships from 0.51 to 0.42, but F1 is similar (from 0.35 to 0.36). ROC-AUC improved from 0.635 to 0.673, which indicates better overall ranking ability. To summarize, Random Forest Classifier is capturing the data structure better than the Logistic Regression Classifier, but because the dataset is imbalanced (18% of pixels are ship-affected), recall vs precision for ship-tracks is still a trade-off.

**Room for improvements on the detection method**

- The imbalance between the ship-affected versus background pixels could significantly be reduced if high temporal resolution AIS data are used instead of the EMODnet vessel maps. This can improve a lot the ship detection algorithm as a denser training set can mitigate the bias of the model towards the ship-free class.
- The impact of meteorology can be further studied if we ingest meteorological parameters (e.g., from from ERA5 Reanalysis)**.** Weather conditions significantly affect pollutant dispersion and must be included as control variables (e.g., wind speed and direction, relative humidity, etc.)
- Provided that ship tracks could be detected from the TROPOMI/S5P cloud product, the S4 high temporal resolution will be the key sensor to monitor the diurnal cycle of shipping emissions and their perturbations into the marine clouds. Future ship-track cloud datasets should be generated based on the S4 $NO_2$/Aerosol/Cloud operational products together with the re-gridded to the S4 footprints cloud data from the FCI (Flexible Combined Imager) sensor.
- Ingestion of other satellite observations from all relevant sensors will improve the detection method, as the additional feature variables will impact significantly the performance of the classifier to predict the target variable.

### 4.2.2 Impact Assessment

#### 4.2.2.1 Radiative Impact

The analysis is started with a sensitivity study of the TOA reflection (upwelling shortwave) function as a function of cloud optical thickness at a set of wavelengths located in atmospheric transmission windows. These wavelengths are chosen to minimize gaseous absorption, so that the observed variability is dominated by cloud scattering and, to first order, by the dependence of cloud reflectance on optical depth. In all simulations considered here, the cloud top height is fixed at 3 km. For sensitivity study also the case of high-altitude clouds with the cloud top height set to 10 km is considered.

To interpret the COT-dependence, the simulated TOA reflection are compared with a widely used two-stream (broadband) approximation for the cloud albedo/reflectance of a plane-parallel, weakly absorbing (nearly conservative) scattering layer. In its simplest form, the reflectance is represented as a saturating function of optical thickness, $R(\tau) \approx \tau/(\tau+\beta)$, where $\tau$ is the cloud optical thickness and $\beta$ is an empirical

constant, that depends on the chosen two-stream closure and on the effective scattering anisotropy of cloud droplets. For liquid-water clouds in the shortwave, a value $\beta \approx 7–8$ is frequently used as a practical broad-band approximation; in this analysis $\beta = 7.7$ is adopted

This functional form follows from classical two-stream radiative transfer parameterizations and has been used extensively in cloud-albedo sensitivity studies.

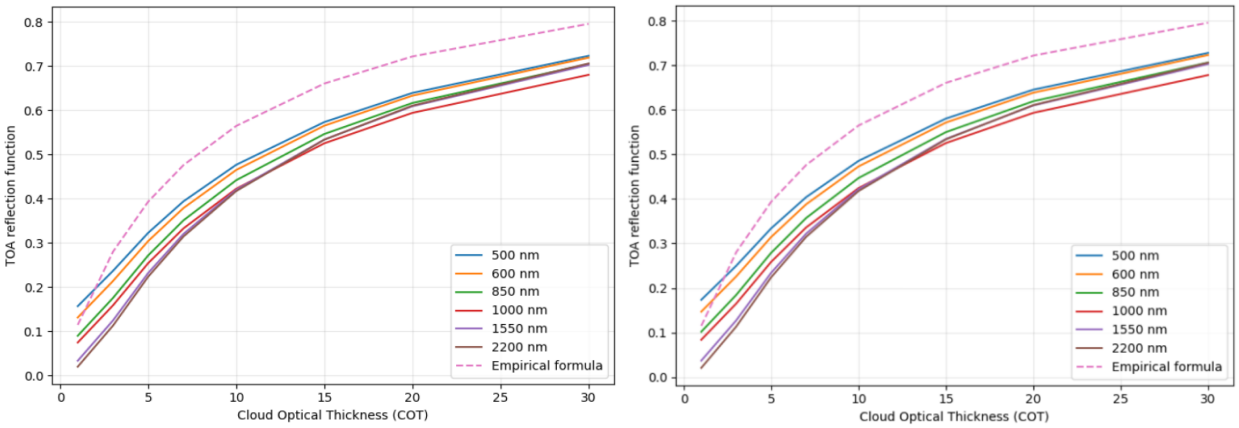


**Figure 106** Reflection function at TOA as a function of cloud optical thiclkness at different wavelengths (corresponding to atmospheric windows) and results of empirical formula for a purely cloudy layer. The clout top height is 3 km (left) and 10 km (right).

The sensitivity analysis reveals that the change in the TOA reflection function with respect to COT is similar across the considered atmospheric window wavelengths. In other words, although the absolute magnitude of the upwelling irradiance varies spectrally, the functional dependence on optical thickness exhibits nearly the same shape at all selected wavelengths.

To quantify the radiative impact of a perturbation in cloud optical thickness, the TOA shortwave radiative forcing is estimated directly from the change in simulated upward irradiance. Within a spectral range 400-2500 nm the upwelling TOA irradiance $E$(COT) is computed for a given value of cloud optical thickness. Then the calculation is repeated for the perturbed state COT+ΔCOT, obtaining $E$(COT+ΔCOT). The shortwave radiative forcing at TOA associated with the COT perturbation is defined as the difference between these two states:

$$\mathbf{\Delta F} = -(\boldsymbol{E}(\mathbf{COT} + \mathbf{\Delta COT}) - \boldsymbol{E}(\mathbf{COT})) \cdot \boldsymbol{S_0} \qquad (13)$$

where $S_0$ = 1361 W/m².

With this sign convention, a negative value corresponds to an increase in reflected (upward) irradiance at TOA, implying a cooling tendency of the Earth–atmosphere system, while a positive value indicates a reduction in reflected energy and a warming as a consequence.

**Location MED**

Example of MED scene (see Section 4.2.1.2 for details) with local pixel-by-pixel perturbations in COT and corresponding local radiative forcings are shown in Figure 107.

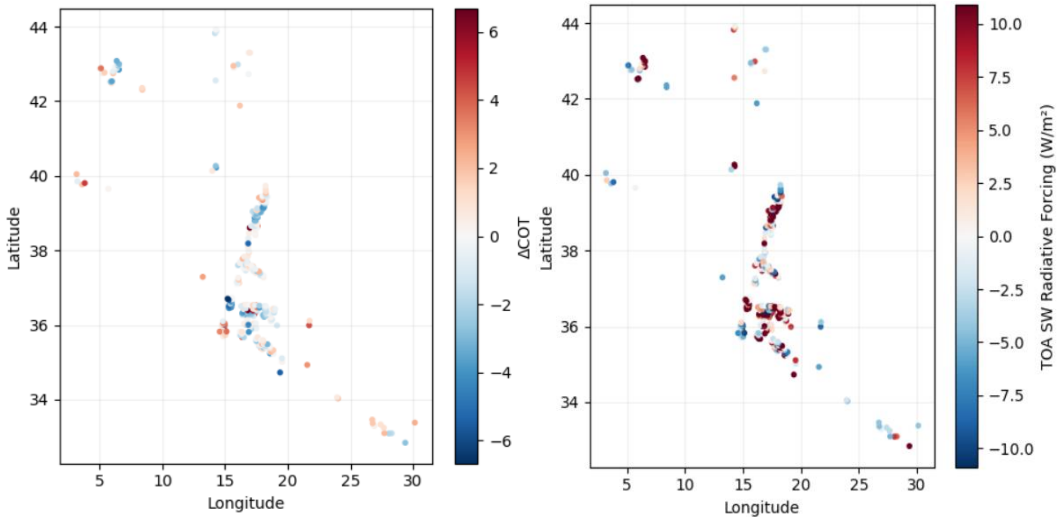


**Figure 107** Example of a scene with COT perturbations and corresponding radiative forcings.

The COT perturbation field is biased toward negative values (thinning), with mean/median ΔCOT ≈ −0.25/−0.15 and wide tails (5–95%: −4.24 to +3.66). Consistently, the instantaneous TOA shortwave flux perturbation computed under SZA=30° exhibits a positive mean (+50 W/m²) and a much smaller positive median (+8 W/m²), indicating a strongly skewed distribution dominated by a positive tail (95th percentile +331 W/m²). This suggests that a limited number of pixels with large negative ΔCOT (likely in optically thin regimes or near cloud edges) control the mean response. Such large radiative forcing values correspond to the cases with relatively small COT but comparable perturbations.

For a more accurate assessment of radiative forcing, it is essential to account not only for changes in cloud optical thickness but also for perturbations in cloud droplet effective radius. Variations in droplet size modify the cloud's scattering properties and therefore its reflectance, even if the optical thickness remains unchanged.

An increase in droplet effective radius leads to a more forward-peaked scattering phase function (i.e., a higher asymmetry parameter g). As a result, a larger fraction of radiation is scattered in the forward direction, reducing backscattering and decreasing cloud reflectance. This reduction in reflected shortwave radiation at the top of the atmosphere produces a positive radiative forcing (warming).

Conversely, a decrease in droplet effective radius makes scattering more isotropic (lower g), enhancing backscattering and increasing cloud reflectance. This mechanism, commonly referred to as the Twomey effect, leads to an increase in reflected solar radiation and thus to negative radiative forcing (cooling). An example of the radiative forcing map is shown in Figure 108.

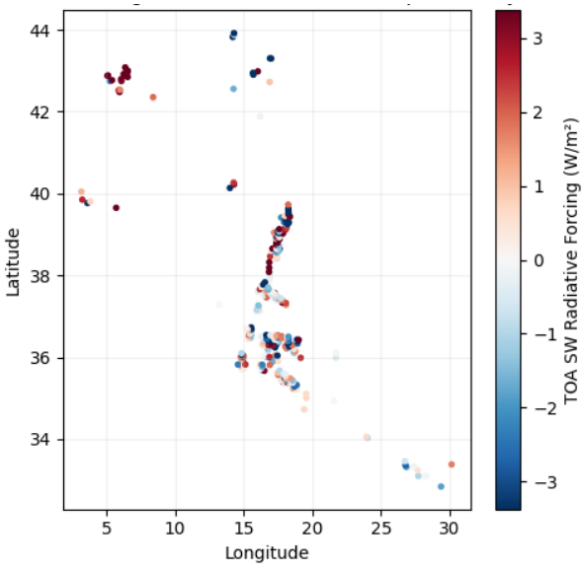


**Figure 108** Radiative forcing due to perturbation in the droplet radius.

Radiative forcing calculated at the level of individual pixels can reach large magnitudes. These values represent highly localized responses to microphysical perturbations in cloud optical thickness and droplet effective radius. At pixel scale, radiative forcing is sensitive to nonlinearities in cloud reflectance, variations in background cloud properties, and instantaneous solar geometry. Consequently, individual pixels may exhibit strong positive or negative forcing. However, such values should not be interpreted as large-scale climate forcing. They reflect local, short-term radiative adjustments rather than an integrated atmospheric response.

To obtain a physically meaningful estimate of the climatic impact, spatial averaging over the domain of interest was performed. This averaging reduces the influence of extreme local values and provides an estimate of the mean radiative effect associated with the perturbation. The resulting area-averaged forcing represents the net radiative impact at regional scale and is the appropriate metric for assessing the potential large-scale influence of the perturbation. The histograms of the local radiative forcing values, together with their corresponding mean values, are presented in Figure 118. The results indicate a net negative radiative forcing, implying an overall cooling effect associated with the cloud microphysical perturbations. However, the distributions of local radiative forcing are broad, and individual pixel-level values can be substantially larger in magnitude than the domain-averaged forcing. This reflects the strong spatial variability and nonlinear sensitivity of radiative response to local cloud properties. Consequently, while the mean forcing provides an estimate of the net effect, the wide spread of values highlights significant local heterogeneity. Therefore, this analysis should be regarded as illustrative rather than as a precise quantitative assessment of regional or climate-scale radiative forcing.

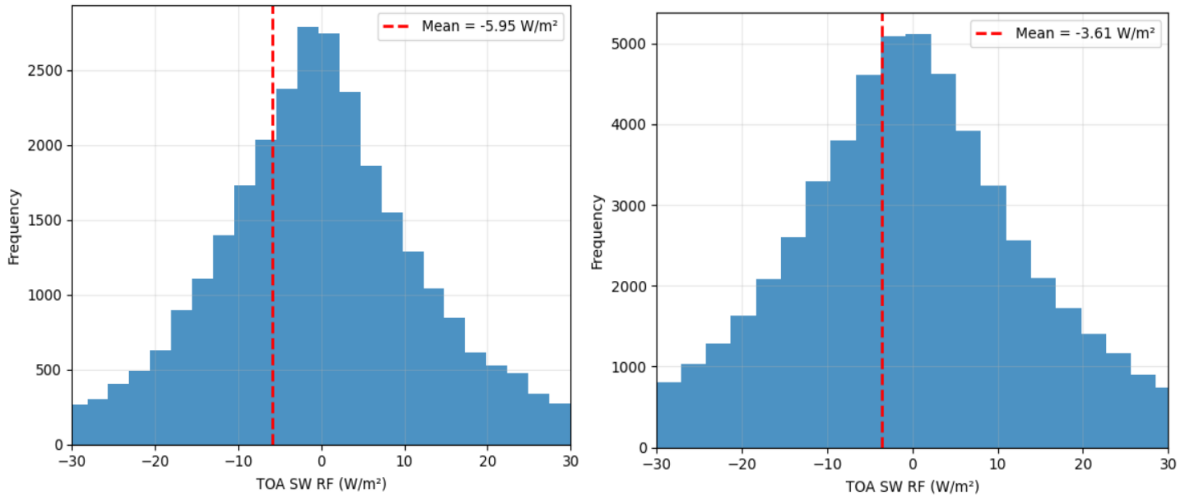


**Figure 109** Histograms of radiative forcings in MED region (left) and NEA region (right)

#### 4.2.2.2 Results and consequences for ERF

For the observations-derived perturbation of a mere 1%, no clear perturbation to the top-of-atmosphere radiation budget or surface air temperature is detected within the region of interest (Figure 110), suggesting that the imposed perturbation is masked by signals arising from cloud adjustments. In turn, for the strong perturbation of a factor of 10, a regional effective radiative forcing of –15 $Wm^{-2}$ was obtained, with little perturbation to the top-of-atmosphere radiation budget outside the region of interest. Similarly, a regional effective radiative forcing of –15 $Wm^{-2}$ was obtained for the perturbation in the Eastern Mediterranean, again with little perturbation to the top-of-atmosphere radiation budget outside the region of interest.

In consequence, there is no discernible perturbation of temperatures in the observations-tied perturbation (Figure 111). For the strong perturbation, in turn, surface air temperature increased locally by up to 0.5K, which is not fully understood but may be related to the fixed sea surface temperature condition in the model. Precipitation responses extend beyond the region of imposed perturbation (Figure 111), reflecting the strong coupling between latent heating, large-scale circulation, and atmospheric energy balance. A similar spatial pattern of precipitation response is obtained for the strong and the weak perturbation simulations. The absence of a clear scaling of precipitation response with the magnitude of the imposed liquid water path perturbation suggests that the observed precipitation changes are not directly caused by the perturbation, but are instead dominated by internal variability and rapid adjustment processes.

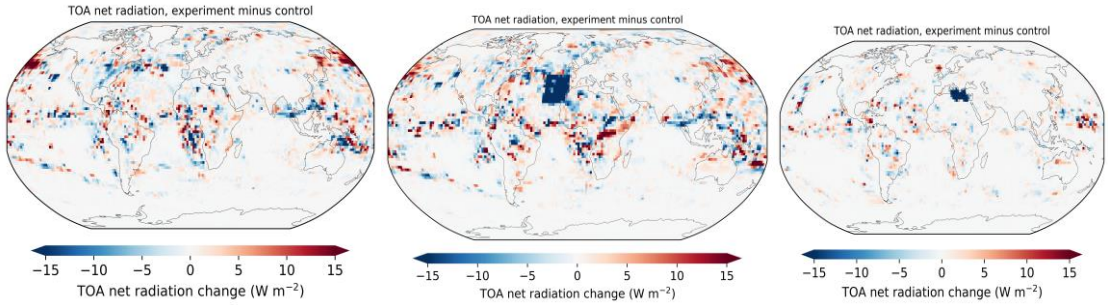


Figure 110 Sensitivity study for MCB within the ICON model. Left: perturbation domain in the Eastern Mediterranean (blue outline). Within this domain, cloud liquid water content is perturbed by an idealised factor of 10. Right: resulting effective radiative forcing

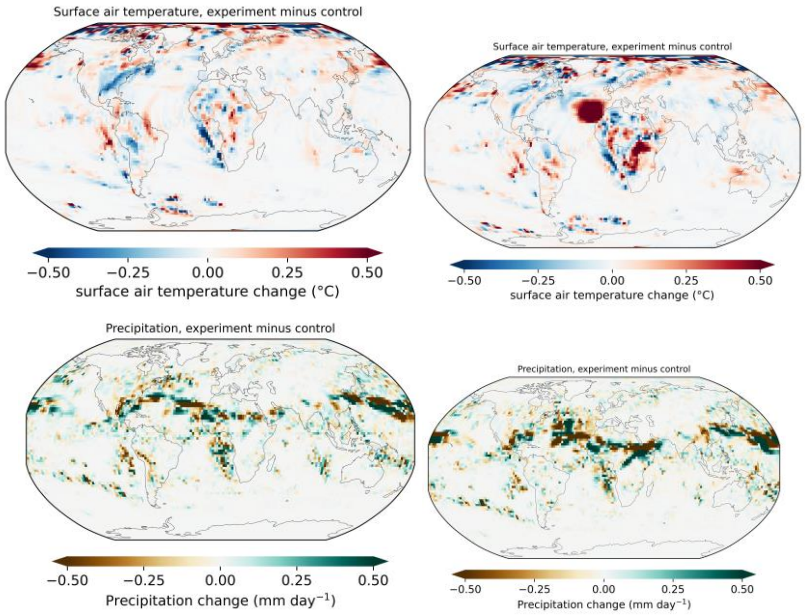


**Figure 111** Climate consequences of MCB. Top row: near-surface air temperature response to (left) 1% perturbation of cloud water, (right) factor of 10 increase. Bottom row: precipitation responses.

### 4.2.3 Risks

The ICON simulations point to the importance of Earth system feedbacks in the response to MCB. Specifically, the interaction of ocean and atmospheric dynamics matters. The current simulation setup - atmosphere/land-only simulations, with ocean decoupled and replaced by imposed patterns of sea surface temperature - mimics an ocean with infinite response timescales. But also a coupled ocean would have response time scales much longer than the atmospheric ones, and so the lack of cooling effect in the region is a signal that needs to be taken seriously. Further model and data analysis is required to investigate the risk of not obtaining a pattern of cooling that matches the expectations.

### 4.2.4 Outlook

The shipping emissions can be detected in the $NO_2$ Tropospheric column. The sign of the perturbation is always positive; the magnitude of the $NO_2$ perturbation is large (~30% for the Mediterranean region). On the contrary, the perturbations of the cloud parameters may change sign from day to day. The natural variability of the clouds masks the signal of the modification due to the ship-emitted particles at their cloud base. Therefore, the ship-track detection in all conditions could be challenging. The primary goal is to develop a ship-track detection model accurate enough to enable the estimation of local pixel-by-pixel cloud perturbations. The latter is only possible with densely populated ship-relevant datasets which could be used for the training of the ML classifier. Until that trustworthy ship-track detection model is built, the most robust way to quantify cloud perturbations due to ships is the regional mean perturbation formula.

The framework developed in *ACtIon4Cooling* provides a robust conceptual structure for advancing MCB detectability studies. The **local** pixel-by-pixel **perturbation dataset (nearest-**neighbor **reference)** is particularly strong for process attribution, as it isolates ship-induced cloud modifications relative to their immediate background environment. By minimizing the influence of large-scale meteorological variability, this framework enables a clearer mechanistic interpretation of microphysical and macrophysical cloud responses, thereby supporting causal attribution studies and model evaluation efforts. In addition to that the **regional daily perturbation dataset (ship-mean versus background-mean approach)** is more directly aligned with policy-relevant detectability questions. By aggregating signals at regional and daily scales, it reflects how monitoring systems for SRM would likely be operationalized in practice. This approach enables statistical robustness and provides a bridge between process-level understanding and operational climate intervention monitoring strategies. Together, these complementary perspectives establish a scientifically coherent pathway from mechanistic understanding to real-world monitoring capability, forming a strong analytical foundation for future MCB observation and attribution frameworks.

#### 4.2.4.1 Future work for ship-track MCB analysis

Similar scientific analysis needs to be extended to other regions, like the NorthEastern Pacific (−155° to −115° W and 10° to 40° N): one of the major stratocumulus decks that coincides with major shipping corridors (Zhang et al. 2025). Long-Term Analysis for IMO2020 Impacts can give some insight on the open scientific question whether the SST anomalies have been amplified by the recent reduction in aerosol emissions from shipping, linked to the implementation of the International Maritime Organization (IMO) 2020 regulation. This regulation, effective from 1 January 2020, mandated a global reduction in the sulfur content of marine fuels from 3.5% to 0.5%. As a result, sulfur dioxide ($SO_2$) emissions from ships have decreased substantially, leading to a reduction in the formation of sulfate aerosols in the marine boundary layer. To study the effect of the IMO2020 fuel-sulfur reduction, longer EO datasets are required—covering multiple years before and after 2020—to assess how reductions in sulfate aerosol emissions influence cloud brightness, SSTs, and radiative forcing.

For complementary ACI information over oceans, PACE payload sensors could be used to provide valuable data (if time permits). The Ocean Color Instrument (OCI) is capable of retrieving aerosol optical properties over oceans and detecting aerosol plumes, as well as surface albedo, using high-spectral-resolution measurements from UV to NIR wavelengths. SPEXone, a multi-angle polarimeter, is highly relevant for precise aerosol characterization, including aerosol size, composition, and refractive index. This instrument could be instrumental in assessing cloud condensation nuclei (CCN) efficiency, which is crucial for understanding MCB mechanisms. HARP2, also a multi-angle and multi-spectral polarimeter, extends the capabilities of SPEXone by offering higher spatial coverage and providing additional cloud-related data. It is designed to measure cloud properties such as droplet size, phase, and thickness, making it well-suited for MCB studies.

The developed methodology to detect the MCB-like perturbations for the natural analogue of ship-tracks would benefit from a validation of the *ACtIon4Cooling* output dataset. Measurements from ground-based aerosol/cloud networks (e.g., ACTRIS and AERONET network) over sites which favor the marine cloud presence and are located close shipping lines can be used. Among the suitable sites, which capture marine clouds observations, is PANGEA (PANhellenic GEophysical observatory of Antikythera) observatory at the island of Antikythera (35.861N, 23.310E, 110m a.s.l). PANGEA is an active member of ACTRIS and AERONET network and a satellite Cal/Val center in the Mediterranean region. Validation of the MCB dataset can be also strengthened from ESA funded experimental campaigns (e.g. ESA ASKOS campaign conducted at the Ocean Science Centre in Mindelo on São Vicente Island, Cabo Verde). Finally, the ESA EarthCARE mission (Illingworth et al. 2015, Wehr et al., 2023), supported by the complementary datasets of the NASA PACE mission (Werdell et al., 2019), thanks to their unique designs, offers the unparalleled opportunity to validate the *ACtIon4Cooling* MCB datasets.

#### 4.2.4.2 Other Potential Analogues

Volcanic eruptions have also been considered as potential analogues to MCB studies (Breen et al., 2021) by analyzing the effects of aerosols on marine clouds after volcanic eruptions or degassing events. The researchers identify a significant increase in reflected sunlight, primarily due to aerosol-induced enhancements in cloud cover. These findings suggest that MCB could be more effective than previously estimated, especially when implemented under humid and stable meteorological conditions.

Smoke from Biomass Burning emissions as the 2019–20 Australian wildfires (Fasullo et al, 2023) or other types of aerosols which could have a brightening impact on clouds.

## 4.3 CCT mechanism

### 4.3.1 Scientific Analysis

The CCT mechanism has been studies with aviation-relevant cirrus clouds as a natural analogue based on the analysis of EO observations in the frame of *ACtIon4Cooling*, which is very much promising for the corresponding perspectives. Previous studies reported that aviation emissions in the cirrus levels likely increase heterogeneous freezing and exert indirect effects on naturally occurring cirrus, resulting in enhanced PLDR (Urbanek et al., 2018). This can be considered as an indicator for cirrus clouds that formed and evolved in the high-aviation regions. Further, high-PLDR-mode cirrus clouds tend to exhibit larger size and lower number concentration (e.g. Groß et al., 2023), which mimics the CCT strategies. With the lidar measurements of CALIOP and IIR-CALIOP retrievals, the changes in optical and microphysical properties of

cirrus clouds induced by aviation impacts have been investigated by comparing their properties at different latitude domains and in a long-term period.

Figure 112 presents the distributions of cirrus PLDR for each 5-degree latitude bin in autumn derived from both day- and night-time observations from years of 2014 and 2018-2021 as well as all 5 years combined. The year-to-year variabilities in PLDR show larger values in the pre-COVID years than in 2020 and 2021 under the aviation reduction due to the COVID-19 pandemic at midlatitudes (Li and Groß, 2021), which, however, is less apparent at high latitudes due to the already low aviation densities. Furthermore, the composite values of PLDR of 5 years combined show a clear decrease with increasing latitude, which is also seen in other seasons. Besides the seasonality, a direct comparison between different latitudes shows generally larger PLDR values at midlatitudes than high latitudes. The exceptions with enhancements in autumn 2019 and winter 2019/2020 are presumed to be related to lower temperatures as well as higher aerosol loading (including soot and smoke) caused by the long-lasting strong stratospheric polar vortex during this period (Manney et al., 2022; Ansmann et al., 2023). Except for the reductions in PLDR at midlatitudes during the COVID-19 restriction, the values of PLDR at midlatitudes are relatively stable, showing small year-to-year variabilities. In contrast, the year-to-year variabilities in PLDR at high latitudes are much larger, which are discernible in all seasons.

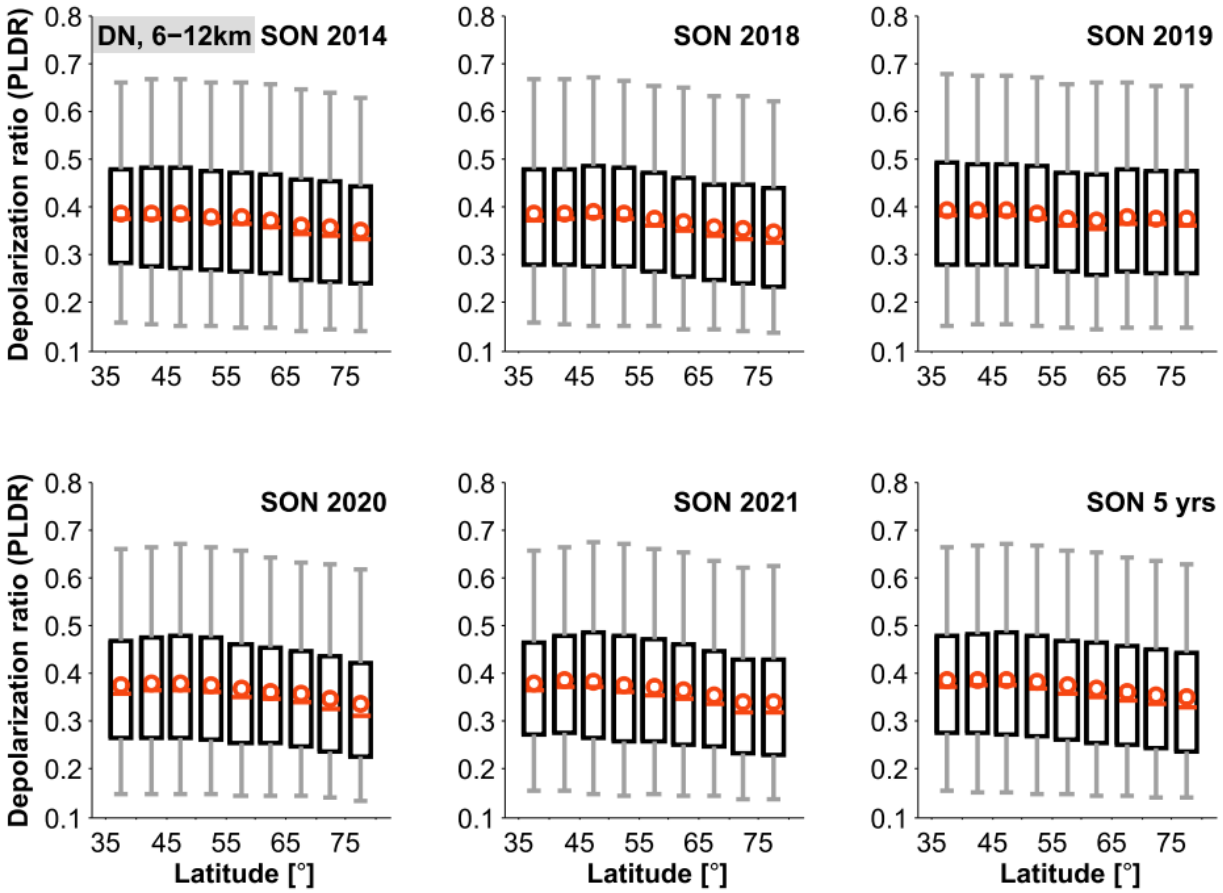


**Figure 112** Box plot representation of the composite distribution of particle linear depolarization ratio (PLDR) of cirrus clouds in each 5-degree latitude bin from 35–80°N in autumn (September-October-November) in years of 2014 and 2018-2021 as well as the composite results of all 5 years combined. Boxes represent the 25th-75th percentiles of the PLDR distributions (top and bottom, respectively). Solid lines through the corresponding boxes stand for the medians and circles for the means. Whiskers indicates the 5$^{th}$ and 95$^{th}$ percentiles, and outliers with values falling within the largest 5% and the smallest 5% of the PLDR distributions are not shown here.

The resulting vertical profiles of cirrus extinction coefficient (medians) in autumn are shown in the left panel of Figure 113. In general, they reveal a decrease with increasing altitude for all the cases in different years and for both mid- and high latitudes, indicating smaller and fewer ice crystals at higher altitudes.

Besides the differences in the altitudes containing cirrus formation at different latitudes (with nearly 1.5-km discrepancy), cirrus clouds probed at high latitudes are characterized with smaller extinction coefficients than those at midlatitudes (Gasparini et al., 2018). This is closely linked to the dominant formation processes of ice crystals depending on temperature and relative humidity over ice (RHi). While liquid-origin cirrus clouds dominate at relatively warmer and moister midlatitudes via heterogeneous nucleation, in situ-formed cirrus clouds dominate at colder and drier air masses prone to occurring at high latitudes (Gasparini et al., 2018). Further, the differences between cirrus extinction coefficients at mid- and high latitudes become smaller with increasing altitudes from 0.14 to 0.03 km−1 derived from the composite values of all 5-year observations.

In the right panel of Figure 113, the distribution of extinction coefficients at latitudes in box plots is shown. At mid-latitudes, the year-to-year variations in extinction coefficients are discernible with a slight increase from 2014 to 2019 and with notable reductions in 2020 and 2021, which might be partially related to the aviation reduction during the COVID-19 period. However, the influences of variable meteorological conditions cannot be ruled out (e.g. Schumann et al., 2021a; Quaas et al., 2021; Li and Groß, 2021). At high latitudes, however, extinction coefficients are comparable in different years with an exception of a small enhancement in 2019 with medians. The comparison of extinction coefficient distributions across latitudes shows a clear consistence in different years, i.e. the extinction coefficients are larger at midlatitudes than at high latitudes. The seasonality in extinction coefficient distributions is noticeable, showing the largest extinction coefficients in winter and the smallest in summer. In addition, the latitudinal comparison shows a stronger seasonal variation at high latitudes than at midlatitudes. Furthermore, the year-to-year variations are stronger in autumn and winter than in spring and summer for both latitude domains. In particular, extinction coefficients during the COVID-19 pandemic are in general smaller than those in the other non-COVID years at midlatitudes, whereas at high latitudes, the reductions in extinction coefficient cannot be clearly recognized.

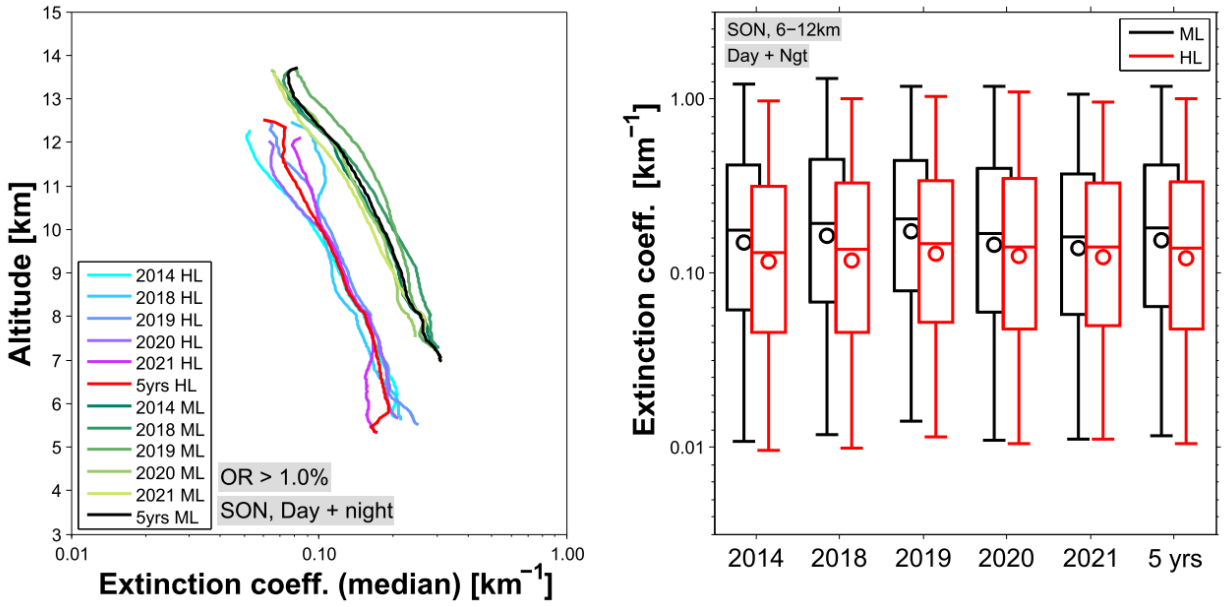


**Figure 113** Left panel: Profiles of the extinction coefficient medians of ice crystals within cirrus clouds observed with CALIPSO in autumn in years of 2014 and 2018-2021. Data with the cirrus occurrence rates less than 1.0% are ignored. Right panel: Box plot representations of the extinction coefficient distributions in different year and all 5 years combined. The results in the high-latitude regions are shown in red and in the midlatitude regions in black.

From the DARDAR CLOUD product, the effective radius of ice crystals $R_{eff}$ in 2014 and their distributions was determined along latitudes are shown in Figure 114. The seasonal dependence in the distributions of $R_{eff}$ is discernable, which is stronger at midlatitudes than high latitudes. Besides the seasonality, $R_{eff}$ show a clear decrease with increasing latitudes in spring, autumn, and winter. In summer, however, no pronounced latitudinal dependence of $R_{eff}$ is evident, although the $R_{eff}$ values at high latitudes are slightly larger than those at midlatitudes. The comparison of $R_{eff}$ across latitudes shown in the box plots exhibits larger

values at midlatitudes than high latitudes in other seasons than in summer when there is a different tendency in $R_{eff}$. The larger ice crystals are presumed to be related to more heterogeneous freezing with specific aerosols acting as INPs, such as aviation soot, taking place at midlatitudes, since the aviation density at midlatitudes are much denser than high latitudes. However, the aviation effects on cirrus cloud in summer are weaker, if they are not negligible, than in other seasons, which has been reported in the previous studies (e.g. Li and Groß, 2022).

Aviation-induced soot particles that are more significant at midlatitudes than high latitudes are emitted directly into the cirrus regime and could often show larger concentrations compared to other aerosols at aviation cruising altitudes. Although soot particles from modern aircraft engines may not be efficient INPs (Testa et al., 2024a, b; Yu et al., 2024), they can act as condensation nuclei for forming tiny water droplets, especially, as they aggregate and mix with other substances. These processes will influence ice cloud formation indirectly by competing with other aerosols for available water vapor and suppressing homogeneous nucleation. Furthermore, soot particles play a crucial role in the formation of contrails and contrail-cirrus. They may undergo multiple cloud cycles during their residence time in the atmosphere and thus improve their ice-nucleating ability via PCF. Notably, ice crystals forming through heterogeneous freezing are characterized by larger sizes and more irregular shapes. In turn it is hypothesized that the differences between heterogeneous and homogeneous freezing depending on latitudes may be responsible for the observed latitudinal dependency of cirrus cloud properties.

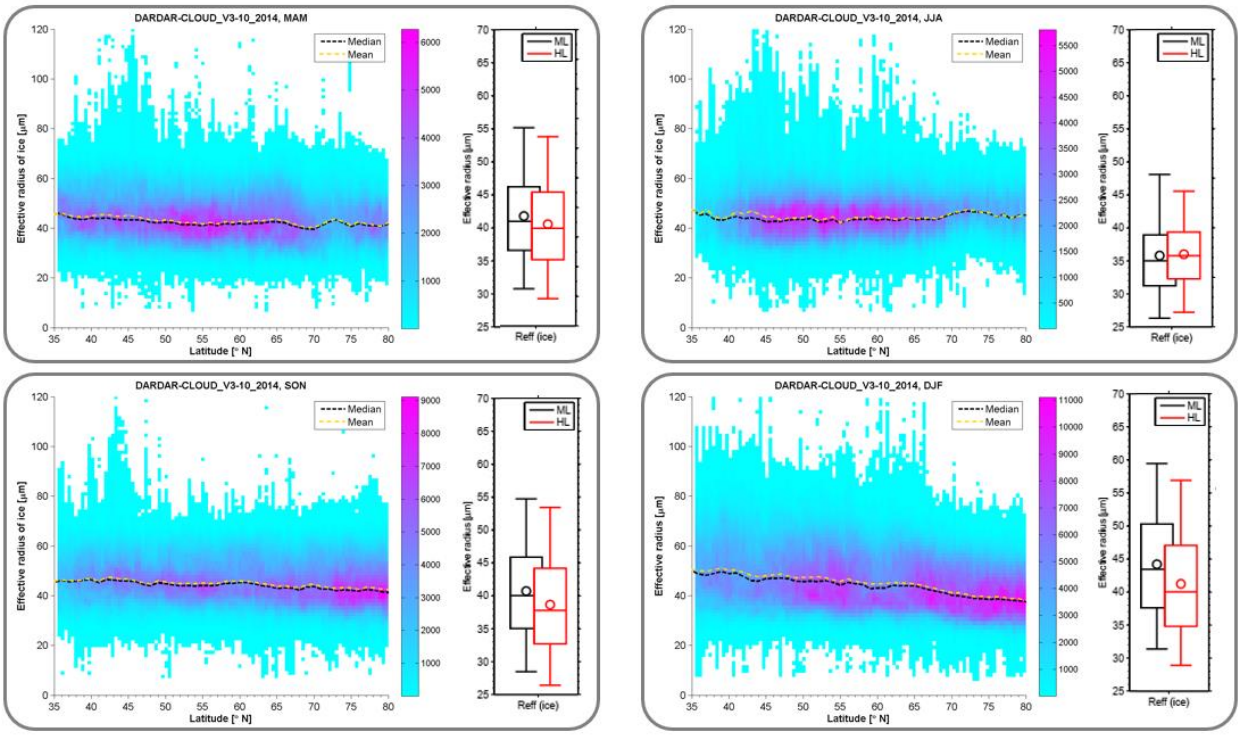


**Figure 114** The variations of effective radius of ice crystals depending on latitudes from the DARDAR cloud products in 2014 with different seasons shown in different panels. The number densities of the effective radius distribution are shown in different colours. The box plots represent the distributions of ice crystal radii at midlatitudes (in black) and high latitudes (in red), respectively.

From the IIR-CALIOP retrievals (Mitchell et al., 2025), the effective diameters (De) and number concentrations (Ni) of cirrus clouds are derived for spring in the 11 years from 2010 to 2020. Their distributions are shown in box plots in Figure 115. In general, cirrus clouds at midlatitudes exhibit larger De but lower Ni compared to high latitudes. The middle 50% of De at midlatitudes roughly range from ~27 to 52 μm and at high latitudes from ~24 to 49 μm. And for Ni, the middle 50% of the data fall within the range from ~20 to 300 $L^{-1}$ at midlatitudes and from ~30 to 500 $L^{-1}$ at high latitudes. Furthermore, there is an increasing trend in De but a decreasing trend in Ni for both latitude domains. The reasons for the trends could be connected to aviation emissions as well as other anthropogenic activities. When looking at the latitudinal differences in both De and Ni more closely, we can see that the differences become smaller along the timelines of years.

This tendency may be attributed to the well-known Arctic amplification (AA) which is the near-surface air temperature in the Arctic increase in a larger rate compared to the rest of the planet by a factor of four (Rantanen et al., 2022). An exception with a clear reduction in De and an enhancement in Ni can be seen in 2020 at high latitudes, which, however, likely attribute to meteorological conditions other than aviation impacts since the reduction in aviation due to the COVID-19 pandemic is slight.

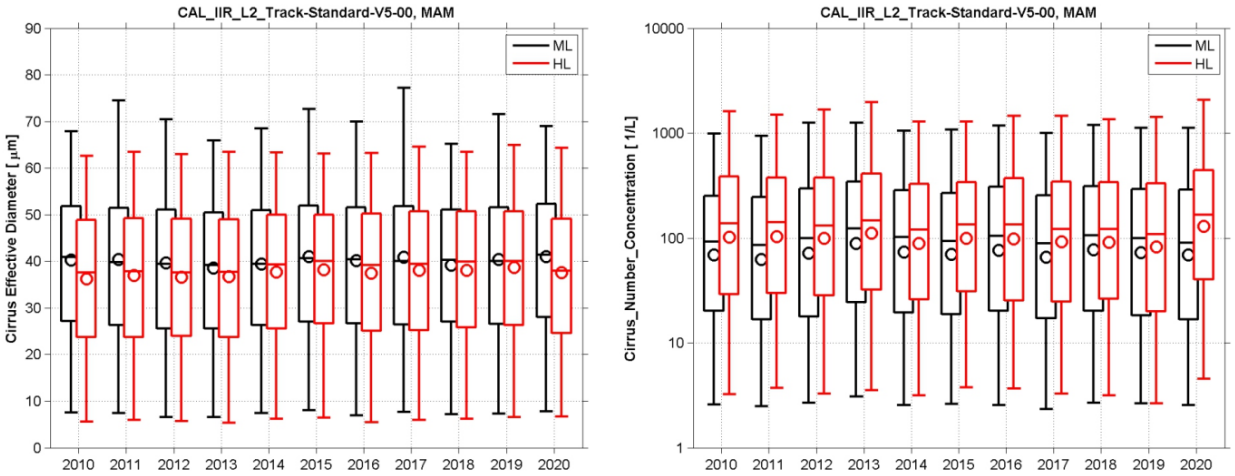


**Figure 115** Box plot representation of the composite distribution of cirrus effective diameter (De, in the left panel) and cirrus number concentration (Ni, in the right panel) derived from IIR-CALIOP retrievals in years of 2010-2020. The descriptions of box plots in details can be found in the caption of Figure 112. The results at high latitudes are shown in red and midlatitudes in black.

With the climatological values of De and Ni in 10 years, the baseline values of them can be calculated with all the observations in years of 2010-2019. The perturbations of De and Ni are further calculated and the distributions in 2019 and 2020 in different latitude domains are shown in Figure 116. In the case of De, the perturbations fall mostly within the range from -15 to 15 µm. At high latitudes the perturbations are larger in 2019 than in 2020, whereas at midlatitudes those are smaller in 2019 than in 2020. For Ni, the perturbations mostly vary from -200 to 200 $L^{-1}$. At high latitudes, the values are much smaller with a negative median in 2019 than in 2020. At midlatitudes, however, the perturbations are both of negative medians and slightly larger in 2019 than in 2020.

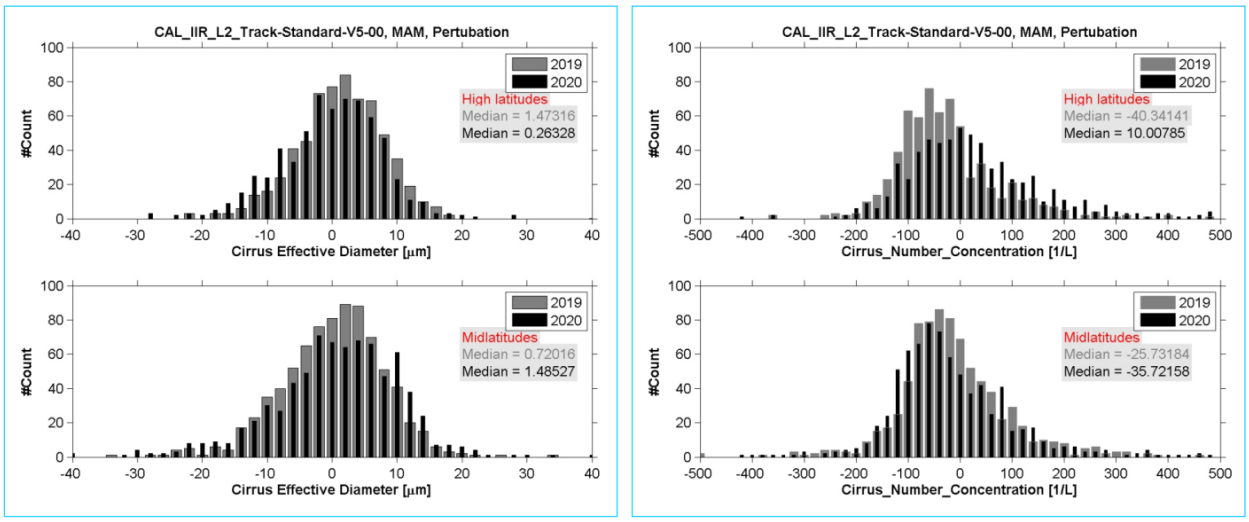


**Figure 116** Histograms of the perturbations in cirrus De (left panels) and cirrus Ni (right panels). The results at high latitudes are shown in the upper panels and midlatitude in the lower panels. Furthermore, the results in 2019 and 2020 for comparisons are shown in different grayscales.

As mentioned above that civil aviation grew strongly in terms of $CO_2$ emissions and flight densities in the past years and even decades until the outbreak of the COVID-19 in 2020. Previous study shows that the monthly median PLDR (as well as the de-seasonalised time series) follows a statistically significant positive trend over the 10-year pre-COVID period, which is closely correlated with $CO_2$ emissions from aviation over Europe (Li and Groß, 2022). They also report that the cirrus occurrence shows a slight negative trend over the same period. The dataset was extended to 2007 and calculate the geometrical thickness of cirrus clouds defined as the sum of altitude extension with cirrus formation despite of the layers of cirrus clouds (i.e., either clouds are continually distributed or not). The resulting distributions of cirrus geometrical thickness are shown in normalized number concentrations in Figure 117. The data are derived from the lidar observations of CALIPSO at the typical altitudes of cirrus formation from 8 to 12 km and at temperatures below -38°C to assure only ice clouds considered.

Figure 117 provides a general climatology of the distributions of cirrus geometrical thickness in the European part of midlatitudes. The majority of cirrus geometrical thickness falls within the range below 1.5 km. The distributions show a clear seasonality as expected with the maxima in winter and the minima in summer. There are no clear reductions in geometrical thickness like in depolarization during the COVID-19 period from March to December 2020 (Li and Groß, 2021 and 2022). The 14-year trends in the quartiles of geometrical thickness are determined with a degree polynomial fitting and the calculated slopes for all the quartiles are shown in the insets of Figure 117. It seems there are CCT-like effects that aviation exhaust particles can lead to a decrease in cirrus cloud thickness under certain atmospheric conditions, which are supported by previous studies (Tully et al., 2022; Maciel et al., 2023). For the concrete reason, however, it cannot be excluded, that the influence of changing thermodynamic conditions. This should further be explored with more efforts.

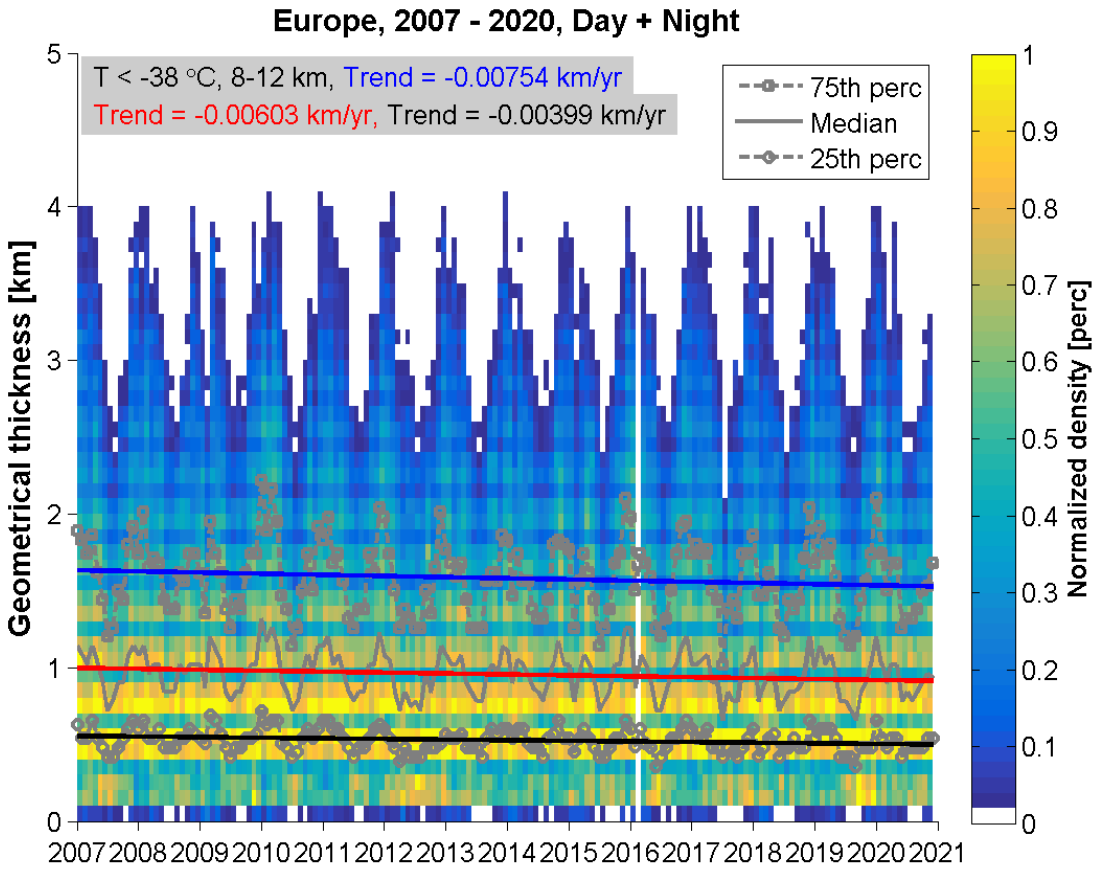


**Figure 117** Number densities of the distributions of cirrus geometrical thickness normalized for each month from January 2007 to December 2020 at midlatitudes (35–60° N; 15° W–15° E). The results are derived from lidar observations of CALIPSO at the typical cirrus levels from 8 to 12 km and at temperatures below -38 $^{O}$C. The colour codes are used to visualize the relative number densities of scatter point data with the maximum number density indicated by 1 in the colour bar.

### 4.3.2 Impact Assessment

#### 4.3.2.1 Radiative Impact

To estimate the radiative impact of CCT, it is necessary to account for both shortwave and longwave components of the radiative budget. Cirrus clouds influence the Earth's radiation balance in two competing ways: they reflect incoming solar radiation in the shortwave range and trap outgoing terrestrial radiation in the longwave range. Therefore, a consistent assessment of CCT requires quantifying both effects.

The shortwave response is evaluated using the pyDOME radiative transfer model in the spectral range 400–2500 nm. For each prescribed COT, we compute the upward irradiance at the TOA. The broadband SW radiative effect is obtained by spectrally integrating the reflected flux. Examples of such simulations for different cirrus optical thicknesses are shown in Figure 118.

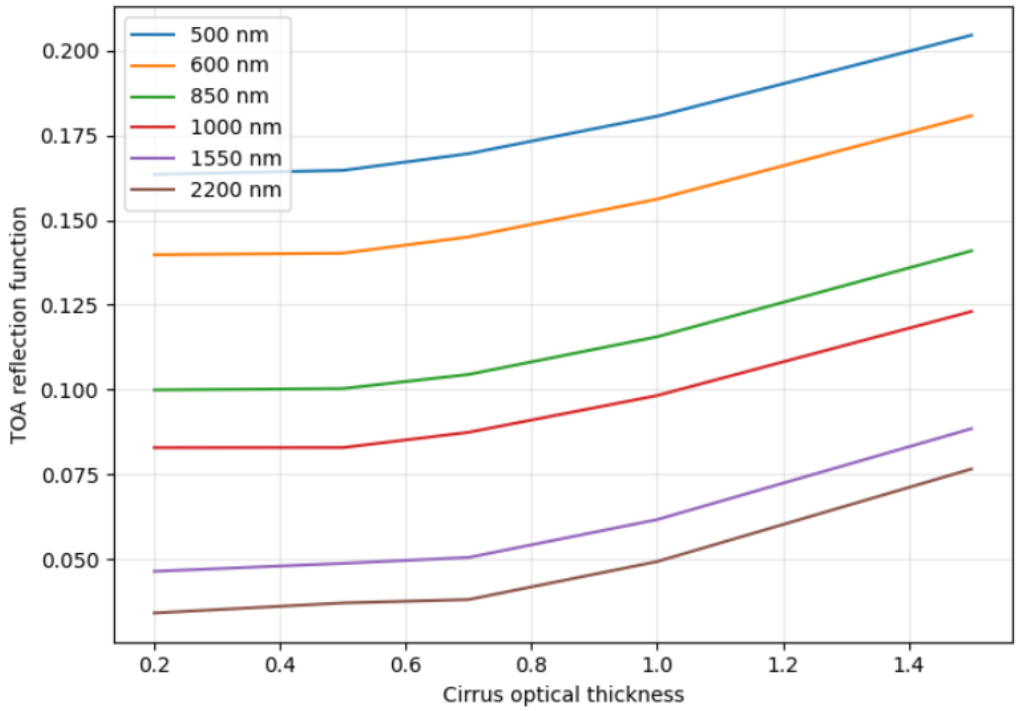


**Figure 118** Dependence of the reflection function at TOA as a function of cirrus optical thickness

The results clearly demonstrate the expected behavior: reducing COT decreases the cloud reflectance, leading to lower TOA upward irradiance. This corresponds to a positive shortwave radiative forcing (warming), since less solar radiation is reflected back to space. Thus, in the shortwave domain, cirrus cloud thinning produces a warming tendency.

In the longwave domain, the radiative effect of cirrus clouds is different. Cirrus clouds act as semi-transparent emitters and absorbers of terrestrial radiation. A reduction in COT decreases the cloud emissivity, allowing more outgoing longwave radiation to escape to space. This leads to a negative longwave radiative forcing (cooling). The current configuration of the pyDOME model is optimized for shortwave simulations and is not tuned for full longwave radiative transfer calculations. However, the longwave radiative effect can be approximated using a grey-emissivity framework. The cloud is considered as a semi-transparent layer characterized by optical thickness $\boldsymbol{\tau}$. In the thermal infrared, a cirrus cloud both transmits upwelling terrestrial radiation and emits radiation at its own temperature. The outgoing longwave radiation at the top of the atmosphere can therefore be approximated as

$$\boldsymbol{E_{TOA}(\tau) = e^{-\tau}\,\sigma T_S^4 + (1 - e^{-\tau})\,\sigma T_c^4,} \quad (14)$$

where $T_s$ is the surface temperature, $T_c$ is the cloud-top temperature, and σ is the Stefan–Boltzmann constant. The first term represents transmitted surface emission, while the second term represents cloud emission. The longwave radiative forcing due to thinning is then computed as the difference between perturbed and background states:

$$\boldsymbol{\Delta E_{LW} = \sigma(T_S^4 - T_C^4)[e^{-\tau 2} - e^{-\tau 1}],} \quad (15)$$

where $\tau 1$ and $\tau 2$ denote the background and perturbed optical thickness, respectively.

Since $T_s > T_c$, a reduction in optical thickness ($\tau 1 < \tau 2$) increases transmission of terrestrial radiation and enhances outgoing longwave irradiance. This produces a negative longwave radiative forcing, corresponding to a cooling effect.

Using the scene *CAL_IIR_L2_Track-Standard-V5-00_Apr.nc*, a quantitative assessment of the radiative impact is now provided. For this case, the mean change in cirrus optical depth between 2020 and the background state is 0.00566, indicating a slight increase in cloud optical thickness (see Figure 119). The shortwave radiative forcing computed from the empirical parameterization yields a mean value of −0.14 W m$^{-2}$. The negative sign reflects enhanced reflection of solar radiation due to the increase in optical thickness,

resulting in a weak cooling effect in the shortwave domain. The longwave radiative forcing, calculated using the two-temperature formulation with a surface temperature of 288 K and a cloud-top temperature of 220 K, is substantially larger. The mean longwave forcing amounts to 14.15 W $m^{-2}$. The positive sign indicates a reduction of outgoing longwave radiation caused by the increased cirrus optical thickness, corresponding to a warming effect. Comparing both components, the longwave contribution clearly dominates over the shortwave contribution in this scene. Despite the weak shortwave cooling, the net radiative response is controlled by the longwave greenhouse effect of cirrus, leading overall to a warming tendency. The shortwave and longwave radiative forcings maps are shown in Figure 120 and Figure 119, respectively.

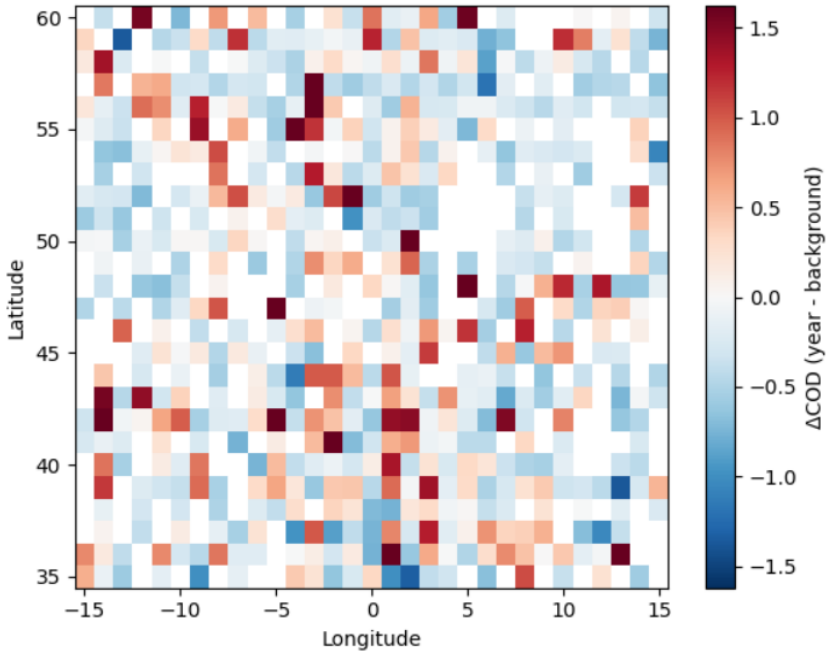


**Figure 119** Spatial distribution of the cirrus optical depth perturbation ($\Delta COT = COT_{2020} - COT_{background}$) for the CALIPSO/IIR scene *CAL_IIR_L2_Track-Standard-V5-00_Apr*. Positive values indicate an increase in cirrus optical thickness relative to the background state.

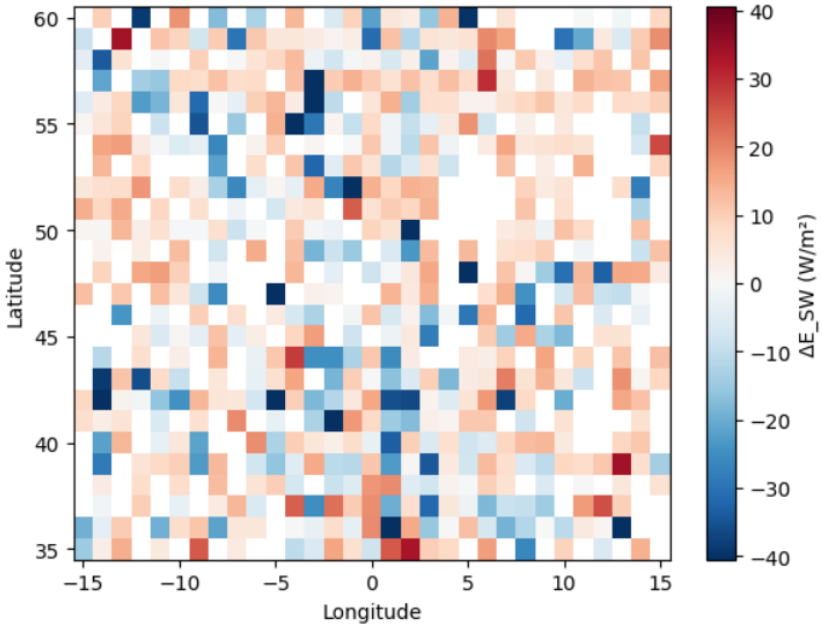


**Figure 120** Shortwave radiative forcing at the top of the atmosphere derived from the pyDOME calculations. Negative values correspond to enhanced reflection (cooling), while positive values indicate reduced reflection (warming)

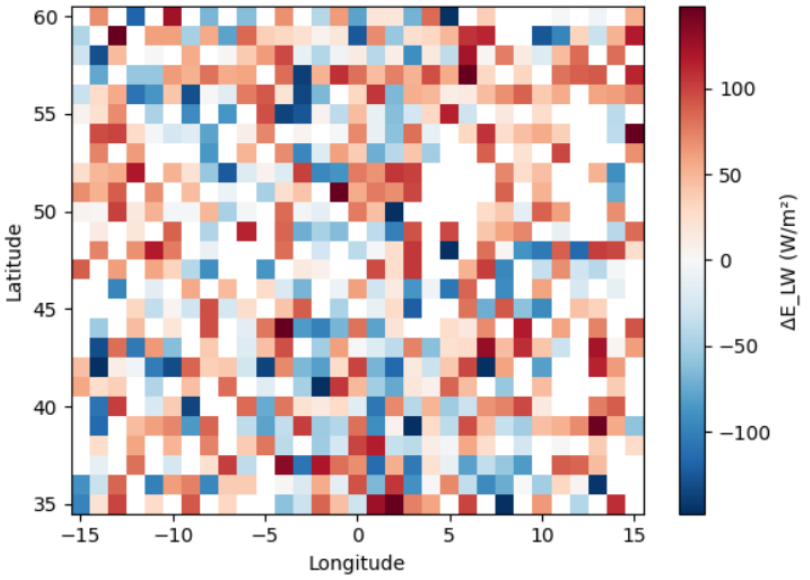


**Figure 121** Longwave radiative forcing at the top of the atmosphere computed using the two-temperature radiative transfer approximation. Positive values indicate reduced outgoing longwave radiation (warming), while negative values correspond to enhanced emission to space (cooling).

#### 4.3.2.2 Results and Consequences for ERF

No clear perturbation to the top-of-atmosphere radiation budget is detected within the region of interest (see Figure 122), suggesting that the imposed perturbation is masked by signals arising from cloud adjustments. Changes in the top-of-atmosphere radiation budget induced by cloud adjustments are particularly pronounced in the tropics. A small increase in surface air temperature of approximately 0.2 K is detected within the region of interest, even if the expected signal was a cooling. Globally, a mean decrease of 0.01 K in surface air temperature is simulated. The magnitude of the change in surface air temperature over land exceeds that over the oceans. Precipitation responses extend beyond the region of imposed perturbation

(Figure 122, right), reflecting the strong coupling between latent heating, large-scale circulation, and atmospheric energy balance.

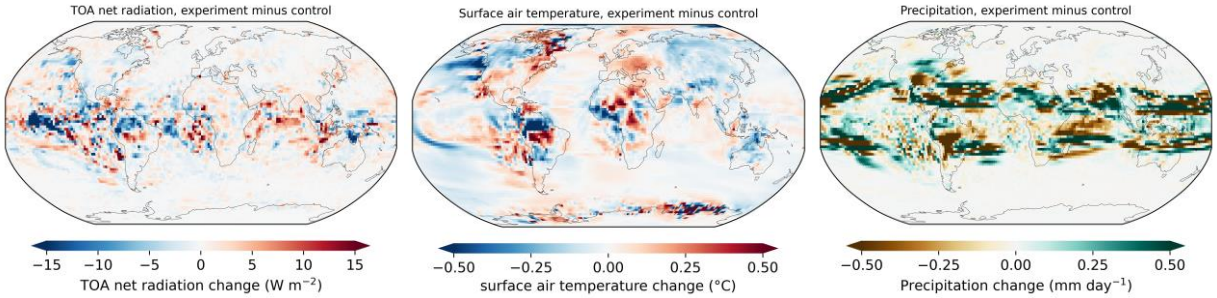


**Figure 122** Study for CCT with a reduced ice number concentration by 12%. Left: perturbation of the net top-of-atmosphere radiation flux density (effective radiative forcing). Middle: response of surface temperature. Right: response of surface precipitation flux.

### 4.3.3 Risks

The results shown above in combination with previous studies indicate that aviation-induced cirrus cloud modification can partially mimic the CCT strategies. That is, cirrus clouds originating from high-aviation regions likely exhibit fewer but larger ice crystals. Aviation exhaust particles at cirrus levels may shift the ice nucleation pathway to more heterogeneous nucleation and indirectly influence the naturally forming cirrus clouds, leading to enhanced PLDR. So far, however, the CCT-like effects can only be determined from the statistical results with airborne and satellite observations. Direct measurements are still missing. CCT relies on modifying heterogeneous ice nucleation. Unfortunately, however, ice nucleation pathways in reality are poorly constrained and INP parameterizations strongly depend on model simulations (e.g., EMAC). Thanks to the abundant observations, corresponding studies on CCT are mainly carried out at midlatitudes. But cirrus cloud occurrence can be highly region-dependent. The CCT studies in regional and global scales should be further carried out and compared. The current study on CCT has been carried out with observational efforts, which can suffer from instrumental limits, such as low SNR for CALIPSO, which leads to biased results in radiative transfer calculations.

The ICON results indicate that even a perturbation of cirrus such as in consequence of the Covid lockdown has a very small, virtually non-detectable, impact on the climate system. Any deployment thus needs to be of much larger magnitude than this perturbation. Even for field trials aiming to examine an effect on top-of-atmosphere radiation, it is necessary to seed by more than this effect.

### 4.3.4 Outlook

The aviation-relevant CCT study advances our understanding of the changes in optical and microphysical properties of cirrus clouds influenced by aviation emissions. Looking forward, it is planned to extend the analysis with higher-resolution observational datasets, such as airborne measurements, which focus on more specific clouds which are also visible for other instruments. Furthermore, more comprehensive aircraft emission inventories could be integrated and combined with modelling feedbacks of large-scale dynamics, which could further enhance predictive capability. However, it remains challenging to isolate the aviation signal from the concurrent background aerosol loading. In addition, aviation-induced soot particles may not be highly efficient INPs for direct ice crystal formation at cirrus levels (Testa et al., 2024a, b; Righi et al., 2025). In the future work it is planned to extend to a study how smoke particles modify ice nucleation processes and thereby produce CCT-like effects in the solar radiative forcing and climatological system.

In the one-year period of *ACtIon4Cooling*, the changes in cirrus cloud properties (PLDR, extinction, and geometric thickness) were investigated with the lidar measurements of CALIOP at high- and midlatitudes. With IIR-CALIOP retrievals, also the microphysical parameters (IWC, Ni, and De) of cirrus clouds were derived and the variabilities were compared at different latitude domains in different years. With a focus on the midlatitudes, a long-term evolution of cirrus cloud properties was derived in terms of geometric thickness. A study on the long-term variabilities in the microphysical properties of cirrus clouds at midlatitudes (at high latitudes) however is still missing due to a lack of time. It is however planned to be carried out in near future. The microphysical (IWC, Ni, De) and optical (PLDR, extinction, geometric thickness)

parameters at midlatitudes in years 2010-2020 have been provided for further model simulation with pyDOME and ICON.

For an observations-guided assessment of CCT, the modelling results suggest that it is imperative to analyse a less “noisy” situation in which the signal is veiled by strong noise and signals in low-level clouds and thus solar radiative effects. Potentially a focus on polar night could help. Similar to the analysis of SAI and MCB, a careful analysis of signals using model-derived fingerprints is necessary for a successful detection-and-attribution analysis.

## 4.4 Summary & Conclusions

### 4.4.1 Summary of climate model results, including uncertainty assessment and multi-model context

A quantification of the uncertainty of the results in terms of effective forcing (top-of-atmosphere radiation perturbation, Figure 59 and Figure 110) is possible by comparing the signal inside the perturbation area to the noise in other parts of the globe.

As expected, uncertainty is very large for all the observations-guided perturbations that rely on opportunistic experiments. In case of the SAI analogue, even for the top-of-atmosphere radiation, a very noisy signal is found for which even the domain-average has the opposite sign of the one expected (Figure 59). For the MCB and CCT analogue cases, it is evident that a perturbation of the scale of the observations is too small and too short in time to obtain a signal-to-noise ratio sufficiently large to identify the perturbation in top-of-atmosphere radiation with statistical significance. This is in line with previous assessments (Seidel et al., 2014; Aswathy, 2017).

However, a clear signal is found for clear-sky radiation for the SAI analogue case (Figure 49), and to the extent a strong perturbation may be obtained, also MCB would yield a discernible signal in top-of-atmosphere radiation (Figure 110).

For the climate response, there are systematic changes that depend on the spatial structure of the perturbation. A particularly striking result is the shift in precipitation patterns in response to the SAI analogue (Figure 61 and Figure 63). Also the MCB and CCT analogues yield precipitation responses outside the region in which the perturbation is imposed. The fact that the signal in temperatures and precipitation is noisy is corroborated by the multi-model context e.g. in light of the Geoengineering Model Intercomparison Project (GeoMIP, Kravitz et al. 2013; 2015).

While the results so far are partly clouded by the uncertainty, they offer a promising way forward to explore further the opportunities and challenges with regard to solar radiation modification. For a careful sampling and analysis, signals in various relevant parameters might be detected and attributed using model-data synergy for opportunistic experiments to all three classes of SRM (SAI, MCB, CCT). The modelling further is able to infer the degree of uncertainty and the spillover effects of SRM in case of regional application, as well as other unintended and side-effects. In principle, detection-and-attribution for such effects is also possible from model-data synergy.

## 4.5 Roadmap for future developments/projects

The current *ACtIon4Cooling* project has delivered substantial contributions to the understanding of fundamental physical processes related to MCB, SAI and CCT, their natural analogues and how they impact Earth’s radiation budget. At the same time, *ACtIon4Cooling* has revealed critical knowledge gaps that must be addressed to enable a scientifically robust assessment of SRM.

In particular, interactions between smoke aerosols and SRM-relevant particles, their effects on cloud microphysics and dynamics, and the regional heterogeneity of SRM impacts remain major sources of uncertainty. A project extension is therefore required to systematically address these open questions and to significantly strengthen the scientific robustness and relevance of the results obtained so far.

### 4.5.1 Impact of Smoke on Aerosol–Cloud Interactions in SRM

A key aspect that is still insufficiently understood concerns the role of smoke and combustion-related aerosols (e.g., from wildfires or anthropogenic sources) in combination with intentionally introduced or simulated SRM aerosols. Smoke particles differ from idealized SRM aerosols (such as sulfate) with respect to size distribution, chemical composition, hygroscopicity, and optical properties.

These differences directly influence aerosol-cloud interactions, including cloud condensation nuclei (CCN), droplet size distributions, cloud albedo, and precipitation formation. Under realistic atmospheric conditions, SRM aerosols will not act in isolation but will interact and compete with existing background and smoke aerosols. This is particularly relevant for Marine Cloud Brightening (MCB), where ship-emitted aerosols or deliberately introduced particles interact with a complex marine aerosol background.

Within the extended project, MCB-related aerosol-cloud interactions will be investigated by expanding existing ship-track detection methodologies to additional regions and by incorporating observations from geostationary sensors such as SEVIRI or Sentinel-4. Earth observation (EO) capabilities will be exploited to identify and analyze further MCB analogues, including volcanic eruptions and wildfire smoke plumes over marine environments. Special emphasis will be placed on assessing the detectability of small-scale MCB experiments, such as the Great Barrier Reef field trials and planned activities within the ARIA framework.

In addition, the feasibility of targeted MCB experiments in the Mediterranean will be explored, building on existing ESA-led and international campaign activities (e.g. ESA-NASA CoSENSE in Lavrio and Antikythera, as well as CERTAINTY and CleanCloud). Where necessary, complementary observations will be proposed to better constrain aerosol and cloud properties. Addressing these combined smoke-SRM processes is essential to ensure that conclusions drawn from idealized SRM scenarios remain applicable under real-world atmospheric conditions.

### 4.5.2 Cloud Closure as a Central Methodological Framework

A further core element of the proposed project extension is the systematic application and advancement of cloud-closure approaches. Cloud closure aims to consistently derive observed or simulated cloud properties from known aerosol, dynamical, and thermodynamical boundary conditions. As such, it represents a key methodological bridge between process understanding, observations, and model representation.

In the context of SRM, cloud closure is particularly important because even small changes in aerosol assumptions or cloud parameterizations can lead to substantial differences in simulated radiative effects. This applies both to low-level clouds relevant for MCB and to high-level ice clouds relevant for (CCT).

For CCT, the project extension will exploit the unique capabilities of CALIPSO and especially EarthCARE to compare cirrus cloud properties at mid-latitudes in the Northern Hemisphere, characterized by high aviation density, with those in the more pristine Southern Hemisphere. Analyses will focus on cirrus occurrence, geometrical thickness, particle linear depolarization ratio (PLDR), extinction, and cloud optical depth, taking advantage of EarthCARE's ability to jointly retrieve optical and microphysical properties.

Furthermore, potential natural analogues for CCT will be examined, including cirrus clouds influenced by mineral dust, wildfire smoke, and volcanic emissions. Dedicated analyses will target clouds sampled during past and ongoing airborne campaigns (e.g. ML-CIRRUS, CIRRUS-HL, and forthcoming campaigns such as AEROCLOUD-Fire), combining in situ and remote-sensing observations. The coordinated matching of aircraft flight tracks with satellite overpasses will enable a direct quantification of changes in cirrus properties with and without aviation-induced perturbations, providing a stringent cloud-closure test under SRM-relevant conditions.

### 4.5.3 Investigating Regional SRM Effects with ICON

Global-mean metrics alone are insufficient to assess the potential benefits and risks of SRM, as its impacts are expected to exhibit pronounced regional variability. Such regional effects may manifest in changes in temperature, precipitation patterns, cloud cover, and extreme events, with potentially uneven socio-environmental consequences.

The proposed project extension will therefore place strong emphasis on investigating regional SRM effects using ICON. Particular attention will be given to land-based cloud brightening strategies and their potential role in mitigating extreme events, such as heat waves. This includes analyzing both intended effects and possible side effects at regional scales.

The modelling activities will integrate new information and products from recent and forthcoming ESA and EUMETSAT missions, coupled with optimized optical particle models to better constrain radiative transfer calculations. These developments will feed into global and regional climate simulations and support the evolution of operational frameworks such as the Copernicus Atmosphere Monitoring Service (CAMS).

For SAI, the project will focus on improving the representation of stratospheric aerosols in models by inter-comparing different observational products (e.g. solar occultation and lidar-based retrievals) to identify those with the lowest uncertainties. Updated aerosol models accounting for sulfates, ash, and smoke will be developed to more accurately constrain RT calculations. Natural analogues, such as volcanic eruptions and stratospheric smoke events, will be exploited to discriminate SAI-relevant signals using synergistic observations from lidars and polarimeters (e.g. CALIPSO, Aeolus, EarthCARE, POLDER, PACE, 3MI, and airborne measurements).

A dedicated dialogue with CAMS will be pursued to explore the inclusion of stratospheric aerosols, for example through EarthCARE-informed assimilation approaches, while explicitly distinguishing between volcanic and fire-related aerosol types. This integrated modelling strategy is essential to robustly assess regional SRM effects, including their potential for extreme-event mitigation and their associated risks.

# 5. Datapool

This chapter describes the input and output datasets used in *ACtIon4Cooling.*

## 5.1 SAI

### 5.1.1 Input Datasets

The input datasets consists of the publicly available EARTHCARE ATLID Level -2A (ATL_EBD_2A) product used as the input for the observation dataset of AOD at 0.355 µm. Data acquisition and processing were performed within the ESA MAAP platform. Also, the publicly available EARTHCARE MSI Level 2A product (MSI_COP_2A) and publicly available PACE HARP2 L2 data used to examine atmospheric scene stability in terms of cloud properties (PACE_HARP2.CLOUD_GPC.V3_0) between EarthCARE and PACE overpasses. Finally, the publicly available PACE HARP2 L1C (PACE_HARP2.L1C.V3.5km) are utilized for the polarimetric retrievals of stratospheric particles above liquid clouds. A complete overview of SAI input datasets and their sources can be found in Table 13.

**Table 13** Overview of SAI Input datasets

| File name | File content | Variable description | Data source / access |
|---|---|---|---|
| *ATL_EBD_2A* | EarthCARE ATLID Level-2A aerosol optical properties | Aerosol extinction, backscatter, particle linear depolarization | EarthCARE L2 product, DOI: https://doi.org/10.57780/eca-4644a1f (accessed via ESA MAAP) |
| *MSI_COP_2A* | EarthCARE MSI cloud optical properties | Cloud top height, cloud optical depth, cloud droplet/ice crystal effective radius, cloud water path | EarthCARE L2 product, DOI: https://doi.org/10.57780/eca-4644a1f (accessed via ESA MAAP) |
| *PACE_HARP2.L1C.V3.5km* | PACE HARP2 geo-rectified radiances | I, Q and U Stokes vector components, Degree of Linear Polarization (DoLP), Angle of Linear Polarization (AoLP) | https://ntrs.nasa.gov/citations/20240003353 https://pace.oceansciences.org/data_table.htm#75 (accessed via Earthdata) |
| *PACE_HARP2.CLOUD_GPC.V3_0* | PACE HARP2 cloud optical properties | Cloud top height, cloud optical depth, cloud liquid index, liquid cloud droplet effective radius and variance, liquid water path | https://pace.oceansciences.org/data_table.htm#75 (accessed via Earthdata) |
| *Monthly_AOD_YYYYMM.nc* | Monthly aggregated derived product | Aerosol Optical Depth (AOD) | Derived from ATL_EBD_2A (this project) |
| Database of stratospheric particle properties | Simulated aerosol optical properties | Extinction coefficient, single scattering albedo, scattering matrix, effective radius, complex refractive index | Derived using MOPSMAP scattering code (this project) |

### 5.1.2 Output datasets

The output dataset consists of monthly aggregated NetCDF files containing AOD derived from ATLID extinction profiles. The dataset covers the period from August 2024 to September 2025 (16 months in total).

Specifically, the variable *particle_extinction_coefficient_low_resolution* was used to calculate the AOD values through vertical integration. The resulting AOD values represent monthly averages over the latitude band 25°S–25°N and are provided on a 1° × 1° latitude–longitude grid. The dataset also includes supporting aerosol intensive optical properties, such as lidar ratio, particle extinction coefficient, and particle linear depolarisation ratio.

One output file is produced per calendar month, resulting in 12 files per year and 16 files in total for the full dataset. Each monthly file has a typical size of ~330 MB, resulting in a total dataset volume of approximately 5,5 GB. The output files are provided in NetCDF4 format and follow CF metadata conventions. Table 14 describes the output variables in each dataset.

**Table 14** SAI output variables in each dataset

| Variable | Units | Description | Dim | Type |
|---|---|---|---|---|
| `count` | - | Number of valid observations contributing to the monthly aggregated value at each grid point | latitude, longitude | integer |
| `latitude` | degree_north | Latitude of aggregated grid cell centre | latitude, longitude | double |
| `longitude` | degree_east | Longitude of aggregated grid cell centre | latitude, longitude | double |
| `aod` | - | Monthly mean Aerosol Optical Depth derived from vertical integration of extinction profiles | latitude, longitude | double |
| `layer_bottom` | m | Bottom altitude of detected stratospheric aerosol layer | latitude, longitude | double |
| `layer_top` | m | Top altitude of detected stratospheric aerosol layer | latitude, longitude | double |
| `layer_thickness` | m | Thickness of stratospheric aerosol layer (layer_top − layer_bottom) | latitude, longitude | double |
| `lidar_ratio_355nm` | sr | Aerosol lidar ratio at 355 nm | latitude, longitude | double |
| `particle_extinction_coefficient_355nm` | $m^{-1}$ | Aerosol particle extinction coefficient at 355 nm | latitude, longitude | double |
| `particle_linear_depol_ratio_355nm` | - | Particle linear depolarisation ratio at 355 nm | latitude, longitude | Double |
| `tas` | K | Surface temperature | latitude, longitude | real |
| `pr` | kg m-2 s-1 | Precipitation flux | latitude, longitude | Real |
| `rsut` | W m-2 | Radiation flux density at top-of-atmosphere, solar | latitude, longitude | real |
| `rsut,cs` | W m-2 | Radiation flux density at top-of-atmosphere, solar (assuming clear sky) | latitude, longitude | real |
| `rlut` | W m-2 | Radiation flux density at top-of-atmosphere, terrestrial (long-wave) | latitude, longitude | real |

The output dataset also contains volcanic ash and sulfate particle simulated optical properties derived from MOPSMAP database. For these properties the microphysical properties described in Table 15 are used as input. One output file is produced per size distribution, shape description, spectral refractive index and relative humidity value, resulting in ~600 files for ash and sulfate particles. Each file has an approximate size of 1MB resulting in a total volume of 600MB of files, provided in CDF format, which is self-describing and includes embedded metadata.

**Table 15** Output variables for the volcanic ash and sulfate particle simulated optical properties

| Variable | Units | Description | Dimension | Type |
|---|---|---|---|---|
| ext | $km^{-1}$ / (g $m^{-3}$) | Extinction coefficient divided by the particle mass per atmospheric volume | Number of wavelengths, number of $r_{eff}$ | double |
| nmom | - | Number of moments of the phase function | Number of wavelengths, number of $r_{eff}$, number of scattering matrix elements | int |
| ntheta | - | Number of scattering angles used to sample the phase matrix | Number of wavelengths, number of $r_{eff}$, number of scattering matrix elements | int |
| phase | - | Phase function | Number of wavelengths, number of $r_{eff}$, number of scattering matrix elements, number of scattering angles | float |
| pmom | m | Legendre moments of the phase function | Number of wavelengths, number of $r_{eff}$, number of scattering matrix elements, number of scattering angles | float |
| reff | m | Particle effective radius | Number of $r_{eff}$ | double |
| refim | m | Imaginary part of the refractive index | Number of wavelengths | double |
| refre | sr | Real part of the refractive index | Number of wavelengths | double |
| rho | $m^{-1}$ | Relative humidity | Number of $r_{eff}$ | double |
| ssa | - | Single scattering albedo | Number of wavelengths, number of $r_{eff}$, | double |
| theta | degrees | Scattering angles | Number of wavelengths, number of $r_{eff}$, number of scattering matrix elements, number of scattering angles | float |
| wavelength | µm | Wavelengths | Number of wavelengths | double |

## 5.2 MCB

### 5.2.1 Input datasets

The input dataset was constructed by combining multiple satellite and ancillary products to characterize ship-induced cloud perturbations, see Table 16. All of these sources were merged and aggregated into the

final working dataset named *merged_TROPOMI_VIIRS_EMODNET_{region}_{date}.nc* containing cloud, aerosol, $NO_2$, and ship density variables at the TROPOMI footprint, serving as the input for both pixel-by-pixel and regional mean perturbation calculations.

**Table 16** Overview of MCB input datasets

| File name | File content | Variable description | Data source / access |
|---|---|---|---|
| *S5P_OFFL_L2__NO2____<date>.nc* | TROPOMI tropospheric $NO_2$ column densities. | NO2 VCD | Sentinel-5P $NO_2$ Operational Product (OFFL L2), DOI: https://doi.org/10.5270/S5P-9bnp8q8 |
| *S5P_OFFL_L2__AER_AI_<date>.nc* | TROPOMI Aerosol Absorbing Index | AAI | Sentinel-5P Aerosol Index Operational Product (OFFL L2), DOI: https://doi.org/10.5270/S5P-3dgz66p |
| *S5P_OFFL_L2__CLOUD__<date>.nc* | TROPOMI cloud fraction, cloud top height and cloud optical thickness | Cloud parameters | Sentinel-5P Cloud Operational Product (OFFL L2), DOI: https://doi.org/10.5270/S5P-w1qgt16 |
| *S5P_NASA_OFFL_L2_ TROPOMAER_<date>.nc* | TROPOMAER aerosol parameters | Aerosol parameters | Sentinel-5P TROPOMAER product |
| *S5P_OFFL_L2__NP_BD3_<date>.nc* | VIIRS cloud parameters re-gridded to the TROPOMI footprints. | Cloud parameters | VIIRS Product re-gridded at TROPOMI BD3 footprints (NP_BD3) |
| *wid-all_traffic-all_europe-monthly-<month>.tif* | EMODnet spatial distribution of ship traffic per month, used to identify ship-affected pixels | EMODnet ship density | EMODnet Vessel Density Monthly Aggregated Data https://emodnet.ec.europa.eu/geonetwork/srv/eng/catalog.search#/metadata/0f2f3ff1-30ef-49e1-96e7-8ca78d58a07c |
| *merged_TROPOMI_VIIRS_EMODNET_{region}_{date}.nc* | Final merged and aggregated dataset named serving as the input for both pixel-by-pixel and regional mean perturbation calculations | cloud, aerosol, $NO_2$, and ship density variables at the TROPOMI footprint | Internal project dataset |

### 5.2.2 Output Datasets

Two output datasets have been generated as summarized in Table 17.

**Table 17** Overview of MCB output datasets

| Dataset | Scale | Reference | Purpose |
|---|---|---|---|
| Local NN dataset | Pixel | Closest background pixel | Process-level detection |
| Regional dataset | Regional / daily | Ship mean vs background mean | Statistical detectability |

The **local pixel-by-pixel cloud perturbation dataset** (Nearest-Neighbor Reference) contains pixel-by-pixel cloud perturbations due to ships during the period July-December 2024. The delta variables quantify ship-induced perturbations in cloud properties. They are computed as the difference between ship-affected pixels and background reference pixels within the same scene and meteorological regime.

**Table 18** Variables in the pixel-by-pixel cloud perturbation dataset

| Variable | Unit | Description |
|---|---|---|
| latitude | degrees (°) | Geographic latitude of pixel center |
| longitude | degrees (°) | Geographic longitude of pixel center |
| cloud_top_height_m_VIIRS | m | Cloud Top Height retrieved from VIIRS |
| cloud_top_emissivity_VIIRS | – | Cloud top emissivity from VIIRS |
| cloud_effective_radius_um_VIIRS | µm | Cloud droplet effective radius from VIIRS |
| liquid_water_path_gm2_VIIRS | g $m^{-2}$ | Liquid Water Path from VIIRS |
| cloud_optical_depth_VIIRS | – | Cloud optical depth from VIIRS |
| cloud_top_height_m | m | Cloud Top Height from TROPOMI |
| cloud_optical_thickness | – | Cloud optical thickness from TROPOMI |
| cloud_fraction | – | Cloud fraction from TROPOMI |
| aerosol_index_354_388 | – | UV Aerosol Index (354–388 nm) |
| aerosol_index_340_380 | – | UV Aerosol Index (340–380 nm) |
| aerosol_index_335_367 | – | UV Aerosol Index (335–367 nm) |
| aerosol_index_UV_TROPOMAER | – | UV Aerosol Index from TROPOMAER |
| aerosol_type_TROPOMAER | categorical (int) | Aerosol type classification (e.g., dust, smoke, polluted continental) |
| NO2_tropospheric_column | molec $cm^{-2}$ | Tropospheric $NO_2$ column density |
| vessel_density_hours_per_km2 | hours $km^{-2}$ | Shipping density proxy derived from AIS data |
| emodnet_distance_km | km | Distance to nearest shipping lane (EMODNet) |
| ship_affected | 0 / 1 | Binary label: 1 = ship-affected pixel (based on vessel |

| | | |
|---|---|---|
| | | density & distance thresholds), 0 = background |
| delta_cloud_top_height_m_VIIRS | m | Perturbation in VIIRS CTH |
| delta_cloud_top_emissivity_VIIRS | – | Perturbation in emissivity |
| delta_cloud_effective_radius_um_VIIRS | µm | Perturbation in droplet size |
| delta_liquid_water_path_gm2_VIIRS | g $m^{-2}$ | Perturbation in LWP |
| delta_cloud_optical_depth_VIIRS | – | Perturbation in VIIRS optical depth |
| delta_cloud_top_height_m | m | Perturbation in TROPOMI CTH |
| delta_cloud_optical_thickness | – | Perturbation in optical thickness |
| delta_cloud_fraction | – | Perturbation in cloud fraction |

**The ship-induced cloud perturbation metrics dataset** (Regional Aggregation) contains cloud perturbations due to ships during the period July-December 2024. It contains the regional mean daily perturbation statistics for ship-affected vs. background cloud fields over NE-Atlantic and Mediterranean. Perturbations are computed as the difference of the mean of ship-affected pixels per day and grid box minus the mean of background pixels per day and grid box. This approach removes nearest-neighbor sensitivity and provides a robust regional signal estimate, appropriate for detection/attribution-style analyses relevant to MCB.

**Table 19** Variables in ship-induces cloud perturbation dataset

| Variable | Description | Units | Type |
|---|---|---|---|
| region | | | |
| date | Date of aggregation (daily resolution) | YYYY-MM-DD | datetime |
| variable | Name of analysed cloud or atmospheric parameter | – | string |
| N_ship | Number of ship-affected pixels used in daily mean | count | integer |
| N_background | Number of background pixels used in daily mean | count | integer |
| ship_mean | Daily mean value over ship-affected pixels | variable-dependent | float |
| background_mean | Daily mean value over background pixels | variable-dependent | float |
| abs_diff | Absolute difference: ship_mean − background_mean | same as variable | float |
| rel_diff_percent | Relative difference: (abs_diff / background_mean) × 100 | % | float |
| z_score | Standardized difference using pooled standard deviation | – | float |
| cohens_d | Effect size (Cohen's d) between ship and background distributions | – | float |
| p_value | Statistical significance from two-sample test | – | float |

## 5.3 CCT

### 5.3.1 Input Datasets

The airborne lidar measurements with WALES and in-situ measurements during ML-CIRRUS have used to study the aviation impacts on cirrus cloud properties. From the different distributions of PLDR, cirrus clouds with either high- or low-PLDR are classified. The in-situ measurements according to high- and low-mode are collected for further calculation. The input datasets consist of ice crystal effective diameter (De), number concentration (Ni) and ice water content (IWC). For satellite observations, we exploit the publicly available CALIPSO Version 4.2 Level 2 5 km cloud profile products (*CAL_LID_L2-Standard-V4-20.<date>T<time>.hdf*) containing particle extinction, backscatter and depolarization from all the atmospheric entities as well as auxiliary data of temperatures in cloud interpolated from the GEOS-5 analysis fields along the satellite tracks. To distinguish cirrus clouds from other features, the vertical feature mask (VFM) products have been applied to mask out aerosols and non-cirrus clouds. Finally, the microphysical retrievals combining IIR and CALIOP are exploited for microphysical parameters of cirrus clouds including IWC, Ni, and De which are retrieved from the IIR Level 2 track data at 1-km pixel resolution under the lidar track along the flight track (*CAL_IIR_L2_Track_Standard-V5-00.<date>T<time>.hdf*)

**Table 20** CCI Input datasets

| File name | File content | Variable description | Data source / access |
|---|---|---|---|
| *CAL_LID_L2-Standard-V4-20.<date>T<time>.hdf* | CALIPSO Version 4.2 Level 2 5 km cloud profile product | particle extinction, backscatter, depolarization, auxiliary data of temperatures, VFM | https://subset.larc.nasa.gov/calipso/login.php (login needed) |
| *CAL_IIR_L2_Track_Standard-V5-00.<date>T<time>.hdf* | CALIPSO Version 4.2 IIR Level 2 track data | cirrus number concentration, cirrus optical depth, cirrus effective diameter, cirrus ice water content, and cirrus ice water path | https://www.icare.univ-lille.fr/login/?prourl=/asd-content/archive/?dir=IIR/CAL_IIR_L2.v5.00/ (login needed) |

### 5.3.2 Output datasets

The output datasets from in-situ measurements consist of the merged data during ML-CIRRUS aggregated into NetCDF files, see Table 21. The datasets are saved for all the campaign flights taking place in March-April 2014. The information of the variables of output datasets can be found in the following tables.

The description of CALIOP data and example codes for handling the VFM products are available at [URL27] and in Table 22. The post-processed optical parameters including extinction and depolarization used for the comparison of cirrus cloud properties at high- and midlatitudes are provided in MATLAB format and publicly available at Zenodo (see Li and Gross, 2025b). Each monthly file has a typical size of 500 MB, resulting in a total dataset volume of 31 GB for 5-year observations in 2014 and 2018-2021. Furthermore, optical parameters with CALIOP over midlatitudes in 10 years are projected into 1° × 1° latitude-longitude grid boxes and used to calculate a baseline and thereby the perturbations in 2019 and 2020 can be calculated as the deviation of the corresponding years to the baseline. The file of mapped data has a small size of 70 MB.

From IIR-CALIOP retrievals, microphysical parameters, such as cirrus number concentration (i.e. Ni), cirrus effective diameter, ice water content, and etc. have been processed for a baseline with 10-year observations in 2010-2019, see Table 23. Finally, the perturbations in 2019 and 2020 are calculated, resulting in datasets of a total 1 MB.

**Table 21** Output variables in in-situ each dataset

| Variable | Units | Description | Dim | Type |
|---|---|---|---|---|

| | | | | |
|---|---|---|---|---|
| Time | second | Seconds from 00 hours on flight date | latitude, longitude | double |
| Altitude | meter | IGI height above WGS84 ellipsoid | latitude, longitude | double |
| latitude | degree | degrees_north | latitude, longitude | double |
| longitude | degree | degrees_east | latitude, longitude | double |
| IWC | g $m^{-3}$ | Ice water content, from BF1995 | latitude, longitude | double |
| dIWC | g $m^{-3}$ | IWC perturbation | latitude, longitude | double |
| Nice | $cm^{-3}$ | Ambient total number concentration | latitude, longitude | double |
| dNice | $cm^{-3}$ | Nice perturbation | latitude, longitude | double |

**Table 22** Output variables in CALIOP retrievals

| Variable | Units | Description | Dim | Type |
|---|---|---|---|---|
| Height | km | Vertical resolution: 30-60 m below 20 km and 60-180 m above 20 km | - | double |
| latitude | degree | degrees_north | latitude, longitude | double |
| longitude | degree | degrees_east | latitude, longitude | double |
| Depol_background | - | Integrated particle linear depolarization ratio of cirrus clouds only from CALIOP observations in years 2010-2019 | latitude, longitude | double |
| Extinct_background | $km^{-1}$ | Integrated extinction coefficients of cirrus clouds only from CALIOP observations in years 2010-2019 | latitude, longitude | double |
| Totbsc_background | $km^{-1}$ $sr^{-1}$ | Integrated total backscatter coefficients of cirrus clouds only from CALIOP observations in years 2010-2019 | latitude, longitude | double |
| geothk_background | km | Integrated calculated geometric thickness of cirrus clouds only from CALIOP observations in years 2010-2019 | latitude, longitude | double |
| Depol_2019 | | Particle linear depolarization ratio of cirrus clouds only from CALIOP observations in 2019 | latitude, longitude | double |
| Extinct_2019 | $km^{-1}$ | Extinction coefficients of cirrus clouds only from CALIOP observations in 2019 | latitude, longitude | double |
| Totbsc_2019 | $km^{-1}$ $sr^{-1}$ | Total backscatter coefficients of cirrus clouds only from CALIOP observations in 2019 | latitude, longitude | double |
| geothk_2019 | km | Calculated geometric thickness of cirrus clouds only from CALIOP observations in 2019 | latitude, longitude | double |

| | | | | |
|---|---|---|---|---|
| Depol_2020 | | Particle linear depolarization ratio of cirrus clouds only from CALIOP observations in 2020 | latitude, longitude | double |
| Extinct_2020 | $km^{-1}$ | Extinction coefficients of cirrus clouds only from CALIOP observations in 2020 | latitude, longitude | double |
| Totbsc_2020 | $km^{-1}\ sr^{-1}$ | Total backscatter coefficients of cirrus clouds only from CALIOP observations in 2020 | latitude, longitude | double |
| geothk_2020 | km | Calculated geometric thickness of cirrus clouds only from CALIOP observations in 2020 | latitude, longitude | double |

**Table 23** Output variables in IIR-CALIOP retrievals

| Variable | Units | Description | Dim | Type |
|---|---|---|---|---|
| latitude | degree | degrees_north | latitude, longitude | double |
| longitude | degree | degrees_east | latitude, longitude | double |
| month | - | - | - | double |
| Depol_2019 | | Integrated Particle linear depolarization ratio of the upper level derived from CALIOP observations | latitude, longitude | double |
| CNC_2019 | $L^{-1}$ | Layer number concentration | latitude, longitude | double |
| Deff_2019 | µm | Effective diameter | latitude, longitude | double |
| COD_2019 | - | Visible optical depth | latitude, longitude | double |
| IWC_2019 | $mg\ m^{-3}$ | Layer ice water content | latitude, longitude | double |
| IWP_2019 | $g\ m^{-2}$ | Ice water path | latitude, longitude | double |
| Depol_2020 | | Integrated Particle linear depolarization ratio of the upper level derived from CALIOP observations | latitude, longitude | double |
| CNC_2020 | $L^{-1}$ | Layer number concentration | latitude, longitude | double |
| Deff_2020 | µm | Effective diameter | latitude, longitude | double |
| COD_2020 | - | Visible optical depth | latitude, longitude | double |
| IWC_2020 | $mg\ m^{-3}$ | Layer ice water content | latitude, longitude | double |
| IWP_2020 | $g\ m^{-2}$ | Ice water path | latitude, longitude | double |
| Depol_bg | | Climatological values of PLDR from observations in 10 years 2010-2019 | latitude, longitude | double |
| CNC_bg | $L^{-1}$ | Climatological values of cirrus number concentration in 10 years 2010-2019 | latitude, longitude | double |

| | | | | |
|---|---|---|---|---|
| `Deff_bg` | µm | Climatological values of cirrus effective diameter in 10 years 2010-2019 | latitude, longitude | double |
| `COD_bg` | - | Climatological values of cirrus optical depth in 10 years 2010-2019 | latitude, longitude | double |
| `IWC_bg` | mg $m^{-3}$ | Climatological values of cirrus ice water content in 10 years 2010-2019 | latitude, longitude | double |
| `IWP_bg` | g $m^{-2}$ | Climatological values of cirrus ice water path in 10 years 2010-2019 | latitude, longitude | double |

## 5.4 pyDOME

## 5.5 ICON

**Table 24** ICON output datasets containing the output of simulations for assessment of the perturbations as observed in the opportunistic experiments

| File name | File content | Variable description |
|---|---|---|
| *ICON_SAI_CTL.nc* | SAI control simulations | Surface air temperature, precipitation rates, top-of-atmosphere radiation fluxes |
| *ICON_SAI_SAI.nc* | SAI analogue perturbations | |
| *ICON_MCB_CTL.nc* | MCB control simulations NEA – North-East Atlantic ocean | |
| *ICON_MCB_NEA.nc* | MCB-analogue perturbation NEA – North-East Atlantic ocean | |
| *ICON_MCB_10x.nc* | MCB-analogue perturbation NEA – North-East Atlantic ocean<br>Tenfold increase in LWP rather than 1% | |
| *ICON_MCB_MED_CTL.nc* | MCB-analogue perturbation MED – Mediterranean | |
| *ICON_MCB_MED_PER.nc* | MCB-analogue perturbation MED – Mediterranean<br>Tenfold increase in LWP rather than 1% | |

# 6. Outreach

This chapter provides an overview of communication, education and promotion activities of the *ACtIon4Cooling* project-

## 6.1 Project website

The *ACtIon4Cooling* project website can be found at [URL01]. It provide direct access to general information as well as deliverables

## 6.2 Social media

The *ACtIon4Cooling* LinkedIn group can be found at [URL02].

## 6.3 Webinars

During the *ACtIon4Cooling* project phase, a webinar series was conducted, inviting several experts from different international SRM projects:

- 05 May 2025: Scientific coordinator of CERTAINTY project, Dr. Harri Kokkola (FMI)
- 29 May 2025: Project and Scientific coordinators of CleanCloud project, Dr. Ulas Im (FMI), Dr. Athanasios
- 06 June 2025: The Table of Cloud Optics (TaCO) of MIRA, Masa Saito (Univ. Wyoming)
- 13 June 2025: Webinar on data assimilation in models, Thanos Tsikerdekis (KNMI)

## 6.4 Presentations

The *ACtIon4Cooling* project was presented at the following meetings:

- Presentation at the De-Risking Cirrus Modification (DCM) kick-off meeting on 6 November 2025
- Joint contribution with STATISTICS at the EUMETSAT Climate Symposium on 28 October 2025
- Participation in the German National Science Expert Group “Requirements for meteorological satellites 2024+” workshops:
    - EUMETSAT Foresight Workshop, 20–21 October 2025,, Darmstadt
    - Workshop “Shaping scientific satellite needs for 2040+”, DWD, 20–21 November 2025, Offenbach.

Findings related to *ACtIon4Cooling* results will also be presented in the following upcoming conferences:

EGU General Assembly 2026, Vienna, Austria, 3–8 May 2026

- Karipis, A., Gialitaki, A., Luo, H., Quass, J., Karkani, D., Tsekeri, A., Argyrouli, A., Hedelt, P., and Amiridis, V.: EarthCARE Stratospheric Aerosol Optical Depth and Its Impact on ICON Forecast , EGU26-17090, 2026.
- Gialitaki, A., Karipis, A., Tsekeri, A., Karkani, D., Argyrouli, A., Hedelt, P., and Amiridis, V.: Stratospheric Aerosol Property retrievals using polarimetric observations above clouds, EGU26-13702, 2026.
- Argyrouli, A., Hedelt, P., Seo, S., Lutz, R., Loyola, D., Efremenko, D., Li, Q., Groß, S., Gialitaki, A., Karipis, A., Tsekeri, A., Marinou, E., Voudouri, K.-A., Tsichla, M., Amiridis, V., Luo, H., Quaas, J., Retscher C., and Eisinger, M.: Investigating the Shipping Effect on Marine Clouds Using Satellite Observations and Vessel Density Data, EGU26-20255

EUMETSAT Meteorological Satellite Conference 2026

- Argyrouli, A., Hedelt, P., Seo, S., Lutz, R., Loyola, D., Efremenko, D., Li, Q., Groß, S., Gialitaki, A., Karipis, A., Tsekeri, A., Marinou, E., Voudouri, K.-A., Tsichla, M., Amiridis, V., Luo, H., Quaas, J., Retscher C., and Eisinger, M.: Detecting Solar Radiation Modification Using Natural Analogues: Insights from the ESA ACtIon4Cooling Project

## 6.5 Project related publications

*ACtIon4Cooling* results were published in the following peer-reviewed journals:

- Li, Q. & Groß, S. (2025). Lidar observations of cirrus cloud properties with CALIPSO from midlatitudes towards high-latitudes, Atmospheric Chemistry and Physics, 25, 16657–16677.

# Bibliography

Abiodun, B. J., Odoulami, R. C., Sawadogo, W., Oloniyo, O. A., Abatan, A. A., New, M., … MacMartin, D.G. (2021). Potential impacts of stratospheric aerosol injection on drought risk managements over major river basins in Africa. Climatic Change, 169(3), 31. https://doi.org/10.1007/s10584-021-03268-w

Alexandrov, M. D., Cairns, B., Wasilewski, A. P., Ackerman, A. S., McGill, M. J., Yorks, J. E., Hlavka, D. L., Platnick, S. E., Arnold, G. T., van Diedenhoven, B., Chowdhary, J., Ottaviani, M., and Knobelspiesse, K. D.: Liquid water cloud properties during the Polarimeter Definition Experiment (PODEX), Remote Sens. Environ., 169, 20–36, https://doi.org/10.1016/j.rse.2015.07.029, 2015.

Alterskjær, K., Kristjánsson, J. E., & Seland, Ø. (2012). Sensitivity to deliberate sea salt seeding of marine clouds – observations and model simulations.Atmospheric Chemistry and Physics, 12, 3563–3582. https://doi.org/10.5194/acp-12-2795-2012

Ansmann, A., Wagner, F., Wandinger, U., Mattis, I., Görsdorf, U., Dier, H.-D., & Reichardt, J. (1996). Pinatubo aerosol and stratospheric ozone reduction: Observations over central Europe. Journal of Geophysical Research: Atmospheres, 101(D13), 18775-18785. https://doi.org/https://doi.org/10.1029/96JD01373

Ansmann, A., Ohneiser, K., Engelmann, R., Radenz, M., Griesche, H., Hofer, J., Althausen, D., Creamean, J. M., Boyer, M. C., Knopf, D. A., Dahlke, S., Maturilli, M., Gebauer, H., Bühl, J., Jimenez, C., Seifert, P., and Wandinger, U.: Annual cycle of aerosol properties over the central Arctic during MOSAiC 2019–2020 – light-extinction, CCN, and INP levels from the boundary layer to the tropopause, Atmos. Chem. Phys., 23, 12821–12849, https://doi.org/10.5194/acp-23-12821-2023, 2023.

Aquila, V., Garfinkel, C., Newman, P., Oman, L., & Waugh, D. (2014). Modifications of the Quasi-Biennial Oscillation by a geoengineering perturbation of the stratospheric aerosol layer. Geophysical Research Letters, 41. https://doi.org/10.1002/2013GL058818

Argyrouli, A., Loyola, D., Romahn, F., Lutz, R., Molina García, V., Hedelt, P., Heue, K.-P., & Siddans, R. (2024). An advanced spatial coregistration of cloud properties for the atmospheric Sentinel missions: application to TROPOMI. Atmospheric Measurement Techniques, 17, 6345–6367. https://doi.org/10.5194/amt-17-6345-2024

Arora, V. K., & Boer, G. J. (2014). Terrestrial ecosystems response to future changes in climate and atmospheric $CO_2$ concentration. Biogeosciences, 11(15), 4157–4171. https://doi.org/10.5194/bg-11-4157-2014

Aswathy, N., Learning about marine cloud brightening : benefits, risks and detection. PhD thesis, Leipzig University, 150 pp., 2017.

Baum, C.M., Low, S. and Sovacool, B.K. (2022). Between the sun and us: expert perceptions on the innovation, policy, and deep uncertainties of space-based solar geoengineering. Renewable and Sustainable Energy Reviews, 158, 112179. https://doi.org/10.1016/j.rser.2022.112179

Bednarz, E. M., Visioni, D., Kravitz, B., Jones, A., Haywood, J. M., Richter, J., MacMartin, D. G., & Braesicke, P. (2023). Climate response to off-equatorial stratospheric sulfur injections in three Earth system models – Part 2: Stratospheric and free-tropospheric response. Atmospheric Chemistry and Physics, 23(1), 687–709. https://doi.org/10.5194/acp-23-687-2023

Bellouin, N., W. Davies, K. Shine, J. Quaas, J. Mülmenstädt, P. Forster, C. Smith, L. Lee, L. Regayre, G. Brasseur, N. Sudarchikova, I. Bouarar, O. Boucher, and G. Myhre, Radiative forcing of climate change from the Copernicus reanalysis of atmospheric composition, Earth Syst. Sci. Data, 12, 1649-1677, doi:10.5194/essd-12-1649-2020, 2020.

Bellouin, N., J. Quaas, E. Gryspeerdt, S. Kinne, P. Stier, D. Watson-Parris, O. Boucher, K. Carslaw, M. Christensen, A. Daniau, J. Dufresne, G. Feingold, S. Fiedler, P. Forster, A. Gettelman, J. Haywood, U. Lohmann, F. Malavelle, T. Mauritsen, D. McCoy, G. Myhre, J. Mülmenstädt, D. Neubauer, A. Possner, M. Rugenstein, Y. Sato, M. Schulz, S. Schwartz, O. Sourdeval, T. Storelvmo, V. Toll, D. Winker, and B. Stevens, Bounding global aerosol radiative forcing of climate change, Rev. Geophys., 58, e2019RG000660, doi:10.1029/2019RG000660, 2020.

Benas, N., Meirink, J. F., Roebeling, R., & Stengel, M. (2025). Analysis of ship emission effects on clouds over the southeastern Atlantic using geostationary satellite observations. Atmospheric Chemistry and Physics, 25, 6957–6973. https://doi.org/10.5194/acp-25-6957-2025

Bender, F. A.-M., Karlsson, J., Engström, A., Wood, R., Marsham, J., & Gordon, H. (2016). Factors controlling cloud albedo in marine subtropical stratocumulus regions in climate models and satellite observations. Journal of Climate, 29(10), 3685–3703. https://doi.org/10.1175/JCLI-D-15-0095.1.

Beer, C. G., Hendricks, J., and Righi, M.: Impacts of ice-nucleating particles on cirrus clouds and radiation derived from global model simulations with MADE3 in EMAC, Atmos. Chem. Phys., 24, 3217–3240, https://doi.org/10.5194/acp-24-3217-2024, 2024.

Bingaman, D. C., Rice, C. V, Smith, W., & Vogel, P. (2020). A Stratospheric Aerosol Injection Lofter Aircraft Concept: Brimstone Angel. In AIAA SciTech Forum. AIAA Scitech 2020 Forum. https://doi.org/doi:10.2514/6.2020-0618

Bingen, C., Vanhellemont, F., and Fussen, D.: A new regularized inversion method for the retrieval of stratospheric aerosol size distributions applied to 16 years of SAGE II data (1984–2000): method, results and validation, Ann. Geophys., 21, 797–804, https://doi.org/10.5194/angeo-21-797-2003, 2003

Bingen, C., Fussen, D., and Vanhellemont, F.: A global climatology of stratospheric aerosol size distribution parameters derived from SAGE II data over the period 1984–2000: 1. Methodology and climatological observations, J. Geophys. Res., 109, D06201, https://doi.org/10.1029/2003JD003518, 2004

Bodhaine, B. A., Wood, N. B., Dutton, E. G., & Slusser, J. R. (1999). On Rayleigh optical depth calculations. Journal of Atmospheric and Oceanic Technology, 16(11), 1854–1861

Bourassa, A. E., Degenstein, D. A., and Llewellyn, E. J.: Retrieval of stratospheric aerosol size information from OSIRIS limb scattered sunlight spectra, Atmos. Chem. Phys., 8, 6375–6380, https://doi.org/10.5194/acp-8-6375-2008, 2008

Breen, K. H., Barahona, D., Yuan, T., Bian, H., & James, S. C. (2021). Effect of volcanic emissions on clouds during the 2008 and 2018 Kilauea degassing events. Atmospheric Chemistry and Physics, 21(10), 7749–7771. https://doi.org/10.5194/acp-21-7749-2021

Breon, F. M. and Goloub, P.: Cloud droplet effective radius from spaceborne polarization measurements, Geophys. Res. Lett., 25, 1879–1882, https://doi.org/10.1029/98gl01221, 1998.

Buck, H., Geden, O., Sugiyama, M. and Corry, O. Pandemic politics—lessons for solar geoengineering. Communications Earth and Environment. 2020; 1,16.

Caldeira, K. and Keith, D. The Need for Climate Engineering Research. Issues in Science and Technology. 27: 57–62, 2010.

Campbell, J. R., Lolli, S., Lewis, J. R., Gu, Y., & Welton, E. J. (2016). Daytime cirrus cloud top-of-atmosphere radiative forcing properties at a midlatitude site and their global consequence. Journal of Applied Meteorology and Climatology, 55(8), 1667–1679. https://doi.org/10.1175/JAMC-D-15-0217.1

Carlson, C. J., Johnson, L. R., & Ryan, S. J. (2020). Vector-borne disease in a changing climate: The role of environmental and ecological factors. Trends in Parasitology, 36(4), 393–403. https://doi.org/10.1016/j.pt.2020.02.001

Chen, J., Liu, Y., Zhang, M., and Peng, Y.: Height Dependency of Aerosol-Cloud Interaction Regimes, Journal of Geophysical Research: Atmospheres, 123(1):491–506, doi:10.1002/2017JD027431, 2018

Chen, J., Rossow, W. B., and Zhang, Y.: Radiative effects of cloud-type variations, J. Climate, 13, 264--286, https://doi.org/10.1175/1520-0442(2000)013<0264:REOCTV>2.0.CO;2, 2000.

Cheng, W., MacMartin, D. G., Dagon, K., Kravitz, B., Tilmes, S., Richter, J. H., Mills, M. J., & Simpson, I. R. (2019). Soil moisture and other hydrological changes in a stratospheric aerosol geoengineering large ensemble. Journal of Geophysical Research: Atmospheres, 124(23), 12,773–12,793. https://doi.org/10.1029/2018JD030237

Chen, T., Y.-C. Zhang, and W.B. Rossow, 2000: Sensitivity of atmospheric radiative heating rate profiles to variations of cloud layer overlap. *J. Climate*, **13**, 2941-2959, doi:10.1175/1520-0442(2000)013<2941:SOARHR>2.0.CO;2.

Contzen, N., Perlaviciute, G., Steg, L. et al. Public opinion about solar radiation management: A cross-cultural study in 20 countries around the world. Climatic Change 177, 65 (2024). https://doi.org/10.1007/s10584-024-03708-3

Conover, J. H., Anomalous cloud lines. J. Atmos. Sci. 23, 778–785, https://doi.org/10.1175/1520-0469(1966)023<0778:ACL>2.0.CO;2, 1966

Crook, J. A., Jones, A., Kravitz, B., Haywood, J., & Irvine, P. J. (2017). Potential impacts of solar geoengineering on solar power generation. Journal of Applied Meteorology and Climatology, 56(5), 1359–1371. https://doi.org/10.1175/JAMC-D-16-0298.1

Cohen, J. (1988). Statistical power *analysis for the behavioral sciences* (2nd ed.). Hillsdale, NJ: Lawrence Erlbaum Associates.

Costantino, L. and Bréon, F.-M.: Aerosol indirect effect on warm clouds over South-East Atlantic, from co-located MODIS and CALIPSO observations, Atmos. Chem. Phys., 13, 69–88, doi:10.5194/acp-13-69-2013, 2013.

Cziczo, D., and Froyd, K.Sampling the composition of cirrus ice residuals, Atmospheric Research, Volume 142, 2014, Pages 15-31, ISSN 0169-8095, https://doi.org/10.1016/j.atmosres.2013.06.012 .

Dai, Z., Weisenstein, D. K., Keutsch, F. N. & Keith, D. W., “Experimental reaction rates constrain estimates of ozone response to calcium carbonate geoengineering.” Communications Earth & Environment 2020.

de Coninck, H. et al. Strengthening and Implementing the Global Response. In: Global Warming of 1.5°C. An IPCC Special Report on the impacts of global warming of 1.5°C above pre-industrial levels and related global greenhouse gas emission pathways, in the context of strengthening the global response to the threat of climate change, (eds. Masson- Delmotte, V. et al.) 313–444. Cambridge University Press; 2018. https://doi.org/10.1017/9781009157940.006

Deschamps, P.-Y., Breon, F.-M., Leroy, M., Podaire, A., Bricaud, A., Buriez, J.-C., & Seze, G. (1994). The POLDER mission: instrument characteristics and scientific objectives. IEEE Transactions on Geoscience and Remote Sensing, 32(3), 598–615. https://doi.org/10.1109/36.297978

Deshler, T., Johnson, B. J., & Rozier, W. R. (1993). Balloonborne measurements of Pinatubo aerosol during 1991 and 1992 at 41°N: Vertical profiles, size distribution, and volatility. Geophysical Research Letters, 20(14), 1435–1438. https://doi.org/https://doi.org/10.1029/93GL01337

Deshler, T., Hervig, M. E., Hofmann, D. J., Rosen, J. M., and Liley, J. B.: Thirty years of in situ stratospheric aerosol size distribution measurements from Laramie, Wyoming (41◦N), using balloon-borne instruments, J. Geophys. Res., 108, 4167, https://doi.org/10.1029/2002JD002514, 2003

Deshler, T.: A review of global stratospheric aerosol: Measurement, importance, life cycle, and local stratospheric aerosol, Atmos. Res., 90, 223–232, https://doi.org/10.1016/j.atmosres.2008.03.016, 2008

Devasthale, A., Andersson, S., Engström, E., Kaspar, F., Trentmann, J., Duguay-Tetzlaff, A., Meirink, J.F., Kjellström, E., Landelius, T., Thomas, M.A., & Karlsson, K.-G. (2025). Leveraging the satellite-based climate data record CLARA-A3 to understand the climatic trend regimes relevant for solar energy applications over Europe. Earth System Dynamics, 16, 1169–1182.

Diamond, M. S., Director, H. M., Eastman, R., Possner, A., & Wood, R. (2020). Substantial cloud brightening from shipping in subtropical low clouds. AGU Advances, 1(1), e2019AV000111. https://doi.org/10.1029/2019AV000111

Di Noia, A., Hasekamp, O. P., van Diedenhoven, B., and Zhang, Z.: Retrieval of liquid water cloud properties from POLDER-3 measurements using a neural network ensemble approach, Atmos. Meas. Tech., 12, 1697–1716, https://doi.org/10.5194/amt-12-1697-2019, 2019.

Dipu, S., M. Schwarz, A. Ekman, E. Gryspeerdt, T. Goren, O. Sourdeval, J. Mülmenstädt, and J. Quaas, Exploring satellite-derived relationships between cloud droplet number concentration and liquid water path using large-domain large-eddy simulation, Tellus, 74, 176- 188, doi:10.16993/tellusb.27, 2022 .

Dodangodage, R., Bernath, P. F., Wyatt, M., and Boone, C.: Atmospheric Chemistry Experiment (ACE) satellite observations of aerosols and SO2 emissions from the 2024 Ruang volcanic eruption, J. Quant. Spectrosc. Radiat. Transf., 333, 109333, https://doi.org/https://doi.org/10.1016/j.jqsrt.2024.109333, 2025.

Donovan, D. P., van Zadelhoff, G.-J., & Wang, P. (2024). The EarthCARE lidar cloud and aerosol profile processor (A-PRO): the A-AER, A-EBD, A-TC, and A-ICE products. Atmospheric Measurement Techniques, 17(17), 5301–5340. https://doi.org/10.5194/amt-17-5301-2024

Dubovik, O., Herman, M., Holdak, A., Lapyonok, T., Tanré, D., Deuzé, J. L., Ducos, F., Sinyuk, A., & Lopatin, A. (2011). *Statistically optimized inversion algorithm for enhanced retrieval of aerosol properties from spectral multi-angle polarimetric satellite observations*. Atmospheric Measurement Techniques, 4, 975-1018. https://doi.org/10.5194/amt-4-975-2011

Dubovik, O., Fuertes, D., Litvinov, P., Lopatin, A., Lapyonok, T., Doubovik, I., Xu, F., Ducos, F., Chen, C., Torres, B., Derimian, Y., Li, L., Herreras-Giralda, M., Herrera, M., Karol, Y., Matar, C., Schuster, G. L., Espinosa, R., Puthukkudy, A., Li, Z., Fischer, J., Preusker, R., Cuesta, J., Kreuter, A., Cede, A., Aspetsberger, M., Marth, D., Bindreiter, L., Hangler, A., Lanzinger, V., Holter, C., & Federspiel, C. (2021). *A comprehensive description of multi-term LSM for applying multiple a priori constraints in problems of atmospheric remote sensing: GRASP algorithm, concept, and applications*. *Frontiers in Remote Sensing, 2*, Article 706851. https://doi.org/10.3389/frsen.2021.706851

Duffey, A., Henry, M., Smith, W., Tsamados, M., & Irvine, P. J. (2025). Low-Altitude High-Latitude Stratospheric Aerosol Injection Is Feasible With Existing Aircraft. Earth's Future, 13(4), e2024EF005567. https://doi.org/10.1029/2024EF005567

Dutkiewicz, S., Hickman, A. E., Jahn, O., Gregg, W. W., Mouw, C. B., & Follows, M. J. (2015). Capturing optically important constituents and properties in a marine biogeochemical and ecosystem model. Biogeosciences, 12(14), 4447–4481. https://doi.org/10.5194/bg-12-4447-2015

Dykema, J., Keith, D., & Keutsch, F. (2016). Assessing risks of solar geoengineering starts with accurate aerosol radiative properties: Accurate aerosol properties for SRM. Geophysical Research Letters, 43. https://doi.org/10.1002/2016GL069258

Eastham, S. D., A. H. Butler, S. J. Doherty, B. Gasparini, E. Bednarz, U. Burkhardt, G. Chiodo, D. J. Cziczo, M. Diamond, D. W. Keith, T. Leisner, D. G. MacMartin, J. Quaas, P. J. Rasch, O. Sourdeval, I. Steinke, C. Thompson, D. Visioni, R. Wood, L. Xia, and P. Yu, Key gaps in models' physical representation of climate intervention and its impacts, J. Adv. Model. Earth Syst., 17, 6, doi:10.1029/2024MS004872, 2025.

Effiong, U., & Neitzel, R. L. (2016). Assessing the direct occupational and public health impacts of solar radiation management with stratospheric aerosols. Environmental Health, 15(1), 7. https://doi.org/10.1186/s12940-016-0089-0

Efremenko, D., V. Molina García, S. Gimeno García & A. Doicu, "A review of the matrix-exponential formalism in radiative transfer," Journal of Quantitative Spectroscopy & Radiative Transfer, Vol. 196, pp. 17–45 (2017), DOI: 10.1016/j.jqsrt.2017.02.015.

Emde, C., Buras-Schnell, R., Kylling, A., Mayer, B., Gasteiger, J., Hamann, U., Kylling, J., Richter, B., Pause, C., Dowling, T., and Bugliaro, L.: The libRadtran software package for radiative transfer calculations (version 2.0.1), Geosci. Model Dev., 9, 1647–1672, https://doi.org/10.5194/gmd-9-1647-2016, 2016.

Emmons, L. K., Schwantes, R. H., Orlando, J. J., Tyndall, G., Kinnison, D., Lamarque, J.-F., Marsh, D., Mills, M. J., Tilmes, S., Bardeen, C., Buchholz, R. R., Conley, A., Gettelman, A., Garcia, R., Blake, D. R., Meinardi, S., & Pétron, G. (2020). The Chemistry Mechanism in the Community Earth System Model Version 2 (CESM2). Journal of Advances in Modeling Earth Systems, 12(9), e2019MS001882. https://doi.org/10.1029/2019MS001882

Erfani, E., and D. L. Mitchell, Estimating the surface cooling potential of cirrus cloud thinning in polar regions using CALIPSO retrievals, EGUsphere, [preprint], doi:10.5194/egusphere-2025-1165, 2024.

Erfani, E., and D. L. Mitchell, Constraining a Radiative Transfer Model with Satellite Retrievals: Implications for Cirrus Cloud Thinning, EGUsphere [preprint], doi:10.5194/egusphere-2025-1165, 2025.

Fan Jiwen, Yuan Wang, Daniel Rosenfeld, and Xiaohong Liu. Review of Aerosol–Cloud Interactions: Mechanisms, Significance, and Challenges. Journal of the Atmospheric Sciences, 73(11):4221–4252, doi:10.1175/JAS-D-16-0037.1, 2016.

Fasullo, J.T., Rosenblum, N. and Buchholz, R. (2023). A multiyear tropical Pacific cooling response to recent Australian wildfires in CESM2. Science Advances, 9, eadg1213. https://doi.org.10.1126/sciadv.adg1213 .

Feingold, G., P. J. Rasch, H. Wang, D. Rosenfeld, and B. Stevens, Physical science research needed to evaluate the viability and risks of marine cloud brightening, Sci. Adv., 10, eadi8594, doi:10.1126/sciadv.adi8594, 2024.

Forster, P., T. Storelvmo, K. Armour, W. Collins, J. L. Dufresne, D. Frame, D. J. Lunt, T. Mauritsen, M. D. Palmer, M. Watanabe, M. Wild, and H. Zhang, The Earth's Energy Budget, Climate Feedbacks, and Climate Sensitivity. In: Climate Change 2021: The Physical Science Basis. Contribution of Working Group I to the Sixth Assessment Report of the Intergovernmental Panel on Climate Change, Cambridge University Press, 923–1054, doi: 10.1017/9781009157896.009, 2021.

Fu, Q., and Liou, K. N.: Parameterization of the radiative properties of cirrus clouds, J. Atmos. Sci., 50, 2008–2025, 1993.

Fujimori, S., Hasegawa, T., Krey, V., Riahi, K., Bertram, C., Bodirsky, B. L., Bosetti, V., Callen, J., Després, J., Doelman, J., Drouet, L., Emmerling, J., Frank, S., Fricko, O., Havlík, P., Humpenöder, F., Koopman, J. F. L., van Meijl, H., Ochi, Y., Popp, A., Schmitz, A., Takahashi, K., & van Vuuren, D. (2019). A multi-model assessment of food security implications of climate change mitigation. Nature Sustainability, 2, 386–396. https://doi.org/10.1038/s41893-019-0286-2

Fu, Q., and Liou, K. N.: Parameterization of the radiative properties of cirrus clouds, J. Atmos. Sci., 50, 2008–2025, 1993.

Gao, R.-S., Rosenlof, K. H., Kärcher, B., Tilmes, S., Toon, O. B., Maloney, C., & Yu, P. (2025). Toward practical stratospheric aerosol albedo modification: Solar-powered lofting. Science Advances, 7(20), eabe3416. https://doi.org/10.1126/sciadv.abe3416

Gasparini, B., McGraw, Z., Storelvmo, T., & Lohmann, U. (2020). To what extent can cirrus cloud seeding counteract global warming? Environmental Research Letters, 15(5), 054002. https://doi.org/10.1088/1748-9326/ab71a3

Gasparini, B., and Lohmann, U.: Why cirrus cloud seeding cannot substantially cool the planet, J. Geophys. Res.: Atmos. 121 4877–893, https://doi.org/10.1002/2015JD024666, 2016.

Gasteiger, J., Groß, S., Freudenthaler, V., & Wiegner, M. (2011). Volcanic ash from Iceland over Munich: mass concentration retrieved from ground-based remote sensing measurements. Atmospheric Chemistry and Physics, 11(5), 2209–2223. https://doi.org/10.5194/acp-11-2209-2011

Gasteiger, Josef, & Wiegner, M. (2018). MOPSMAP v1.0: a versatile tool for the modeling of aerosol optical properties. Geoscientific Model Development, 11(7), 2739–2762. https://doi.org/10.5194/gmd-11-2739-2018

Georgoulias, A. K., Boersma, K. F., van Vliet, J., Zhang, X., van der A, R., Zanis, P., & de Laat, J., Detection of $NO_2$ pollution plumes from individual ships with the TROPOMI/S5P satellite sensor. Environmental Research Letters, 15(12), 124037. https://doi.org/10.1088/1748-9326/abc445, 2020.

Gettelman, A., Chen, C.–C., & Bardeen, C. G., et al. (2021). The climate impact of COVID-19-induced contrail changes. Atmospheric Chemistry and Physics, 21, 9405–9416. https://doi.org/10.5194/acp-21-9405-2021

Gierens, K.: On the transition between heterogeneous and homogeneous freezing, Atmos. Chem. Phys., 3, 437–446, https://doi.org/10.5194/acp-3-437-2003, 2003.

Groß, S., Jurkat-Witschas, T., Li, Q., Wirth, M., Urbanek, B., Krämer, M., Weigel, R., and Voigt, C.: Investigating an indirect aviation effect on mid-latitude cirrus clouds – linking lidar-derived optical properties to in situ measurements, Atmos. Chem. Phys., 23, 8369–8381, https://doi.org/10.5194/acp-23-8369-2023, 2023.

Grosvenor, D., O. Sourdeval, P. Zuidema, A. Ackerman, M. Alexandrov, R. Bennartz, R. Boers, B. Cairns, C. Chiu, M. Christensen, H. Deneke, M. Diamond, G. Feingold, A. Fridlind, A. Hünerbein, C. Knist, P. Kollias, A. Marshak, D. McCoy, D. Merk, D. Painemal, J. Rausch, D. Rosenfeld, H. Russchenberg, P. Seifert, K. Sinclair, P. Stier, B. Van Diedenhoven, M. Wendisch, F. Werner, R. Wood, Z. Zhang, and J. Quaas, Remote sensing of cloud droplet number concentration in warm clouds: A review of the current state of knowledge and perspectives, Rev. Geophys., 56, 409-453, doi:10.1029/2017RG000593, 2018.

Gruber, S., Blahak, U., Haenel, F., Kottmeier, C., Leisner, T., Muskatel, H.,...Vogel, B.: A process study on thinning of Arctic winter cirrus clouds with high-resolution ICON-ART simulations, J. Geophys. Res.: Atmosphere, 124(11), 5860-5888, https://doi.org/10.1029/2018JD029815, 2019.

Gryspeerdt, E., Goren, T., and Smith, T. W. P.: Observing the timescales of aerosol–cloud interactions in snapshot satellite images, Atmos. Chem. Phys., 21, 6093–6109, https://doi.org/10.5194/acp-21-6093-2021, 2021.

Gryspeerdt, E., Povey, A. C., Grainger, R. G., Hasekamp, O., Hsu, N. C., Mulcahy, J. P., Sayer, A. M., and Sorooshian, A.: Uncertainty in aerosol–cloud radiative forcing is driven by clean conditions, Atmos. Chem. Phys, 23, 4115–4122, https://doi.org/10.5194/acp-23-4115-2023 2023.

Hack, M., McNeill, V. F., Steingart, D., Wagner, G., et al. (2025). Engineering and logistical concerns add practical limitations to stratospheric aerosol injection strategies. Scientific Reports, 15, 34635. https://doi.org/10.1038/s41598-025-20447-2

HALO database; editing status 2025-11-25; re3data.org - Registry of Research Data Repositories. https://doi.org/10.17616/R39Q0T last accessed: 2026-02-09

Hansen, J., Lacis, A., Ruedy, R., & Sato, M. (1992). Potential climate impact of Mount Pinatubo eruption. Geophysical Research Letters, 19. https://doi.org/10.1029/91GL02788

Haywood, J., Jones, A., Bellouin, N., & Stephenson, D. (2013). Asymmetric forcing from stratospheric aerosols impacts Sahelian drought. Nature Climate Change, 3, 660–665. https://doi.org/10.1038/nclimate1857

Henneberger, J., and Coauthors, 2023: Seeding of Supercooled Low Stratus Clouds with a UAV to Study Microphysical Ice Processes: An Introduction to the CLOUDLAB Project. Bull. Amer. Meteor. Soc., 104, E1962–E1979, https://doi.org/10.1175/BAMS-D-22-0178.1 .

Hernandez-Jaramillo, D. C., Medcraft, C., Braga, R. C., Butcherine, P., Doss, A., Kelaher, B., Rosenfeld, D., & Harrison, D. P. (2024). New airborne research facility observes sensitivity of cumulus cloud microphysical properties to aerosol regime over the Great Barrier Reef. Environmental Science: Atmospheres, 4(8), 861–871. https://doi.org/10.1039/D4EA00009A

Hess, M., Koepke, P., & Schult, I. (1998). Optical Properties of Aerosols and Clouds: The Software Package OPAC. Bulletin of the American Meteorological Society, 79(5), 831–844. https://doi.org/10.1175/1520-0477(1998)079<0831:OPOAAC>2.0.CO;2

Heymsfield, A. J., Krämer, M., Luebke, A., Brown, P., Cziczo, D. J., Franklin, C., Lawson, P., Lohmann, U., McFarquhar, G., Ulanowski, Z., and Van Tricht, K.: Cirrus clouds, Meteor. Mon., 58, 2.1–2.26, https://doi.org/10.1175/AMSMONOGRAPHS-D-16-0010.1, 2017.

Hobbs P. V., et al. 2000. Emissions from ships with respect to their effects on clouds. J. Atmos. Sci. 57, 2570–2590 https://doi.org/10.1175/1520-0469(2000)057%3C2570:EFSWRT%3E2.0.CO;2

Hohenegger, C., Korn, P., Linardakis, L., Redler, R., Schnur, R., Adamidis, P., Bao, J., Bastin, S., Behravesh, M., Bergemann, M., Biercamp, J., Bockelmann, H., Brokopf, R., Brüggemann, N., Casaroli, L.,

Chegini, F., Datseris, G., Esch, M., George, G., Giorgetta, M., Gutjahr, O., Haak, H., Hanke, M., Ilyina, T., Jahns, T., Jungclaus, J., … Stevens, B. (2023). ICON-Sapphire: simulating the components of the Earth system and their interactions at kilometer and subkilometer scales. Geoscientific Model Development, 16, 779–811. https://doi.org/10.5194/gmd-16-779-2023

Illingworth, Anthony J., H. W. Barker, A. Beljaars, Marie Ceccaldi, H. Chepfer, Nicolas Clerbaux, J. Cole et al. "The EarthCARE satellite: The next step forward in global measurements of clouds, aerosols, precipitation, and radiation." Bulletin of the American Meteorological Society 96, no. 8 (2015): 1311-1332, https://doi.org/10.1175/BAMS-D-12-00227.1, 2015.

IPCC, 1999 – J.E. Penner, D.H. Lister, D.J. Griggs, D.J. Dokken, M. McFarland (Eds.) Prepared in collaboration with the Scientific Assessment Panel to the Montreal Protocol on Substances that Deplete the Ozone Layer Cambridge University Press, UK. pp 373 Available from Cambridge University Press, The Edinburgh Building Shaftesbury Road, Cambridge CB2 2RU ENGLAND

Izrael, Y. A., Zakharov, V. M., Petrov, N. N., Ryaboshapko, A. G., Ivanov, V. N., Savchenko, A. V., Andreev, Y. V., Puzov, Y. A., Danelyan, B. G., & Kulyapin, V. P. (2009). Field experiment on studying solar radiation passing through aerosol layers. Russian Meteorology and Hydrology, 34, 265–273.

Izrael, Y.A., Zakharov, V.M., Ivanov, V.N. et al. A field experiment on modeling the impact of aerosol layers on the variability of solar insolation and meteorological characteristics of the surface layer. Russ. Meteorol. Hydrol. 36, 705–711 (2011). https://doi.org/10.3103/S106837391111001X .

Izrael, Y., Volodin, E., Kostrykin, S., Revokatova, A., & Ryaboshapko, A. (2014). The ability of stratospheric climate engineering in stabilizing global mean temperatures and an assessment of possible side effects. Atmospheric Science Letters, 15. https://doi.org/10.1002/asl2.481

Irvine, P., Emanuel, K., He, J. et al. Halving warming with idealized solar geoengineering moderates key climate hazards. Nat. Clim. Chang. 9, 295–299 (2019). https://doi.org/10.1038/s41558-019-0398-8

Jenkins, A. K. L., Forster, P. M., and Jackson, L. S.: The effects of timing and rate of marine cloud brightening aerosol injection on albedo changes during the diurnal cycle of marine stratocumulus clouds, Atmos. Chem. Phys., 13, 1659–1673, https://doi.org/10.5194/acp-13-1659-2013, 2013.

Jia, H., J. Quaas, E. Gryspeerdt, C. Böhm, and O. Sourdeval, Addressing the difficulties in quantifying droplet number response to aerosol from satellite observations, Atmos. Chem. Phys., 22, 7353-7372, doi:10.5194/acp-22-7353-2022, 2022.

Jin, X., Cao, L., Zhang, J. Effects of solar radiation modification on the ocean carbon cycle: An earth system modeling study, Atmospheric and Oceanic Science Letters, Volume 15, Issue 3, https://doi.org/10.1016/j.aosl.2022 .100187, 2022.

Jinnah, S., Talati, S., Bedsworth, L., Gerrard, M., Kleeman, M., Lempert, R., et al. (2024). Do small outdoor geoengineering experiments require governance? Standardized and/or centralized proactive research governance can lessen tensions. Science, 385(6709), 600–603. https://doi.org/10.1038/d41586-024-00876-1

Jones, A., Haywood, J., Boucher, O., & Kravitz, B. (2009). Climate Impacts of Marine Cloud Brightening: An Overview with a Climate Model. Atmospheric Chemistry and Physics, 9, 4749–4765. https://doi.org/10.1029/2008JD011450

Jones, A. C., Haywood, J. M., Dunstone, N., Emanuel, K., Hawcroft, M. K., Hodges, K. I., & Jones, A. (2017). Impacts of hemispheric solar geoengineering on tropical cyclone frequency. Nature Communications, 8(1), 1382. https://doi.org/10.1038/s41467-017-01606-0

Jones, A., Haywood, J. M., Scaife, A. A., Boucher, O., Henry, M., Kravitz, B. et al. The impact of stratospheric aerosol intervention on the North Atlantic and Quasi-Biennial Oscillations in the Geoengineering Model Intercomparison Project (GeoMIP) G6sulfur experiment. Atmospheric Chemistry and Physics. 2022; 22: 2999–3016.

Jurkat-Witschas, T., Voigt, C., Groß, S., Kaufmann, S., Sauer, D., De la Torre Castro, E., Krämer, M., Schäfler, A., Afchine, A., Attinger, R., Bartolome Garcia, I., Beer, C. G., Bugliaro, L., Clemen, H.,

Dekoutsidis, G., Ehrlich, A., Grawe, S., Hahn, V., Hendricks, J., Järvinen, E., Thomas, K., Krüger, K., Ovid, K., Lucke, J., Luebke, A. E., Marsing, A., Mayer, B., Mayer, J., Mertes, S., Moser, M., Müller, H., Nenakhov, V., Pöhlker, M., Pöschl, U., Pörtge, V., Rautenhaus, M., Righi, M., Röttenbacher, J., Rubin-Zuzic, M., Schaefer, J., Schnaiter, M., Schneider, J., Schumann, U., Spelten, N., Stratmann, F., Tomsche, L., Wagner, S., Wang, Z., Weber, A., Wendisch, M., Wernli, H., Wetzel, B., Wirth, M., Zahn, A., Ziereis, H., and Zöger, M.: CIRRUSHL: Picturing high- and mid-latitude summer cirrus and contrail cirrus above Europe with airborne measurements aboard the research aircraft HALO, Bulletin of the American Meteorological Society, https://doi.org/10.1175/BAMS-D-23-0270.1, 2025.

Keith, D. W., Weisenstein, D. K., Dykema, J. A., & Keutsch, F. N. (2016). Stratospheric solar geoengineering without ozone loss. Proceedings of the National Academy of Sciences - PNAS, 113(52), 14910-14914. https://doi.org/10.1073/pnas.1615572113

Keller, D., Feng, E. & Oschlies, A. Potential climate engineering effectiveness and side effects during a high carbon dioxide-emission scenario. Nat Commun 5, 3304 (2014). https://doi.org/10.1038/ncomms4304

Khaykin, S., Sicard, M., Leblanc, T., Sakai, T., Balugin, N., Berthet, G., Chevrier, S., Chouza, F., Feofilov, A., Gantois, D., Godin-Beekmann, S., Haddouche, A., Jin, Y., Morino, I., Kadygrov, N., Lecas, T., Liley, B., Querel, R., Taha, G., and Yushkov, V.: Global transport of stratospheric aerosol produced by Ruang eruption from EarthCARE ATLID, limb-viewing satellites and ground-based lidar observations, EGUsphere [preprint], https://doi.org/10.5194/egusphere-2025-4377, 2025.

Kilburn, K. H., & Warshaw, R. H. (1995). Hydrogen sulfide and reduced-sulfur gases adversely affect neurophysiological functions. Toxicology and Industrial Health, 11(2), 185–197. https://doi.org/10.1177/074823379501100206

Kleber, C., Wiesinger, R., Schnöller, J., Hilfrich, U., Hutter, H., & Schreiner, M. (2008). Initial oxidation of silver surfaces by S2−and S4+ species. Corrosion Science, 50(4), 1112–1121. https://doi.org/https://doi.org/10.1016/j.corsci.2007.12.001

Kleine, J., Voigt, C., Sauer, D., Schlager, H., Scheibe, M., JurkatWithschs, T., Kaufmann, S., Kärcher, B., and Anderson, B. E.: In Situ Observations of Ice Particle Losses in a Young Persistent Contrail, Geophys. Res. Lett., 45, 13553–13561, https://doi.org/10.1029/2018GL079390, 2018.

Koepke, P., Gasteiger, J., & Hess, M. (2015). Technical Note: Optical properties of desert aerosol with non-spherical mineral particles: data incorporated to OPAC. Atmospheric Chemistry and Physics, 15(10), 5947–5956. https://doi.org/10.5194/acp-15-5947-2015

Kokhanovsky A. A., Budak V. P., Cornet C., Duan M., Emde C., Katsev I. L., Klyukov D. A., Korkin S. V., Labonnote L. C., Mayer B., Min Q., Nakajima T., Ota Y., Prikhach A. S., Rozanov V. V., Yokota T., Zege E. P.: Benchmark results in vector atmospheric radiative transfer. Journal of Quantittive Spectroscopy and Radiative Transfer. 2010;111:1931-1946

Kooreman, M. L., Stammes, P., Trees, V., Sneep, M., Tilstra, L. G., de Graaf, M., Stein Zweers, D. C., Wang, P., Tuinder, O. N. E., and Veefkind, J. P.: Effects of clouds on the UV Absorbing Aerosol Index from TROPOMI, Atmos. Meas. Tech., 13, 6407–6426, https://doi.org/10.5194/amt-13-6407-2020, 2020.

Kravitz, B., Robock, A., Boucher, O., Schmidt, H., Taylor, K. E., Stenchikov, G., & Schulz, M. (2011), The Geoengineering Model Intercomparison Project (GeoMIP). Atmospheric Science Letters, 12(2), 162–167, https://doi.org/10.1002/asl.316

Kravitz, B., Caldeira, K., Boucher, O., Robock, A., Rasch, P. J., Alterskjær, K.,. . .Yoon, J.-H. (2013). Climate model response from the Geoengineering Model Intercomparison Project (GeoMIP). Journal of Geophysical Research: Atmospheres, 118(15), 8320-8332. https://doi.org/10.1002/jgrd.50646

Kravitz, B, MacMartin, D. G., Wang, H., & Rasch, P. J. (2016). Geoengineering as a design problem. Earth System Dynamics, 7(2), 469–497. https://doi.org/10.5194/esd-7-469-2016

Kravitz, Ben, MacMartin, D. G., Mills, M. J., Richter, J. H., Tilmes, S., Lamarque, J.-F., … Vitt, F. (2017). First Simulations of Designing Stratospheric Sulfate Aerosol Geoengineering to Meet Multiple Simultaneous Climate Objectives. Journal of Geophysical Research: Atmospheres, 122(23), 12,612-616,634. https://doi.org/https://doi.org/10.1002/2017JD026874

Krämer, M., Rolf, C., Luebke, A., Afchine, A., Spelten, N., Costa, A., Meyer, J., Zöger, M., Smith, J., Herman, R. L., Buchholz, B., Ebert, V., Baumgardner, D., Borrmann, S., Klingebiel, M., Avallone, L.: A microphysics guide to cirrus clouds – Part 1: Cirrus types, Atmos. Chem. Phys., 16, 3463–3483, doi:10.5194/acp-16-3463-2016, 2016.

Krishnamohan, K.-P. S.-P., Bala, G., Cao, L., Duan, L., & Caldeira, K. (2019). Climate system response to stratospheric sulfate aerosols: sensitivity to altitude of aerosol layer. Earth System Dynamics, 10(4), 885-900. https://doi.org/10.5194/esd-10-885- 2019.

Kurchaba, S., van Vliet, J., Verbeek, F. J., & Veenman, C. J.. Anomalous $NO_2$ emitting ship detection with TROPOMI satellite data and machine learning. Remote Sensing of Environment, 297, 113761. https://doi.org/10.1016/j.rse.2023.113761, 2023.

Kylling, A., Vandenbussche, S., Capelle, V., Cuesta, J., Klüser, L., Lelli, L., Popp, T., Stebel, K., and Veefkind, P.: Comparison of dust-layer heights from active and passive satellite sensors, Atmos. Meas. Tech., 11, 2911-2936., https://doi.org/10.5194/amt-11-2911-2018, 2018.

Laakso, A., Niemeier, U., Visioni, D., Tilmes, S., & Kokkola, H. (2022). Dependency of the impacts of geoengineering on the stratospheric sulfur injection strategy -- Part 1: Intercomparison of modal and sectional aerosol modules. Atmospheric Chemistry and Physics, 22(1), 93–118. https://doi.org/10.5194/acp-22-93-2022

Laakso, A., Visioni, D., Niemeier, U., Tilmes, S., & Kokkola, H. (2024). Dependency of the impacts of geoengineering on the stratospheric sulfur injection strategy -- Part 2: How changes in the hydrological cycle depend on the injection rate and model used. Earth System Dynamics, 15(2), 405–427. https://doi.org/10.5194/esd-15-405-2024

Latham, J., Rasch, P., Chen, C.-C., Kettles, L., Gadian, A., Gettelman, A., Morrison, H., Bower, K., & Choularton, T. (2008), Global temperature stabilization via controlled albedo enhancement of low-level maritime clouds. Philosophical Transactions of the Royal Society A, 366(1882), 3969–3987, https://doi.org/10.1098/rsta.2008.0137

Latham, J., Bower, K., Choularton, T., Coe, H., Connolly, P., Cooper, G., Craft, T., Foster, J., Gadian, A., Galbraith, L., Iacovides, H., Johnston, D., Launder, B., Leslie, B., Meyer, J., Neukermans, A., Ormond, B., Parkes, B., Rasch, P., Rush, J., Salter, S., Stevenson, T., Wang, H., Wang, Q., & Wood, R. (2012). Marine cloud brightening. Philosophical Transactions of the Royal Society A: Mathematical, Physical and Engineering Sciences, 370(1974), 4217–4262. https://doi.org/10.1098/rsta.2012.0086

Lawrence, D., Rosie, F., Koven, C., Oleson, K., Swenson, S., Vertenstein, M., … Xu, C. (2018). CLM5.0 Technical Description.

Lee, W. R., MacMartin, D. G., Visioni, D., Kravitz, B., Chen, Y., Moore, J. C., … Bailey, D. A. (2023). High-Latitude Stratospheric Aerosol Injection to Preserve the Arctic. Earth's Future, 11(1), e2022EF003052. https://doi.org/https://doi.org/10.1029/2022EF003052

Lelli, L., A. A. Kokhanovsky, V. V. Rozanov, M. Vountas, A. M. Sayer, and J. P. Burrows. Seven years of global retrieval of cloud properties using space-borne data of GOME. Atmospheric Measurement Techniques, 5(7):1551–1570, 2012. doi:10.5194/amt-5-1551-2012, 2012.

Lelli, L., Kokhanovsky, A. A., Rozanov, V. V., Vountas, M., and Burrows, J. P.: Linear trends in cloud top height from passive observations in the oxygen A-band, Atmos. Chem. Phys., 14, 5679–5692, https://doi.org/10.5194/acp-14-5679-2014, 2014.

Lelli, L., S. Gimeno-Garcia, A.F.J. Sanders, D. Loyola, R. Lutz, and M. Sneep. Sentinel-5P/TROPOMI Science Verification Report (Sect. 13.4 and 14.4). Technical report, European Space Agency, 2015. URL https://earth.esa.int/documents/247904/2474724/Sentinel-5PTROPOMI-Science-Verification-Report . Ref: S5P-IUP-L2-ScVR-RP (last access: 3/9/2019), 2015.

Lelli, L. Statistics of aerosol and cloud interactions from satellite (STARCLINT), CCI Living Planet Fellowship Final Report 4000116253/13/INB, 2019.

Levy II H., L. W. Horowitz, M. D. Schwarzkopf, Y. Ming, J.-C. Golaz, V. Naik, V. Ramaswamy, The roles of aerosol direct and indirect effects in past and future climate change, https://doi.org/10.1002/jgrd.50192 (2013).

Li, Q., and Groß, S.: Changes in cirrus cloud properties and occurrence over Europe during the COVID-19-caused air traffic reduction, Atmos. Chem. Phys., 21, 14573-14590, https://doi.org/10.5194/acp-21-14573-2021, 2021.

Li, Q. and Groß, S.: Satellite observations of seasonality and long-term trends in cirrus cloud properties over Europe: investigation of possible aviation impacts, Atmos. Chem. Phys., 22, 15963–15980, https://doi.org/10.5194/acp-22-15963-2022, 2022.

Li, Q. and Groß, S.: Lidar observations of cirrus cloud properties with CALIPSO from midlatitudes towards high-latitudes, Atmos. Chem. Phys., 25, 16657–16677, https://doi.org/10.5194/acp-25-16657-2025, 2025a.

Li, Q., & Groß, S. Lidar observations of cirrus cloud properties with CALIPSO from midlatitudes towards high-latitudes [Data set] 2025b. Zenodo. https://doi.org/10.5281/zenodo.15063832

Li, Y., Mahnke, C., Rohs, S., Bundke, U., Spelten, N., Dekoutsidis, G., Groß, S., Voigt, C., Schumann, U., Petzold, A., and Krämer, M.: Upper-tropospheric slightly ice-subsaturated regions: frequency of occurrence and statistical evidence for the appearance of contrail cirrus, Atmos. Chem. Phys., 23, 2251–2271, https://doi.org/10.5194/acp-23-2251-2023, 2023.

Liou, K. N.: Influence of cirrus clouds on weather and climate processes: A global perspective, Mon. Weather Rev., 114, 1167–1199, 1986.

Lombardozzi, D. L., Lu, Y., Lawrence, P. J., Lawrence, D. M., Swenson, S., Oleson, K. W., Wieder, W. R., & Ainsworth, E. A. (2020). Simulating agriculture in the Community Land Model Version 5. *Journal of Geophysical Research: Biogeosciences*, 125(8), e2019JG005529. https://doi.org/10.1029/2019JG005529

Lohmann, U., and Gasparini, B.: A cirrus cloud climate dial? Science 357 248-249, DOI: 10.1126/science.aan3325, 2017.

Lopatin, A., Dubovik, O., Chaikovsky, A., Goloub, P., Lapyonok, T., Tanré, D., & Litvinov, P. (2013). Enhancement of aerosol characterization using synergy of lidar and sun-photometer coincident observations: the GARRLiC algorithm. Atmospheric Measurement Techniques, 6(8), 2065–2088. https://doi.org/10.5194/amt-6-2065-2013

Lopatin, Anton, Dubovik, O., Fuertes, D., Stenchikov, G., Lapyonok, T., Veselovskii, I., … Parajuli, S. (2021). Synergy processing of diverse ground-based remote sensing and in situ data using the GRASP algorithm: applications to radiometer, lidar and radiosonde observations. Atmospheric Measurement Techniques, 14(3), 2575–2614. https://doi.org/10.5194/amt-14-2575-2021

Lopes, F. J. S., Silva, J. J., Antuña Marrero, J. C., Taha, G., & Landulfo, E. (2019). *Synergetic Aerosol Layer Observation After the 2015 Calbuco Volcanic Eruption Event*. Remote Sensing, 11(2), 195. https://doi.org/10.3390/rs11020195

Loyola, D. G.: Automatic cloud analysis from polar-orbiting satellites using neural network and data fusion techniques, 540 in: IGARSS 2004. 2004 IEEE International Geoscience and Remote Sensing Symposium, vol. 4, pp. 2530–2533 vol.4, https://doi.org/10.1109/IGARSS.2004.1369811, 2004.

Loyola, D. G., Thomas, W., Spurr, R., and Mayer, B.: Global patterns in daytime cloud properties derived from GOME backscatter UV-VIS measurements, International Journal of Remote Sensing, 31, 4295–4318, https://doi.org/10.1080/01431160903246741, 2010.

Loyola, D. G., Gimeno García, S., Lutz, R., Argyrouli, A., Romahn, F., Spurr, R. J. D., Pedergnana, M., Doicu, A., Molina García, V., and Schüssler, O.: The operational cloud retrieval algorithms from TROPOMI on board Sentinel-5 Precursor, Atmos. Meas. Tech., 11, 409– 427,https://doi.org/10.5194/amt-11-409-2018, 2018.

Luebke, A. E., Afchine, A., Costa, A., Grooß, J.-U., Meyer, J., Rolf, C., Spelten, N., Avallone, L. M., Baumgardner, D., and Krämer, M.: The origin of midlatitude ice clouds and the resulting influence on their

microphysical properties, Atmos. Chem. Phys., 16, 5793–5809, https://doi.org/10.5194/acp-16-5793-2016, 2016.

Lutz, R., Loyola, D. G., Gimeno García, S., and Romahn, F.: OCRA radiometric cloud fractions for GOME-2 on MetOp-A/B, Atmospheric Measurement Techniques, 9, 2357–2379, https://doi.org/10.5194/amt-9-2357-2016, 2016.

Lutz, R., Molina Garcia, V., Argyrouli, A., Romahn, F., and Loyola, D.: A cloud product for Sentinel-4 to support the Geo-Ring for Air Quality, EGU General Assembly 2024, Vienna, Austria, 14–19 Apr 2024, EGU24-9883, https://doi.org/10.5194/egusphere-egu24-9883, 2024.

McCormick, M., Thomason, L. & Trepte, C.: Atmospheric effects of the Mt Pinatubo eruption. Nature 373, 399–404. https://doi.org/10.1038/373399a0, 1995.

Ma, X., H. Jia, F. Yu, and J. Quaas. Opposite aerosol index-cloud droplet effective radius correlations over major industrial regions and their adjacent oceans. Geophysical Research Letters, 45(11):5771–5778, doi:10.1029/2018GL077562, 2018.

MacMartin, D. G., Ricke, K. L. and Keith, D. W. Solar geoengineering as part of an overall strategy for meeting the 1.5°C Paris target. Philosophical Transactions of the Royal Society A: Mathematical, Physical and Engineering Sciences. 2018; 376, 20160454.

MacMartin, D. G., Wang, W., Kravitz, B., Tilmes, S., Richter, J. H., & Mills, M. J. (2019). Timescale for Detecting the Climate Response to Stratospheric Aerosol Geoengineering. Journal of Geophysical Research: Atmospheres, 124(3), 1233–1247. https://doi.org/https://doi.org/10.1029/2018JD028906

Macnaghten, P., & Szerszynski, B. (2013). Living the global social experiment. Global Environmental Change.

Maciel, F. V., Diao, M., and Patnaude, R.: Examination of aerosol indirect effects during cirrus cloud evolution, Atmos. Chem. Phys., 23, 1103–1129, https://doi.org/10.5194/acp-23-1103-2023, 2023.

Malik, A., Nowack, P. J., Haigh, J. D., Cao, L., Atique, L., & Plancherel, Y. (2020). Tropical Pacific climate variability under solar geoengineering: impacts on ENSO extremes. Atmospheric Chemistry and Physics, 20(23), 15461–15485. https://doi.org/10.5194/acp-20-15461-2020

Malinina, E., Rozanov, A., Rozanov, V., Liebing, P., Bovensmann, H., and Burrows, J. P.: Aerosol particle size distribution in the stratosphere retrieved from SCIAMACHY limb measurements, Atmos. Meas. Tech., 11, 2085–2100, https://doi.org/10.5194/amt-11-2085-2018, 2018

Manney, G. L., Millán, L. F., Santee, M. L., Wargan, K., Lambert, A., Neu, J. L., Werner, F., Lawrence, Z. D., Schwartz, M. J., Livesey, N. J., and Read, W. G., Signatures of anomalous transport in the 2019/2020 Arctic stratospheric polar vortex. J. Geophys. Res.: Atmospheres, 127(20). https://doi.org/10.1029/2022jd037407, 2022.

Matthews, H. D. and Caldeira, K. Transient climate–carbon simulations of planetary geoengineering. Proceedings of the National Academy of Sciences. 104: 9949–9954, https://www.jstor.org/stable/25435864, 2007

Märkl, R. S., Voigt, C., Sauer, D., Dischl, R. K., Kaufmann, S., Harlaß, T., Hahn, V., Roiger, A., Weiß-Rehm, C., Burkhardt, U., Schumann, U., Marsing, A., Scheibe, M., Dörnbrack, A., Renard, C., Gauthier, M., Swann, P., Madden, P., Luff, D., Sallinen, R., Schripp, T., and Le Clercq, P.: Powering aircraft with 100 % sustainable aviation fuel reduces ice crystals in contrails, Atmos. Chem. Phys., 24, 3813–3837, https://doi.org/10.5194/acp-24-3813-2024, 2024.

Marsing, A., Meerkötter, R., Heller, R., Kaufmann, S., Jurkat-Witschas, T., Krämer, M., Rolf, C., and Voigt, C.: Investigating the radiative effect of Arctic cirrus measured in situ during the winter 2015–2016, Atmos. Chem. Phys., 23, 587–609, https://doi.org/10.5194/acp-23- 587- 2023, 2023.

Mayer, B., and Kylling, A.: Technical note: The libRadtran software package for radiative transfer calculations - description and examples of use, Atmos. Chem. Phys., 5, 1855-1877, 2005.

McBride, B. A., Martins, J. V., Cieslak, J. D., Fernandez-Borda, R., Puthukkudy, A., Xu, X., Sienkiewicz, N., Cairns, B., and Barbosa, H. M. J.: Pre-launch calibration and validation of the Airborne Hyper-Angular Rainbow Polarimeter (AirHARP) instrument, Atmos. Meas. Tech., 17, 5709–5729, https://doi.org/10.5194/amt-17-5709-2024, 2024.

McKenzie, R. L., Bernhard, G., Liley, J. B., Disterhoft, P., Rhodes, S., Bais, A., Morgenstern, O., Newman, P., Oman, L., Brogniez, C., & Simic, S. (2011). Success of the Montreal Protocol demonstrated by comparing high-quality UV measurements with "World Avoided" calculations from two chemistry-climate models. Scientific Reports, 9, 12332. https://doi.org/10.1038/s41598-019-48625-z

McLinden, C. A., McConnell, J. C., McElroy, C. T., and Griffioen, E.: Observations of stratospheric aerosol using CPFM polarized limb radiances, J. Atmos. Sci., 56, 233–240, 1999

Mei, L., Rozanov, V., Vountas, M., Burrows, J. P., Levy, R. C., & Lotz, W.: Retrieval of aerosol optical properties using MERIS observations: Algorithm and some first results. Remote sensing of environment, 197, 125-140. https://doi.org/10.1016/j.rse.2016.11.015, 2017.

Mei, L., Vountas, M., Gómez-Chova, L., Rozanov, V., Jäger, M., Lotz, W., Burrows, J.P. and Hollmann, R.: A Cloud masking algorithm for the XBAER aerosol retrieval using MERIS data. Remote Sensing of Environment, 197, pp.141-160. https://doi.org/10.1016/j.rse.2016.11.016, 2017.

Mei, L., Rozanov, V., Vountas, M., Burrows, J. P., and Richter, A.: XBAER-derived aerosol optical thickness from OLCI/Sentinel-3 observation, Atmos. Chem. Phys., 18, 2511–2523, https://doi.org/10.5194/acp-18-2511-2018, 2018.

Meyer, K., Yang, P., & Gao, B.-C. Optical thickness of tropical cirrus clouds derived from the MODIS 0.66 and 1.375 μm channels. *IEEE Transactions on Geoscience and Remote Sensing. 2004:* 42(4), 833–841.

Mills, M. J., Richter, J. H., Tilmes, S., Kravitz, B., MacMartin, D. G., Glanville, A. A., … Kinnison, D. E. (2017). Radiative and Chemical Response to Interactive Stratospheric Sulfate Aerosols in Fully Coupled CESM1(WACCM). Journal of Geophysical Research: Atmospheres, 122(23), 13,13-61,78. https://doi.org/https://doi.org/10.1002/2017JD027006

Mitchell, D. L., and W. Finnegan.: Modification of cirrus clouds to reduce global warming, Environ. Res. Lett., 4(4), 045102, http://dx.doi.org/10.1088/1748-9326/4/4/045102, 2009.

Mitchell, D. L., Garnier, A., Pelon, J., and Erfani, E.: CALIPSO (IIR–CALIOP) retrievals of cirrus cloud ice-particle concentrations, Atmos. Chem. Phys., 18, 17325–17354, https://doi.org/10.5194/acp-18-17325-2018, 2018.

Mitchell, D. L., Garnier, A., and Woods, S.: Advances in CALIPSO (IIR) cirrus cloud property retrievals – Part 1: Methods and testing, Atmos. Chem. Phys., 25, 14071–14098, https://doi.org/10.5194/acp-25-14071-2025, 2025.

Mitchell, D. L. and Garnier, A.: Advances in CALIPSO (IIR) cirrus cloud property retrievals – Part 2: Global estimates of the fraction of cirrus clouds affected by homogeneous ice nucleation, Atmos. Chem. Phys., 25, 14099–14129, https://doi.org/10.5194/acp-25-14099-2025, 2025.

Molina García, V.: Retrieval of cloud properties from EPIC/DSCOVR, Ph.D. thesis, Technische Universität München, https://mediatum.ub. tum.de/?id=1662361, 2022.

Moore, J., Jevrejeva, S., & Grinsted, A. (2010). Efficacy of geoengineering to limit 21st century sea-level rise. Proceedings of the National Academy of Sciences of the United States of America, 107, 15699–15703. https://doi.org/10.1073/pnas.1008153107

Niemeier, U., Richter, J. H., & Tilmes, S. (2020). Differing responses of the quasi-biennial oscillation to artificial \chem{SO_2} injections in two global models. Atmospheric Chemistry and Physics, 20(14), 8975–8987. https://doi.org/10.5194/acp-20-8975-2020

Niemeier, U., Schmidt, H., & Timmreck, C. (2011). The dependency of geoengineered sulfate aerosol on the emission strategy. Atmospheric Science Letters, 12(2), 189–194. https://doi.org/10.1002/asl.304

Norval, M., Lucas, R. M., Cullen, A. P., de Gruijl, F. R., Longstreth, J., Takizawa, Y., & van der Leun, J. C. (2011). The human health effects of ozone depletion and interactions with climate change. Photochemical & Photobiological Sciences, 10(2), 199–225. https://doi.org/10.1039/c0pp90044c

Pappalardo, G., Amodeo, A., Apituley, A., Comeron, A., Freudenthaler, V., Linné, H., … Wiegner, M. (2014). EARLINET: towards an advanced sustainable European aerosol lidar network. Atmospheric Measurement Techniques, 7(8), 2389–2409. https://doi.org/10.5194/amt-7-2389-2014

Parker, A., Geden, O. No fudging on geoengineering. Nature Geosci 9, 859–860, https://doi.org/10.1038/ngeo2851, 2016.

Patt, A., Rajamani, L., Bhandari, P., Ivanova Boncheva, A., Caparrós, A. Djemouai, K. et al. International cooperation. In: IPCC, 2022: Climate Change 2022: Mitigation of Climate Change. Contribution of Working Group III to the Sixth Assessment Report of the Intergovernmental Panel on Climate Change [P.R. Shukla, J. Skea, R. Slade, A. Al Khourdajie, R. van Diemen, D. McCollum, M. Pathak, S. Some, P. Vyas, R. Fradera, M. Belkacemi, A. Hasija, G. Lisboa, S. Luz, J. Malley, (eds.)]. Cambridge University Press, Cambridge, UK and New York, NY, USA, https://doi.org/10.1017/9781009157926.016, 2022.

Patti, B., Torri, M., & Cuttitta, A. (2022). Interannual summer biodiversity changes in ichthyoplankton assemblages of the Strait of Sicily (Central Mediterranean) over the period 2001–2016. Frontiers in Marine Science, 9, 960929. https://doi.org/10.3389/fmars.2022.960929

Penner, J.E., Lister, D.H., Griggs, D.J., Dokken, D.J., & McFarland, M. (Eds.). (1999). Aviation and the Global Atmosphere.Prepared in collaboration with the Scientific Assessment Panel to the Montreal Protocol on Substances that Deplete the Ozone Layer.Cambridge University Press, Cambridge, UK. 373 pp.

Petro, S., Pham, K., & Hilton, G. (2020). Plankton, Aerosol, Cloud, ocean Ecosystem (PACE) Mission Integration and Testing. 2020 IEEE Aerospace Conference, 1–20. https://doi.org/10.1109/AERO47225.2020.9172326

Pierce, J. R., Weisenstein, D. K., Heckendorn, P., Peter, T., & Keith, D. W. (2010). Efficient formation of stratospheric aerosol for climate engineering by emission of condensible vapor from aircraft. Geophysical Research Letters, 37(18). https://doi.org/10.1029/2010GL043975

Pitari, G., Aquila, V., Kravitz, B., Robock, A., Watanabe, S., Cionni, I., … Tilmes, S. (2014). Stratospheric ozone response to sulfate geoengineering: Results from the Geoengineering Model Intercomparison Project (GeoMIP). Journal of Geophysical Research: Atmospheres, 119(5), 2629–2653. https://doi.org/https://doi.org/10.1002/2013JD020566

Pongratz, J., Lobell, D. B., Cao, L., & Caldeira, K. (2012). Crop yields in a geoengineered climate. Nature Climate Change, 2, 101–105. https://doi.org/10.1038/nclimate1373

Pope, F., Braesicke, P., Grainger, R., Kalberer, M., Watson, I. M., Davidson, P., & Cox, R. (2012). Stratospheric aerosol particles and solar-radiation management. Nature Clim. Change, 2, 713–719. https://doi.org/10.1038/nclimate1528

Proctor, J., Hsiang, S., Burney, J., Burke, M., & Schlenker, W. Estimating global agricultural effects of geoengineering using volcanic eruptions. Nature 560, 480–483. https://doi.org/10.1038/s41586-018-0417-3, 2018.

Quaas, J., A. Arola, B. Cairns, M. Christensen, H. Deneke, A. Ekman, G. Feingold, A. Fridlind, E. Gryspeerdt, O. Hasekamp, Z. Li, A. Lipponen, P. Ma, J. Mülmenstädt, A. Nenes, J. Penner, D. Rosenfeld, R. Schrödner, K. Sinclair, O. Sourdeval, P. Stier, M. Tesche, B. Van Diedenhoven, and M. Wendisch, Constraining the Twomey effect from satellite observations: Issues and perspectives, Atmos. Chem. Phys., 20, 15079-15099, doi:10.5194/acp-20-15079-2020, 2020.

Quaas, J., and E. Gryspeerdt, Aerosol-cloud interactions in liquid clouds, In: Aerosols and Climate, K. Carslaw (ed.), 489-544, doi:10.1016/C2019-0-00121-5, 2022.

Quaas, J., Y. Ming, S. Menon, T. Takemura, M. Wang, J.E. Penner, A. Gettelman, U. Lohmann, N. Bellouin, O. Boucher, A.M. Sayer, G.E. Thomas, A. McComiskey, G. Feingold, C. Hoose, J.E. Kristjánsson, X. Liu, Y. Balkanski, L.J. Donner, P.A. Ginoux, P. Stier, J. Feichter, I. Sednev, S.E. Bauer, D. Koch, R.G.

Grainger, A. Kirkevåg, T. Iversen, Ø. Seland, R. Easter, S.J. Ghan, P.J. Rasch, H. Morrison, J.-F. Lamarque, M.J. Iacono, S. Kinne, and M. Schulz, 2009: Aerosol indirect effects — General circulation model intercomparison and evaluation with satellite data. Atmos. Chem. Phys., 9, 8697-8717, doi:10.5194/acp-9-8697-2009 .

Quaas, J., E. Gryspeerdt, R. Vautard, and O. Boucher, Climate impact of aircraft-induced cirrus assessed from satellite observations before and during COVID-19, Environ. Res. Lett., 16, 064051, doi:10.1088/1748-9326/abf686, 2021.

Quaas, J., T. Andrews, N. Bellouin, K. Block, O. Boucher, P. Ceppi, G. Dagan, S. Doktorowski, H. Eichholz, P. Forster, T. Goren, E. Gryspeerdt, O. Hodnebrog, H. Jia, R. Kramer, C. Lange, A. Maycock, J. Mülmenstädt, G. Myhre, F. O'Connor, R. Pincus, B. Samset, F. Senf, K. Shine, C. Smith, C. Stjern, T. Takemura, V. Toll, and C. Wall, Adjustments to climate perturbations - mechanisms, implications, observational constraints, AGU Advances, 5, e2023AV001144, doi:10.1029/2023AV001144, 2024.

Quagraine, K. A., Tye, M. R., Quagraine, K. T., Tilmes, S., Simpson, I. R., Nkrumah, F., Egbebiyi, T. S., Odoulami, R. C., and Klutse, N. A. B.: Assessing the impact of stratospheric aerosol injection on precipitation extremes in Africa using the ARISE-SAI-1.5 dataset, Environ. Res. Clim., 4, 35006, https://doi.org/10.1088/2752-5295/adee3c, 2025.

Rasch, P.J., Tilmes, S., Turco, R. P., Robock, A., Oman, L., Chen J., Stenchikov, G. L., Garcia, R. R.; An overview of geoengineering of climate using stratospheric sulphate aerosols. *Philos Trans A Math Phys Eng Sci* 13 November 2008; 366 (1882): 4007–4037. https://doi.org/10.1098/rsta.2008.0131

Reynolds, J. L. (2019). Solar geoengineering to reduce climate change: A review of governance proposals. Proceedings of the Royal Society A: Mathematical, Physical and Engineering Sciences, 475(2229), 20190255. https://doi.org/10.1098/rspa.2019.0255

Riess, T. C. V. W., Boersma, K. F., van Vliet, J., Peters, W., Sneep, M., Eskes, H., & van Geffen, J., Improved monitoring of shipping $NO_2$ with TROPOMI: Decreasing $NO_x$ emissions in European seas during the COVID-19 pandemic. Atmospheric Measurement Techniques, 15(5), 1415–1438. https://doi.org/10.5194/amt-15-1415-2022, 2022.

Righi, M., B. Testa, C. G. Beer, J. Hendricks, and Z. A. Kanji, Aviation soot is unlikely to impact natural cirrus clouds, EGUsphere [preprint], doi:10.5194/egusphere-2025-2589, 2025.

Robock, A., Oman, L., & Stenchikov, G. L. (2008). Regional climate responses to geoengineering with tropical and Arctic SO2 injections. Journal of Geophysical Research: Atmospheres, 113(D16). https://doi.org/https://doi.org/10.1029/2008JD010050

Robock, A., Marquardt, A., Kravitz, B., & Stenchikov, G. (2009). Benefits, risks, and costs of stratospheric geoengineering. Geophysical Research Letters, 36(19). https://doi.org/https://doi.org/10.1029/2009GL039209

Robock, A., MacMartin, D.G., Duren, R. et al. Studying geoengineering with natural and anthropogenic analogs. Climatic Change 121, 445–458, https://doi.org/10.1007/s10584-013-0777-5, 2013.

Robock, A.: Important research questions on volcanic eruptions and climate, Past Global Changes Magazine, 23, 68, 2015

Rosenfeld, D., Meinrat O. Andreae, Ari Asmi, Mian Chin, Gerrit de Leeuw, David P. Donovan, Ralph Kahn, Stefan Kinne, Niku Kivekas, Markku Kulmala, William Lau, K. Sebastian Schmidt, Tanja Suni, Thomas Wagner, Martin Wild, and J. Quaas. Global observations of aerosol-cloud-precipitation-climate interactions. Reviews of Geophysics, 52 (4):750–808, 2014. ISSN 1944-9208. doi:10.1002/2013RG000441, 2013.

Russell, L. M., and Coauthors, 2013: Eastern Pacific Emitted Aerosol Cloud Experiment. Bull. Amer. Meteor. Soc., 94, 709–729, https://doi.org/10.1175/BAMS-D-12-00015.1.

Ryan, S. J., Carlson, C. J., Mordecai, E. A., & Johnson, L. R. (2019). Global expansion and redistribution of Aedes-borne virus transmission risk with climate change. PLOS Neglected Tropical Diseases, 13(3), e0007213. https://doi.org/10.1371/journal.pntd.0007213

Sanders, A. F. J., de Haan, J. F., Sneep, M., Apituley, A., Stammes, P., Vieitez, M. O., Tilstra, L. G., Tuinder, O. N. E., Koning, C. E., and Veefkind, J. P.: Evaluation of the operational Aerosol Layer Height retrieval algorithm for Sentinel-5 Precursor: application to O2 A band observations from GOME-2A, Atmos. Meas. Tech., 8, 4947–4977,https://doi.org/10.5194/amt-8-4947-2015, 2015.

Samson, J., D. Berteaux, B. J. McGill, and M. M. Humphries. Geographic disparities and moral hazards in the predicted impacts of climate change on human populations. Global Ecology and Biogeography, 20(4):532–544, doi:10.1111/j.1466-8238.2010.00632.x, 2011.

Schumann, U., Poll, I., Teoh, R., Koelle, R., Spinielli, E., Molloy, J., Koudis, G. S., Baumann, R., Bugliaro, L., Stettler, M., and Voigt, C.: Air traffic and contrail changes during COVID-19 over Europe: A model study, Atmos. Chem. Phys., 21, 7429–7450, https://doi.org/10.5194/acp-21-7429-2021, 2021 a.

Schumann, U., Bugliaro, L., Dörnbrack, A., Baumann, R., and Voigt, C.: Aviation contrail cirrus and radiative forcing over Europe during 6 months of COVID-19, Geophys. Res. Lett., 48, e2021GL092771, https://doi.org/10.1029/2021GL092771, 2021b.

Scott, D., Hall, C. M., & Gössling, S. (2020). Tourism and climate change: Impacts, adaptation and mitigation. Routledge.

Seidel, D. J., Feingold, G., Jacobson, A. R., and Loeb, N. (2014). Detection limits of albedo changes induced by climate engineering, Nature Climate Change, 4, doi:10.1038/NCLIMATE2076.

Smith, W., & Wagner, G. (2018). Stratospheric aerosol injection tactics and costs in the first 15 years of deployment. Environmental Research Letters, 13(12), 124001. https://doi.org/10.1088/1748-9326/aae98d

Smith, W. (2020). The cost of stratospheric aerosol injection through 2100. Environmental Research Letters, 15(11), 114004. https://doi.org/10.1088/1748-9326/aba7e7

Stephens, G. L., et al., The CloudSat mission and the A-train: A new dimension of space-based observations of clouds and precipitation, Bull. Am. Meteorol. Soc., 83, 1771–1790, https://doi.org/10.1175/BAMS-83-12-1771, 2002.

Stier, P.: Limitations of passive remote sensing to constrain global cloud condensation nuclei, Atmos. Chem. Phys., 16, 6595–6607, doi:10.5194/acp-16-6595-2016, 2016.

Stjern, C. W., Muri, H., Ahlm, L., Boucher, O., Cole, J. N. S., Ji, D.,...Kristjánsson, J. E. (2018). Response to marine cloud brightening in a multi-model ensemble. Atmospheric Chemistry and Physics, 18(2), 621-634. https://doi.org/10.5194/acp-18-621-2018 .

Storelvmo, T., & Herger, N. (2014). Cirrus cloud susceptibility to the injection of ice nuclei in the upper troposphere. Journal of Geophysical Research: Atmospheres, 119(5), 2375–2389. https://doi.org/10.1002/2013JD020816

Storelvmo, T., Kristjansson, J. E., Muri, H., Pfeffer, M., Barahona, D., and Nenes, A.: Cirrus cloud seeding has potential to cool climate, Geophys. Res. Lett., 40, 178–182, https://doi.org/10.1029/2012GL054201, 2013.

Sugiyama, M., Asayama, S., & Kosugi, T. (2020). The North–South divide on public perceptions of stratospheric aerosol geoengineering? A survey in six Asia–Pacific countries. Environmental Communication, 14(5), 641–656. https://doi.org/10.1080/17524032.2019.1699137

Suhendro, I., Agroli, G., Naen, G. N. R. B., Gurusinga, M. A., Nurfiani, D., Ayunda, F. P., Manullang, R. J. Y., and Tsuchiya, N.: The fate of an extremely phenocryst-rich magma in producing small sub-Plinian plumes during the 17th and 30th April 2024 eruption of Mt. Ruang (North Sulawesi, Indonesia): The role of clast density, J. Volcanol. Geotherm. Res., 463, 108332, https://doi.org/https://doi.org/10.1016/j.jvolgeores.2025.108332, 2025.

Sun, H., Bourguet, S., Eastham, S., & Keith, D. (2023). Optimizing injection locations relaxes altitude-lifetime trade-off for stratospheric aerosol injection. Geophysical Research Letters, 50(16), e2023GL105371. https://doi.org/10.1029/2023GL105371 .

Tackett, J. L., Kar, J., Vaughan, M. A., Getzewich, B. J., Kim, M.-H., Vernier, J.-P., … Winker, D. M. (2023). The CALIPSO version 4.5 stratospheric aerosol subtyping algorithm. Atmospheric Measurement Techniques, 16(3), 745–768. https://doi.org/10.5194/amt-16-745-2023

Teoh, R., Engberg, Z., Schumann, U., Voigt, C., Shapiro, M., Rohs, S., and Stettler, M. E. J.: Global aviation contrail climate effects from 2019 to 2021, Atmos. Chem. Phys., 24, 6071–6093, https://doi.org/10.5194/acp-24-6071-2024, 2024.

Testa, B., Durdina, L., Alpert, P. A., Mahrt, F., Dreimol, C. H., Edebeli, J., Spirig, C., Decker, Z. C. J., Anet, J., and Kanji, Z. A.: Soot aerosols from commercial aviation engines are poor ice-nucleating particles at cirrus cloud temperatures, Atmos. Chem. Phys., 24, 4537–4567, https://doi.org/10.5194/acp-24-4537-2024, 2024.

Testa, B., Durdina, L., Edebeli, J., Spirig, C., and Kanji, Z. A.: Simulated contrail-processed aviation soot aerosols are poor ice-nucleating particles at cirrus temperatures, Atmos. Chem. Phys., 24, 10409–10424, https://doi.org/10.5194/acp-24-10409-2024, 2024.

Tilmes, S., Visioni, D., Jones, A., Haywood, J., Séférian, R., Nabat, P., Boucher, O., Bednarz, E. M., and Niemeier, U.: Stratospheric ozone response to sulfate aerosol and solar dimming climate interventions based on the G6 Geoengineering Model Intercomparison Project (GeoMIP) simulations, Atmos. Chem. Phys., 22, 4557–4579, https://doi.org/10.5194/acp-22-4557-2022, 2022 a.

Tilmes, S, Richter, J. H., Kravitz, B., MacMartin, D. G., Glanville, A. S., Visioni, D., … Müller, R. (2021). Sensitivity of Total Column Ozone to Stratospheric Sulfur Injection Strategies. Geophysical Research Letters, 48(19), e2021GL094058. https://doi.org/https://doi.org/10.1029/2021GL094058

Tilmes, S, MacMartin, D. G., Lenaerts, J. T. M., van Kampenhout, L., Muntjewerf, L., Xia, L., … Robock, A. (2020). Reaching 1.5 and 2.0\,{\degree}C global surface temperature targets using stratospheric aerosol geoengineering. Earth System Dynamics, 11(3), 579–601. https://doi.org/10.5194/esd-11-579-2020

Tilmes, Simone, Richter, J. H., Kravitz, B., MacMartin, D. G., Mills, M. J., Simpson, I. R., … Ghosh, S. (2018). CESM1(WACCM) Stratospheric Aerosol Geoengineering Large Ensemble Project. Bulletin of the American Meteorological Society, 99(11), 2361–2371. https://doi.org/https://doi.org/10.1175/BAMS-D-17-0267.1

Tilmes, S., Richter, J. H., Mills, M. J., Kravitz, B., MacMartin, D. G., Vitt, F.,...Lamarque, J.-F. (2017). Sensitivity of aerosol distribution and climate response to stratospheric SO2 injection locations. Journal of Geophysical Research: Atmospheres, 122(23), 12,591- 512,615. https://doi.org/10.1002/2017JD026888

Tilmes, S, Sanderson, B. M., & O'Neill, B. C. (2016). Climate impacts of geoengineering in a delayed mitigation scenario. Geophysical Research Letters, 43(15), 8222–8229. https://doi.org/https://doi.org/10.1002/2016GL070122

Tilmes, S., Müller, R., & Salawitch, R. J. (2008), The sensitivity of polar ozone depletion to proposed geoengineering schemes. Science, 320(5880), 1201–1204, https://doi.org/10.1126/science.1153966

Tilmes, S., Müller, R., & Salawitch, R. (2013). The hydrological impact of geoengineering in the Geoengineering Model Intercomparison Project (GeoMIP). Journal of Geophysical Research: Atmospheres, 118(12), 6531–6543. https://doi.org/10.1002/jgrd.50868

Tollefson, J. (2021). Can artificially altered clouds save the Great Barrier Reef? Nature, 596, 476–478. https://doi.org/10/1038/d41586-021-02290-3 .

Torres, O., Bhartia, P. K., Herman, J. R., Ahmad, Z., and Gleason, J.: Derivation of aerosol properties from satellite measurements of backscattered ultraviolet radiation: Theoretical basis, J. Geophys. Res., 103, 17099–17110, https://doi.org/10.1029/98JD00900, 1998. a.

Torres, O., Jethva, H., Ahn, C., Jaross, G., and Loyola, D. G.: TROPOMI aerosol products: evaluation and observations of synoptic-scale carbonaceous aerosol plumes during 2018–2020, Atmos. Meas. Tech., 13, 6789–6806, https://doi.org/10.5194/amt-13-6789-2020, 2020.

Trenberth, Jones, P., Ambenje, Bojariu, R., Easterling, D., Tank, K., … Folland, C. (2007). Observations: Surface and Atmospheric Climate Change.

Trisos, C. H., et al. (2018). Potentially dangerous consequences for biodiversity of solar geoengineering implementation and termination. Nature Ecology & Evolution, 2, 475–482. https://doi.org/10.1038/s41559-018-0494-6

Tully, C., Neubauer, D., Omanovic, N., and Lohmann, U.: Cirrus cloud thinning using a more physically based ice microphysics scheme in the ECHAM-HAM general circulation model, Atmos. Chem. Phys., 22, 11455–11484, https://doi.org/10.5194/acp-22-11455-2022, 2022.

Ugolnikov, O. S. and Maslov, I. A.: Investigations of the Background Stratospheric Aerosol Using Multi-color Wide-Angle Measurements of the Twilight Glow Background, Cosmic Research, 56, 85–93, https://doi.org/10.1134/S0010952518020119, 2018

Urban, M. C., Bocedi, G., Hendry, A. P., Mihoub, J.-B., Pe'er, G., Singer, A., Bridle, J. R., Crozier, L. G., De Meester, L., Godsoe, W., González, A., Hellmann, J. J., Holt, R. D., Huth, A., Johst, K., Krug, C. B., Leadley, P. W., Palmer, S. C. F., Pantel, J. H., Schmitz, A., Zollner, P. A., & Travis, J. M. J. (2016). Improving the forecast for biodiversity under climate change. Science, 353(6304), aad8466. https://doi.org/10.1126/science.aad8466

Urbanek, B., Groß, S., Wirth, M., Rolf, C., Krämer, M., and Voigt, C.: High depolarization ratios of naturally occurring cirrus clouds near air traffic regions over Europe, Geophys. Res. Lett., 45, 13,166–13,172, https://doi.org/10.1029/2018GL079345, 2018.

Veefkind, J.P., I. Aben, K. McMullan, H. Förster, J. de Vries, G. Otter, J. Claas, H.J. Eskes, J.F. de Haan, Q. Kleipool, M. van Weele, O. Hasekamp, R. Hoogeveen, J. Landgraf, R. Snel, P. Tol, P. Ingmann, R. Voors, B. Kruizinga, R. Vink, H. Visser, P.F. Levelt, TROPOMI on the ESA Sentinel-5 Precursor: A GMES mission for global observations of the atmospheric composition for climate, air quality and ozone layer applications, Remote Sensing of Environment, Volume 120, Pages 70-83, https://doi.org/10.1016/j.rse.2011.09.027, 2012.

Vernier, J.-P., Fairlie, T. D., Deshler, T., Natarajan, M., Knepp, T., Foster, K., … Trepte, C. (2016). In situ and space-based observations of the Kelud volcanic plume: The persistence of ash in the lower stratosphere. Journal of Geophysical Research: Atmospheres, 121(18), 11,104-111,118. https://doi.org/https://doi.org/10.1002/2016JD025344

Villanueva, D., A. Possner, D. Neubauer, B. Gasparini, U. Lohmann, and M. Tesche, Mixed-phase regime cloud thinning could help restore sea ice, Environ. Res. Lett., 17, 114057, doi:10.1088/1748-9326/aca16d, 2022.

Visioni, Daniele, Quaglia, I., & Steinke, I. (2024). A Living Assessment of Different Materials for Stratospheric Aerosol Injection—Building Bridges Between Model World and the Messiness of Reality. Geophysical Research Letters, 51(10), 1–5. https://doi.org/10.1029/2024GL108314

Visioni, D, Bednarz, E. M., Lee, W. R., Kravitz, B., Jones, A., Haywood, J. M., & MacMartin, D. G. (2023). Climate response to off-equatorial stratospheric sulfur injections in three Earth system models -- Part 1: Experimental protocols and surface changes. Atmospheric Chemistry and Physics, 23(1), 663–685. https://doi.org/10.5194/acp-23-663-2023

Visioni, D., Bednarz, E. M., MacMartin, D. G., Kravitz, B., & Goddard, P. B. (2020). What goes up must come down: Impacts of deposition in a sulfate geoengineering scenario. Environmental Research Letters, 15(9), 094063, https://iopscience.iop.org/article/10.1088/1748-9326/ab94ebp

Visioni, D., MacMartin, D. G., Kravitz, B., Lee, W., Simpson, I. R., & Richter, J. H. (2020). Reduced poleward transport due to stratospheric heating under stratospheric aerosols geoengineering. Geophysical Research Letters, 47(17), e2020GL089470. https://doi.org/10.1029/2020GL089470 .

Vogel, F., Lacher, L., Nadolny, J., Saathoff, H., Leisner, T., and Möhler, O.: Development and validation of a new cloud simulation experiment for lab-based aerosol-cloud studies, Rev. Sci. Instrum. 93, 095106, https://doi.org/10.1063/5.0098777, 2022.

Vogel, A., Diplas, S., Durant, A. J., Azar, A. S., Sunding, M. F., Rose, W. I., … Stohl, A. (2017). Reference data set of volcanic ash physicochemical and optical properties. Journal of Geophysical Research: Atmospheres, 122(17), 9485–9514. https://doi.org/https://doi.org/10.1002/2016JD026328

Voigt, C., Kleine, J., Sauer, D., Moore, R. H., Bräuer, T., Clercq, P. L., Kaufmann, S., Scheibe, M., Jurkat-Witschas, T., Aigner, M., Bauder, U., Boose, Y., Borrmann, S., Crosbie, E., Diskin, G. S., DiGangi, J., Hahn, V., Heckl, C., Huber, F., Nowak, J. B., Rapp, M., Rauch, B., Robinson, C., Schripp, T., Shook, M., Winstead, E., Ziemba, L., Schlager, H., and Anderson, B. E.: Cleaner burning aviation fuels can reduce contrail cloudiness, Commun. Earth Environ., 2, 114, https://doi.org/10.1038/s43247-021-00174-y, 2021.

Voigt, C., Schumann, U., Minikin, A., Abdelmonem, A., Afchine, A., Borrmann, S., Boettcher, M., Buchholz, B., Bugliaro, L., Costa, A., Curtius, J., Dollner, M., Dörnbrack, A., Dreiling, V., Ebert, V., Ehrlich, A., Fix, A., Forster, L., Frank, F., Fütterer, D., Giez, A., Graf, K., Grooß, J.-U., Groß, S., Heimerl, K., Heinold, B., Hüneke, T., Järvinen, E., Jurkat, T., Kaufmann, S., Kenntner, M., Klingebiel, M., Klimach, T., Kohl, R., Krämer, M., Krisna, T. C., Luebke, A., Mayer, B., Mertes, S., Molleker, S., Petzold, A., Pfeilsticker, K., Port, M., Rapp, M., Reutter, P., Rolf, C., Rose, D., Sauer, D., Schäfler, A., Schlage, R., Schnaiter, M., Schneider, J., Spelten, N., Spichtinger, P., Stock, P., Walser, A., Weigel, R., Weinzierl, B., Wendisch, M., Werner, F., Wernli, H., Wirth, M., Zahn, A., Ziereis, H., and Zöger, M.: ML-CIRRUS: The airborne experiment on natural cirrus and contrail cirrus with the high-altitude long-range research aircraft HALO, B. Am. Meteorol. Soc., 98, 271–288, https://doi.org/10.1175/BAMS-D-15- 00213.1, 2017.

Volodin, E. M., Kostrykin, S. V, & Ryaboshapko, A. G. (2011). Climate response to aerosol injection at different stratospheric locations. Atmospheric Science Letters, 12(4), 381–385. https://doi.org/https://doi.org/10.1002/asl.351

Wandinger, U., Floutsi, A. A., Baars, H., Haarig, M., Ansmann, A., Hünerbein, A., … Cole, J. (2023). HETEAC – the Hybrid End-To-End Aerosol Classification model for EarthCARE. Atmospheric Measurement Techniques, 16(10), 2485–2510. https://doi.org/10.5194/amt-16-2485-2023

Wang, H., Rasch, P. J., and Feingold, G.: Manipulating marine stratocumulus cloud amount and albedo: a process-modelling study of aerosol-cloud-precipitation interactions in response to injection of cloud condensation nuclei, Atmos. Chem. Phys., 11, 4237–4249, https://doi.org/10.5194/acp-11-4237-2011, 2011.

Watson-Parris, D., Smith, C.J. Large uncertainty in future warming due to aerosol forcing. Nat. Clim. Chang. 12, 1111–1113 (2022). https://doi.org/10.1038/s41558-022- 01516-0

Waquet, F., Riedi, J. C., Labonnote, L., Goloub, P., Cairns, B., Deuzé, J.-L., & Tanré, D. (2009). Aerosol remote sensing over clouds using A-Train observations. *Journal of the Atmospheric Sciences, 66*(8), 2468–2480. https://doi.org/10.1175/2009JAS3026.1

Weger, M., Heinold, B., Engler, C., Schumann, U., Seifert, A., Fößig, R., Voigt, C., Baars, H., Blahak, U., Borrmann, S., Hoose, C., Kaufmann, S., Krämer, M., Seifert, P., Senf, F., Schneider, J., and Tegen, I.: The impact of mineral dust on cloud formation during the Saharan dust event in April 2014 over Europe, Atmos. Chem. Phys., 18, 17545–17572, https://doi.org/10.5194/acp-18-17545-2018, 2018.

Weigel, R., Spichtinger, P., Mahnke, C., Klingebiel, M., Afchine, A., Petzold, A., Krämer, M., Costa, A., Molleker, S., Reutter, P., Szakáll, M., Port, M., Grulich, L., Jurkat, T., Minikin, A., and Borrmann, S.: Thermodynamic correction of particle concentrations measured by underwing probes on fast-flying aircraft, Atmos. Meas. Tech., 9, 5135–5162, https://doi.org/10.5194/amt-9- 5135-2016, 2016.

Wehr, T., Kubota, T., Tzeremes, G., Wallace, K., Nakatsuka, H., Ohno, Y., Koopman, R., Rusli, S., Kikuchi, M., Eisinger, M., Tanaka, T., Taga, M., Deghaye, P., Tomita, E., and Bernaerts, D.: The EarthCARE mission – science and system overview, Atmos. Meas. Tech., 16, 3581–3608, https://doi.org/10.5194/amt-16-3581-2023, 2023.

Wei-Kuo Tao, Jen-Ping Chen, Zhanqing Li, Chien Wang, and Chidong Zhang. Impact of aerosols on convective clouds and precipitation. Reviews of Geophysics, 50(2), doi:10.1029/2011RG000369, 2012.

Weisenstein, D. K., Visioni, D., Franke, H., Niemeier, U., Vattioni, S., Chiodo, G., … Keith, D. W. (2022). An interactive stratospheric aerosol model intercomparison of solar geoengineering by stratospheric injection of SO$_{2}$ or accumulation-mode sulfuric acid aerosols. Atmospheric Chemistry and Physics, 22(5), 2955–2973. https://doi.org/10.5194/acp-22-2955-2022

Weisenstein, D. K., Keith, D. W., & Dykema, J. A. (2015). Solar geoengineering using solid aerosol in the stratosphere. Atmospheric Chemistry and Physics, 15(20), 11835–11859. https://doi.org/10.5194/acp-15-11835-2015

Wells, A. F., M. Henry, E. M. Bednarz, D. G. MacMartin, A. Jones, M. Dalvi, and J. M. Haywood: Identifying climate impacts from different stratospheric aerosol injection strategies in UKESM1, Earth Space Sci., 11(3), e2023EF004358, https://doi.org/10.1029/2023EF004358, 2024

Werdell, P. Jeremy, Michael J. Behrenfeld, Paula S. Bontempi, Emmanuel Boss, Brian Cairns, Gary T. Davis, Bryan A. Franz et al. "The Plankton, Aerosol, Cloud, ocean Ecosystem mission: status, science, advances." Bulletin of the American Meteorological Society 100, no. 9 (2019): 1775-1794, https://doi.org/10.1175/BAMS-D-18-0056.1, 2019.

Wigley, T. M. L. (2006). A combined mitigation/geoengineering approach to climate stabilization. Science (New York, N.Y.), 314(5798), 452–454. https://doi.org/10.1126/science.1131728

Winker, David M., Mark A. Vaughan, Ali Omar, Yongxiang Hu, Kathleen A. Powell, Zhaoyan Liu, William H. Hunt, and Stuart A. Young. "Overview of the CALIPSO mission and CALIOP data processing algorithms." Journal of Atmospheric and Oceanic Technology 26, no. 11: 2310-2323, doi:10.1175/2009JTECHA1281.1, 2009.

Wrana, F., von Savigny, C., Zalach, J., and Thomason, L. W.: Retrieval of stratospheric aerosol size distribution parameters using satellite solar occultation measurements at three wavelengths, Atmos. Meas. Tech., 14, 2345–2357, https://doi.org/10.5194/amt-14-2345-2021, 2021

Yuan, T., Song, H., Oreopoulos, L. et al. Abrupt reduction in shipping emission as an inadvertent geoengineering termination shock produces substantial radiative warming. Commun Earth Environ 5, 281 (2024). https://doi.org/10.1038/s43247-024-01442-3

Yu F., Kärcher B., Anderson B.E.: Revisiting Contrail Ice Formation: Impact of Primary Soot Particle Sizes and Contribution of Volatile Particles, Environ Sci Technol. 2024 Oct 8;58(40):17650-17660. doi: 10.1021/acs.est.4c04340, 2024.

Vattioni, S., et al., “Injecting solid particles into the stratosphere could mitigate global warming but currently entails great uncertainties.” Communications Earth & Environment / Nature-type article 2025.Zarnetske, P. L., Gurevitch, J., Franklin, J., Groffman, P. M., Harrison, C. S., Hellmann, J. J.,...Tilmes, S. (2021). Potential ecological impacts of climate intervention by reflecting sunlight to cool Earth. Proceedings of the National Academy of Sciences, 118(15), e1921854118. https://doi.org/10.1073/pnas.1921854118

Zalach, J., von Savigny, C., Langenbach, A., Baumgarten, G., Lübken, F.-J., and Bourassa, A.: Challenges in retrieving stratospheric aerosol extinction and particle size from ground-based RMR-LIDAR observations, Atmos. Meas. Tech. Discuss., https://doi.org/10.5194/amt-2019-267, 2019

Zhang, J., Chen, Y.-S., Gryspeerdt, E., Yamaguchi, T., & Feingold, G. (2025). Radiative forcing from the 2020 shipping fuel regulation is large but hard to detect. Communications Earth & Environment, 6, 18. https://doi.org/10.1038/s43247-024-01911-9

Zhang, Y., MacMartin, D. G., Visioni, D., Bednarz, E., & Kravitz, B. (2023). Introducing a Comprehensive Set of Stratospheric Aerosol Injection Strategies. EGUsphere, 2023, 1–32. https://doi.org/10.5194/egusphere-2023-117

Zhao, M., Cao, L., Bala, G., & Duan, L. (2021). Climate response to latitudinal and altitudinal distribution of stratospheric sulfate aerosols. Journal of Geophysical Research: Atmospheres, 126(24), e2021JD035379. https://doi.org/10.1029/2021JD035379 .

Zheng, Y. and Rosenfeld, D.: Linear relation between convective cloud base height and updrafts and application to satellite retrievals, Geophys. Res. Lett., 42, 6485-6491, https://doi.org/10.1002/2015GL064809, 2015.

Zhu, Y., Toon, O. B., Jensen, E. J., Bardeen, C. G., Mills, M. J., Tolbert, M. A., … Woods, S. (2020). Persisting volcanic ash particles impact stratospheric SO2 lifetime and aerosol optical properties. Nature Communications, 11(1), 4526. https://doi.org/10.1038/s41467-020-18352-5

Zhu, Y., Toon, O. B., Jensen, EZhu, Y., Toon, O. B., Jensen, E. J., Bardeen, C. G., Mills, M. J., Tolbert, M. A., Yu, P., and Woods, S.: Persisting volcanic ash particles impact stratospheric SO2 lifetime and aerosol optical properties, Nat. Commun., 11, 4526, https://doi.org/10.1038/s41467-020-18352-5, 2020.

Zhu, J., Penner, J. E., Garnier, A., Boucher, O., Gao, M., Song, L., Deng, J., Liu, C, and Fu, P.: Decreased aviation leads to increased ice crystal number and a positive radiative effect in cirrus clouds, AGU Advances, 3, e2021AV000546, https://doi.org/10.1029/2021AV000546, 2022.